

# High-Performance Computing and Engineering Applications in Electromagnetics

Guest Editors: Ning Yuan, Joshua Le-Wei Li, Jun Hu,  
and Ashutosh Bhardwaj





---

# **High-Performance Computing and Engineering Applications in Electromagnetics**

International Journal of Antennas and Propagation

---

## **High-Performance Computing and Engineering Applications in Electromagnetics**

Guest Editors: Ning Yuan, Joshua Le-Wei Li, Jun Hu,  
and Ashutosh Bhardwaj



---

Copyright © 2012 Hindawi Publishing Corporation. All rights reserved.

This is a special issue published in “International Journal of Antennas and Propagation.” All articles are open access articles distributed under the Creative Commons Attribution License, which permits unrestricted use, distribution, and reproduction in any medium, provided the original work is properly cited.

## Editorial Board

M. Ali, USA  
Charles Bunting, USA  
Dau-Chyrh Chang, Taiwan  
Deb Chatterjee, USA  
Z. Chen, Singapore  
Christos Christodoulou, USA  
Shyh-Jong Chung, Taiwan  
Tayeb A. Denidni, Canada  
Karu P. Esselle, Australia  
Miguel Ferrando, Spain  
Wei Hong, China  
Hon Tat Hui, Singapore  
Tamer S. Ibrahim, USA

Shyh-Kang Jeng, Taiwan  
Mandeep Jit Singh, Malaysia  
Ahmed A. Kishk, Canada  
Ju-Hong Lee, Taiwan  
Byungje Lee, Republic of Korea  
L. Li, Singapore  
Yilong Lu, Singapore  
Andrea Massa, Italy  
Derek McNamara, Canada  
Ananda Mohan, Australia  
Pavel Nikitin, USA  
A. D. Panagopoulos, Greece  
Matteo Pastorino, Italy

Sadasiva M. Rao, USA  
Stefano Selleri, Italy  
Krishnasamy T. Selvan, Malaysia  
Zhongxiang Q. Shen, Singapore  
Seong-Youp Suh, USA  
Parveen Wahid, USA  
Yuanxun Ethan Wang, USA  
Quan Xue, Hong Kong  
Tat Soon Yeo, Singapore  
Wenhua Yu, USA  
Lei Zhu, Singapore

# Contents

**High-Performance Computing and Engineering Applications in Electromagnetics**, Ning Yuan, Joshua Le-Wei Li, Jun Hu, and Ashutosh Bhardwaj  
Volume 2012, Article ID 258078, 2 pages

**A High-Performance Parallel FDTD Method Enhanced by Using SSE Instruction Set**, Dau-Chyrh Chang, Lihong Zhang, Xiaoling Yang, Shao-Hsiang Yen, and Wenhua Yu  
Volume 2012, Article ID 851465, 10 pages

**Analytical Method and Semianalytical Method for Analysis of Scattering by Anisotropic Sphere: A Review**, Chao Wan and Hongning Li  
Volume 2012, Article ID 782320, 13 pages

**Transient Response of Thin Wire above a Layered Half-Space Using TDIE/FDTD Hybrid Method**, Bing Wei, Qiong He, Jie Li, Ren-xian Li, and Li-xin Guo  
Volume 2012, Article ID 321452, 7 pages

**Design of Meander-Line Antennas for Radio Frequency Identification Based on Multiobjective Optimization**, X. L. Travassos, A. C. Lisboa, and D. A. G. Vieira  
Volume 2012, Article ID 795464, 5 pages

**Hierarchical Matrices Method and Its Application in Electromagnetic Integral Equations**, Han Guo, Jun Hu, Hanru Shao, and Zaiping Nie  
Volume 2012, Article ID 756259, 9 pages

**Study on High Performance of MPI-Based Parallel FDTD from WorkStation to Super Computer Platform**, Z. L. He, K. Huang, Y. Zhang, Y. Yan, and C. H. Liang  
Volume 2012, Article ID 659509, 7 pages

**Application of OpenMP to Wireline Triaxial Induction Logging in 1D Layered Anisotropic Medium**, Zhijuan Zhang, Ning Yuan, and Richard Liu  
Volume 2012, Article ID 864748, 12 pages

**Full-Wave Analysis of Traveling-Wave Field-Effect Transistors Using Finite-Difference Time-Domain Method**, Koichi Narahara  
Volume 2012, Article ID 948972, 9 pages

**RCS Computation by Parallel MoM Using Higher-Order Basis Functions**, Ying Yan, Yu Zhang, Chang-Hong Liang, Hui Zhao, and D. García-Doñoro  
Volume 2012, Article ID 745893, 8 pages

**Design and Optimization of an EBG Antenna with an Efficient Electromagnetic Solver**, Josefa Gómez, Abdelhamid Tayebi, José Ramón Almagro, Iván González, and Felipe Cátedra  
Volume 2012, Article ID 427178, 8 pages

**On the Finite Element Tearing and Interconnecting Method for Scattering by Large 3D Inhomogeneous Targets**, Ming-Lin Yang and Xin-Qing Sheng  
Volume 2012, Article ID 898247, 6 pages

**Optimized Operator-Splitting Methods in Numerical Integration of Maxwell's Equations**, Z. X. Huang, X. L. Wu, W. E. I. Sha, and B. Wu  
Volume 2012, Article ID 956431, 8 pages

## Editorial

# High-Performance Computing and Engineering Applications in Electromagnetics

Ning Yuan,<sup>1</sup> Joshua Le-Wei Li,<sup>2</sup> Jun Hu,<sup>2</sup> and Ashutosh Bhardwaj<sup>3</sup>

<sup>1</sup>Department of Electrical and Computer Engineering, University of Houston, Houston, TX 77004, USA

<sup>2</sup>Department of Microwave Engineering, University of Electronic Science and Technology of China, Chengdu 610054, China

<sup>3</sup>Department of Physics & Astrophysics, University of Delhi, Delhi 11007, India

Correspondence should be addressed to Ning Yuan, nyuan@uh.edu

Received 19 December 2011; Accepted 19 December 2011

Copyright © 2012 Ning Yuan et al. This is an open access article distributed under the Creative Commons Attribution License, which permits unrestricted use, distribution, and reproduction in any medium, provided the original work is properly cited.

With continuously enhanced computing power and practical application demand, high performance computing and its engineering applications in computational electromagnetics turn to be a topic of great importance and extensive interests. In recent years, some significant progresses have been achieved in computational efficiency enhancement by (a) developing new numerical techniques, (b) improving existing electromagnetic numerical methods (in terms of, e.g., unstructured mesh, faster direct or iterative solutions, higher-order basis functions, and characteristic basis functions), and (c) implementing parallel programming techniques such as message passing interface (MPI), OpenMP or graphics processing unit (GPU) technique. There is, however, still a large margin beyond it to move. In this special issue on high-performance computing and engineering application in electromagnetics, we have solicited 12 papers on some recent advances in the field covering a wide range from new techniques to applications of developed techniques.

The paper by H. Guo et al. of this special issue proposes a multilevel-SAI preconditioner to accelerate the convergence rate of Krylov iterations for solving the matrix equation of the method of moments (MoM) based on the hierarchical matrix method. The numerical performance of the preconditioner is investigated in detail and proved to be more efficient than the conventional “single level” preconditioners. The paper by Y. Yan et al. describes the Message Passing Interface (MPI) parallel implementation of the MoM solution with higher-order basis functions. The method can be used to calculate the radar cross section (RCS) of various electrically large objects with high efficiencies. The paper by J. Gómez et

al. presents an efficient EM solver based on the MoM with the inclusion of hybrid (asymptotic and rigorous) techniques, MPI, multilevel fast multipole algorithm (MLFMA), and domain decomposition methods. The EM solver is used to the design and optimization of an EBG antenna, and gain enhancement was achieved by using the EBG structure.

The paper by X. L. Travassos et al. of this special issue presents optimization problem formulations to design meander line antennas for passive UHF radiofrequency identification tags based on given specifications of input impedance, frequency range, and geometric constraints. The paper by Z. Zhang et al. applies OpenMP to parallelize the simulation of triaxial induction logging tools in 1D multilayered anisotropic formations based on the transmission theory. The parallel process is explained in detail, and the effect of the parallel code is demonstrated.

The paper by M.-L. Yang and X.-Q. Sheng applies the finite element-tearing and interconnecting (FETI) method with the absorbing boundary condition (ABC) to characterize electromagnetic scattering by large inhomogeneous objects. Two algorithms of FETI method are implemented, and their performances are investigated in detail. The paper by Z. X. Huang et al. proposes an optimized operator splitting methods for numerical integration of the time-domain Maxwell's equations. It is found that the optimized schemes with coarse discrete grid and large CFL number can obtain satisfactory numerical results. The paper by W. Chao and H. Li is a review of EM-scattering methods for two general cases of anisotropic spheres, that is, Cartesian anisotropic and spherical anisotropic. The paper uses plane wave decomposition and T matrix to deal with Cartesian

anisotropic sphere and separation of variables for spherically anisotropic sphere.

Other 4 papers all focus on the FDTD method. The paper by Z. L. He et al. presents a parallel finite difference time domain (FDTD) method to analyze electrically large targets on a super computer. The influence of different virtual topology schemes on parallel performance of parallel FDTD is studied in detail, and general rules to obtain the highest efficiency are presented. The paper by K. Narahara developed an FDTD model of the field-effect transistors (FETs) by using piecewise-linear modeling to eliminate route-finding routines in an FDTD solver. Then FETs are characterized in FDTD scheme without significant computational costs for analysis of traveling-wave field effect transistors (TWFETs). The paper by W. Bing et al. describes a TDIE/FDTD hybrid method for calculating the transient responses of thin wire above a lossy half space. The method is highly efficient and requires less memory. The paper by D.-C. Chang et al. of this special issue introduces a hardware acceleration technique for the parallel finite difference time domain (FDTD) method using the SSE (streaming SIMD (single instruction multiple data) extensions) instruction set. The implementation of SSE instruction significantly improves the performance of the parallel FDTD.

*Ning Yuan*  
*Joshua Le-Wei Li*  
*Jun Hu*  
*Ashutosh Bhardwaj*

## Application Article

# A High-Performance Parallel FDTD Method Enhanced by Using SSE Instruction Set

**Dau-Chyrh Chang,<sup>1</sup> Lihong Zhang,<sup>2</sup> Xiaoling Yang,<sup>3</sup> Shao-Hsiang Yen,<sup>4</sup> and Wenhua Yu<sup>5</sup>**

<sup>1</sup> *Oriental Institute of Technology, Taipei 22061, Taiwan*

<sup>2</sup> *Communication University of China, Beijing 100024, China*

<sup>3</sup> *Pennsylvania State University, University Park, PA 16803, USA*

<sup>4</sup> *Oriental Institute of Technology, Taipei 22061, Taiwan*

<sup>5</sup> *2COMU, State College, PA 16803, USA*

Correspondence should be addressed to Dau-Chyrh Chang, dcchang@mail.oit.edu.tw

Received 20 July 2011; Accepted 30 November 2011

Academic Editor: Joshua Le-Wei Li

Copyright © 2012 Dau-Chyrh Chang et al. This is an open access article distributed under the Creative Commons Attribution License, which permits unrestricted use, distribution, and reproduction in any medium, provided the original work is properly cited.

We introduce a hardware acceleration technique for the parallel finite difference time domain (FDTD) method using the SSE (streaming (single instruction multiple data) SIMD extensions) instruction set. The implementation of SSE instruction set to parallel FDTD method has achieved the significant improvement on the simulation performance. The benchmarks of the SSE acceleration on both the multi-CPU workstation and computer cluster have demonstrated the advantages of (vector arithmetic logic unit) VALU acceleration over GPU acceleration. Several engineering applications are employed to demonstrate the performance of parallel FDTD method enhanced by SSE instruction set.

## 1. Introduction

Since the FDTD method is firstly proposed by Yee in 1966 [1] for solving Maxwell's equations as a type of difference algorithm, it has grown into a popular computational electromagnetic technique after decades of development and become a major electromagnetic simulation tool today. Compared to other computational methods, the FDTD method becomes more and more popular for the practical and complex problems because of its simplicity and flexibility. In addition, the broadband characteristics of the FDTD method allow us to achieve the wideband frequency response in a single simulation. For the electrically large and multiscale problems, it may take too long time for the FDTD simulation to reach the convergent solution. In order to overcome this disadvantage of the FDTD method, there are a large number of publications on the related topics such as conformal technique [2] to enlarge the cell size, subgridding scheme [3] to use local fine mesh, and ADI algorithm [4] to increase the size of time step. On other hand, to use the multicore PC, multi-CPU workstation, and computer cluster to speed up

the electromagnetic simulation, the parallel processing based on the (message passing interface) MPI library [5] and (open multiprocessing) OpenMP [6].

With development of the multicore processors, (graphics processing unit) GPU [7] has drawn a lot of attentions in the past ten years since an advanced GPU contains up to several hundreds of computing cores. Since the field update formula in the FDTD method is similar to the format that GPU is used to display acceleration, the FDTD method is introduced to the GPU acceleration in the earlier time. However, to use GPU acceleration, the simulation format has to be in the certain requirement. For example, the data inside memory must be continuous; otherwise, the performance will be degraded dramatically. In the practical problems, the data structure inside the memory varies from one case to another. In addition, the GPU can only use the high-performance memory installed on the GPU card. Any communication between the GPU memory and main memory will cause reducing the simulation performance. Unlike the GPU acceleration, VALU acceleration will fully use the features built inside the regular CPU. Though the VALU unit has existed

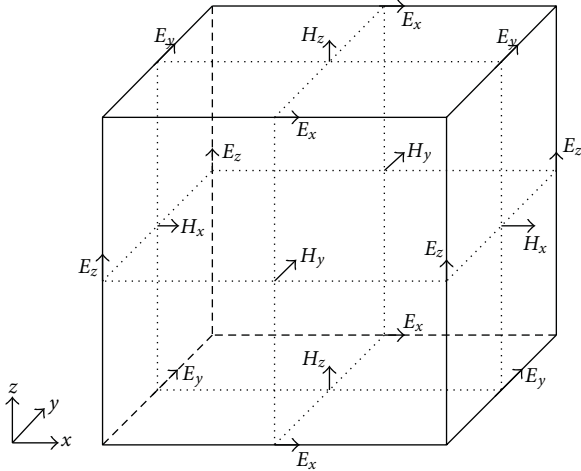


FIGURE 1: Position of E- and H-fields in the FDTD cell.

inside the CPU for many years since the Intel Pentium III. However, it has not used for the acceleration of engineering simulations. Compared to the GPU acceleration, VALU acceleration is more powerful and flexible, and it is the most important that the VALU acceleration is a general platform, and it does not require any extra hardware devices.

The VALU acceleration has been illustrated through several typical examples on both Intel and AMD processors. Since the AMD processor includes more physical cores today than Intel processor. The FDTD simulation accelerated by using VALU units can get more benefit from the AMD than Intel processors. A waveguide filter and patch antenna array are used to validate the VALU acceleration technique. In this paper, we first briefly introduce the parallel FDTD method in Section 2, and then describe the basic architecture of a regular CPU in the Section 3. Section 4 concentrates on the implementation of SSE instruction set in the parallel FDTD code. Section 5 uses several examples to demonstrate the performance improvement of SSE instruction set for the FDTD simulation. Section 6 uses a waveguide filter and patch array to demonstrate the performance improvement of SSE instruction set for the practical problem solving. Finally, we summarize the works in this paper and point out the future works.

## 2. Parallel FDTD Acceleration Method

In FDTD method, Maxwell's equations are discretized into a set of difference equations through the central difference formula. The electromagnetic wave propagation and the interaction of electromagnetic wave with the environment are analyzed through update of the electric and magnetic fields in space and time. The electric/magnetic fields in spatial and time domains can be calculated by the explicit way through its previous value at the same location and the four magnetic/electric fields around it at the half time step earlier as illustrated in Figure 1.

It is observed from Figure 1 that the FDTD method is parallel in nature due to its localized characteristics and suitable for the SSE implementation.

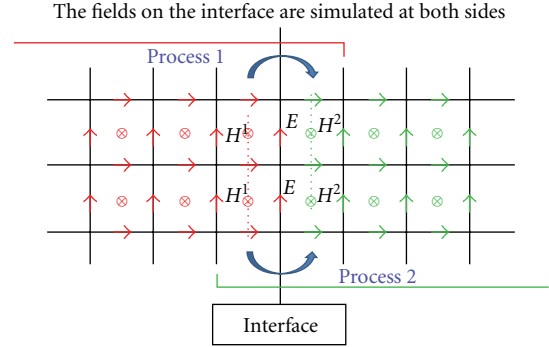


FIGURE 2: Concept of field exchange between the subdomains in the parallel processing.

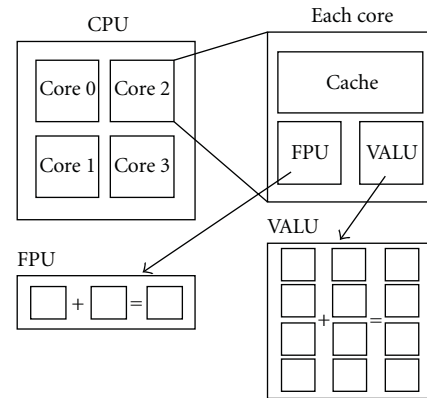


FIGURE 3: CPU architecture including FPU and VALU.

Using this feature, we can achieve an excellent parallel performance when we use the FDTD code on the multiple core processor and computer cluster because it only requires the exchange of information on the interface between the subdomains. In the several popular data exchanging methods [1], the robust one is described in Figure 2.

The MPI library is designed for the communication of distributed processors. The exchanging data in the FDTD simulation is located on the interface between the adjacent processors, as we can see from Figure 2. The parallel efficiency depends not only on the parallel code structure but also the network system. On other hand, the parallel computing on the multicore processors and multi-CPU workstation is based on the OpenMP, which is a shared memory parallel algorithm. OpenMp requires that all the cores or CPUs have the same hostname. In a practical cluster or multi-CPU workstation, MPI and OpenMp are combined to achieve a better simulation performance.

Vector unit has been existed in a regular CPU for many years; however, it was never used in the engineering simulations. In this paper, we describe the implementation approach to apply the vector unit into the FDTD simulation through the SSE instruction set. Compared to the GPU acceleration, the VALU acceleration technique is general platform and does not require any extra hardware devices. Now, we briefly introduce the architecture of regular CPU and then describe how to implement the VALU unit to speed up the FDTD simulation. Each core in the multicore

```

for(i = 0; i <= nx; i++) {
  vHi_Coeff = _mm_load1_ps(&H_i_Coeff);
  //load single float value to vector
  for(j = 0; j <= ny; j++) {
    vHj_Coeff = _mm_load1_ps(&H_j_Coeff);
    //load single float value to vector
    vEz = ( _m128 *) E_z[i][j];
    vHy = ( _m128 *) H_y[i][j];
    vHx = ( _m128 *) H_x[i][j];
    vHy_minus = ( _m128 *) H_y[i-1][j];
    vHx_minus = ( _m128 *) H_x[i][j-1];
    for(k = 0, vk = 0; k < nz; k += 4, vk++) {
      vEk_Coeff = _mm_load1_ps(&Ek_Coeff);
      xmm0 = _mm_sub_ps(vHx[vk], vHx_minus [vk]);
      xmm0 = _mm_mul_ps( vH_j_Coeff, xmm0);
      xmm1 = _mm_sub_ps(vHy[vk], vHy_minus [vk] );
      xmm1 = _mm_mul_ps(vH_i_Coeff, xmm1 );
      xmm0 = _mm_sub_ps(xmm1, xmm0);
      xmm1 = _mm_mul_ps(vEk [vk], vEk_Coeff);
      vEk [vk] = _mm_add_ps(xmm1, xmm0);
    }
  }
}

```

ALGORITHM 1

processor has its own cache, FPU and VALU, as shown in Figure 3. Unlike the FPU, the VALU allows us to operate on four data at the same time. VALU unit is a unit that allows us to arrange for 32-bit floating numbers and operate the four numbers at the same time. By the way described, we use the VALU through the SSE instruction set to accelerate the parallel conformal FDTD code.

Next, we use the electric field component update as an example to explain how the FDTD code is accelerated by using VALU unit. For example, the electric field  $E_z$  can be expressed as follows [8, 9]:

$$\begin{aligned}
E_z^{n+1}\left(i, j, k + \frac{1}{2}\right) &= E_z\_Coeff \cdot E_z^n\left(i, j, k + \frac{1}{2}\right) \\
&+ H_y\_Coeff \\
&\cdot \left[ H_y^{n+1/2}\left(i + \frac{1}{2}, j, k + \frac{1}{2}\right) \right. \\
&\quad \left. - H_y^{n+1/2}\left(i - \frac{1}{2}, j, k + \frac{1}{2}\right) \right] \quad (1) \\
&- H_x\_Coeff \\
&\cdot \left[ H_x^{n+1/2}\left(i, j + \frac{1}{2}, k + \frac{1}{2}\right) \right. \\
&\quad \left. - H_x^{n+1/2}\left(i, j - \frac{1}{2}, k + \frac{1}{2}\right) \right],
\end{aligned}$$

where  $E_z\_Coeff$ ,  $H_x\_Coeff$ , and  $H_y\_Coeff$  are coefficients in the field update equations [4]. Using the following procedure VALU can be used to compute four  $E_z$  at the same time to accelerate the simulation, which is described as follows.

- (i) Load the coefficient of the magnetic field  $H_y$  into the SSE registers.

- (ii) Load the coefficient of the magnetic field  $H_x$  into the SSE registers.
- (iii) Convert the float pointer to the SSE 128 bit pointer.
- (iv) Calculate the difference of magnetic fields.
- (v) Multiply the difference of magnetic fields and their coefficients.
- (vi) Calculate the contribution of magnetic fields to the electric fields.
- (vii) Multiply the previous electric fields and their coefficients.
- (viii) Calculate the electric fields and write them to memory (Algorithm 1).

A 3-D array in the FDTD code is allocated using the *malloc* function in C language, and *\_aligned\_malloc* function in SSE in this paper. For example, if we need a 3D array *array\_name* [*x\_size*, *y\_size*, *z\_size*], we can first define a 1D array *array\_name\_tmp* [*N*] whose size is  $N = x\_size * y\_size * z\_size$ , and then map the 1D memory address to 3D array *array\_name*. The pseudocode segment is demonstrated as below (see Algorithm 2).

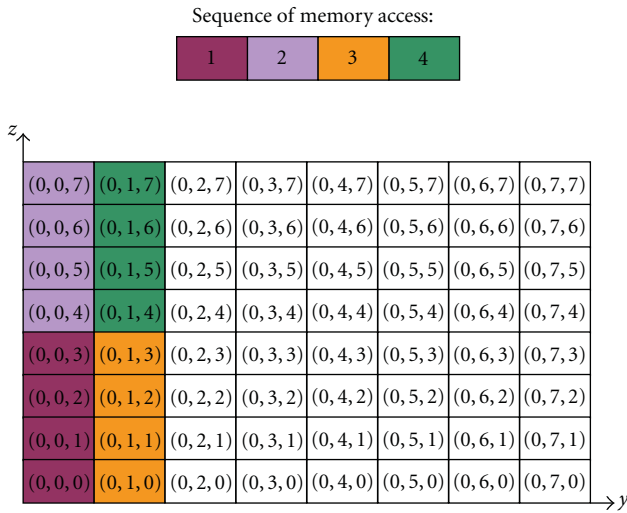
In the C programming language, the data inside the memory is contiguous in *y-z* plane. Suppose that the *y\_size* and *z\_size* are equal to 8, and the data structure of the array *array\_name* in the *y-z* plane is shown in Figure 3. The memory addresses of the data elements (0,0,0), (0,0,1)...(0,0,7) are continuous likewise, the addresses of (0,1,0), (0,1,1)...(0,1,7) are continuous too. The address of (0,0,7) is continuous and is followed by the element (0,1,0). When we calculate the electric and magnetic fields in the *y-z* plane, we only need to know the address of the first element and the total number of elements, as shown in Figure 4.

```

//allocate the 1D memory
array_name_tmp = (float*)_aligned_malloc(
    sizeof(float) * x_size * y_size * z_size, 16);
array_name = (float***)_aligned_malloc(
    sizeof(float**) * x_size, 16);
for(i = 0; i < x_size; i++) {
    array_name[i] = (float**)_aligned_malloc(
        sizeof(float*) * y_size, 16);
    for(j = 0; j < y_size; j++) {
        //map the 1D memory address to 3D array
        map_address = i * y_size * z_size + j * z_size;
        array_name[i][j] = &array_name_tmp[map_address];
    }
}

```

ALGORITHM 2

FIGURE 4: Data structure in the  $y$ - $z$  plane.

Using the VALU and the procedure mentioned above can significantly accelerate the multiplication operation compared to the traditional FDTD code. In any case, the data continuity in the FDTD code and memory bandwidth is the most important factors for the VALU acceleration. To evaluate the performance of the FDTD code, we define the performance as follows:

$$\text{Performance} = \frac{(N_x \times N_y \times N_z) \times \text{Number\_of\_timesteps}}{\text{Simulation\_time(second)}}. \quad (2)$$

For example, the performance of a regular parallel conformal FDTD code on an Intel Core i7-965 3.2 GHz is 87 Mcells/sec, as shown in Figure 4. If we apply the optimized synchronization technique on the parallel FDTD code, the performance increases to 124 Mcells/sec. When we implement the VALU acceleration technique on the parallel conformal FDTD code, the performance increases to 191 Mcells/sec. Besides the field update module, further optimization on the material list table, cache usage, dispersive medium, and near-to-far field

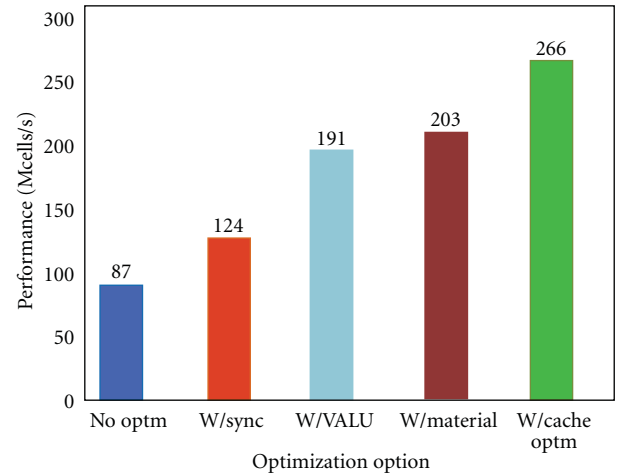


FIGURE 5: Performance improvement of the parallel conformal FDTD code using VALU acceleration technique.

transformation will also significantly improve the FDTD performance, as shown in Figure 5.

Finally, we use the parallel conformal FDTD code to simulate an ideal test case that is a hollow box with the simplest excitation and output, and its domain is truncated by using the perfect electric conductor (PEC). We ran the problem with the different sizes using the regular FDTD code (Intel Core i7-965), and the FDTD code with the VALU (Intel Core i7-965 with 4 VALUs, the total memory bandwidth is 32 GB). The simulation summary is plotted in Figure 6. It is observed from Figure 5 that the peak performance of the VALU FDTD code is four times faster than the FDTD code on a regular CPU for the ideal test case.

### 3. FDTD Performance Investigation

In this part, we employ a typical example to demonstrate the performance improvement by using the SSE instruction set on the multi-CPU workstations. The acceleration factor here reflects the simulation acceleration gained by using the SSE implementation. A typical test case includes only voltage

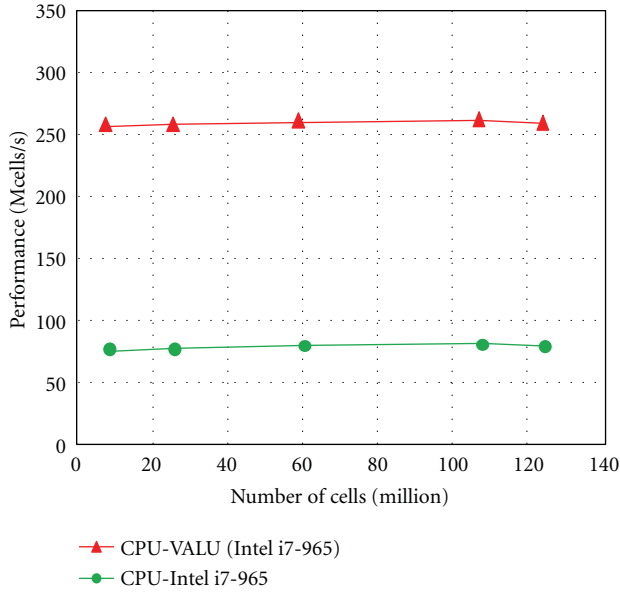


FIGURE 6: FDTD performance on CPU and CPU value for the ideal test case.

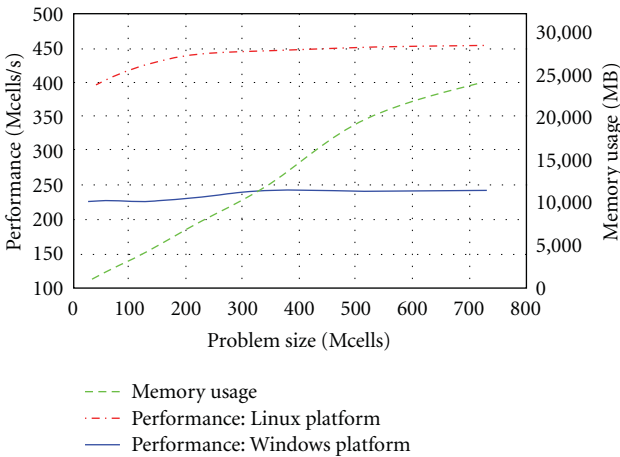


FIGURE 7: Performance of parallel FDTD enhanced by using SSE instruction set on a 2-CPU workstation platform for the different operating systems.

source and field output at a specific point. The empty box truncated by the PEC boundary is discretized into from  $300 \times 300 \times 300$  (27 Mcells),  $400 \times 400 \times 400$  (64 Mcells),  $500 \times 500 \times 500$  (125 Mcells),  $600 \times 600 \times 600$  (216 Mcells),  $700 \times 700 \times 700$  (343 Mcells),  $800 \times 800 \times 800$  (512 Mcells), and  $900 \times 900 \times 900$  (729 Mcells) uniform cells, respectively. The numerical experiments were carried out on a 2-CPU workstation that is installed with two AMD Opteron 6128 2.0 GHz processors. The simulation performance is [summarized in Figure 7].

We compare the FDTD simulation performance on one 18-node high-performance cluster and a popular nVidia Tesla C1060 GPU. The cluster with 36 Intel Xeon X5550 CPUs is installed in 18 nodes, which are connected through

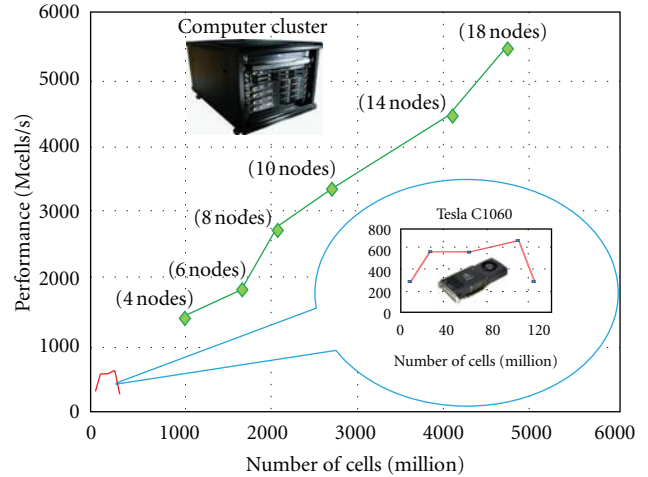


FIGURE 8: Performance of parallel FDTD enhanced by using SSE instruction set on a cluster platform and comparison to the GPU acceleration.

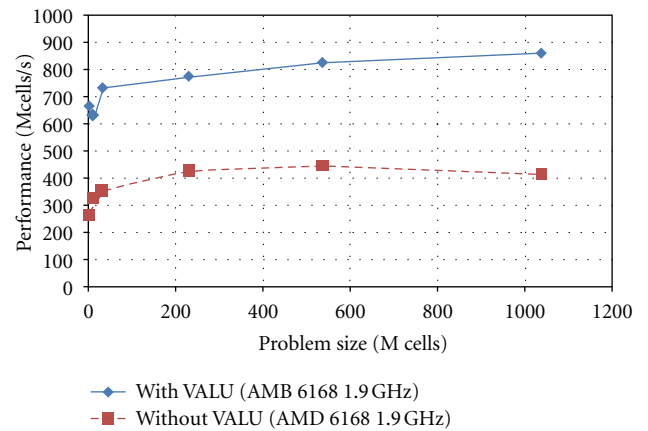


FIGURE 9: FDTD performance of the VALU acceleration on one 4-CPU workstation.

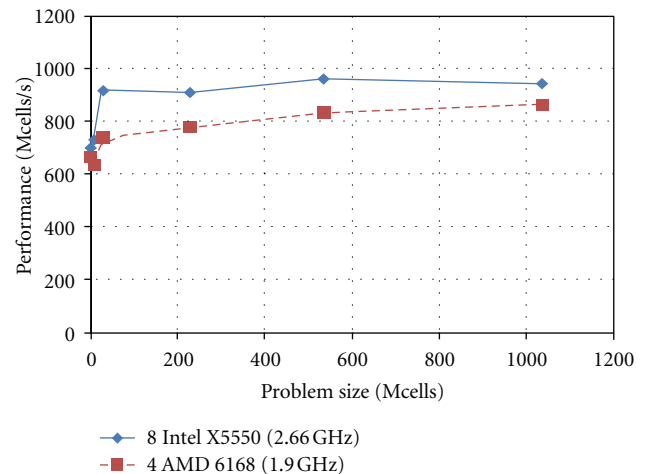


FIGURE 10: Performance comparison of parallel FDTD code on a workstation with 4 AMD CPUs and a cluster with 4 nodes (8 Intel CPUs).

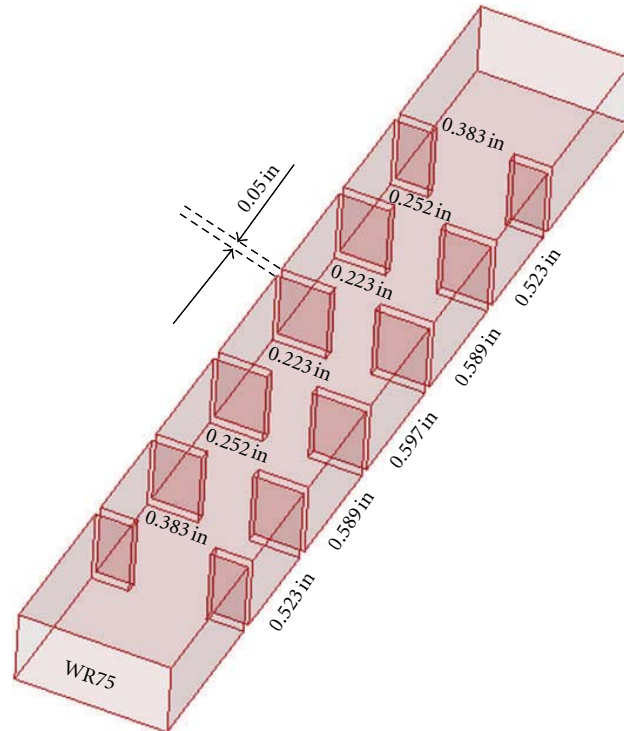


FIGURE 11: Configuration of waveguide filter with 5 open cavities.

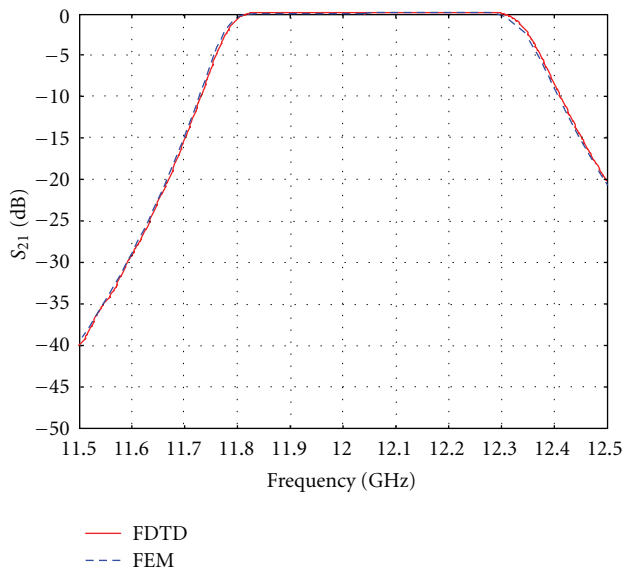


FIGURE 12: Transmission coefficient of waveguide filter generated by using enhanced FDTD method and FEM.

the 10G Ethernet system. The performance comparison between two platforms is summarized in Figure 8. For the ideal test case, one nVidia Tesla C1060 GPU has the similar performance to two Intel X5550 CPUs.

Next, we investigate the simulation performance of parallel FDTD code on a workstation installed with 4 AMD Opteron 6168 1.9 GHz CPUs. The 6-layer PML in this case

is used to truncate the computational domain. The performance of VALU acceleration is shown in Figure 9.

We can observe from Figure 8 that the VALU can improve the simulation performance 200% for the practical problem with 6-layer PML truncation. Next, we compare the performance of the workstation with 4 AMD Opteron 6168 CPUs and a cluster with 8 Intel Xeon X5550 CPUs for simulation of the same problem. The 4-node cluster with 8 Intel CPUs is connected with each other using the 10G Ethernet. The performance comparison is plotted in Figure 10, which shows that 4 AMD CPUs have the similar performance to 8 Intel CPUs. Since each AMD CPU includes 12 cores and 12 VALUs, the AMD workstation has total 48 VALUs; however, each Intel X5550 CPU only has 4 cores and 4 VALUs.

In the practical problems, the simulation factors such as output types, dispersive media, and near-to-far field transformation will influence the SSE performance due to the discontinuous data structure inside memory. However, it can be improved by optimizing the cache hit ratio.

#### 4. Engineering Applications

In this part, we use the parallel FDTD code accelerated by using the SSE instruction set to simulate a waveguide (WR75) filter problem [8], as shown in Figure 11. The filter includes five cavities and is excited by  $TE_{10}$  mode at one end. The output parameter transmission coefficient for the  $TE_{10}$  mode is measured at another end. The purpose is to

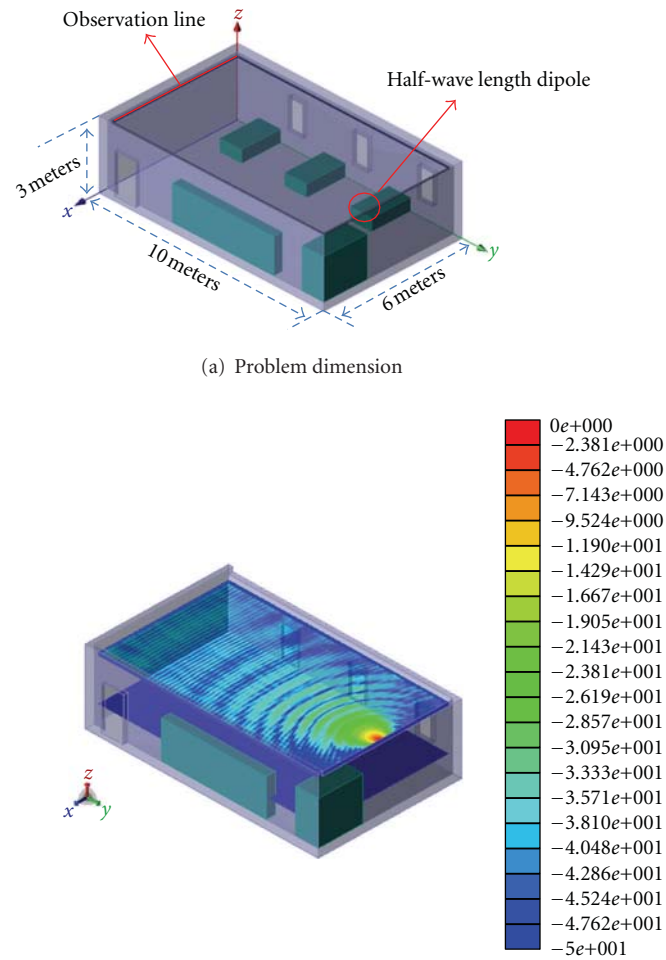
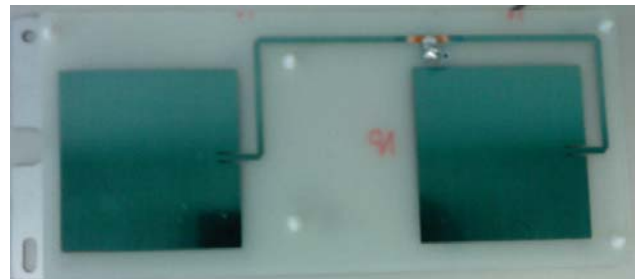
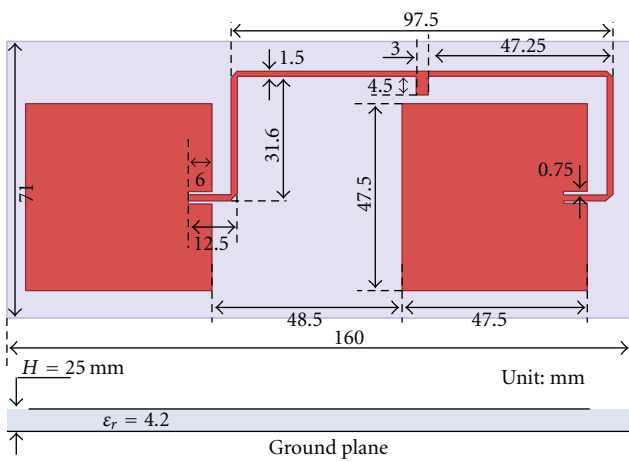


FIGURE 13: A typical patient room as an example to demonstrate the FDTD performance enhanced with SSE instruction set.



(a) Top and side views of the patch array

(b) Prototype of the patch array

FIGURE 14: Configuration of a patch array and the prototype. (a) Configuration of the patch array; (b) prototype of the patch array.

TABLE 1: Parallel FDTD performance with the SSE acceleration.

	FDTD with SSE acceleration	FDTD without SSE acceleration
Workstation	2 × AMD Opteron 6128 2.0 GHz	
Memory usage	37 MB	37 MB
Simulation time	145 sec	345 sec

TABLE 2: Performance comparison of parallel FDTD method on 4-CPU workstation and high-performance cluster.

Platform	CPU type	Network	Simulation time
Workstation (4 CPUs, 64 GB RAM)	AMP Opteron 6168 1.9 GHz(\$795 each)	No network	319 min. (with hardware acceleration and NUMA)
2 CPUs (24 GB RAM)	Intel Xeon X5570 2.93 GHz(\$1465 each)	No network	1720 min. (with hardware acceleration, no NUMA)
128 CPUs (1536 GB RAM)	Intel Xeon X5570 2.93 GHz(\$1465 each)	Infiniband	29 min.37 sec. (with hardware acceleration no NUMA)

investigate the performance of SSE acceleration on the 2-CPU workstation for the practical problem.

For the sake of comparison, we use the FEM method [9] to simulate the same problem and plot the results in Figure 11. It is evident from Figure 12 to observe the good agreement. It is worthwhile to mention that the results are same with and without the SSE acceleration.

The parallel FDTD performance with the SSE acceleration is summarized in Table 1. It is observed from Table 1 that the SSE can accelerate the FDTD code 2.37 times for this practical problem.

Next, we use the parallel FDTD performance with the SSE acceleration to simulate a patient room, as shown in Figure 13, in which the field distribution is generated by a dipole antenna, as shown in Figure 13. The room dimension is  $10 \times 5 \times 3$  meters, which is discretized into  $3333 \times 1666 \times 1000$  uniform cells. The simulation performance is summarized in Table 2. It is observed from Table 2 that a workstation with 4 AMD Opteron 6168 1.9 GHz CPUs has the similar performance as the 10 Intel Xeon X5570 2.93 GHz CPUs. It is worthwhile to mention that, without the SSE acceleration, one AMD AMD Opteron 6168 1.9 GHz CPU has the same performance as one Intel Xeon X5570 2.93 GHz CPU.

The simulation on the cluster platform was provided by an independent third party. The cluster does not support the NUMA architecture. Otherwise, the cluster performance should be better.

Finally, we use the parallel FDTD code enhanced by SSE instruction set to simulate a patch array [10] for IEEE802.11b. The array includes 2 patch antenna elements and arrayed in E-plane. The simulation model and hardware implementation are shown in Figure 14. The substrate is FR4 with relative dielectric constant 4.2. The size of array is 71 mm (width) by 160 mm (length) and by 0.8 mm (thickness). The substrate is 2.5 mm above ground plane. The array is measured at Communication Research Center of Oriental Institute of Technology by

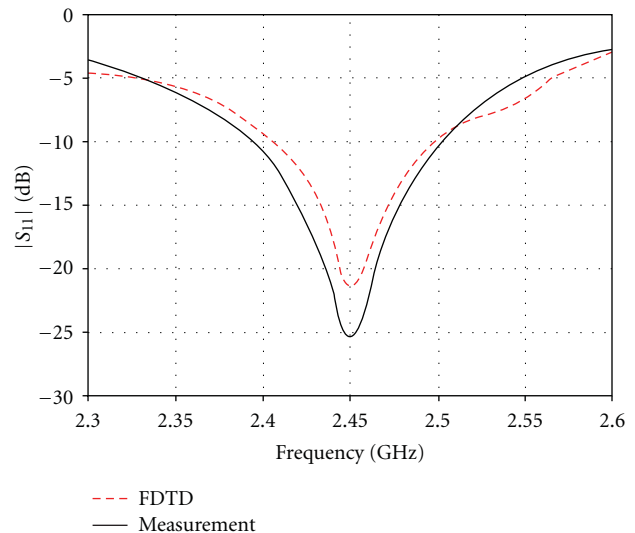


FIGURE 15: Return loss of the antenna array.

vector network analyzer for return loss and near field range for power pattern. It is observed from Figures 15 and 16 for the return loss and power patterns of the array the good agreement between the FDTD simulation and measurement. The E-plane power patterns at frequencies 2.41 GHz, 2.44 GHz, and 2.46 GHz are shown in Figure 16. The copolar patterns are in agreement for both FDTD simulation and measurement. The minor difference of x-polar patterns for both FDTD simulation and measurement may be caused by the improper hardware implementation or measurement.

## 5. Conclusions

In this paper, we propose a new hardware acceleration technique based on the SSE instruction set and give an implementation technique. The result shows that this technique

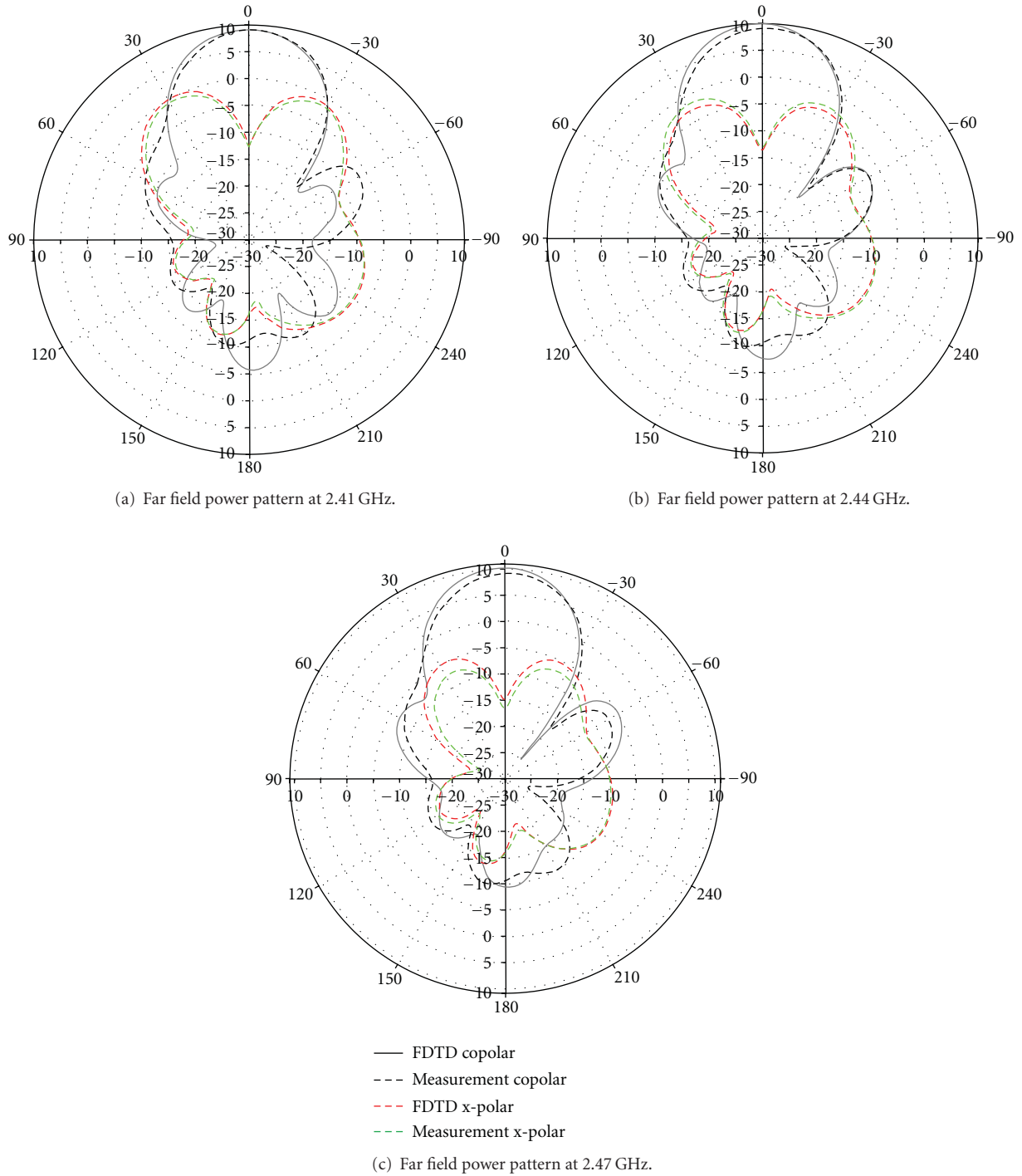


FIGURE 16: E-plane far field power pattern of the patch antenna array at 2.41 GHz, 2.44 GHz, and 2.47 GHz.

dramatically improves the computing efficiency without any extra hardware investment and provides an efficient and economical technique for the electromagnetic simulations.

**References**

[1] K. Yee, "Numerical solution of initial boundary value problems involving Maxwell's equations in isotropic media," *IEEE*

*Transactions on Antennas and Propagation*, vol. 14, no. 5, pp. 302–307, 1966.  
 [2] W. Gropp, E. Lusk, and A. Skjellum, *Using MPI: Portable Parallel Programming with the Message-Passing Interface*, MIT Press, Cambridge, Mass, USA, 2nd edition, 1999.  
 [3] <https://computing.llnl.gov/tutorials/openMP/>.  
 [4] A. Elsherbeni and V. Demir, *The Finite Difference Time Domain Method for Electromagnetics: With MATLAB Simulations*, SciTech Publisher, Raleigh, NC, USA, 2009.

- [5] Intel corporation, Intel Architecture Optimization Reference Manual, <http://www.intel.com/design/pentiumii/manuals/245127.htm>.
- [6] A. Taflove and S. Hagness, *Computational Electrodynamics the Finite-Difference Time Domain Method*, Artech House, Norwood, Mass, USA, 2005.
- [7] W. Yu, X. Yang, Y. Liu, R. Mittra, and A. Muto, *Advanced FDTD Method: Acceleration, Parallelization and Engineering Applications*, Artech House, Norwood, Mass, USA, 2011.
- [8] M. Yu, "Power-handling capability for RF filters," *IEEE Microwave Magazine*, vol. 8, no. 5, pp. 88–97, 2007.
- [9] J. M. Jin, *The Finite Element Method in Electromagnetics*, John Wiley & Sons, New York, NY, USA, 2002.
- [10] C. Balanis, *Antenna Theory*, John Wiley & Sons, New York, NY, USA, 1987.

## Review Article

# Analytical Method and Semianalytical Method for Analysis of Scattering by Anisotropic Sphere: A Review

Chao Wan<sup>1</sup> and Hongning Li<sup>2</sup>

<sup>1</sup>Department of Electrical and Computer Engineering, National University of Singapore, Kent Ridge, Singapore 117583

<sup>2</sup>State Key Laboratory of Integrated Service Networks, Xidian University, Xi'an, Shaanxi 710071, China

Correspondence should be addressed to Chao Wan, wanchao@nus.edu.sg

Received 14 July 2011; Accepted 3 November 2011

Academic Editor: Joshua Le-Wei Li

Copyright © 2012 C. Wan and H. Li. This is an open access article distributed under the Creative Commons Attribution License, which permits unrestricted use, distribution, and reproduction in any medium, provided the original work is properly cited.

The history of methods for the electromagnetic scattering by an anisotropic sphere has been reviewed. Two main methods, angular expansion method and T-matrix method, which are widely used for the anisotropic sphere, are expressed in Cartesian coordinate firstly. The comparison of those and the further exploration on the scattering field are illustrated afterwards. Based on the most general form concluded by variable separation method, the coupled electric field and magnetic field of radial anisotropic sphere can be derived. By simplifying the condition, simpler case of uniaxial anisotropic media is expressed with confirmed coefficients for the internal and external field. Details of significant phenomenon are presented.

## 1. Introduction

Since the properties of isotropic homogeneous sphere is formulated by Lorentz [1] and Mie [2], due to plenty of corresponding significant phenomena [3–6] and increasing applications in atmospheric optics, remote sensing, computational electromagnetic and photonics, electromagnetic wave propagation and scattering for a sphere has been a subject of great interest in recent years. The amazing properties of solid anisotropic materials in nature and classes of artificial metamaterials of anisotropy would possibly produce plentiful technological applications. In the meantime, fabrication technology development has greatly enlarged the area of the anisotropic materials.

Cartesian anisotropic medium and Radial anisotropic medium are considered as two classic kinds of anisotropic materials [7]. Some novel properties of Cartesian anisotropy medium have been studied: magnetic plasma realizing the subdiffraction imaging [8], optical cavity made by indefinite medium of anisotropy [9], the sharply asymmetric reflection (SAR) effect [10], formation of tunable resonant photonic band gaps [11], negative-refractive behavior manipulation [12], and self-guiding unidirectional electromagnetics edge [13]. Based on the general anisotropic materials, those amazing properties can greatly enlarge the possibility to control light and wave in special structure and also open a new

research area in the interaction between the electromagnetic wave and materials. For radial anisotropic materials, the spherical particle is of great interest [14–16]. The radial anisotropic particle scattering provides an insight into the interaction between the microparticles and the microwave or optical illumination by external devices [17–19], which could help to detect the position for some abnormal proteins [7, 20]. The classic spherical cloaks have been achieved by radial anisotropic materials [21]. The surface plasma resonance invisibility and extraordinary scattering of the RA particle provide a good opportunity to study the physical phenomena of microparticles.

For most of these published works, many properties of anisotropic material have been explored and applied. However, little work has been done so far on summaries and analysis for the methods to deal with problems of such anisotropic material. Scientists and engineers have to check the anisotropic class first and then choose a convenient numerical method or some commercial software. Either way will encounter redundant difficulties: for numerical method like FDTD, FEM, MOM, and other improved ones [22], prediction of the properties of medium is quite a difficulty, let alone the new structure design; for commercial software, the methods embedded in them are commonly standard, which are not able to deal with the possible novel materials

with abnormal parameters. Therefore, modeling of those novel materials becomes extremely difficult. Fortunately, the analytical method and semianalytical method such as angular expansion method and T-matrix method will be very helpful in concluding good predictions for the anisotropic problems while keeping the accuracy [23–33].

It is of major purpose to summarize the analytical and semianalytical methods and their material parameter's effects on the scattering patterns, which will be of great use in electromagnetic wave properties for Cartesian and the Radial anisotropic spheres. In Section 2, besides two general analytical and semianalytical algorithms of anisotropy in Cartesian are reviewed, advantages and disadvantages of these two methods are also illustrated. In Section 3, the variables separation method for a single radial anisotropic sphere is demonstrated and numerical results obtained. A short conclusion is provided in Section 4.

## 2. Electromagnetic Wave Scattering by a Cartesian Anisotropic Sphere

*2.1. Cartesian Anisotropy of Spheres.* For Cartesian anisotropic medium, the constitutive relations are given by

$$\bar{\epsilon} = \epsilon_s \begin{pmatrix} \epsilon_r & -i\epsilon_\kappa & 0 \\ i\epsilon_\kappa & \epsilon_r & 0 \\ 0 & 0 & 1 \end{pmatrix} \quad \bar{\mu} = \mu_s \begin{pmatrix} \mu_r & -i\mu_\kappa & 0 \\ i\mu_\kappa & \mu_r & 0 \\ 0 & 0 & 1 \end{pmatrix}, \quad (1)$$

where the identity dyadic is expressed as  $\hat{\mathbf{I}} = \hat{\mathbf{x}}\hat{\mathbf{x}} + \hat{\mathbf{y}}\hat{\mathbf{y}} + \hat{\mathbf{z}}\hat{\mathbf{z}}$ . By extending Mie theory in isotropic cases, many methods such as FDTD, FEM, and MOM have been established to analyzed wave interaction issue in the medium. However, they cannot provide an explicit explanation for the physical phenomenon. Being able to deal with multilayered problems, the dyadic green's function is considered as one analytical approach [34]. However, the researchers have to encounter the singularities while they choose the integration path, then the expression turns to be rather complicated. In [35], Uzunoglu first employed the Fourier form to state the field, followed by a lot of work on this direction for its clear computation procedure [36, 37]. Using the angular expansion to present electromagnetic field, Ren successfully transferred the three-dimensional problem into a two-dimension integration [23]. The field can be treated as combination of infinite plane wave, while only four kinds of Bessel function need to be considered according to the wave direction. After that, Dr. Sarkar gives an explicit expression of the plane wave using vector spherical wave functions, where the field in the media is a form of that infinite plane wave [38, 39]. Based on these clear field and plane wave expression, Dr. Geng proposed a transpicuous procedure and made a fundamental computation [24–28]. The same result

has been achieved by other researcher when compared with Geng's work [29]. Besides, the method firstly dealing with the photonic band problem can be seen as another way [40]. Instead of giving an explicit expression and using the integral form on the surface, Lin used the transfer matrix method to gather the information in the medium [41]. By using the complete matrix form, they express the wave number  $k$  by a matrix vector instead of an expression [32, 42], and this approach obtains great success [10–13]. Herein, we mainly focus on the review and analysis of these two analytical and semianalytical methods.

*2.2. Angular Expansion Method.* Inside the sourceless and homogeneous anisotropic sphere, the constitutive relationships as used in the Maxwell equations are

$$\nabla \times \mathbf{E} = i\omega\mathbf{B}, \quad (2)$$

$$\nabla \times \mathbf{H} = -i\omega\mathbf{D}, \quad (3)$$

$$\nabla \cdot \mathbf{D} = 0, \quad (4)$$

$$\nabla \cdot \mathbf{B} = 0. \quad (5)$$

The relations between the electric displacement vector  $\mathbf{D}$ , the magnetic induction  $\mathbf{B}$ , the electric field  $\mathbf{E}$ , and the magnetic field  $\mathbf{H}$  inside the medium are given by

$$\mathbf{D} = \bar{\epsilon} \cdot \mathbf{E}, \quad \mathbf{B} = \bar{\mu} \cdot \mathbf{H}. \quad (6)$$

The parameters are defined in Cartesian coordinates as (1). We can rewrite the Maxwell's equations in a convenient form [27]:

$$\nabla \times [\bar{\mu}^{-1} \cdot \nabla \times \mathbf{E}] - \omega^2 \bar{\epsilon} \cdot \mathbf{E} = 0. \quad (7)$$

The solution to (7) can be written in the Fourier transform:

$$\mathbf{E}(\mathbf{r}) = \int_{-\infty}^{+\infty} dk_x \int_{-\infty}^{+\infty} dk_y \int_{-\infty}^{+\infty} \mathbf{E}(\mathbf{k}) e^{i\mathbf{k} \cdot \mathbf{r}} dk_z, \quad (8)$$

where the vector wave number is expressed as  $\mathbf{k} = k_x \hat{\mathbf{x}} + k_y \hat{\mathbf{y}} + k_z \hat{\mathbf{z}}$ , the space vector as  $\mathbf{r} = x\hat{\mathbf{x}} + y\hat{\mathbf{y}} + z\hat{\mathbf{z}}$ , and  $\hat{\mathbf{x}}$ ,  $\hat{\mathbf{y}}$ ,  $\hat{\mathbf{z}}$  being the unit vectors in Cartesian coordinates. Here, the problem is transferred from spatial domain to spectrum domain. For each point in the medium, the electric field  $\mathbf{E}$  can be seen as a combination of infinite plane wave. Then, for any direction wave, we have  $\nabla = i\mathbf{k}$ . Substituting (8) into (7), the electric field equation is transformed into

$$\int_{-\infty}^{+\infty} dk_x \int_{-\infty}^{+\infty} dk_y \int_{-\infty}^{+\infty} \bar{\mathbf{A}}(\mathbf{k}) \cdot \mathbf{E}(\mathbf{k}) e^{i\mathbf{k} \cdot \mathbf{r}} dk_z = 0, \quad (9)$$

where

$$\bar{\mathbf{A}}(\mathbf{k}) = \begin{pmatrix} -b_1 k_z^2 - b_3 k_z^2 + a_1 & b_3 k_x k_y - ib_2 k_z^2 - ia_2 & b_1 k_x k_z + ib_2 k_y k_z \\ b_3 k_x k_y - ib_2 k_z^2 - ia_2 & -b_1 k_z^2 - b_3 k_z^2 + a_1 & b_1 k_y k_z - ib_2 k_x k_z \\ b_1 k_x k_z - ib_2 k_y k_z & b_1 k_y k_z + ib_2 k_x k_z & -b_1 (k_x^2 + k_y^2) + a_3 \end{pmatrix} \quad (10)$$

with

$$\begin{aligned} a_1 &= \omega^2 \varepsilon_s \varepsilon_r & a_2 &= \omega^2 \varepsilon_s \varepsilon_\kappa & a_3 &= \omega^2 \varepsilon_s, \\ b_1 &= \frac{\mu_r}{\mu_s(\mu_r^2 - \mu_\kappa^2)} & b_2 &= \frac{\mu_\kappa}{\mu_s(\mu_r^2 - \mu_\kappa^2)} & b_3 &= \frac{1}{\mu_s}. \end{aligned} \quad (11)$$

In order to make (9) exist all the time, we write the eigenvalue equation as

$$\text{Det}[\bar{\mathbf{A}}(\mathbf{k})] = 0. \quad (12)$$

Here, the eigenvalue  $k$  is a function of the angular  $(\theta_k, \phi_k)$ , the equation turns to be

$$A(\theta_k, \phi_k)k^4 - B(\theta_k, \phi_k)k^2 + C = 0, \quad (13)$$

where

$$\begin{aligned} A(\theta_k, \phi_k) &= [b_1 b_3 \sin^2 \theta_k + (b_1^2 - b_2^2) \cos^2 \theta_k] \\ &\quad \times [a_1 \sin^2 \theta_k + a_3 \cos^2 \theta_k], \\ B(\theta_k, \phi_k) &= [b_1(a_1^2 - a_2^2) + b_3 a_1 a_3] \sin^2 \theta_k \\ &\quad + 2a_3(b_1 a_1 + b_2 a_2) \cos^2 \theta_k, \\ C &= a_3(a_1^2 - a_2^2), \\ k^2 &= k_x^2 + k_y^2 + k_z^2, \\ \theta_k &= \tan^{-1} \left( \frac{\sqrt{k_x^2 + k_y^2}}{k_z} \right), \\ \phi_k &= \tan^{-1} \left( \frac{k_y}{k_x} \right), \\ k_{1,3}^2 &= \frac{B + \sqrt{B^2 - 4AC}}{2A}, \\ k_{2,4}^2 &= \frac{B - \sqrt{B^2 - 4AC}}{2A}, \end{aligned} \quad (14)$$

and the eigenvectors can also be obtained from (10) at the same time and are given as follows:

$$\begin{aligned} \mathbf{E}_q &= \mathbf{F}_q^e f_q(\theta_k, \phi_k) \\ &= [F_{qx}^e(\theta_k, \phi_k) \hat{\mathbf{x}} + F_{qy}^e(\theta_k, \phi_k) \hat{\mathbf{y}} + F_{qz}^e(\theta_k, \phi_k) \hat{\mathbf{z}}] f_q(\theta_k, \phi_k), \end{aligned} \quad (15)$$

where  $q = 1, 2, 3$ , or  $4$ , here  $\mathbf{E}_q$  is a plane wave, and

$$\begin{aligned} F_{qx}^e &= -\frac{\Delta_1}{\Delta} \sin \phi_k + \frac{\Delta_2}{\Delta} \cos \phi_k, \\ F_{qy}^e &= \frac{\Delta_1}{\Delta} \cos \phi_k + \frac{\Delta_2}{\Delta} \sin \phi_k, \\ F_{qz}^e &= 1 \end{aligned} \quad (16)$$

with

$$\begin{aligned} \Delta_1 &= i(b_1 a_2 + b_2 a_1) k_q^2 \sin \theta_k \cos \theta_k, \\ \Delta_2 &= [b_1 b_3 k_q^2 \sin^2 \theta_k + (b_1^2 - b_2^2) k_q^2 \cos^2 \theta_k] \\ &\quad \times k_q^2 \sin \theta_k \cos \theta_k - (b_1 a_1 + b_2 a_2) \\ \Delta &= -(b_2 k_q^2 \cos^2 \theta_k + a_2)^2 + (b_1 k_q^2 \cos^2 \theta_k - a_1) \\ &\quad \times (b_1 k_q^2 \cos^2 \theta_k + b_3 k_q^2 \sin^2 \theta_k - a_1). \end{aligned} \quad (17)$$

Here, all the angular and eigenvalues should be considered. The  $\mathbf{E}$ -field in (7) is then given as

$$\mathbf{E}(\mathbf{r}) = \sum_{q=1}^2 \int_0^\pi \int_0^{2\pi} F_q^e(\theta_k, \phi_k) f_q(\theta_k, \phi_k) e^{i\mathbf{k}_q \cdot \mathbf{r}} k_q^2 \sin \theta_k d\theta_k d\phi_k, \quad (18)$$

$$\mathbf{k}_q = k_q \sin \theta_k \cos \phi_k \hat{\mathbf{x}} + k_q \sin \theta_k \sin \phi_k \hat{\mathbf{y}} + k_q \cos \theta_k \hat{\mathbf{z}}. \quad (19)$$

Only two roots need to be considered, while the periodic function  $f_q(\theta_k, \phi_k)$  denoting the angular spectrum amplitude can be expressed as

$$f_q(\theta_k, \phi_k) = \sum_{m', n'} G_{m' n' q} P_{n'}^{m'}(\cos \theta_k) e^{im' \phi_k}, \quad (20)$$

where  $P_n^m(x)$  is the associated Legendre function, and  $\sum_{m', n'}$  means that  $n'$  is from  $0$  to  $+\infty$  and  $m'$  is from  $-n'$  to  $n'$ . Substituting (20) to (18), we obtain

$$\begin{aligned} \mathbf{E}(\mathbf{r}) &= \sum_{q=1}^2 \sum_{m', n'} G_{m' n' q} \int_0^\pi \int_0^{2\pi} F_q^e(\theta_k, \phi_k) P_{n'}^{m'} \\ &\quad \times (\cos \theta_k) e^{im' \phi_k} e^{i\mathbf{k}_q \cdot \mathbf{r}} k_q^2 \sin \theta_k d\theta_k d\phi_k. \end{aligned} \quad (21)$$

Using the identity to stand for the part  $e^{i\mathbf{k}_q \cdot \mathbf{r}}$ ,

$$\begin{aligned} e^{i\mathbf{k} \cdot \mathbf{r}} &= \sum_{n=0}^\infty i^n (2n+1) j_n(kr) \\ &\quad \times \left[ \sum_{m=0}^n \frac{(n-m)!}{(n+m)!} P_n^m(\cos \theta_k) P_n^m(\cos \theta) e^{im(\phi - \phi_k)} \right. \\ &\quad \left. + \sum_{m=0}^n \frac{(n-m)!}{(n+m)!} P_n^m(\cos \theta_k) P_n^m(\cos \theta) e^{-im(\phi - \phi_k)} \right]. \end{aligned} \quad (22)$$

Substituting (22) into (21), we achieve the solution of  $\mathbf{E}(\mathbf{r})$  for a general homogeneous gyrotropic anisotropic media. Then, the vector spherical wave functions is employed to express the eigenvector, which is one key step. After this, the internal field can be in the form of VSWFs:

$$\begin{aligned} \mathbf{F}_q^e(\theta, \phi) e^{i\mathbf{k}_q \cdot \mathbf{r}} &= \sum_{m, n} [A_{mnq}^e(\theta_k) \mathbf{M}_{mn}^{(1)}(r, k_q) + B_{mnq}^e(\theta_k) \mathbf{N}_{mn}^{(1)}(r, k_q) \\ &\quad + C_{mnq}^e(\theta_k) \mathbf{L}_{mn}^{(1)}(r, k_q)] e^{-im\phi_k}. \end{aligned} \quad (23)$$

The other internal field parameters,  $A_{mnq}^e(\theta_k)$ ,  $B_{mnq}^e(\theta_k)$ , and  $C_{mnq}^e(\theta_k)$  can be obtained and details are from [27, 33].

Inserting (23) into (21), and integrating with respect to  $\phi_k$ , we have

$$\begin{aligned} \mathbf{E}(r) = & \sum_{q=1}^2 \sum_{m,n} \sum_{n'} 2\pi G_{mn'q} \\ & \times \int_0^\pi \left[ A_{mnq}^e(\theta_k) \mathbf{M}_{mn}^{(1)}(r, k_q) + B_{mnq}^e(\theta_k) \mathbf{N}_{mn}^{(1)}(r, k_q) \right. \\ & \left. + C_{mnq}^e(\theta_k) \mathbf{L}_{mn}^{(1)}(r, k_q) \right] \\ & \times P_{n'}^{m'}(\cos \theta_k) e^{im' \phi_k} k_q^2 \sin \theta_k d\theta_k d\phi_k, \end{aligned} \quad (24)$$

which is an eigenfunction representation of the  $\mathbf{E}$ -field in gyrotropic anisotropic media. We can get the  $\mathbf{H}$ -field in a similar form [27, 33].

From the result in (24), it is found that we can use the VSWFs to present the field, and this procedure is also suitable for the external area. Afterwards, we take the plane wave as an example. Assuming that an incident plane wave is  $\mathbf{E} = \hat{\mathbf{x}} E_0 e^{ik_0 z}$ , the incident electromagnetic fields can be expanded by an infinite series of spherical vector wave functions for an isotropic medium as follows:

$$\begin{aligned} \mathbf{E}^{\text{inc}} = & E_0 \sum_{n,m} [\delta_{m,1} + \delta_{m,-1}] \\ & \times \left[ a_{mn}^x \mathbf{M}_{mn}^{(1)}(k_0, \mathbf{r}) + b_{mn}^x \mathbf{N}_{mn}^{(1)}(k_0, \mathbf{r}) \right], \\ \mathbf{H}^{\text{inc}} = & \frac{k_0}{i\omega\mu_0} E_0 \sum_{n,m} [\delta_{m,1} + \delta_{m,-1}] \\ & \times \left[ a_{mn}^x \mathbf{M}_{mn}^{(1)}(k_0, \mathbf{r}) + b_{mn}^x \mathbf{N}_{mn}^{(1)}(k_0, \mathbf{r}) \right], \end{aligned} \quad (25)$$

where

$$\begin{aligned} a_{mn}^x = & \begin{cases} i^{n+1} \frac{2n+1}{2n(n+1)}, & m = 1, \\ i^{n+1} \frac{2n+1}{2}, & m = -1, \end{cases} \\ b_{mn}^x = & \begin{cases} i^{n+1} \frac{2n+1}{2n(n+1)}, & m = 1, \\ -i^{n+1} \frac{2n+1}{2}, & m = -1, \end{cases} \\ \delta_{s,l} = & \begin{cases} 1, & s = l, \\ 0, & s \neq l, \end{cases} \end{aligned} \quad (26)$$

the scattering fields are expanded as

$$\begin{aligned} \mathbf{E}^s = & \sum_{n,m} \left[ A_{mn}^s \mathbf{M}_{mn}^{(3)}(k_0, \mathbf{r}) + B_{mn}^s \mathbf{N}_{mn}^{(3)}(k_0, \mathbf{r}) \right], \\ \mathbf{H}^s = & \frac{k_0}{i\omega\mu_0} \sum_{n,m} \left[ A_{mn}^s \mathbf{M}_{mn}^{(3)}(k_0, \mathbf{r}) + B_{mn}^s \mathbf{N}_{mn}^{(3)}(k_0, \mathbf{r}) \right], \end{aligned} \quad (27)$$

where  $A_{mn}^s$  and  $B_{mn}^s$  are unknown coefficients and stand for the external field information, and  $k_0 = \omega\sqrt{\mu_0\epsilon_0}$ ,  $\mu_0$  and  $\epsilon_0$  denote the free space, wave number, permeability, and permittivity. Until here, this method is being discussed in an unbounded material. We should match the boundary condition on the surface when we limit it to an anisotropic sphere. The tangential components of the electromagnetic field continues at  $r = a$  and we have

$$\begin{aligned} & \sum_{q=1}^2 \sum_{n'}^\infty 2\pi G_{mn'q} \int_0^\pi Q_{mnq} P_{n'}^{m'}(\cos \theta_k) k_q^2 \sin \theta_k d\theta_k \\ & = E_0 [\delta_{m,1} + \delta_{m,-1}] a_{mn}^x \cdot \frac{i}{(k_0 a)^2}, \end{aligned} \quad (28)$$

$$\begin{aligned} & \sum_{q=1}^2 \sum_{n'}^\infty 2\pi G_{mn'q} \int_0^\pi R_{mnq} P_{n'}^{m'}(\cos \theta_k) k_q^2 \sin \theta_k d\theta_k \\ & = E_0 [\delta_{m,1} + \delta_{m,-1}] b_{mn}^x \cdot \frac{i}{(k_0 a)^2}, \end{aligned}$$

where

$$\begin{aligned} Q_{mnq} = & \left\{ A_{mnq}^e \frac{1}{k_0 r} \frac{d}{dr} [r h_n^{(1)}(k_0 r)] j_n(k_q r) \right. \\ & \left. - \frac{i\omega\mu_0}{k_0} \left[ B_{mnq}^h \frac{1}{k_q r} \frac{d}{dr} [r j_n(k_q r)] + C_{mnq}^h \frac{j_n(k_q r)}{r} \right] \right. \\ & \left. \cdot h_n^{(1)}(k_0 r) \right\}_{r=a}, \\ R_{mnq} = & \left\{ \frac{i\omega\mu_0}{k_0} A_{mnq}^h \frac{1}{k_0 r} \frac{d}{dr} [r h_n^{(1)}(k_0 r)] j_n(k_q r) \right. \\ & \left. - \left[ B_{mnq}^e \frac{1}{k_q r} \frac{d}{dr} [r j_n(k_q r)] + C_{mnq}^e \frac{j_n(k_q r)}{r} \right] \right. \\ & \left. \cdot h_n^{(1)}(k_0 r) \right\}_{r=a}. \end{aligned} \quad (29)$$

The scattering coefficients  $A_{mn}^s$  and  $B_{mn}^s$ , are thus expressed as

$$\begin{aligned} A_{mn}^s = & \frac{1}{h_n^{(1)}(k_0 a)} \left[ \sum_{n'=0}^\infty \sum_{q=1}^2 2\pi G_{mnq} \int_0^\pi A_{mnq}^e j_n(k_q a) \right. \\ & \times P_{n'}^{m'}(\cos \theta_k) k_q^2 \sin \theta_k d\theta_k \\ & \left. - E_0 [\delta_{m,1} + \delta_{m,-1}] a_{mn}^x j_n(k_0 a) \right], \end{aligned}$$

$$B_{mn}^s = \frac{1}{h_n^{(1)}(k_0 a)} \left[ \frac{i\omega\mu_0}{k_0} \sum_{n'=0}^{\infty} \sum_{q=1}^2 2\pi G_{mnq} \int_0^\pi A_{mnq}^h j_n(k_q a) \times P_{n'}^{m'}(\cos\theta_k) k_q^2 \sin\theta_k d\theta_k - E_0[\delta_{m,1} + \delta_{m,1}] b_{mn}^x j_n(k_0 a) \right]. \quad (30)$$

Then the internal and external field can be expressed in the form of the coefficients.

2.3. *T-Matrix Method.* Different from the angular expansion method, here we use magnetic induction  $\mathbf{B}$  to rewrite the Maxwell equation [32]:

$$\nabla \times [\varepsilon_s \bar{\varepsilon}^{-1} \cdot (\nabla \times \mu_s \bar{\mu}^{-1} \cdot \mathbf{B})] - k_s^2 \mathbf{B} = 0. \quad (31)$$

The divergenceless property (31) suggests that  $\mathbf{B}$  be expanded in terms of the vector spherical wave functions  $\mathbf{M}_{mn}^{(1)}(k, \mathbf{r})$  and  $\mathbf{N}_{mn}^{(1)}(k, \mathbf{r})$  [32, 41, 42]:

$$\mathbf{B} = \sum_{n,m} \bar{E}_{mn} \left[ d_{mn} \mathbf{M}_{mn}^{(1)}(k, \mathbf{r}) + c_{mn} \mathbf{N}_{mn}^{(1)}(k, \mathbf{r}) \right], \quad (32)$$

where  $k$  is not undetermined. As mentioned above, there are three kinds of VSWF's  $\mathbf{M}_{mn}^{(1)}(k, \mathbf{r})$ ,  $\mathbf{N}_{mn}^{(1)}(k, \mathbf{r})$  and  $\mathbf{L}_{mn}^{(1)}(k, \mathbf{r})$ . For this reason, (31) does not involve  $\mathbf{L}_{mn}^{(1)}(k, \mathbf{r})$ , because its curl is 0, for details of the parameters see [32, 41, 42]. Since the VSWFs is a complete frame and can stand for all vectors in the space, we can use them to present the elements in (31), written as

$$\begin{aligned} \varepsilon_s \bar{\varepsilon}^{-1} \cdot \mathbf{M}_{mn} &= \sum_{v=0}^{+\infty} \sum_{u=-v}^v [\bar{\sigma}_{uv}^{mn} \mathbf{M}_{uv} + \bar{p}_{uv}^{mn} \mathbf{N}_{uv} + \bar{q}_{uv}^{mn} \mathbf{L}_{uv}], \\ \varepsilon_s \bar{\varepsilon}^{-1} \cdot \mathbf{N}_{mn} &= \sum_{v=0}^{+\infty} \sum_{u=-v}^v [\bar{\sigma}'_{uv}{}^{mn} \mathbf{M}_{uv} + \bar{p}'_{uv}{}^{mn} \mathbf{N}_{uv} + \bar{q}'_{uv}{}^{mn} \mathbf{L}_{uv}], \\ \mu_s \bar{\mu}^{-1} \cdot \mathbf{M}_{mn} &= \sum_{v=0}^{+\infty} \sum_{u=-v}^v [\tilde{\sigma}_{uv}^{mn} \mathbf{M}_{uv} + \tilde{e}_{uv}^{mn} \mathbf{N}_{uv} + \tilde{f}_{uv}^{mn} \mathbf{L}_{uv}], \\ \mu_s \bar{\mu}^{-1} \cdot \mathbf{N}_{mn} &= \sum_{v=0}^{+\infty} \sum_{u=-v}^v [\tilde{\sigma}'_{uv}{}^{mn} \mathbf{M}_{uv} + \tilde{e}'_{uv}{}^{mn} \mathbf{N}_{uv} + \tilde{f}'_{uv}{}^{mn} \mathbf{L}_{uv}], \end{aligned} \quad (33)$$

with

$$\begin{aligned} \bar{\sigma}_{uv}^{mn} &= \delta_{nv} \delta_{mu} + \frac{[(n^2 + n - m^2) \bar{\varepsilon}'_r + m \varepsilon'_\kappa] \delta_{nv} \delta_{mu}}{n(n+1)}, \\ \bar{p}_{uv}^{mn} &= \frac{i(n+m)[m \bar{\varepsilon}'_r - (n+1) \varepsilon'_\kappa] \delta_{n-1,v} \delta_{mu}}{n(2n+1)} + \frac{i(n-m+1)[m \bar{\varepsilon}'_r + n \varepsilon'_\kappa] \delta_{n+1,v} \delta_{mu}}{(n+1)(2n+1)}, \\ \bar{q}_{uv}^{mn} &= \frac{-i(n+m)[m \bar{\varepsilon}'_r - (n+1) \varepsilon'_\kappa] \delta_{n-1,v} \delta_{mu}}{(2n+1)} + \frac{i(n-m+1)[m \bar{\varepsilon}'_r + n \varepsilon'_\kappa] \delta_{n+1,v} \delta_{mu}}{(2n+1)}, \\ \bar{\sigma}'_{uv}{}^{mn} &= -\frac{i(n+m)(n+1)[m \bar{\varepsilon}'_r + (n-1) \varepsilon'_\kappa] \delta_{n-1,v} \delta_{mu}}{n(n-1)(2n+1)} - \frac{i(n-m+1)n[m \bar{\varepsilon}'_r - (n+2) \varepsilon'_\kappa] \delta_{n+1,v} \delta_{mu}}{(n+1)(n+2)(2n+1)}, \\ \bar{p}'_{uv}{}^{mn} &= \delta_{nv} \delta_{mu} + \frac{[(2n^2 + 2n + 3)m^2 + (2n^2 + 2n - 3)n(n+1)] \bar{\varepsilon}'_r + (4n^2 + 4n - 3)m \varepsilon'_\kappa}{n(n+1)(2n-1)(2n+3)} \\ &\quad - \frac{(n+1)(n+m-1)(n+m) \bar{\varepsilon}'_r \delta_{n-2,v} \delta_{mu}}{(n-1)(2n-1)(2n+1)} - \frac{n(n-m+1)(n-m+2) \bar{\varepsilon}'_r \delta_{n+2,v} \delta_{mu}}{(n+2)(2n+1)(2n+3)}, \\ \bar{q}'_{uv}{}^{mn} &= -\frac{[(n^2 + n - 3m^2) \bar{\varepsilon}'_r - m(2n-1)(2n+3) \varepsilon'_\kappa] \delta_{nv} \delta_{mu}}{(2n-1)(2n+3)} + \frac{(n+1)(n+m-1)(n+m) \bar{\varepsilon}'_r \delta_{n-2,v} \delta_{mu}}{(2n-1)(2n+1)} \\ &\quad - \frac{n(n-m+1)(n-m+2) \bar{\varepsilon}'_r \delta_{n+2,v} \delta_{mu}}{(2n+1)(2n+3)}, \\ \tilde{\sigma}_{uv}^{mn} &= \delta_{nv} \delta_{mu} + \frac{[(n^2 + n - m^2) \bar{\mu}'_r + m \mu'_\kappa] \delta_{nv} \delta_{mu}}{n(n+1)}, \\ \tilde{\sigma}'_{uv}{}^{mn} &= \frac{i(n+m)[m \bar{\mu}'_r - (n+1) \mu'_\kappa] \delta_{n-1,v} \delta_{mu}}{n(2n+1)} + \frac{i(n-m+1)[m \bar{\mu}'_r + n \mu'_\kappa] \delta_{n+1,v} \delta_{mu}}{(n+1)(2n+1)}, \end{aligned}$$

$$\begin{aligned}
\tilde{f}_{uv}^{mn} &= \frac{-i(n+m)[m\bar{\mu}'_r - (n+1)\mu'_\kappa]\delta_{n-1,v}\delta_{mu}}{(2n+1)} + \frac{i(n-m+1)[m\bar{\mu}'_r + n\mu'_\kappa]\delta_{n+1,v}\delta_{mu}}{(2n+1)}, \\
\tilde{g}_{uv}^{mn} &= -\frac{i(n+m)(n+1)[m\bar{\mu}'_r + (n-1)\mu'_\kappa]\delta_{n-1,v}\delta_{mu}}{n(n-1)(2n+1)} - \frac{i(n-m+1)n[m\bar{\mu}'_r - (n+2)\mu'_\kappa]\delta_{n+1,v}\delta_{mu}}{(n+1)(n+2)(2n+1)}, \\
\tilde{e}_{uv}^{mn} &= \delta_{nv}\delta_{mu} + \frac{\left\{[(2n^2+2n+3)m^2 + (2n^2+2n-3)n(n+1)]\bar{\mu}'_r + (4n^2+4n-3)m\mu'_\kappa\right\}\delta_{nv}\delta_{mu}}{n(n+1)(2n-1)(2n+3)} \\
&\quad - \frac{(n+1)(n+m-1)(n+m)\bar{\mu}'_r\delta_{n-2,v}\delta_{mu}}{(n-1)(2n-1)(2n+1)} - \frac{n(n-m+1)(n-m+2)\bar{\mu}'_r\delta_{n+2,v}\delta_{mu}}{(n+2)(2n+1)(2n+3)}, \\
\tilde{f}_{uv}^{mn} &= -\frac{\left[(n^2+n-3m^2)\bar{\mu}'_r - m(2n-1)(2n+3)\mu'_\kappa\right]\delta_{nv}\delta_{mu}}{(2n-1)(2n+3)} + \frac{(n+1)(n+m-1)(n+m)\bar{\mu}'_r\delta_{n-2,v}\delta_{mu}}{(2n-1)(2n+1)} \\
&\quad - \frac{n(n-m+1)(n-m+2)\bar{\mu}'_r\delta_{n+2,v}\delta_{mu}}{(2n+1)(2n+3)}.
\end{aligned} \tag{34}$$

Here, all the coefficients are obtained using the orthogonality of the VSWFs [32, 41, 42].

Therefore, one has

$$\begin{aligned}
&\mu_s \bar{\mu}^{-1} \cdot \mathbf{B} \\
&= \sum_{n,m} \bar{E}_{mn} \left[ \bar{d}_{mn} \mathbf{M}_{mn}^{(1)}(k, \mathbf{r}) + \bar{c}_{mn} \mathbf{N}_{mn}^{(1)}(k, \mathbf{r}) + \bar{w}_{mn} \mathbf{L}_{mn}^{(1)}(k, \mathbf{r}) \right] \\
&\quad + \bar{w}_{00} \mathbf{L}_{00}^{(1)}(k, \mathbf{r}),
\end{aligned} \tag{35}$$

where

$$\begin{aligned}
\bar{d}_{mn} &= \sum_{v,u} \frac{\bar{E}_{uv}}{\bar{E}_{mn}} \left[ \tilde{g}_{mn}^{uv} d_{uv} + \tilde{g}_{mn}^{uv} c_{uv} \right], \\
\bar{c}_{mn} &= \sum_{v,u} \frac{\bar{E}_{uv}}{\bar{E}_{mn}} \left[ \tilde{e}_{mn}^{uv} d_{uv} + \tilde{e}_{mn}^{uv} c_{uv} \right], \\
\bar{w}_{mn} &= \sum_{v,u} \frac{\bar{E}_{uv}}{\bar{E}_{mn}} \left[ \tilde{f}_{mn}^{uv} d_{uv} + \tilde{f}_{mn}^{uv} c_{uv} \right], \\
\bar{w}_{00} &= -\left[ \sqrt{\frac{2}{3}} \mu'_\kappa d_{01} + \sqrt{\frac{2}{15}} \bar{\mu}'_r c_{02} \right] E_0.
\end{aligned} \tag{36}$$

Repeat the procedure and reuse the properties of the VSWFs below until (31) can be written in the form of  $\mathbf{M}_{mn}^{(1)}(k, \mathbf{r})$ ,  $\mathbf{N}_{mn}^{(1)}(k, \mathbf{r})$ , and  $\mathbf{L}_{mn}^{(1)}(k, \mathbf{r})$ :

$$\begin{aligned}
\nabla \times \mathbf{M}_{mn}^{(j)} - k \mathbf{N}_{mn}^{(j)} &= 0, \\
\nabla \times \mathbf{N}_{mn}^{(j)} - k^2 \mathbf{M}_{mn}^{(j)} &= 0, \\
\nabla \times \mathbf{L}_{mn}^{(j)} &= 0.
\end{aligned} \tag{37}$$

One gets

$$\sum_{n,m} \bar{E}_{mn} \left[ \tilde{d}_{mn} \mathbf{M}_{mn}^{(1)}(k, \mathbf{r}) + \tilde{c}_{mn} \mathbf{N}_{mn}^{(1)}(k, \mathbf{r}) \right] = 0 \tag{38}$$

with

$$\begin{aligned}
\tilde{d}_{mn} &= k^2 \sum_{v,u} \frac{\bar{E}_{uv}}{\bar{E}_{mn}} \left[ \tilde{P}_{mn}^{uv} \bar{d}_{uv} + \tilde{P}_{mn}^{uv} \bar{c}_{uv} \right] - k_s^2 d_{mn}, \\
\tilde{c}_{mn} &= k^2 \sum_{v,u} \frac{\bar{E}_{uv}}{\bar{E}_{mn}} \left[ \tilde{\sigma}_{mn}^{uv} \bar{d}_{uv} + \tilde{\sigma}_{mn}^{uv} \bar{c}_{uv} \right] - k_s^2 c_{mn}.
\end{aligned} \tag{39}$$

Then, we write the equation form:

$$\begin{pmatrix} \tilde{P} & \bar{P} \\ \tilde{\sigma} & \bar{\sigma} \end{pmatrix} \begin{pmatrix} d \\ c \end{pmatrix} = \lambda \begin{pmatrix} d \\ c \end{pmatrix}. \tag{40}$$

The expression for  $\tilde{P}$ ,  $\bar{P}$ ,  $\tilde{\sigma}$ ,  $\bar{\sigma}$  is in [32]. Let  $\lambda_l$  and  $(d_{mn,l}, c_{mn,l})^T$ , denote, respectively, the eigenvalues and the corresponding eigenvectors of eigensystem (40), with  $l$  representing the index of eigenvalues and corresponding eigenvectors. One can then build a new set of vector  $\mathbf{V}_l$  in space based on the eigenvectors:

$$\mathbf{V}_l = -\frac{k_l}{\omega} \sum_{n,m} \bar{E}_{mn} \left[ d_{mn,l} \mathbf{M}_{mn}^{(1)}(k_l, \mathbf{r}) + c_{mn,l} \mathbf{N}_{mn}^{(1)}(k_l, \mathbf{r}) \right]. \tag{41}$$

Thus, we can express  $\mathbf{B}$  as

$$\begin{aligned}
\mathbf{B} &= \sum_l \alpha_l \mathbf{V}_l \\
&= -\sum_l \alpha_l \frac{k_l}{\omega} \sum_{n,m} \bar{E}_{mn} \left[ d_{mn,l} \mathbf{M}_{mn}^{(1)}(k_l, \mathbf{r}) + c_{mn,l} \mathbf{N}_{mn}^{(1)}(k_l, \mathbf{r}) \right].
\end{aligned} \tag{42}$$

Use the relation of (6),  $\mathbf{H}$  and  $\mathbf{E}$  fields can be written as

$$\begin{aligned}\mathbf{H} &= \bar{\boldsymbol{\mu}}^{-1} \cdot \mathbf{B} \\ &= -\sum_{n,m} \bar{E}_{mn} \sum_l \frac{k_l}{\omega \mu_s} \alpha_l \\ &\quad \times \left[ \bar{d}_{mn,l} \mathbf{M}_{mn}^{(1)}(k_l, \mathbf{r}) + \bar{c}_{mn,l} \mathbf{N}_{mn}^{(1)}(k_l, \mathbf{r}) + w_{mn,l} \mathbf{L}_{mn}^{(1)}(k_l, \mathbf{r}) \right] \\ &\quad - \sum_l \frac{k_l}{\omega \mu_s} \alpha_l \left[ w_{00,l} \mathbf{L}_{00}^{(1)}(k, \mathbf{r}) \right], \\ \mathbf{E} &= -i \sum_{n,m} \bar{E}_{mn} \sum_l \alpha_l \left[ c_{mn,l} \mathbf{M}_{mn}^{(1)}(k_l, \mathbf{r}) + d_{mn,l} \mathbf{N}_{mn}^{(1)}(k_l, \mathbf{r}) \right. \\ &\quad \left. + \frac{w_{mn,l}}{\lambda_l} \mathbf{L}_{mn}^{(1)}(k_l, \mathbf{r}) \right] - i \sum_l \alpha_l \left[ \frac{\bar{w}_{00,l}}{\lambda_l} \mathbf{L}_{00}^{(1)}(k, \mathbf{r}) \right].\end{aligned}\quad (43)$$

As we have discussed in the angular expansion method, here, we also give the form of the incident wave and scattered wave.

For incident wave,

$$\begin{aligned}\mathbf{E}_{\text{inc}} &= -\sum_{n,m} i \bar{E}_{mn} \left[ p_{mn} \mathbf{N}_{mn}^{(1)}(k, \mathbf{r}) + q_{mn} \mathbf{M}_{mn}^{(1)}(k, \mathbf{r}) \right], \\ \mathbf{H}_{\text{inc}} &= -\frac{k_0}{\omega \mu_0} \sum_{n,m} \bar{E}_{mn} \left[ q_{mn} \mathbf{N}_{mn}^{(1)}(k, \mathbf{r}) + p_{mn} \mathbf{M}_{mn}^{(1)}(k, \mathbf{r}) \right].\end{aligned}\quad (44)$$

For scattered wave,

$$\begin{aligned}\mathbf{E}_s &= \sum_{n,m} i \bar{E}_{mn} \left[ a_{mn} \mathbf{N}_{mn}^{(3)}(k_0, \mathbf{r}) + b_{mn} \mathbf{M}_{mn}^{(3)}(k_0, \mathbf{r}) \right], \\ \mathbf{H}_s &= \frac{k_0}{\omega \mu_0} \sum_{n,m} \bar{E}_{mn} \left[ b_{mn} \mathbf{N}_{mn}^{(3)}(k_0, \mathbf{r}) + a_{mn} \mathbf{M}_{mn}^{(3)}(k_0, \mathbf{r}) \right].\end{aligned}\quad (45)$$

The relevant coefficients are in [41]. Then, match boundary conditions on the sphere surface, we can get a system of equations for the coefficients, which is

$$\begin{aligned}\left[ \begin{array}{c} \xi'_n(x) \\ \psi'_n(x) \end{array} \right] a_{mn} + \sum_l \left[ \begin{array}{c} 1 \\ m_s \bar{k}_l \end{array} \frac{\psi'_n(\bar{k}_l m_s x)}{\psi'_n(x)} d_{mn,l} \right] \alpha_l \\ + \sum_l \left[ \begin{array}{c} \mu_0 j_n(\bar{k}_l m_s x) \\ \mu_s \psi'_n(x) \end{array} \right] \omega_{mn,l} \alpha_l = p_{mn}, \\ \left[ \begin{array}{c} \xi_n(x) \\ \psi_n(x) \end{array} \right] b_{mn} + \sum_l \left[ \begin{array}{c} 1 \\ m_s \bar{k}_l \end{array} \frac{\psi_n(\bar{k}_l m_s x)}{\psi_n(x)} c_{mn,l} \right] \alpha_l = q_{mn}, \\ \left[ \begin{array}{c} \xi_n(x) \\ \psi_n(x) \end{array} \right] a_{mn} + \sum_l \left[ \begin{array}{c} \mu_0 \lambda_l \psi_n(\bar{k}_l m_s x) \\ \mu_s \psi_n(x) \end{array} \right] d_{mn,l} \alpha_l = p_{mn}, \\ \left[ \begin{array}{c} \xi'_n(x) \\ \psi'_n(x) \end{array} \right] b_{mn} + \sum_l \left[ \begin{array}{c} \mu_0 \lambda_l \psi'_n(\bar{k}_l m_s x) \\ \mu_s \psi'_n(x) \end{array} \right] c_{mn,l} \alpha_l \\ + \sum_l \left[ \begin{array}{c} \mu_0 j_n(\bar{k}_l m_s x) \\ \mu_s \psi'_n(x) \end{array} \right] \omega_{mn,l} \alpha_l = q_{mn},\end{aligned}\quad (46)$$

then rewrite the matrix in a clear form:

$$\begin{aligned}\left( \begin{array}{cc} \Lambda & 0 \\ 0 & \bar{\Lambda} \end{array} \right) \begin{pmatrix} a \\ b \end{pmatrix} + \left( \begin{array}{c} V \\ \bar{V} \end{array} \right) \tilde{\alpha} = \begin{pmatrix} p \\ q \end{pmatrix}, \\ \left( \begin{array}{cc} \bar{\Lambda} & 0 \\ 0 & \Lambda \end{array} \right) \begin{pmatrix} a \\ b \end{pmatrix} + \left( \begin{array}{c} \bar{U} \\ U \end{array} \right) \tilde{\alpha} = \begin{pmatrix} p \\ q \end{pmatrix}\end{aligned}\quad (47)$$

with

$$\begin{aligned}\Lambda_{mn,uv} &= S_n(x) \delta_{nv} \delta_{mu}, \\ \bar{\Lambda}_{mn,uv} &= \bar{S}_n(x) \delta_{nv} \delta_{mu}, \\ U_{mn,l} &= \frac{1}{m_s \bar{k}_l} \bar{T}_n(x, m_s \bar{k}_l x) c_{mn,l}, \\ \bar{U}_{mn,l} &= \frac{1}{m_s \bar{k}_l} \bar{T}_n(x, m_s \bar{k}_l x) d_{mn,l}, \\ V_{mn,l} &= \frac{\mu_0 \lambda_l}{\mu_s} T_n(x, m_s \bar{k}_l x) d_{mn,l}, \\ \bar{V}_{mn,l} &= \frac{\mu_0 \lambda_l}{\mu_s} \bar{T}_n(x, m_s \bar{k}_l x) c_{mn,l} + W_{mn,l}, \\ W_{mn,l} &= \frac{\mu_0}{\mu_s} \frac{1}{m_s \bar{k}_l x} \frac{\bar{T}_n(x, m_s \bar{k}_l x)}{D_n^{(1)}(m_s \bar{k}_l x)} w_{mn,l}, \\ S_n(x) &= \frac{\xi_n(x)}{\psi_n(x)} \quad \bar{S}_n(x) = \frac{\xi'_n(x)}{\psi'_n(x)}, \\ T_n(x, z) &= \frac{\psi_n(z)}{\psi_n(x)} \quad \bar{T}_n(x, z) = \frac{\psi'_n(z)}{\psi'_n(x)}.\end{aligned}\quad (48)$$

Afterwards, we can solve the equations and get the coefficients matrix, and the scattering information is in the matrix  $\begin{pmatrix} a \\ b \end{pmatrix}$ :

$$\tilde{\alpha} = R \begin{pmatrix} p \\ q \end{pmatrix},\quad (49)$$

$$\begin{pmatrix} a \\ b \end{pmatrix} = S \begin{pmatrix} p \\ q \end{pmatrix},$$

where

$$\begin{aligned}Z &= \begin{pmatrix} Y & 0 \\ 0 & -Y \end{pmatrix}^{-1} \begin{pmatrix} V - \bar{U} \\ \bar{V} - U \end{pmatrix}, \\ S &= ZR, \\ Y &= \bar{\Lambda} - \Lambda.\end{aligned}\quad (50)$$

**2.4. Numerical Results and Comparison.** For the two methods mentioned above, difference between them will be analyzed as follows. In angular expansion method, the plane wave expansion is employed and the wave in such complex medium is a combination of plane wave of different direction. The whole procedure is clear and easy to understand.

At the same time, the wave number  $k$  has its physical meaning, which can be expressed. Theoretically, this method can deal with any complex medium. Different from angular expansion method, the T-matrix method does not give an expression for the wave number, the properties of spherical vector wave function are used instead and all the wave information is gathered from the matrix. In computation, the T-matrix method has more advantage over angular expansion method, which does not need to consider grid and can be applied to calculate larger problem.

As many discussions and comparisons published already, here we mainly show the strength of the two methods [32]. Figure 1 shows the gyroelectric influence on the Radar cross-section, here  $\mu_\kappa = 0$ ,  $\mu_s\mu_r = 4\mu_0\mu_s = 2\mu_0$ ,  $\varepsilon_s\varepsilon_r = 4\varepsilon_0$ ,  $\varepsilon_s = 2\varepsilon_0$ . As we can see, when the off-diagonal parameters increase, the backscattering ( $180^\circ$ ) will also increase. Compared to Figure 1, Figure 2 shows the gyromagnetic influence on the RCS, here  $\varepsilon_s\varepsilon_r = 2.4\varepsilon_0$ ,  $\varepsilon_s = 2\varepsilon_0$ , the less scattering areas is reduced from three to one. Figure 3 gives a general case, the influences of permittivity and permeability are both considered; and this is also a lossy sphere, where  $\varepsilon_s = (2 + 1.0i)\varepsilon_0$ ,  $\mu_s = (2 + 1.0i)\mu_0$ . When increasing the permittivity elements of the materials, the scattering for larger than  $80^\circ$  area will increase obviously.

### 3. Electromagnetic Wave Scattering by a Radial Anisotropic Sphere

3.1. *Radial Anisotropy of Spheres.* As another type medium, the radial anisotropy materials have parameters given by [15]

$$\bar{\varepsilon} = \begin{pmatrix} \varepsilon_{rr} & 0 & 0 \\ 0 & \tau & \sigma \\ 0 & -\sigma & \tau \end{pmatrix}, \quad \mu = \begin{pmatrix} \mu_{rr} & 0 & 0 \\ 0 & \gamma & \xi \\ 0 & -\xi & \gamma \end{pmatrix}, \quad (51)$$

where the identity dyadic is expressed as  $\hat{\mathbf{I}} = \hat{\mathbf{r}}\hat{\mathbf{r}} + \hat{\boldsymbol{\theta}}\hat{\boldsymbol{\theta}} + \hat{\boldsymbol{\phi}}\hat{\boldsymbol{\phi}}$ . Different from the Cartesian anisotropic (CA), less discussion have been published, because the radial anisotropic (RA) material is difficult to be fabricated [7]. The research attracts much attention recently due to the properties of materials with novel parameters. How RA particles interact with waves is an essential topic which will provide us a more physical insight into the invisibility phenomenon [43–47], enhanced surface plasmon resonance [48, 49], and Fano resonance [50]. Although Monzon developed the variables separation method and demonstrated a perfect explanation to the solution form [15], researchers prefer the Debye potential or other potentials similar [51–53]. Recently, Novitsky has stated a general form for the material, and then extend the T-matrix method to a multilayer case [54]. When a Hamilton operator is used, the Maxwell equations will be greatly simplified. By employing the impedance matrix, the field area is both simple and clear. However, this solution is just another form of variables separation method and only suitable to the uniaxial anisotropic case, which does not satisfy the general situation [54]. Herein, we explain Monzon's method and conclude an explanation to the solution.

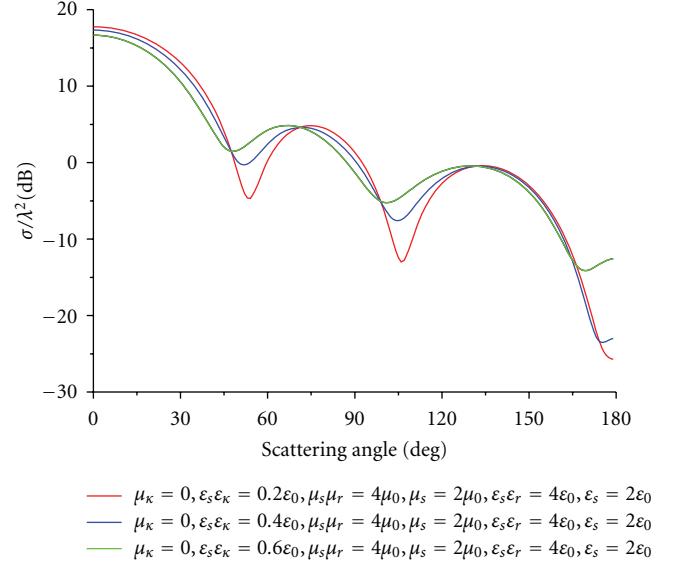


FIGURE 1: Normalized Radar cross-section (RCS) values versus the scattering angle. Different gyroelectric influence is considered. Here,  $k_0r = \pi$ .

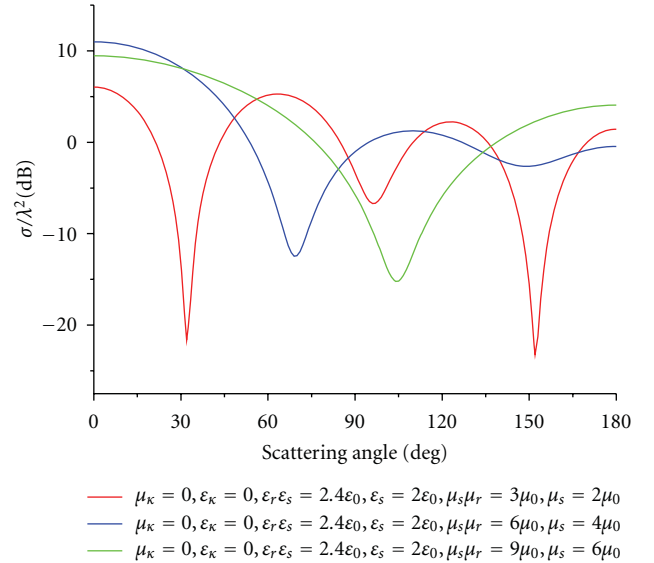


FIGURE 2: Normalized Radar cross-section (RCS) values versus the scattering angle. Different gyromagnetic influence is considered. Here,  $k_0r = 0.75\pi$ .

3.2. *Variables Separation Method.* Firstly, we define new vectors to be [15]

$$\hat{\boldsymbol{\xi}}_\pm = \frac{\hat{\boldsymbol{\theta}} \pm j\hat{\boldsymbol{\phi}}}{\sqrt{2} \sin \theta}. \quad (52)$$

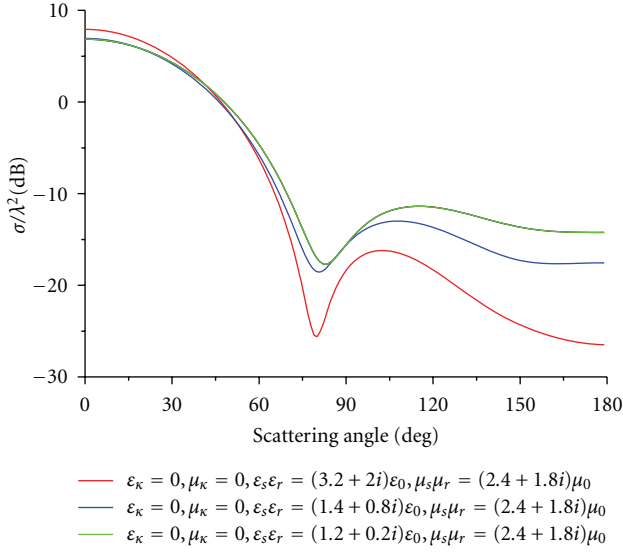


FIGURE 3: Normalized Radar Cross Section (RCS) values versus the scattering angle. Here the permeability and the permittivity are complex number. The Loss gyrotropic influence is considered. Here  $k_0 r = 0.75\pi$ .

Then, the  $\mathbf{E}$ -field and  $\mathbf{H}$ -field can be expressed in the new coordinates:

$$\begin{aligned} \mathbf{E}(\mathbf{r}) &= E_r \hat{\mathbf{r}} + e_- \hat{\xi}_+ + e_+ \bar{\xi}_- \quad e_\pm = \frac{\sin \theta}{\sqrt{2}} (E_\theta \pm jE_\phi), \\ \mathbf{H}(\mathbf{r}) &= H_r \hat{\mathbf{r}} + h_- \hat{\xi}_+ + h_+ \bar{\xi}_- \quad h_\pm = \frac{\sin \theta}{\sqrt{2}} (H_\theta \pm jH_\phi), \end{aligned} \quad (53)$$

Similarly, the displacement vector is provided:

$$\begin{aligned} \bar{\mathbf{e}} \cdot \mathbf{E} &= \epsilon_{rr} E_r \hat{\mathbf{r}} + \alpha_+ e_- \bar{\xi}_+ + \alpha_- e_+ \bar{\xi}_-, \quad \alpha_\pm = \tau \pm j\sigma, \\ \bar{\boldsymbol{\mu}} \cdot \mathbf{H} &= \mu_{rr} H_r \hat{\mathbf{r}} + \beta_+ h_- \bar{\xi}_+ + \beta_- h_+ \bar{\xi}_-, \quad \beta_\pm = \gamma \pm j\zeta. \end{aligned} \quad (54)$$

Here, two operators are defined as

$$D_\pm = \frac{1}{\sqrt{2}r} \left( \sin \theta \frac{\partial}{\partial \theta} \pm j \frac{\partial}{\partial \phi} \right), \quad D_r = \frac{1}{r} \frac{\partial}{\partial r} \cdot r, \quad (55)$$

then the Laplace operator can be written as

$$\nabla = r \frac{\partial}{\partial r} + \hat{\xi}_+ D_- + \hat{\xi}_- D_+, \quad (56)$$

and Maxwell equations is correspondingly rewritten as

$$\begin{aligned} \nabla \times \mathbf{E} &= \frac{j\hat{\mathbf{r}}}{\sin^2 \theta} \{D_+ e_- - D_- e_+\} + j\bar{\xi}_+ \{D_- E_r - D_r e_-\} \\ &\quad + j\bar{\xi}_- \{D_r e_+ - D_+ E_r\}, \\ \nabla \times \mathbf{H} &= \frac{j\hat{\mathbf{r}}}{\sin^2 \theta} \{D_+ h_- - D_- h_+\} + j\bar{\xi}_+ \{D_- H_r - D_r h_-\} \\ &\quad + j\bar{\xi}_- \{D_r h_+ - D_+ H_r\}, \end{aligned} \quad (57)$$

we insert (54) and (57) into (2) and (3). After some calculations including repeated operations on Maxwell's equations, a coupled set of differential equations involving only the radial field components can be obtained [15]:

$$\begin{aligned} \left\{ \frac{\mu_{rr}}{\gamma r} D_r^2 (rH_r) + \frac{2}{\sin^2 \theta} D_+ D_- H_r + \frac{\omega^2}{\tau} \mu_{rr} (\tau^2 + \sigma^2) H_r \right\} \\ + \frac{j\omega \epsilon_{rr}}{\gamma \tau r} (\sigma \gamma + \tau \zeta) D_r (rE_r) = 0, \\ \left\{ \frac{\epsilon_{rr}}{\tau r} D_r^2 (rE_r) + \frac{2}{\sin^2 \theta} D_+ D_- E_r + \frac{\omega^2}{\tau} \epsilon_{rr} (\gamma^2 + \zeta^2) E_r \right\} \\ - \frac{j\omega \mu_{rr}}{\gamma \tau r} (\sigma \gamma + \tau \zeta) D_r (rH_r) = 0, \end{aligned} \quad (58)$$

where

$$D_+ D_- = \frac{1}{2r^2} \left[ \frac{\partial^2}{\partial \phi^2} + \sin \theta \frac{\partial}{\partial \theta} \sin \theta \frac{\partial}{\partial \theta} \right]. \quad (59)$$

The field can be expressed in the following form:

$$\begin{aligned} E_r &= \sum_{n,m} E_{mn}(r) P_n^m(\cos \theta) e^{jm\phi}, \\ H_r &= \sum_{n,m} H_{mn}(r) P_n^m(\cos \theta) e^{jm\phi}. \end{aligned} \quad (60)$$

Also when  $D_+ D_-$  operate on other components, it has the following properties:

$$D_+ D_- = -n(n+1) \frac{\sin^2 \theta}{2r^2}, \quad (61)$$

we write the (58) in a convenient form:

$$d^2 f + \alpha_1(\rho) f - \delta dg = 0 \quad d^2 g + \alpha_2(\rho) g - \delta df = 0 \quad (62)$$

with

$$\begin{aligned} d &= \frac{d}{d\rho} \quad \rho = \kappa r \quad \kappa = \omega \sqrt{\epsilon_{rr} \mu_{rr}} \quad \delta = \frac{(\sigma \gamma + \tau \zeta)}{\sqrt{\tau \gamma \epsilon_{rr} \mu_{rr}}}, \\ \alpha_1(\rho) &= A_1 - \frac{B_1}{\rho^2} \quad \alpha_2(\rho) = A_2 - \frac{B_2}{\rho^2}, \\ A_1 &= \frac{\tau}{\gamma} \frac{(\gamma^2 + \zeta^2)}{\epsilon_{rr} \mu_{rr}}, \quad A_2 = \frac{\gamma}{\tau} \frac{(\tau^2 + \sigma^2)}{\epsilon_{rr} \mu_{rr}}, \\ B_1 &= \frac{\tau}{\epsilon_{rr}} n(n+1), \quad B_2 = \frac{\gamma}{\mu_{rr}} n(n+1). \end{aligned} \quad (63)$$

For (62), there is an analytical solution to the differential equations only when the coupled component is 0 (the isotropic or uniaxial anisotropic case). For a general case ( $\delta \neq 0$ ), there is no analytical solution for this kind of differential equations in mathematics [55]. Therefore, we

have to use the series to stand for the equation roots and the procedure is as follows:

$$f = \sum_{n=-\infty}^{\infty} \rho^{\lambda+n} K_n, \quad (64)$$

$$g = \sum_{n=-\infty}^{\infty} \rho^{\lambda+n} Q_n, \quad (65)$$

$$[(\lambda+n)(\lambda+n-1) - B_1]K_n + A_1 K_{n-2} = \delta(\lambda+n-1)Q_{n-1}, \quad (66)$$

$$[(\lambda+n)(\lambda+n-1) - B_2]Q_n + A_2 Q_{n-2} = \delta(\lambda+n-1)K_{n-1}, \quad (67)$$

$$Q_1 = \frac{\delta(\tau_1 + 1/2)}{[2\tau_1 + 1 + (B_1 - B_2)]}, \quad K_2 = \frac{\delta(\tau_1 + 3/2)Q_1 - A_1}{4(\tau_1 + 1)}. \quad (68)$$

When the original condition is given, the coefficients can be calculated step by step and then an expression for the radial component as we needed from (66) and (67) can be achieved. If the off-diagonal parameters are zero,  $E_r$  and  $H_r$  are not coupled and we encounter the most discussed case [51]:

$$\begin{aligned} E_r &= \frac{\omega}{ik_t^2} \left( \frac{\partial^2}{\partial r^2} + k_t^2 \right) \Psi_{TM}, \\ E_\theta &= \frac{\omega}{ik_t^2} \frac{1}{r} \frac{\partial^2 \Psi_{TM}}{\partial r \partial \theta} - \frac{1}{\varepsilon_0 \varepsilon_t} \frac{1}{r \sin \theta} \frac{\partial \Psi_{TE}}{\partial \phi}, \\ E_\phi &= \frac{\omega}{ik_t^2} \frac{1}{r \sin \theta} \frac{\partial^2 \Psi_{TM}}{\partial r \partial \phi} + \frac{1}{\varepsilon_0 \varepsilon_t} \frac{1}{r} \frac{\partial \Psi_{TE}}{\partial \theta}, \\ H_r &= \frac{\omega}{ik_t^2} \left( \frac{\partial^2}{\partial r^2} + k_t^2 \right) \Psi_{TE}, \\ H_\theta &= \frac{1}{\mu_0 \mu_t} \frac{1}{r \sin \theta} \frac{\partial \Psi_{TM}}{\partial \phi} + \frac{\omega}{ik_t^2} \frac{1}{r} \frac{\partial^2 \Psi_{TE}}{\partial r \partial \theta}, \\ H_\phi &= -\frac{1}{\mu_0 \mu_t} \frac{1}{r} \frac{\partial \Psi_{TM}}{\partial \theta} + \frac{\omega}{ik_t^2} \frac{1}{r \sin \theta} \frac{\partial^2 \Psi_{TE}}{\partial r \partial \phi}. \end{aligned} \quad (69)$$

For a plane wave, there are many discussions already; here, we only show the result for the internal and external field:

$$\begin{aligned} a_n &= \frac{\sqrt{\mu_t/\varepsilon_t} j_n(k_0 a) j'_{v_1}(k_t a) - j'_n(k_0 a) j_{v_1}(k_t a)}{h_n^{(2)'}(k_0 a) j_{v_1}(k_t a) - \sqrt{\mu_t/\varepsilon_t} h_n^{(2)}(k_0 a) j'_{v_1}(k_t a)} T_n, \\ b_n &= \frac{\sqrt{\mu_t/\varepsilon_t} j'_n(k_0 a) j_{v_2}(k_t a) - j_n(k_0 a) j'_{v_2}(k_t a)}{h_n^{(2)}(k_0 a) j'_{v_2}(k_t a) - \sqrt{\mu_t/\varepsilon_t} h_n^{(2)'}(k_0 a) j_{v_2}(k_t a)} T_n, \end{aligned}$$

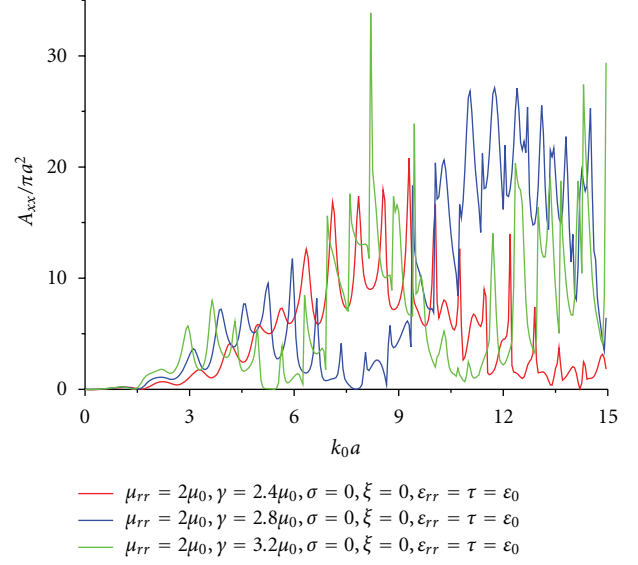


FIGURE 4: Normalized backscattering values versus sphere radius. Different negative anisotropic value influence is considered. Here, we increase the negative values.

$$\begin{aligned} c_n &= \frac{i}{\sqrt{\mu_t/\varepsilon_t} h_n^{(2)}(k_0 a) j'_{v_1}(k_t a) - h_n^{(2)'}(k_0 a) j_{v_1}(k_t a)} T_n, \\ d_n &= \frac{i \sqrt{\mu_t/\varepsilon_t}}{h_n^{(2)}(k_0 a) j'_{v_2}(k_t a) - \sqrt{\mu_t/\varepsilon_t} h_n^{(2)'}(k_0 a) j_{v_2}(k_t a)} T_n, \\ T_n &= \frac{i^{-n} (2n+1)}{n(n+1)}. \end{aligned} \quad (70)$$

Using these coefficients, there are many interesting results [7], which will not be discussed here.

**3.3. Numerical Results.** Results of the method using the above coefficients are presented in the following. Figure 4 states the negative anisotropy ( $\mu_{rr} < \gamma$ ) influence on the backscattering when  $\varepsilon_{rr} = \tau = \varepsilon_0$ . Sharp changes can be observed when the radius changes. Compared to Figure 4, Figure 5 shows the positive anisotropy ( $\mu_{rr} > \gamma$ ) influence on the backscattering, from which the oscillations are more regular. Figures 6 and 7 give a general case for the absorbing sphere. Taking the influence of negative absorbing into accounting, we can see from Figure 6 that the backscattering will approach to a certain value as the radius increases. There will be more backscattering as the sphere has much loss. The positive absorbing properties are discussed in Figure 7, which behaves a similar phenomenon with Figure 6.

## 4. Discussion and Conclusion

In this review, two different types of anisotropy have been discussed in Cartesian and spherical coordinates, respectively. The role of anisotropy in scattering properties is

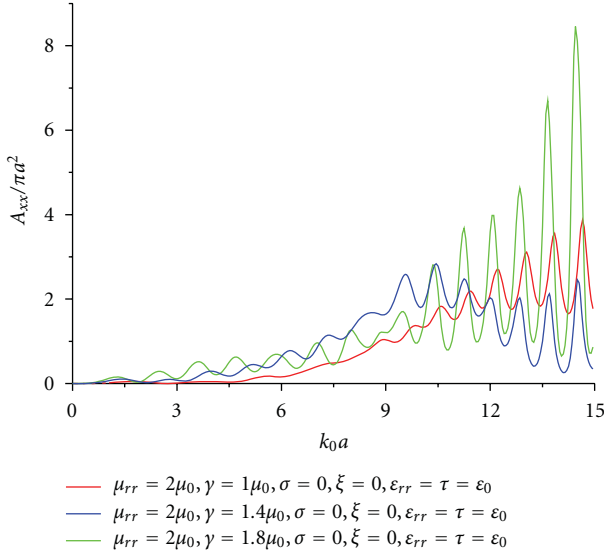


FIGURE 5: Normalized backscattering values versus sphere radius. Different positive anisotropic value influence is considered. Here, we reduce the positive values.

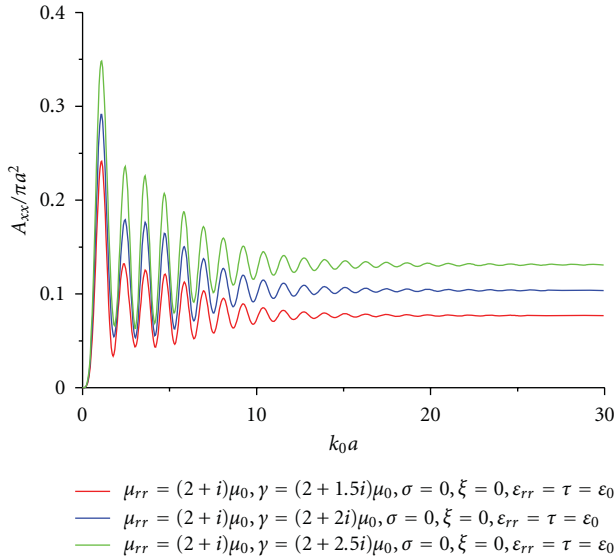


FIGURE 6: Normalized backscattering values versus sphere radius. Lossy negative anisotropic influence is considered. Here, the imaginary part for the permeability is bigger than 1.

characterized analytically. Two main methods are introduced in Cartesian coordinates. As the first one, the angular expansion method can be used in the infinitely large area and present an obvious explanation for the properties of the medium. Different from the first method, the T-matrix method can avoid the complex function by using the orthogonal properties for  $\mathbf{M}_{mn}^{(l)}$ ,  $\mathbf{N}_{mn}^{(l)}$ , and  $\mathbf{L}_{mn}^{(l)}$ . There is no need for researchers to consider the mesh before the calculation. Since these two methods are analytical and semianalytical, respectively, the parameter's influence on

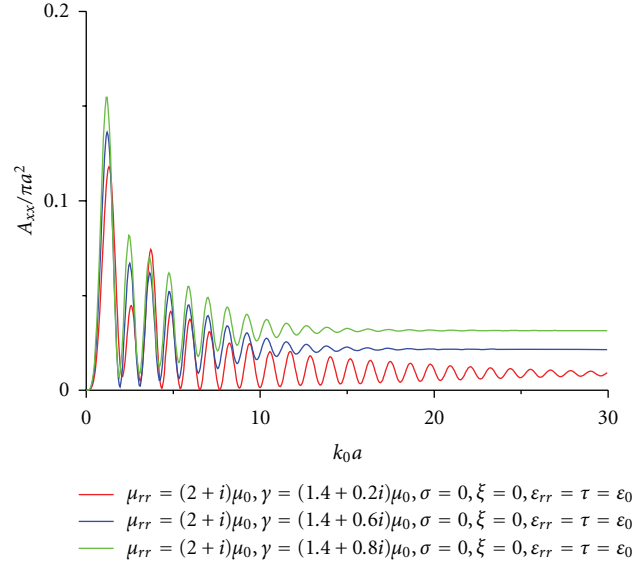


FIGURE 7: Normalized backscattering values versus sphere radius. Lossy positive anisotropic influence is considered. Here, the imaginary part for the permeability is smaller than 1.

every part is very clear and thus gives us an insight into anisotropy materials.

For a spherical coordinate anisotropic material, no matter which operators are used, the variables separation remains the main method to settle the problem. Though the Debye potentials can be widely used based on the properties of the Maxwell equations, it is still not suitable to solve the coupled gyrotropic materials. Monzon's work demonstrated the reason why and how the electric field and magnetic field coupled. When a specific situation is considered, for example, a uniaxial anisotropic media, the electric field and the magnetic field can be separated and be both expressed in the radial function form. This review provides the convenience for researchers who want to explore new properties of anisotropic materials and, therefore, design new structures.

## Acknowledgments

The authors wish to thank Professor Li Lewei, and Ms. Ong Weeling for helpful discussions. This work is supported by CSC scholarship and Key Program of NSFC-Guangdong Union Foundation under Grant no. U0835004.

## References

- [1] L. Lorentz, "Lysbevaegelsen i og uden for en haf plane lysbolger belyst kugle," *Videnskab Selskab Skrifter*, vol. 6, pp. 1–62, 1890.
- [2] G. Mie, "Beiträge zur optik trüber medien, speziell kolloidaler metallösungen," *Annalen der Physik*, vol. 25, no. 3, pp. 377–445, 1908.
- [3] B. S. Luk'yanchuk and V. Ternovsky, "Light scattering by a thin wire with a surface-plasmon resonance: bifurcations of

- the Poynting vector field," *Physical Review B*, vol. 73, no. 23, Article ID 235432, 2006.
- [4] B. S. Luk'yanchuk, M. I. Tribelsky, Z. B. Wang et al., "Extraordinary scattering diagram for nanoparticles near plasmon resonance frequencies," *Applied Physics A*, vol. 89, no. 2, pp. 259–264, 2007.
  - [5] M. I. Tribelsky, S. Flach, A. E. Miroshnichenko, A. V. Gorbach, and Y. S. Kivshar, "Light scattering by a finite obstacle and fano resonances," *Physical Review Letters*, vol. 100, no. 4, Article ID 043903, 2008.
  - [6] W. Fang, J. Y. Xu, A. Yamilov et al., "Large enhancement of spontaneous emission rates of InAs quantum dots in GaAs microdisks," *Optics Letters*, vol. 27, no. 11, pp. 948–950, 2002.
  - [7] C. Qiu, L. Gao, J. D. Joannopoulos, and M. Soljačić, "Light scattering from anisotropic particles: propagation, localization, and nonlinearity," *Laser and Photonics Reviews*, vol. 4, no. 2, pp. 268–282, 2010.
  - [8] S. Zhang, Y. Xiong, G. Bartal, X. Yin, and X. Zhang, "Magnetized plasma for reconfigurable subdiffraction imaging," *Physical Review Letters*, vol. 106, no. 24, 2011.
  - [9] J. Yao, X. Yang, X. Yin, G. Bartal, and X. Zhang, "Three-dimensional nanometer-scale optical cavities of indefinite medium," *Proceedings of the National Academy of Sciences of the United States of America*, vol. 108, no. 28, pp. 11327–11331, 2011.
  - [10] S. Liu, W. Lu, Z. Lin, and S. T. Chui, "Molding reflection from metamaterials based on magnetic surface plasmons," *Physical Review B*, vol. 84, no. 4, 2011.
  - [11] S. Liu, J. Du, Z. Lin, R. X. Wu, and S. T. Chui, "Formation of robust and completely tunable resonant photonic band gaps," *Physical Review B*, vol. 78, no. 15, 2008.
  - [12] S. Liu, W. Chen, J. Du, Z. Lin, S. T. Chui, and C. T. Chan, "Manipulating negative-refractive behavior with a magnetic field," *Physical Review Letters*, vol. 101, no. 15, Article ID 157407, 2008.
  - [13] Y. Poo, R.-X. Wu, Z. Lin, Y. Yang, and C. T. Chan, "Experimental realization of self-guiding unidirectional electromagnetic edge states," *Physical Review Letters*, vol. 106, no. 9, 2011.
  - [14] J. Roth and M. J. Dignam, "Scattering and extinction cross sections for a spherical particle coated with an oriented molecular layer," *The Journal of the Optical Society of America*, vol. 63, no. 3, pp. 308–311, 1973.
  - [15] J. C. Monzon, "Three-dimensional field expansion in the most general rotationally symmetric anisotropic material: application to scattering by a sphere," *IEEE Transactions on Antennas and Propagation*, vol. 37, no. 6, pp. 728–735, 1989.
  - [16] A. D. Kiselev, V. Y. Reshetnyak, and T. J. Sluckin, "Light scattering by optically anisotropic scatterers: T-matrix theory for radial and uniform anisotropies," *Physical Review E*, vol. E65, no. 5, Article ID 056609, pp. 1–16, 2002.
  - [17] M. F. Yanik, H. Cinar, H. N. Cinar, A. D. Chisholm, Y. Jin, and A. Ben-Yakar, "Functional regeneration after laser axotomy," *Nature*, vol. 432, no. 7019, p. 822, 2004.
  - [18] R. D. Weglein, "A model for predicting acoustic material signatures," *Applied Physics Letters*, vol. 34, no. 3, pp. 179–181, 1979.
  - [19] J. Kushibiki, A. Ohkubo, and N. Chubachi, "Anisotropy detection in sapphire by acoustic microscope using line-focus beam," *Electronics Letters*, vol. 17, no. 15, pp. 534–536, 1981.
  - [20] A. C. Guo, J. R. Petrella, J. Kurtzberg, and J. M. Provenzale, "Evaluation of white matter anisotropy in Krabbe disease with diffusion tensor MR imaging: initial experience," *Radiology*, vol. 218, no. 3, pp. 809–815, 2001.
  - [21] J. B. Pendry, D. Schurig, and D. R. Smith, "Controlling electromagnetic fields," *Science*, vol. 312, no. 5781, pp. 1780–1782, 2006.
  - [22] X. Q. Sheng and Z. Peng, "Analysis of scattering by large objects with off-diagonally anisotropic material using finite element-boundary integral-multilevel fast multipole algorithm," *IET Microwaves, Antennas and Propagation*, vol. 4, pp. 492–500, 2010.
  - [23] W. Ren, "Contributions to the electromagnetic wave theory of bounded homogeneous anisotropic media," *Physical Review E*, vol. 47, no. 1, pp. 664–673, 1993.
  - [24] Y. Geng, X. Wu, and L.-W. Li, "Analysis of electromagnetic scattering by a plasma anisotropic sphere," *Radio Science*, vol. 38, no. 6, pp. 12/1–12/12, 2003.
  - [25] Y. L. Geng and X. B. Wu, "A Plane Electromagnetic Wave Scattering By a Ferrite Sphere," *Journal of Electromagnetic Waves and Applications*, vol. 18, no. 2, pp. 161–179, 2004.
  - [26] Y.-L. Geng, X.-B. Wu, L.-W. Li, and B.-R. Guan, "Mie scattering by a uniaxial anisotropic sphere," *Physical Review E*, vol. 70, no. 5, article 056609, pp. 1–8, 2004.
  - [27] Y. L. Geng and C. W. Qiu, "Analytical spectral-domain scattering theory of a general gyrotropic sphere," *Materials Science*. In press, <http://arxiv.org/abs/1102.4057>.
  - [28] Y.-L. Geng, "Scattering of a plane wave by an anisotropic ferrite-coated conducting sphere," *IET Microwaves, Antennas and Propagation*, vol. 2, no. 2, pp. 158–162, 2008.
  - [29] B. Stout, M. Nevière, and E. Popov, "Mie scattering by an anisotropic object. Part I. Homogeneous sphere," *Journal of the Optical Society of America A*, vol. 23, no. 5, pp. 1111–1123, 2006.
  - [30] B. Stout, M. Nevière, and E. Popov, "Mie scattering by an anisotropic object. Part II. Arbitrary-shaped object: differential theory," *Journal of the Optical Society of America A*, vol. 23, no. 5, pp. 1124–1134, 2006.
  - [31] J. Roth and M. J. Dignam, "Scattering and extinction cross sections for a spherical particle coated with an oriented molecular layer," *Journal of the Optical Society of America A*, vol. 63, no. 3, pp. 308–311, 1973.
  - [32] W. L. Ong, "New solutions to EM scattering by a gyrotropic sphere," Bachelor Thesis, National University of Singapore, 2010.
  - [33] Y. L. Geng, "Application of Spherical Vector Wave Function to Electromagnetic Scattering by Anisotropic Media," *PhD. Thesis*, Xi'an, China, Xidian University, 2006.
  - [34] C. T. Tai, *Dyadic Green's Functions in Electromagnetic Theory*, IEEE Press, New York, NY, USA, 1993.
  - [35] N. K. Uzunoglu, P. G. Cottis, and J. G. Fikioris, "Excitation of electromagnetic waves in a gyroelectric cylinder," *IEEE Transactions on Antennas and Propagation*, vol. 33, no. 1, pp. 90–99, 1985.
  - [36] S. N. Papadakis, N. K. Uzunoglu, and N. Christos, "Scattering of a plane wave by a general anisotropic dielectric ellipsoid," *Journal of the Optical Society of America A*, vol. 7, no. 6, pp. 991–997, 1990.
  - [37] W. C. Chew and Y. M. Wang, "Fast algorithm for solution of a scattering problem using a recursive aggregate T-matrix method," *Microwave and Optical Technology Letters*, vol. 3, no. 5, pp. 164–169, 1990.
  - [38] D. Sarkar and N. J. Halas, "General vector basis function solution of Maxwell's equations," *Physical Review E*, vol. 56, no. 1, pp. 1102–1112, 1997.
  - [39] D. Sarkar, *Vector basis function solution of Maxwell's equations*, Ph.D. thesis, Rice University, Houston, Tex, USA, 1996.

- [40] S. Liu, "Electromagnetic properties for three dimensional anisotropic photonic crystal," *PhD. Thesis*, Fudan University, Shanghai, China, 2007.
- [41] Z. Lin and S. T. Chui, "Electromagnetic scattering by optically anisotropic magnetic particle," *Physical Review E*, vol. 69, no. 5, article 056614, pp. 1–14, 2004.
- [42] S. Liu and Z. Lin, "Opening up complete photonic bandgaps in three-dimensional photonic crystals consisting of biaxial dielectric spheres," *Physical Review E*, vol. 73, no. 6, 2006.
- [43] L. Gao, T. H. Fung, K. W. Yu, and C. W. Qiu, "Electromagnetic transparency by coated spheres with radial anisotropy," *Physical Review E*, vol. 78, no. 4, article 046609, 2008.
- [44] C.-W. Qiu, A. Novitsky, H. Ma, and S. Qu, "Electromagnetic interaction of arbitrary radial-dependent anisotropic spheres and improved invisibility for nonlinear-transformation-based cloaks," *Physical Review E*, vol. 80, no. 1, 2009.
- [45] C. W. Qiu, L. Hu, B. Zhang, B. I. Wu, S. G. Johnson, and J. D. Joannopoulos, "Spherical cloaking using nonlinear transformations for improved segmentation into concentric isotropic coatings," *Optics Express*, vol. 17, no. 16, pp. 13467–13478, 2009.
- [46] C.-W. Qiu, L. Hu, X. Xu, and Y. Feng, "Spherical cloaking with homogeneous isotropic multilayered structures," *Physical Review E*, vol. 79, no. 4, article 047602, 2009.
- [47] A. Novitsky, C. W. Qiu, and S. Zouhdi, "Transformation-based spherical cloaks designed by an implicit transformation-independent method: theory and optimization," *New Journal of Physics*, vol. 11, Article ID 113001, 2009.
- [48] B. S. Luk'yanchuk and C.-W. Qiu, "Enhanced scattering efficiencies in spherical particles with weakly dissipating anisotropic materials," *Applied Physics A*, vol. 92, no. 4, pp. 773–776, 2008.
- [49] Y. X. Ni, D. L. Gao, Z. F. Sang, L. Gao, and C. W. Qiu, "Influence of spherical anisotropy on the optical properties of plasmon resonant metallic nanoparticles," *Applied Physics A*, vol. 102, no. 3, pp. 673–679, 2011.
- [50] W.-J. Chen, J. C. W. Lee, J.-W. Dong, C.-W. Qiu, and H.-Z. Wang, "Fano resonance of three-dimensional spiral photonic crystals: paradoxical transmission and polarization gap," *Applied Physics Letters*, vol. 98, no. 8, article 081116, 2011.
- [51] C.-W. Qiu, L.-W. Li, T.-S. Yeo, and S. Zouhdi, "Scattering by rotationally symmetric anisotropic spheres: potential formulation and parametric studies," *Physical Review E*, vol. 75, no. 2, 2007.
- [52] C. F. Bohren and D. R. Huffman, *Absorption and Scattering of Light by Small Particles*, John Wiley & Sons, New York, NY, USA, 1998.
- [53] C.-W. Qiu, L.-W. Li, Q. Wu, and T.-S. Yeo, "Field representations in general gyrotropic media in spherical coordinates," *IEEE Antennas and Wireless Propagation Letters*, vol. 4, no. 1, pp. 467–470, 2005.
- [54] A. Novitsky and L. Barkovsky, "Matrix approach for light scattering from a multilayered rotationally symmetric bianisotropic sphere," *Physical Review A*, vol. 77, no. 3, Article ID 033849, 2008.
- [55] G. Arfken and H. J. Weber, *Mathematical Method for Physicists*, Elsevier Academic Press, 6th edition, 2005.

## Research Article

# Transient Response of Thin Wire above a Layered Half-Space Using TDIE/FDTD Hybrid Method

**Bing Wei, Qiong He, Jie Li, Ren-xian Li, and Li-xin Guo**

*Department of Physics, Xidian University, Xi'an 710071, China*

Correspondence should be addressed to Bing Wei, weibing\_xd@yahoo.com.cn

Received 15 July 2011; Revised 26 September 2011; Accepted 20 October 2011

Academic Editor: Hu Jun

Copyright © 2012 Bing Wei et al. This is an open access article distributed under the Creative Commons Attribution License, which permits unrestricted use, distribution, and reproduction in any medium, provided the original work is properly cited.

The TDIE/FDTD hybrid method is applied to calculate the transient responses of thin wire above a lossy layered half-space. The time-domain reflection of the layered half space is computed by one-dimensional modified FDTD method. Then, transient response of thin wire induced by two excitation sources (the incident wave and reflected wave) is calculated by TDIE method. Finally numerical results are given to illustrate the feasibility and high efficiency of the presented scheme.

## 1. Introduction

Among the available literatures when analyzing transient response of thin-wire above a half-space, the scattering and radiation of thin-wire structure are generally analyzed by employing time-domain integral equation (TDIE) method [1–8] or finite element method (FEM) [9], and the influence of half-space is often considered by introducing the imaging principle, as well as reflection coefficient [3]. In 1980, Parviz Parhami et al. [10] derived the general integral equation for an arbitrarily shaped thin-wire antenna over a lossy half-space, and method of moment (MoM) in frequency domain is employed to solve the equation numerically. In his paper, far-field radiation patterns of center-fed horizontal dipole, center-fed vertical dipole, and center-fed inverted dipole are given. In 1998, Poljak established space-time integral equation of Hallen's type to deal with a straight thin wire horizontally placed above a dissipative half-space. The influence of a lossy half-space is taken into account by the Fresnel space-time reflection coefficient which appears inside the IE kernel [4]. In 2004, he calculated the transient responses of nonlinear loaded wire antenna in half-space with spatial-time Hallen equation combined with reflection coefficient method [5]. Recently, Haddad et al. used complex-time Green's functions to obtain the transient response of thin-wire structures located above half-space [6].

The above literature deals only with the interactions between thin wire and homogeneous or one-layer half-space. In many practical cases, the half-space is composed of complex dielectrics, which is usually in the form of layers. In this paper, a hybrid method that combines TDIE with FDTD is employed to study the transient responses of thin conducting wire above a lossy and layered half-space. It is well known that TDIE method is suited to simulate the scattering or radiation from thin-wire structures, whereas FDTD is a powerful tool that could model the interactions of EM waves with inhomogeneous media [11–29]. Huang et al. used the FDTD/MoM hybrid technique for modeling the radiation field of complex antennas above the heterogeneous grounds [26]. Monorchio et al. used the hybrid time-domain technique that combines the finite element, finite difference, and method of moment techniques to compute the radiation field of a thin-wire antenna near inhomogeneous dielectric bodies [27]. Hybrid method in [26, 27] uses iteration-based technique to couple 3-D FDTD(/FETD) and TDIE. The hybrid method in this paper is connected with one-reflection field (neglecting higher order reflections when the distance of the wire and the interface of the layered half-space are far enough for the problems we interested) without any iteration-based procedure to consider the multiple interactions between wire structure and underlying layered half-space. To calculate first-order reflected field, only

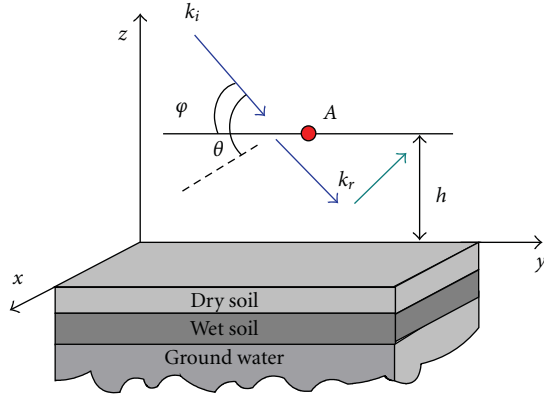


FIGURE 1: The geometry of a thin wire above layered half-space.

1-D FDTD is needed. In this case the original problem is decomposed into two subregions. The first sub-region is single-wire structure in free space, while the second sub-region is the layered dielectric without any wire structure above it. Then transient response on the wire is analyzed using TDIE [1, 2], which has two exciting terms in the formulation, both the original incidence and the reflected wave. This hybrid algorithm utilizes advantages of both TDIE and FDTD, respectively, and furthermore no iteration is needed. Numerical examples show that this hybrid method is a very efficient way to study transient responses of wire structures above a layered half-space.

## 2. Basic Theory of Hybrid Method

The geometry of a straight thin conducting wire above multilayer dielectric media is shown in Figure 1. The thin wire is parallel to the  $y$  axis, the length of wire is  $l$ , and the distance between the wire and interface is  $h$ . The angle between the incident plane and the surface of the half-space is  $\theta$ . The angle between the incident wave and the thin wire is  $\varphi$ . In this paper, the plane of incidence is determined by the incident vector  $\vec{k}_i$  and the direction of the thin wire.

When one analyzes the transient response of the wire in Figure 1, the excitation sources include three parts: (1) the original incident wave (zero-order), (2) the reflected wave reflected by layered half-space from the original incident wave (first-reflection), and (3) the radiated field from the induced current which is reflected by the half-space and becomes incident upon the wire again (second- and higher-order reflections).

The radiation field of thin wire can be regarded as superposition of the radiation field of many electric dipoles which are parallel to the interface. Using the spherical coordinate system, the radiation electric field of an electric dipole can be written as [30]

$$\vec{E} = -i\omega I l \frac{\exp(ikr)}{4\pi r} \left\{ \hat{r} \left( \frac{i}{kr} + \left( \frac{i}{kr} \right)^2 \right) 2 \cos \theta' + \hat{\theta}' \left( 1 + \frac{i}{kr} + \left( \frac{i}{kr} \right)^2 \right) \sin \theta' \right\}, \quad (1)$$

where  $i$ ,  $\omega$ ,  $I$ ,  $l$ ,  $k$ ,  $r$ ,  $\hat{r}$ ,  $\theta'$ , and  $\hat{\theta}'$  are units of the imaginary number, circular frequency of the incident wave, electric current of the wire, length of the dipole, spatial frequency, the distance of the origin point to observation point, the orientation vector, the angle between the  $\hat{r}$  and the  $\hat{z}$  direction, and the unit vector of  $\theta'$  direction, respectively, as illustrated in Figure 2. Equation (1) gives the radiation field of an electric dipole, which is suitable for both near field and far field. The radiation field of the dipole toward all directions in which the field is perpendicularly incident towards the interface of layered half-space can be reflected and becomes incident upon the dipole again ( $\theta' = \pi/2$ ). In this case, (1) can be written as

$$E_{\theta} = \omega I l \frac{\exp(ikr)}{4\pi r} \left[ \frac{1}{kr} + i \left( \frac{1}{(kr)^2} - 1 \right) \right]. \quad (2)$$

To make sure the existence of higher-order reflection does not ruin the hybridization of TDIE and FDTD, the electric field that is radiated by the dipole and reflected by half-space and arriving at the dipole again is estimated. Suppose we have a one-meter-long wire composed of four hundred electric dipoles and the direction of the wire is parallel to the interface. Let  $E_0$ ,  $E_1$ , and  $E_2$  represent the radiation electric field of a dipole at  $r_0 = 0.002$  m (the radius of the wire),  $r_1 = 0.25$  m and  $r_2 = 2.0$  m, respectively. According to (2) we know that the ratios of  $E_1$  to  $E_0$  and  $E_2$  to  $E_0$  basically do not change when the frequency varies from 1 MHz to 20 GHz. Suppose the observation point is  $j$  and the source point is  $i$  ( $i = 1 \sim 400$ ). The radiation electric fields of dipole  $j$  reflected by the ground half-space and reaching dipole  $j$  again can be estimated by (2). The radiation electric fields of dipole  $i$  ( $i \neq j$ ) reflected by the ground half-space and reaching dipole  $j$  again are less than the reflection field which is radiated by the dipole  $j$ . So the maximum reflected fields of point  $j$  on the surface of the thin wire are about

$$\begin{aligned} 400 \times E_1|_{0.25 \text{ m}} &\approx 1.39 \times 10^{-3} R \times E_0, \\ 400 \times E_1|_{2 \text{ m}} &\approx 2.5 \times 10^{-4} R \times E_0, \end{aligned} \quad (3)$$

where  $R < 1$  is the reflection coefficient of the layered half-space and the subscripts 0.25 m and 2 m indicated the wire is located 0.25 meter or 2.0 meters above the interface of the half-space, respectively. It is obvious that in these two cases the contribution of the radiation field reflected by the current is much smaller than original incident field. So high-order interactions between thin wire and half-space could be neglected in this paper.

When one applies the hybrid scheme to analyze the transient responses of wire structure above layered half-space, TDIE is employed to study the above wire with both the original incident and reflected wave as the exciting source. In the hybrid formulations, considering the *thinness* nature of wire structure, the incident wave across the section of the conducting wire approximately has the same value, and the induced current on the wire is considered as line current. In forming the integral equation, the source point will be on the axis of the cylinder, whereas the observation point is positioned at the conductor surface. Therefore, the

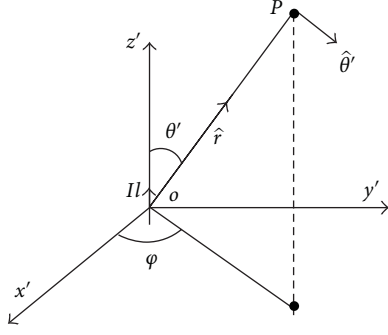


FIGURE 2: The electric dipole.

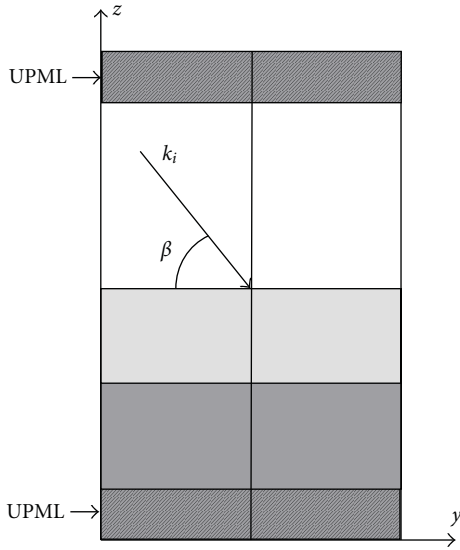


FIGURE 3: The FDTD model.

distance between the source point and observation point is always larger than or equal to the radius of the wire.

Compared with the TDIE method in free space, the TDIE method in the hybrid approach deals with two kinds of incident waves. The first is the original incident wave, which is introduced in analytical form, while the other exciting source is from the reflected wave of the underlying layered half-space, which can be calculated using one-dimensional modified FDTD method. The configuration of the half-space can be arbitrary, and the dielectric parameters can be varied layer by layer.

The FDTD model is given in Figure 3. In order to obtain the reflected wave where the conducting wire is positioned, the location of output point in the scattering field (SF) region of FDTD domain is as high as the wire, whereas the half-space is modeled in the total field region. In the implementation of FDTD, UPML is used to truncate the infinite domain and reduce numerical errors.

The general formulations of FDTD and TDIE methods will be given in the following.

**2.1. FDTD Method.** Suppose a straight thin wire structure is located above the layered half-space as Figure 1 shows. The

electric fields have components along  $y$  and  $z$  axis when the model is impinged by oblique incident wave. The  $y$ -component can stimulate induced current whereas the  $z$ -component cannot.

In FDTD method, a set of finite-difference equations for the time-dependent Maxwell's curl equations system is originated by Yee [13]. These equations can be represented in a discrete form, both in space and time, employing the second-order accurate central difference formula.

Supposing the incident angle is  $\beta$  (the angle of the interface of the layered half-space and the  $\vec{k}_i$  as Figure 3 shows), the parameters of media and the field quantity are independent and denoted by  $y$  and  $z$ , and the modified Maxwell curl equations of one-dimensional case are

$$-\frac{\partial E_{x1D}}{\partial z} = \mu \frac{\partial H_{y1D}}{\partial t}, \quad (4)$$

$$-\frac{1}{\sin^2 \beta} \frac{\partial H_{y1D}}{\partial z} = \varepsilon \frac{\partial E_{x1D}}{\partial t}, \quad (5)$$

where  $\mu = \mu_0 \mu_r$  and  $\varepsilon = \varepsilon_0 \varepsilon_r$  are permeability and permittivity of the media, respectively. Equations (4) and (5) can be employed to compute the reflection and transmission electromagnetic wave in case of an oblique plane wave incident to the surface of the layered half-space.

Considering  $k_y = k \cos \beta$  and  $k_z = k \sin \beta$ , (5) can be written as

$$-\frac{k^2}{k_z^2} \frac{\partial H_{y1D}}{\partial z} = \varepsilon j \omega E_{x1D}. \quad (6)$$

According to the phase match theory,  $k_y = k \cos \beta$  is a constant in each layer. Equation (6) can be written as

$$-k^2 \frac{\partial H_{y1D}}{\partial z} = (k^2 - k_y^2) j \omega \varepsilon_0 \varepsilon_r E_{x1D}, \quad (7)$$

in which  $k = \omega \sqrt{\mu \varepsilon}$ ,  $k_z^2 = k^2 - k_y^2$ . Then we have

$$-\frac{\partial H_{y1D}}{\partial z} = [\varepsilon_r - \varepsilon_1 \cos^2 \beta] \varepsilon_0 j \omega E_{x1D}. \quad (8)$$

Let  $\varepsilon' = \varepsilon_r - \varepsilon_1 \sin^2 \beta$ , and (8) can be written as

$$-\frac{\partial H_{y1D}}{\partial z} = \varepsilon_0 \varepsilon' \frac{\partial E_{x1D}}{\partial t}. \quad (9)$$

The derivatives in (4) and (9) can be approximated by using the central difference formula with the position  $E_x(m)$  being the center point for the central difference formula in space and time instant  $(n + 1/2)\Delta t$  being the center point in time. We can get FDTD updating equation as follows:

$$\begin{aligned} E_{x1D}|_j^{n+1} &= CA(m) \cdot E_{x1D}|_j^n \\ &\quad - CB(m) \cdot \frac{H_{y1D}|_{j+1/2}^{n+1/2} - H_{y1D}|_{j-1/2}^{n+1/2}}{\Delta z}, \\ H_{y1D}|_{j+1/2}^{n+1/2} &= CP(m) \cdot H_{y1D}|_{j+1/2}^{n-1/2} \\ &\quad - CQ(m) \cdot \left[ \frac{E_{x1D}|_{j+1}^n - E_{x1D}|_j^n}{\Delta z} \right], \end{aligned} \quad (10)$$



FIGURE 4: The thin wire is divided into  $N + 1$  subfield.

where  $CA(m)$ ,  $CB(m)$ ,  $CP(m)$ , and  $CQ(m)$  are coefficient of the updating equation.

In this paper, in order to obtain the reflected wave of the layered half-space, the layered half-space is modeled in the total field (TF) region, and the output point of the reflection waves is in the scattering field (SF) region of FDTD domain. UPML absorbing conduction is used to truncate the infinite domain and reduce numerical errors.

**2.2. TDIE Method.** The scattering electric field of the thin wire can be expressed by the vector potential as follows:

$$\frac{\partial \vec{E}}{\partial t} = -\frac{\partial^2 \vec{A}}{\partial t^2} + c^2 \nabla(\nabla \cdot \vec{A}). \quad (11)$$

The directed incident field  $\mathbf{E}_x^i$  and reflected field  $\mathbf{E}_x^r$  can be regarded as a constant across the section of wire. Applying the boundary condition for the total electric field, (11) can be written as

$$\left. \frac{\partial^2 A_x}{\partial x^2} - \frac{1}{c^2} \frac{\partial^2 A_x}{\partial t^2} \right|_{r=a} = -\left. \frac{1}{c^2} \frac{\partial E_x^i}{\partial t} \right|_{r=a} - \left. \frac{1}{c^2} \frac{\partial E_x^r}{\partial t} \right|_{r=a}, \quad (12)$$

$$x \in (0, L).$$

The vector potential is given by

$$A_x(x, t) = \frac{\mu_0}{4\pi} \int_{x'=0}^L \frac{I(x', t - |x - x'|/c)}{\sqrt{|x - x'|^2 + a^2}} dx', \quad (13)$$

where  $a$  and  $c$  represent the radius of thin wire, and velocity of light, respectively.

The thin wire is divided into  $N + 1$  equal segments; the length of the segment is  $\Delta x$  (as the Figure 4 shows). The basis function is defined as follows:

$$f_m(x) = \begin{cases} 1, & x_m - \frac{\Delta x}{2} \leq x \leq x_m + \frac{\Delta x}{2} \\ 0, & \text{otherwise.} \end{cases} \quad (14)$$

Using these expansion functions, we approximate the current  $I$  as follows:

$$I(x, t) \approx \sum_{k=1}^n I_k(t) f_k(x) \quad (15)$$

If central difference approximation is employed, (12) can be written as

$$\frac{A_{m+1,n} - 2A_{m,n} + A_{m-1,n}}{(\Delta x)^2} - \frac{A_{m,n+1} - 2A_{m,n} + A_{m,n-1}}{(c\Delta t)^2} = -F_{m,n}, \quad (16)$$

where the excitation term is

$$F_{m,n} = \frac{\partial E_x^i(x_m, t_n)}{\partial t} + \frac{\partial E_x^r(x_m, t_n)}{\partial t}. \quad (17)$$

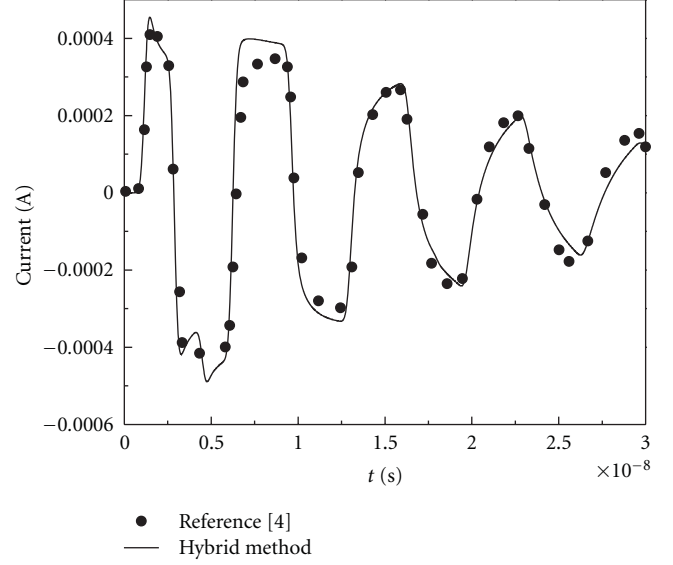


FIGURE 5: Current induced at midpoint of a straight thin wire above half-space.

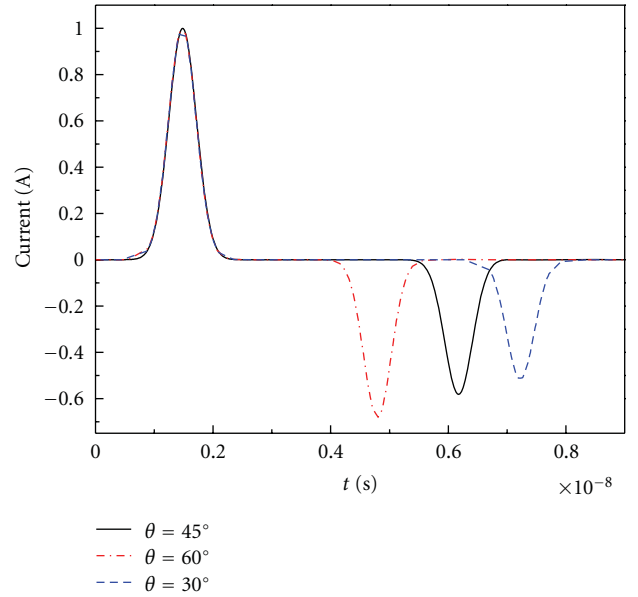


FIGURE 6: The incident and reflected wave on the height of thin wire with different incident angles.

Substituting (17) into (16), we have

$$I_{m,n} \kappa_{m,m} = -A_{m,n} + 2A_{m,n-1} - A_{m,n-2} + (\Delta t)^2 F_{m,n-1} + \left( \frac{c\Delta t}{\Delta x} \right)^2 [A_{m+1,n-1} - 2A_{m,n-1} + A_{m-1,n-1}], \quad (18)$$

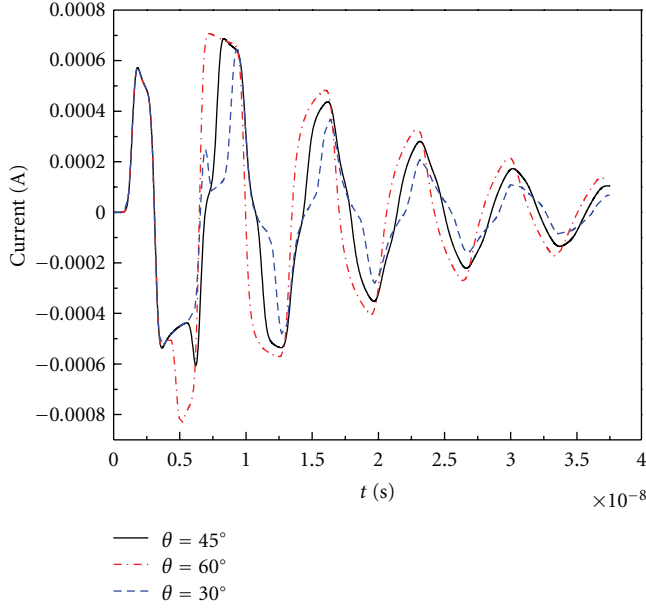


FIGURE 7: The transient current induced at midpoint of thin wire above half-space with different incident angles.

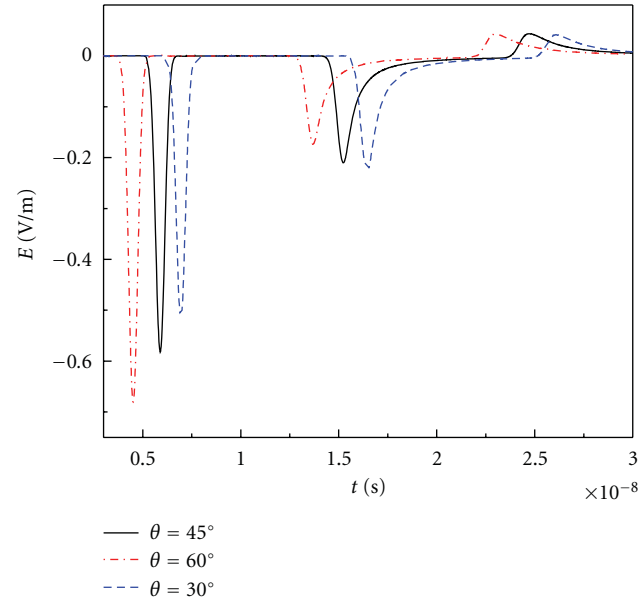


FIGURE 8: The reflected wave on the height of thin wire located above the half-space with different incident angle.

where

$$\begin{aligned}
 A_{m,n} &= I_m(t_n)\kappa_{m,m} + \sum_{\substack{k=1 \\ k \neq m}}^N I_k\left(t_n - \frac{|x_m - x_k|}{c}\right)\kappa_{m,k}, \\
 \mathcal{A}_{m,n} &= \sum_{\substack{k=1 \\ k \neq m}}^N I_k\left(t_n - \frac{|x_m - x_k|}{c}\right)\kappa_{m,k}, \\
 I_{m,n} &\equiv I_m(t_n),
 \end{aligned} \tag{19}$$

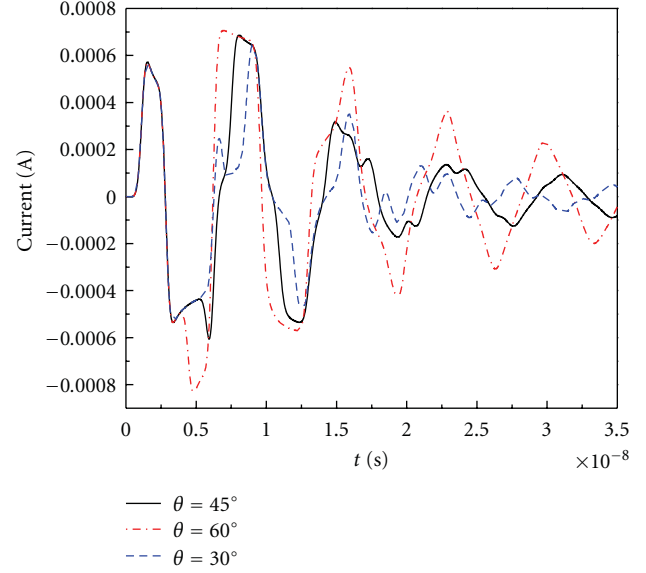


FIGURE 9: The current induced at midpoint of thin wire with different incident angle.

where  $\kappa_{m,k}$  is impedance coefficient matrix. The algorithm may be started by assuming  $I_{m,0} = I_{m,1} = 0$  and calculating  $I_{m,2}$  using (18). Once we obtain  $I_{m,2}$ , coupled with the knowledge of  $I_{m,0}$  and  $I_{m,1}$ , we proceed to calculate  $I_{m,3}$  again using (18). This procedure can be continued to calculate currents at successive time instants  $t_4, t_5, \dots$  until the transient currents die down.

### 3. Numerical Results

In this section, numerical examples are given to verify the accuracy of the presented algorithm. Then, the transient responses of the straight thin wires above different layered half-spaces are analyzed. In all examples of this section, the length of thin wire is  $l = 1$  m, and the time step is the same in both TDIE and FDTD methods, which make it convenient for calculation in hybrid method.

Figure 5 gives the transient current (solid line) induced at the midpoint of this thin wire, which is at the height of  $h = 0.25$  m above the interface. The underlying half-space is homogeneous with relative permittivity  $\epsilon_r = 10$ , and the Gaussian pulse  $E = E_0 \exp(-g^2(t - t_0)^2)$  (where  $E_0 = 1$  V/m,  $g = 4.0 \times 10^9$  s<sup>-1</sup>,  $t_0 = 1.2 \times 10^{-9}$  s) is incident perpendicularly to the interface of the half-space ( $\varphi = 90^\circ$ ,  $\theta = 0^\circ$ ). The polarizing direction of the electric field is along  $y$  axis. The results of [5] (dot) are also given for comparison in Figure 5. It is obvious that the results obtained by hybrid method are in good agreement with the results of [5]. This illustrates the correctness of the presented scheme.

The second example gives the comparison between directly incident wave and the reflected wave by the half-space. The radius  $a = 0.002$  m, and the height  $h = 0.5$  m. It is illuminated by a Gaussian pulse ( $E_0 = 1$  V/m,  $g = 2.5 \times 10^9$  s<sup>-1</sup>,  $t_0 = 1.2 \times 10^{-9}$  s). The half-space is a nonmagnetic

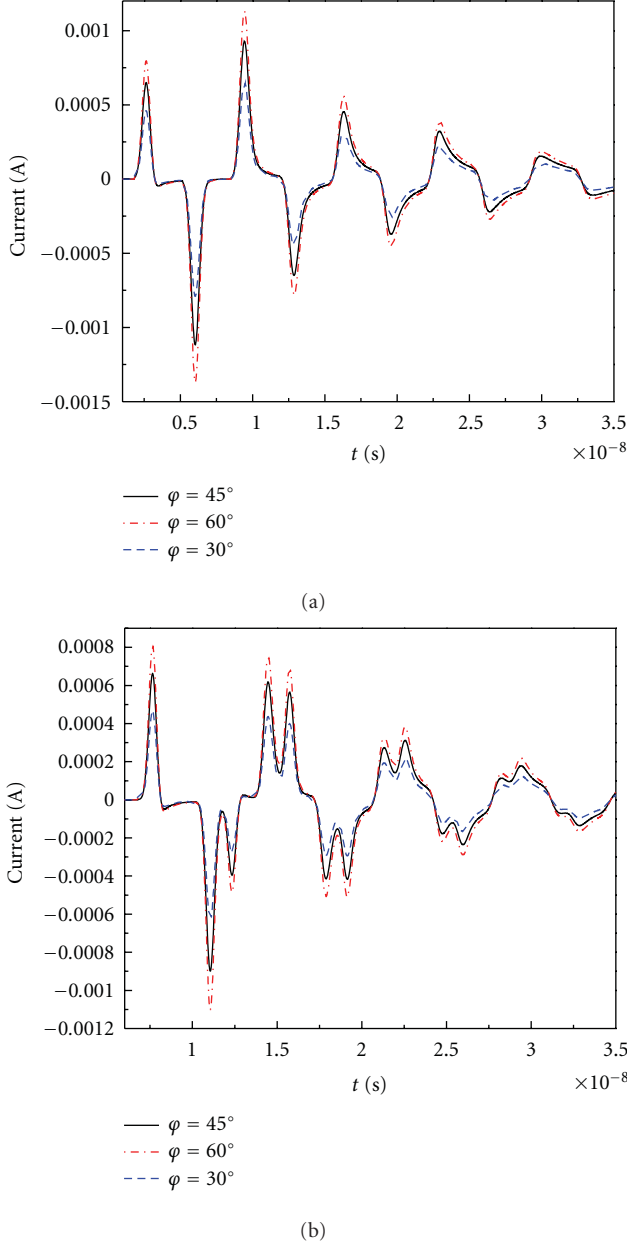


FIGURE 10: The current induced at midpoint of thin wire with different incident angle.

medium with  $\epsilon_r = 4$  and  $\sigma = 10^{-5}$  s/m. Figure 6 presents the incident wave and reflected wave when  $\varphi = 90^\circ$  and the angle between the incident plane and the surface of the half-space is changed. The dash line, solid line, and dash dot line represent incident angle  $\theta = 30^\circ$ ,  $\theta = 45^\circ$ , and  $\theta = 60^\circ$ , respectively. It can be seen from Figure 6 that the amplitude of reflected wave is less than the original incident wave. There is also obvious time delay compared with the original incident wave.

Figure 7 plots the induced currents at the center of thin wire varying with time. The meaning of dashed line, solid line, and dash-dot line is same as above. As shown in the figure, the transient responses of different incident angles

are the same at the early time and afterwards have obvious difference.

Figure 8 gives the reflected wave of the height of thin wire located above the layered half space with different incident angle. The reflected electric fields have multiple peaks, which is due to the presence of three interfaces and the interactions between the layers.

Then let us consider the transient response of a thin wire above layered half-space. As the configuration shown in Figure 1 exhibits, the thin wire is located at the height  $h = 0.5$  m above the interface. The multilayer medium is composed as follows: the first layer is dry soil ( $\epsilon_r = 4$ ,  $\sigma = 10^{-5}$  s/m, thickness  $d_1 = 1.0$  m); the second layer is wet soil ( $\epsilon_r = 10$ ,  $\sigma = 10^{-3}$  s/m, thickness  $d_2 = 1.0$  m); the third layer is ground water ( $\epsilon_r = 81$ ,  $\sigma = 10^{-3}$  s/m). The length and the radius of the thin wire are the same as in the above example. The incident wave is the Guassain pulse ( $E_0 = 1$  V/m,  $g = 2.5 \times 10^9$  s $^{-1}$ ,  $t_0 = 0.86 \times 10^{-9}$  s), which is oblique to the layered interface. Figure 7 gives the reflected wave of the height of thin wire located above the layered half-space with different incident angles. The reflected electric fields have multiple peaks, which is due to the presence of three interfaces and the interactions between the layers.

Figure 9 gives the transient currents induced at the center of thin wire with different incident angles. The meaning of dash line, solid line, and dash-dot line is the same as in the above example. As shown in this figure, the transient responses are the same at the early time and show obvious difference at latter time. This is because the effect of the interfaces reaches the wire at the latter time.

The last example is about the transient responses of thin wire above layered half-space when the incident angle  $\varphi$  and  $\theta$  are changed. The background and the location of wire are the same as in the above example. Figure 10(a) plots the induced current at the center of thin wire when the incident wave vector is at the plane which is perpendicular to the interface of the layered half-space ( $\theta = 90^\circ$ ). The dash line, solid line, and dash dot line represent incident angle  $\varphi = 30^\circ$ ,  $\varphi = 45^\circ$ , and  $\varphi = 60^\circ$ , respectively. Figure 10(b) plots the induced current at the center of thin wire when  $\theta = 45^\circ$ . Also, the dash line, solid line, and dash dot line represent incident angles  $\varphi = 30^\circ$ ,  $\varphi = 45^\circ$ , and  $\varphi = 60^\circ$ , respectively. We can see from these two figures, the amplitudes of the current are different and the fluctuation time periods are obviously different when different incidence angles are used.

#### 4. Conclusion

The TDIE/FDTD hybrid method is efficient for commutating the transient responses of thin wire above layered half-space in the case of the EM oblique incident wave. One-dimensional TDIE is applied to study the above wire structure whereas one-dimensional modified FDTD method is used to get reflected field of the layered half-space. This can save computing time and memory, so the presented algorithm consumes less memory, offers high speed of computing, and is a highly efficient numerical solution.

## Acknowledgment

This work was supported by the National Natural Scientific Foundation of China under Grant 60871071 and the Fundamental Research Funds for the Central Universities.

## References

- [1] S. M. Rao and T. K. Shanker, *Time Domain Electromagnetics*, Academic Press, 1999.
- [2] S. M. Rao, T. K. Sarkar, and S. A. Dianat, "The application of the conjugate gradient method to the solution of transient electromagnetic scattering from thin wires," *Radio Science*, vol. 19, no. 5, pp. 1319–1326, 1983.
- [3] P. R. Barnes and F. M. Tesche, "On the direct calculation of a transient plane wave reflected from a finitely conducting half space," *IEEE Transactions on Electromagnetic Compatibility*, vol. 33, no. 2, pp. 90–96, 1991.
- [4] D. Poljak and V. Roje, "Time domain calculation of the parameters of thin wire antennas and scatterers in a half-space configuration," *IEEE Proceedings—Microwaves, Antennas and Propagation*, vol. 145, no. 1, pp. 57–63, 1998.
- [5] D. Poljak, C. Y. Tham, and A. McCowen, "Transient response of nonlinearly loaded wires in a two media configuration," *IEEE Transactions on Electromagnetic Compatibility*, vol. 46, no. 1, pp. 121–125, 2004.
- [6] M. H. Haddad, M. Ghaffari-Miab, and R. Faraji-Dana, "Transient analysis of thin-wire structures above a multi-layer medium using complex-time Green's functions," *IET Microwaves, Antennas and Propagation*, vol. 4, no. 11, pp. 1937–1947, 2010.
- [7] L. Li, L. Li, C. Gao, X. Gu, and Z. Zhao, "Numerical treatment for time domain integral equations of thin wire structures in half-space configuration," *IEEE Transactions on Magnetics*, vol. 44, no. 6, Article ID 4526938, pp. 774–777, 2008.
- [8] L. Li, L.-J. Li, and C.-Z. Gao, "Direct time-domain method for analyzing scattering from thin wire structures in the dielectric half-space," *Journal of North China Electric Power University*, vol. 34, no. 6, 2005.
- [9] T. C. Tong and A. Sankar, "Transient scattering from curved thin wires by the finite element method," *IEEE Antennas and Propagation Society*, vol. 12, no. 3, 1980.
- [10] P. Parhami and R. Mittra, "Wire antennas over a lossy half-space," *IEEE Transactions on Antennas and Propagation*, vol. AP-28, pp. 397–403, 1980.
- [11] B. Wei, X. Y. Li, F. Wang, and D. B. Ge, "A finite difference time domain absorbing boundary condition for general frequency-dispersive media," *Acta Physica Sinica*, vol. 57, no. 10, pp. 6283–6289, 2008.
- [12] Y. N. Jiang and D. B. Ge, "New scheme for introducing an oblique incidence plane wave to layered media in finite-difference time-domain," *Acta Physica Sinica*, vol. 58, no. 9, pp. 6174–6178, 2009.
- [13] K. S. Yee, "Numerical solution of initial boundary value problems involving Maxwell's equations in isotropic media," *IEEE Transactions on Antennas and Propagation*, vol. 14, pp. 302–307, 1966.
- [14] A. Taflove and M. E. Brodwin, "Numerical solution of steady-state electromagnetic scattering problems using the time-dependent Maxwell's equations," *IEEE Transactions on Microwave Theory and Techniques*, vol. 23, no. 8, pp. 623–630, 1975.
- [15] A. Taflove, "Application of the finite-difference time-domain method to sinusoidal steady-state electromagnetic penetration problems," *IEEE Transactions on Electromagnetic Compatibility*, vol. 22, no. 3, pp. 191–202, 1980.
- [16] A. Taflove and S. C. Hagness, *Computational Electrodynamics: The Finite-Difference Time-Domain Method*, Artech House, Norwood, Mass, USA, 3rd edition, 2005.
- [17] Z. H. Chen and Q. X. Chu, "FDTD modeling of arbitrary linear lumped networks using piecewise linear recursive convolution technique," *Progress in Electromagnetics Research*, vol. 73, pp. 327–341, 2007.
- [18] M. Ali and S. Sanyal, "FDTD analysis of dipole antenna as EMI sensor," *Progress in Electromagnetics Research*, vol. 69, pp. 341–359, 2007.
- [19] L. X. Yang, D. B. Ge, and B. Wei, "FDTD/TDPO hybrid approach for analysis of the EM scattering of combinative objects," *Progress in Electromagnetics Research*, vol. 76, pp. 275–284, 2007.
- [20] Y. N. Jiang, D. B. Ge, and S. J. Ding, "Analysis of TF-SF boundary for 2D-FDTD with plane P-wave propagation in layered dispersive and lossy media," *Progress in Electromagnetics Research*, vol. 83, pp. 157–172, 2008.
- [21] S. W. Yang, Y. K. Chen, and Z. P. Nie, "Simulation of time modulated linear antenna arrays using the FDTD method," *Progress in Electromagnetics Research*, vol. 98, pp. 175–190, 2009.
- [22] Y. Q. Zhang and D. B. Ge, "A unified FDTD approach for electromagnetic analysis of dispersive objects," *Progress in Electromagnetics Research*, vol. 96, pp. 155–172, 2009.
- [23] Y. Tretiakov and G. Pan, "Malvar wavelet based pocklington equation solutions to thin-wire antennas and scatterers," *Progress In Electromagnetics Research*, vol. 47, pp. 123–133, 2000.
- [24] K. Afrooz, A. Abdipour, A. Tavakoli, and M. Movahhedi, "Time domain analysis of active transmission line using FDTD technique (Application to microwave/MM-wave transistors)," *Progress in Electromagnetics Research*, vol. 77, pp. 309–328, 2007.
- [25] M. Y. Wang, J. Xu, J. Wu et al., "FDTD study on wave propagation in layered structures with biaxial anisotropic metamaterials," *Progress in Electromagnetics Research*, vol. 81, pp. 253–265, 2008.
- [26] Z. Huang, K. Demarest, and R. Plumb, "An FDTD/MoM hybrid technique for modeling complex antennas in the presence of heterogeneous grounds," *IEEE Transactions on Geoscience and Remote Sensing*, vol. 37, no. 6, pp. 2692–2698, 1999.
- [27] A. Monorchio, A. Rubio Bretones, R. Mittra, G. Manara, and R. Gómez Martín, "A hybrid time-domain technique that combines the finite element, finite difference and method of moment techniques to solve complex electromagnetic problems," *IEEE Transactions on Antennas and Propagation*, vol. 52, no. 10, pp. 2666–2674, 2004.
- [28] F. Edelvik, "A new technique for accurate and stable modeling of arbitrarily oriented thin wires in the FDTD method," *IEEE Transactions on Electromagnetic Compatibility*, vol. 45, no. 2, pp. 416–423, 2003.
- [29] H. Zhao and Z. Shen, "Weighted Laguerre polynomials-finite difference method for time-domain modeling of thin wire antennas in a loaded cavity," *IEEE Antennas and Wireless Propagation Letters*, vol. 8, Article ID 5286304, pp. 1131–1134, 2009.
- [30] J. A. Kong, *Electromagnetic Wave Theory*, EMW Publishing, Higher Education Press, 2002.

## Research Article

# Design of Meander-Line Antennas for Radio Frequency Identification Based on Multiobjective Optimization

X. L. Travassos,<sup>1</sup> A. C. Lisboa,<sup>2</sup> and D. A. G. Vieira<sup>2</sup>

<sup>1</sup>Integrated Center of Manufacture and Technology, SENAI, 41650-010 Salvador, BA, Brazil

<sup>2</sup>ENACOM Handcrafted Technologies, 31310-260 Belo Horizonte, MG, Brazil

Correspondence should be addressed to X. L. Travassos, lucas.travassos@fieb.org.br

Received 6 July 2011; Revised 9 November 2011; Accepted 26 November 2011

Academic Editor: Ning Yuan

Copyright © 2012 X. L. Travassos et al. This is an open access article distributed under the Creative Commons Attribution License, which permits unrestricted use, distribution, and reproduction in any medium, provided the original work is properly cited.

This paper presents optimization problem formulations to design meander-line antennas for passive UHF radio frequency identification tags based on given specifications of input impedance, frequency range, and geometric constraints. In this application, there is a need for directive transponders to select properly the target tag, which in turn must be ideally isotropic. The design of an effective meander-line antenna for RFID purposes requires balancing geometrical characteristics with the microchip impedance. Therefore, there is an issue of optimization in determining the antenna parameters for best performance. The antenna is analyzed by a method of moments. Some results using a deterministic optimization algorithm are shown.

## 1. Introduction

The low cost of electronic microcircuits and their low power consumption have turned practicable the development of identification systems through radio frequency, especially from the 1990s. Radio frequency identification (RFID) allows not only storing a relatively large amount of information, but also changing and processing information.

Radio frequency identification is a growing and promising technology that has been used in a variety of applications. It has been applied for tracking of products, luggage, books, and animals, where the tags can be attached to the objects, injected under the skin, or mounted in holes made in parts of the items [1]. Antitheft systems, asset management, anesthetic dosages, car manufacturing, and many other identification applications, such as passports and restricted area access, are examples of how the RFID technology is flexible and dynamic.

RFID total market value in 2009 grew to \$5.56 billion, of which \$2.18 billion was spent only on passive tags [2]. Therefore, optimizing radio frequency identification systems has become crucial in improving the productivity and lowering costs in industry and supply chains.

A RFID system consists basically of a receiver (tag), an emitter (reader), and a computational system (direct link). The tags have two main structures: the microchip, which provides the necessary power to transmit and receive information, and the antenna. The tags can be active, passive or semiactive, depending on the mechanism of powering the microchip and transmitting information. Active tags have a local power source and electronics for performing specialized tasks [3]. This local power source, which is usually a battery, provides energy for the operation of the microchip and transmission of information. The semiactive tags also have a battery, but they use the power received from the reader to send the message back. Finally, passive tags do not have any power source and need to rectify the energy received from the reader to generate enough voltage for the microchip operation. The type of the RFID tags is chosen based on a specific application. For low-cost tags and relatively short read ranges (around 3 m [4]), the passive tags are the most appropriate ones.

The entire RFID system depends on the performance of the tag, which relies on its elements. In the direct link, the reader sends modulated RF power that reaches the tag; this power is captured by the tag antenna and is transmitted

to the microchip. In order to ensure a great power transmission coefficient and decrease the losses, the tag antenna impedance must match the complex input impedance of the tag microchip, which is commonly capacitive. Usually, the antenna is the element to be matched to a specific chip available in the market.

Due to the diversity of materials and packages that need to be identified, tag antennas development for passive UHF RFID systems has become challenging. The performance of the tag antennas is very dependent on the properties of the objects which the tags are attached to. The material of the objects can influence the capacitive characteristics of the tag antenna, as well as modify its radiation pattern. Many studies have been carried out in order to investigate these effects on tags attached to metallic surfaces and water [5, 6] and to dielectrics [7, 8]. Efforts to find the most optimized tag antenna for a given application improve the performance of the entire RFID system because it can increase the power transmission coefficient and the read range.

The design in this paper was motivated by application in coffee business. In this business, the product is stored in sacks in the producers' farms and needs to be transported to the local cooperatives. Each cooperative receives coffee sacks from different producers, normally using treadmills, and the receiving process demands time and labor force and is usually inefficient. Besides, the origin of the coffee must be traced until it reaches the final consumer and the material flow must be controlled in real time. In this context, RFID systems can be used to improve the productivity and competitiveness and reduce costs.

Tracking coffee containers in real time using RFID technology, from the shipment to the moment the container arrives in the USA, is already being used by a coffee importer named Sara Lee, in Santos harbour (São Paulo, Brazil). Moreover, the ST Café, a Brazilian company, is using RFID tags to identify the coffee sacks individually in rural properties.

Meander-line antennas are one of the most commonly used in UHF RFID tags, mainly because of their tunability and size. Several papers have been published on RFID meander-line antenna design. Some articles have sought achieving improved antenna gains and small size by using different configurations of meander-line antennas for passive RFID, which were explored applying genetic algorithm (GA) optimization and the method of moments (MoM) [9, 10]. The moment method (MoM) with Rao-Wilton-Glisson (RWG) basis functions [11] is used to calculate the electromagnetic characteristics of the antenna. In [8], a loaded meander-line tag antenna was designed focusing on a specific application: box tracking in warehouses; the box content and the sensitivity to fabrication process were also considered. Some methods have been used to characterize impedances and design meander-line antennas [12], and GA has been shown to be an efficient optimization tool for selecting globally optimal parameters of the antenna [13]. This paper introduces design techniques using optimization in order to cope with operation inside a frequency range, where the main innovation lies in the formulation of single and multiobjective optimization problems and the suit-

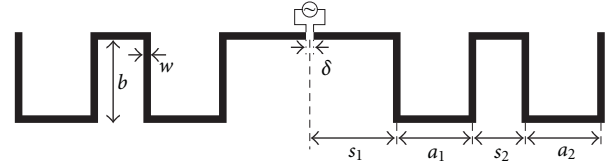


FIGURE 1: Geometry of the meander-line antenna for  $c = 2$ .

ability of state-of-the-art optimization algorithms to solve them.

## 2. Antenna Design

One of the most convenient forms of RFID tags is a labellike, so that they can be stuck on objects. This work analyzes a meander-line antenna that is very suitable for this application.

## 3. Model and Parameterization

The application of coffee business required the use of a passive UHF RFID tag antenna (902-928 MHz). In order to perform the simulations, some design specifications were established. The microchip, which has been used as a reference in this work, is ALIEN Higgs TM-3, EPC Class 1 Gen 2, whose equivalent input impedance is  $(27.41-200.90j)$  at 915 MHz. The meander-line antenna geometry (see Figure 1) is parameterized by the number of meanders  $c$  in each side, feed gap  $\delta$ , trace width  $w$ , height  $b$ , meander step length  $a_i$ , and spacing between meanders  $s_i$ ,  $i = 1, \dots, c$ .

The antenna is discretized into regular quasiregular triangles and analyzed using a method of moments with a voltage gap feed which considers  $\delta = 0$ . The implementation was validated with classical antenna simulation software.

The parameters other than  $\delta$  compose the design variables

$$x = \begin{bmatrix} w \\ b \\ a_1 \\ \vdots \\ a_c \\ s_1 \\ \vdots \\ s_c \end{bmatrix} \quad (1)$$

and can be used to optimize the antenna to desired profiles.

## 4. Optimization Problem

A meander-line antenna cannot provide high directivity. This is a desired behavior considering that isotropic radiation

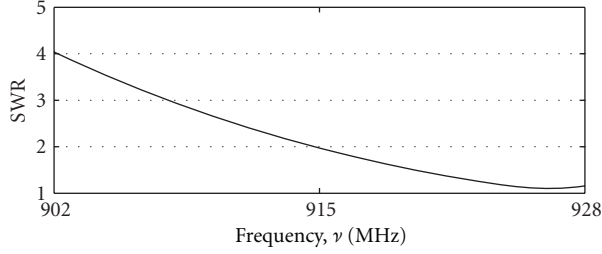


FIGURE 2: Optimal standing wave ratio behavior inside frequency range for multiobjective formulation.

would not be ideal for the application. The remaining features of interest are input impedance and size, which are used in the multiobjective optimization problem formulation

$$\begin{aligned} & \text{minimize } f(x) = \text{SWR}(x, \nu) \\ & \text{subject to } g(x) = \begin{bmatrix} L_{\min} - L(x) \\ L(x) - L_{\max} \end{bmatrix} \leq 0, \\ & x_{\min} \leq x \leq x_{\max}, \end{aligned} \quad (2)$$

where  $x \in \mathbb{R}^n$  is the vector of design variables (1),  $n = 2+2c$ , SWR is the standing wave ratio,  $L$  is the antenna length, and  $\nu \in \mathbb{R}^o$  is the vector of sample frequencies. There is one-objective function for each sample frequency, hence,  $o$ -objective functions.

The optimization problem (2) queries for antennas with minimum SWR in each sample frequency whose overall length and design variables lie inside an interval.

To optimize the worst case SWR inside the frequency range, the monoobjective optimization problem formulation

$$\begin{aligned} & \text{minimize } f(x, t) = t \\ & \text{subject to } g(x, t) = \begin{bmatrix} \text{SWR}(x, \nu) - t \\ L_{\min} - L(x) \\ L(x) - L_{\max} \end{bmatrix} \leq 0, \\ & x_{\min} \leq x \leq x_{\max}, \end{aligned} \quad (3)$$

can be derived, where  $t$  is the worst case SWR.

## 5. Optimization Results

The optimal variables results of (2) for  $c = 4$  and  $o = 5$  sample frequencies inside the frequency range are shown in Table 1. The target impedance, frequency range and length constraints are given in Table 2. The length was 71.51 mm and the worst case standing wave ratio (SWR) was 4.04 for the optimal antenna. SWR behavior inside the frequency range is shown in Figure 2. The result took 395 problem oracle queries within 9 iterations of the multiobjective deterministic algorithm with monotonic convergence [14, 15].

In order to compare the two formulations (multiobjective and worst case), the CEDA algorithm was limited to 395 oracle queries to optimize problem (3) for  $c = 4$ ,  $o = 5$  and settings in Table 2, whose optimal results are shown in Table 3. The length was 62.67 mm and the worst

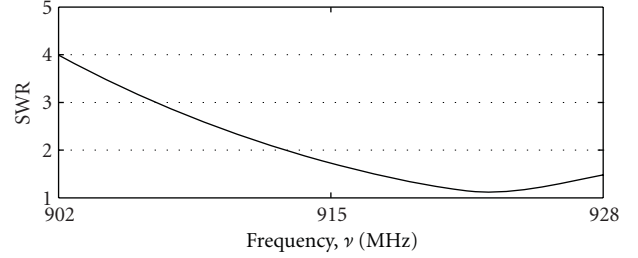


FIGURE 3: Optimal standing wave ratio behavior inside frequency range for worst case formulation.

case standing wave ratio (SWR) was 3.99 for the optimal antenna. SWR behavior inside the frequency range is shown in Figure 3.

## 6. Overview of the Optimization Algorithm

As mentioned before, the optimization algorithm used in the meander-line antenna design, named henceforth the cone of efficient directions algorithm (CEDA) [14], is supported by guarantees on monotonic convergence. Its fundamental idea comes from the cone of efficient directions, that is, the set of directions where there exists at least one infinitesimal step that decreases all objective functions at the same time. When the oracle query point is infeasible, the constraints are treated as objectives. Given an efficient direction, a line search algorithm with guarantees on feasibility preserving and strict improvement of starting point takes place. A brief overview is shown next. For further details, please refer to the original paper [14].

**6.1. Search Direction.** If a point is not a local optimum, then there must be a better feasible neighbor point, by definition. If a function  $f : \mathbb{R}^n \mapsto \mathbb{R}$  is differentiable, then its local behavior is mainly linear by Taylor series, that is,

$$f(x) \approx \tilde{f}(x) = f(x_k) + \nabla^T f(x_k)(x - x_k), \quad (4)$$

here  $x_k$  is the oracle query point at iteration  $k$  and  $\nabla f : \mathbb{R}^n \mapsto \mathbb{R}^n$  denotes the gradient of  $f$ . Hence,  $f(x) < f(x_k)$  whenever  $\nabla^T f(x_k)(x - x_k) < 0$  within some neighborhood of  $x_k$ . Considering a nonnull step  $\alpha > 0$  from  $x_k$  towards a direction  $d_k$ , that is,

$$x_{k+1} = x_k + \alpha d_k, \quad (5)$$

leads to  $\nabla^T f(x_k)d_k < 0$ .

Consider a differentiable multiobjective optimization problem in the form

$$\begin{aligned} & \text{minimize } f(x) \\ & \text{subject to } g(x) < 0, \\ & x_{\min} \leq x \leq x_{\max}. \end{aligned} \quad (6)$$

When the oracle query point  $x_k$  is feasible (i.e.,  $g(x_k) \leq 0$ ), it is desirable to minimize the objective functions in order to get better feasible points. Otherwise, it is desirable

TABLE 1: Optimization problem variables for multiobjective formulation.

	Parameter (mm)									
	$w$	$b$	$a_1$	$a_2$	$a_3$	$A_4$	$s_1$	$s_2$	$s_3$	$s_4$
Max	0.50	12.60	1.00	1.00	1.00	1.00	1.00	1.00	1.00	1.00
Min	0.80	21.00	7.00	7.00	7.00	7.00	7.00	7.00	7.00	7.00
Opt	0.78	15.11	4.70	3.98	6.42	5.66	3.80	1.42	6.00	3.77

TABLE 2: Specifications and optimal antenna profile.

Parameter	Value
$L_{\min}$ (mm)	10
$L_{\max}$ (mm)	100
$V_{\min}$ (MHz)	902
$V_{\max}$ (MHz)	928
$Z_s$ ( $\Omega$ )	27.4–200.9i

to minimize the violated constraint functions (without violating new ones) in order to find a feasible point. Hence, the cone of efficient directions for constrained multiobjective problems in the form (6) can be defined as

$$d_k : M_k^T d_k > 0, \quad (7)$$

where

$$M_k = \begin{cases} -[\nabla f(x_k) \nabla g_{I_k}(x_k)], & g(x_k) \leq 0, \\ -[\nabla g_{J_k}(x_k) \nabla g_{I_k}(x_k)], & \text{otherwise,} \end{cases} \quad (8)$$

where the gradient of a vector function  $\nabla f : \mathfrak{R}^n \mapsto \mathfrak{R}^m$  is  $\nabla f = [\nabla f_1 \cdots \nabla f_m]$ . The set of active  $I_k$  and violated  $J_k$  constraint functions are given by

$$\begin{aligned} I_k &= \{i \mid g_i(x_k) = 0\}, \\ J_k &= \{j \mid g_j(x_k) > 0\}. \end{aligned} \quad (9)$$

Considering unit efficient directions, the one opposite to the gradient would be the best choice for the linear approximation of a single-objective function since it provides the greatest decrease per step length. Thus, the intersection between the cone of efficient directions (7) and its dual cone

$$d_k = M_k \lambda, \quad \lambda \geq 0, \lambda \neq 0, \quad (10)$$

contains good efficient directions. One of these good efficient directions can be found by the linear problem

$$\begin{aligned} &\text{minimize } -1^T \lambda \\ &\text{subject to } -M_k^T M_k \lambda \leq 0, \\ &0 \leq \lambda \leq 1, \end{aligned} \quad (11)$$

which queries for the search direction  $d_k = M_k \lambda^*$  of maximum relative weight  $\lambda^*$  sum. This problem is infeasible or  $\lambda = 0$  only when the cone of efficient directions is empty since the intersection between a cone and its dual is empty only when the cone itself is empty.

**6.2. Multiobjective Line Search.** The multiobjective line search algorithm solves the problem

$$\begin{aligned} &\text{minimize } f(x_k + \alpha d_k) \\ &\text{subject to } g(x_k + \alpha d_k) \leq 0, \\ &0 \leq \alpha \leq \alpha_{\max}, \end{aligned} \quad (12)$$

when  $g(x_k) \leq 0$ , and

$$\begin{aligned} &\text{minimize } g_{\bar{J}_k}(x_k + \alpha d_k) \\ &\text{subject to } g_{\bar{J}_k}(x_k + \alpha d_k) \leq 0, \\ &0 \leq \alpha \leq \alpha_{\max}, \end{aligned} \quad (13)$$

otherwise, where  $\bar{J}_k$  denotes the set of nonviolated constraints (i.e., complement of  $J_k$ ).

The maximum step length is given by

$$\alpha_{\max} = \max \alpha : x_{\min} \leq x_k + \alpha d_k \leq x_{\max}, \quad \alpha > 0, \quad (14)$$

which can be easily solved analytically (point where the ray  $x_k + \alpha d_k$ ,  $\alpha > 0$  intersects the box  $[x_{\min}, x_{\max}]$ ). If  $\alpha^* = \alpha_{\max}$ , then the respective activated constraint (design variables bound) is added to the set of active constraints used in the definition of  $M_{k+1}$ .

**6.3. Stop Criteria.** The natural stop criteria for the multiobjective optimization algorithm are when any column of  $M_k$  is null, problem (11) is infeasible,  $d_k = 0$ , or  $\alpha^* = 0$ .

**6.4. Theoretical Guarantees.** When  $g(x_k) \leq 0$  and no stop criteria are met, it is easy to verify that the conditions

$$\begin{aligned} &f(x_k + \alpha^* d_k) < f(x_k), \\ &g(x_k + \alpha^* d_k) \leq 0 \end{aligned} \quad (15)$$

hold true, which are the respective monotonic convergence and feasibility preserving guarantees.

## 7. Optimization Algorithm Suitability

The first notable features of CEDA are its monotonic convergence and feasibility preserving theoretical guarantees. They are also very desired in practice, considering that they lead to robustness against bad-behavior functions and provide better intermediate results during the optimization process.

Another notable feature of CEDA is that the stop criteria are met earlier when the number of objective functions increases. This can be observed in the optimization of the

TABLE 3: Optimization problem variables for formulation worst case.

	Parameter (mm)									
	$w$	$b$	$a_1$	$a_2$	$a_3$	$a_4$	$s_1$	$s_2$	$s_3$	$s_4$
Max	0.50	12.60	1.00	1.00	1.00	1.00	1.00	1.00	1.00	1.00
Min	0.80	21.00	7.00	7.00	7.00	7.00	7.00	7.00	7.00	7.00
Opt	0.60	15.81	5.95	2.26	3.82	1.94	4.39	3.13	4.25	6.09

meander-line antenna, where minimizing SWR at sample frequencies is faster than minimizing its worst case. This occurs because CEDA treats multiobjective problems as so and the dimension of the Pareto optimal set of a problem is, in nondegenerate cases, the number of objective function minus one. CEDA can be considered an extension of the classical gradient algorithm to multiobjective problems. Indeed, it also presents a slow convergence rate when the functions Hessian matrices are ill conditioned. Second-order directions (e.g., Newton directions) solve this problem for monoobjective and also multiobjective problems [16]. Nevertheless, the CEDA performance in this work was satisfactory. More examples of multiobjective antenna optimization can be found in [17] where satellite antennas and bow tie antennas for ground penetrating radar are studied.

## 8. Conclusion

The best SWR of about 1 was verified inside a frequency range of  $\pm 1.4\%$  around 915 MHz for optimal 4-meander antennas, even though with a worst case SWR of about 4. More degrees of freedom could be considered in order to improve worst cases (e.g., increasing the number of meanders or parameterizing each meander height individually). Nevertheless, the main purpose of this paper was achieved: optimal meander-line antennas for a real-life demand using different formulations.

The multiobjective formulation is faster to converge than the single-objective one. Furthermore, the theoretical guarantee of always improving all objective functions after each iteration may be very suitable in real-world applications. However, considering that SWRs of 1 and 40 at sample frequencies could be considered Pareto optimal for the former formulation, the solution of the worst case formulation may be regarded more meaningful, that is, a good decision rule, even though it is either dominated or included in the optimal Pareto set.

## Acknowledgments

This work was supported by CNPq and FAPESB, Brazil.

## References

- [1] S. Polniak, "The RFID case study book: RFID application stories from around the globe," Tech. Rep., Abhisam Software, 2007.
- [2] P. Harrop, "Printed RFID in 2010," Tech. Rep., IDTechEx, 2010.
- [3] Z. N. Chen, *Antennas for Portable Devices*, Wiley, 2007.
- [4] D. M. Dobkin, *The RF in RFID: Passive UHF RFID in Practice*, Elsevier, 2008.
- [5] N. A. Mohammed, M. Sivakumar, and D. D. Deavours, "An RFID tag capable of free-space and on-metal operation," Tech. Rep., Information and Telecommunications Technology Center, 2008.
- [6] J. Y. Park and J. M. Woo, "Miniaturised dual-band S-shaped RFID tag antenna mountable on metallic surface," *Electronics Letters*, vol. 44, no. 23, pp. 1339–1341, 2008.
- [7] J. D. Griffin and G. D. Durgin, "Radio link budgets for 915MHz RFID antennas placed on various objects," in *Proceedings of the Texas Wireless Symposium*, vol. 44, Atlanta, Ga, USA, 2005.
- [8] K. V. S. Rao, P. V. Nikitin, and S. F. Lam, "Antenna design for UHF RFID tags: a review and a practical application," *IEEE Transactions on Antennas and Propagation*, vol. 53, no. 12, pp. 3870–3876, 2005.
- [9] G. Marrocco, A. Fonte, and F. Bardati, "Evolutionary design of miniaturized meander-line antennas for RFID applications," in *Proceedings of the IEEE AP-S International Symposium*, June 2002.
- [10] G. Marrocco, "Gain-optimized self-resonant meander line antennas for RFID applications," *IEEE Antennas and Wireless Propagation Letters*, vol. 2, pp. 302–305, 2003.
- [11] S. Makarov, "MoM antenna simulations with Matlab: RWG basis functions," *IEEE Antennas and Propagation Magazine*, vol. 43, no. 5, pp. 100–107, 2001.
- [12] X. Qing, C. K. Goh, and Z. N. Chen, "Impedance characterization of rfid tag antennas and application in tag co-design," *IEEE Transactions on Microwave Theory and Techniques*, vol. 57, no. 5, Article ID 4806170, pp. 1268–1274, 2009.
- [13] D. Zhou, R. A. Abd-Alhameed, C. H. See et al., "Meander-line antenna design for UHF RFID tag using a genetic algorithm," in *Proceedings of the Progress in Electromagnetics Research Symposium*, pp. 1253–1257, March 2009.
- [14] D. A. G. Vieira, R. H. C. Takahashi, and R. R. Saldanha, "Multicriteria optimization with a multiobjective golden section line search," *Mathematical Programming, Ser. A*, vol. 131, pp. 131–161, 2012.
- [15] A. C. Lisboa, D. A. G. Vieira, J. A. Vasconcelos, R. R. Saldanha, and R. H. C. Takahashi, "Multiobjective shape optimization of broad-band reflector antennas using the cone of efficient directions algorithm," *IEEE Transactions on Magnetics*, vol. 42, no. 4, pp. 1223–1226, 2006.
- [16] J. Fliege, L. M. G. Drummond, and B. F. Svaiter, "Newton's method for multiobjective optimization," *SIAM Journal on Optimization*, vol. 20, no. 2, pp. 602–626, 2009.
- [17] X. L. Travassos, D. A. G. Vieira, D. A. G. Brandão, and A. C. Lisboa, "Antenna optimization using multi-objective algorithms," in *Proceedings of the 4th European Conference on Antennas and Propagation (EUCAP '10)*, pp. 1–5, April 2010.

## Research Article

# Hierarchical Matrices Method and Its Application in Electromagnetic Integral Equations

Han Guo, Jun Hu, Hanru Shao, and Zaiping Nie

*School of Electronic Engineering, University of Electronic Science and Technology of China, Sichuan, Chengdu 611731, China*

Correspondence should be addressed to Jun Hu, hujun@uestc.edu.cn

Received 15 July 2011; Revised 14 October 2011; Accepted 18 October 2011

Academic Editor: Ning Yuan

Copyright © 2012 Han Guo et al. This is an open access article distributed under the Creative Commons Attribution License, which permits unrestricted use, distribution, and reproduction in any medium, provided the original work is properly cited.

Hierarchical ( $\mathcal{H}$ -) matrices method is a general mathematical framework providing a highly compact representation and efficient numerical arithmetic. When applied in integral-equation- (IE-) based computational electromagnetics,  $\mathcal{H}$ -matrices can be regarded as a fast algorithm; therefore, both the CPU time and memory requirement are reduced significantly. Its kernel independent feature also makes it suitable for any kind of integral equation. To solve  $\mathcal{H}$ -matrices system, Krylov iteration methods can be employed with appropriate preconditioners, and direct solvers based on the hierarchical structure of  $\mathcal{H}$ -matrices are also available along with high efficiency and accuracy, which is a unique advantage compared to other fast algorithms. In this paper, a novel sparse approximate inverse (SAI) preconditioner in multilevel fashion is proposed to accelerate the convergence rate of Krylov iterations for solving  $\mathcal{H}$ -matrices system in electromagnetic applications, and a group of parallel fast direct solvers are developed for dealing with multiple right-hand-side cases. Finally, numerical experiments are given to demonstrate the advantages of the proposed multilevel preconditioner compared to conventional "single level" preconditioners and the practicability of the fast direct solvers for arbitrary complex structures.

## 1. Introduction

Integral equation (IE) method [1] is widely used in electromagnetic analysis and simulation. Compared to finite difference time domain (FDTD) method [2] and Finite element (FE) method [3], IE method is generally more accurate and avoids annoying numerical dispersion problems as well as complex boundary conditions. Despite the many advantages, IE method is often involved in enormous computational consumption, since its numerical discretization leads to dense linear system. With the efforts for years, various fast algorithms had developed focusing on reducing the computational complexity for IE method such as adaptive integral method (AIM) [4], fast multipole method (FMM) [5], IE-Fast Fourier transform (IE-FFT) [6], and fast low-rank compression methods [7]. Though these fast algorithms are based on different theories, they use the same idea to reduce CPU time and memory usage complexity, which is to compute and store the major entries of the dense system matrix indirectly, and employ iterative methods instead of direct methods (such as LU decomposition) to solve the

system. Preconditioners are often used to accelerate the convergence of iterative methods. However, iterative methods cannot always guarantee a reasonable solution with high precision; therefore, in some complex cases, we expect to employ powerful preconditioners to obtain visible acceleration of convergence or even use direct methods to avoid this problem entirely. But to implement these ideas in traditional fast algorithms encounters some difficulties that are, once a fast algorithm is applied, the major entries of the system matrix are computed and stored indirectly, and only a few entries can be accessed to form the sparse pattern which is essential to construct the preconditioners. This condition confines the flexibility of the preconditioning; therefore, a powerful preconditioner is generally hard to get. For direct methods, accessibility of the whole matrix entries is also prerequisite, and employing them in fast algorithms is difficult as well as flexible preconditioning.

Hierarchical ( $\mathcal{H}$ -) matrices method [8, 9] is a general mathematical framework providing a highly compact representation and efficient numerical arithmetic. Applying  $\mathcal{H}$ -matrices in IE method can reduce both CPU time and

memory usage complexity significantly, so it can be regarded as a fast algorithm to IE method. Unlike the traditional fast algorithms mentioned above, any entry of  $\mathcal{H}$ -structured system matrix can be recovered easily, though the major entries are still implicitly expressed. This quality enables us to construct more efficient preconditioners, and moreover, a fast direct solver is available since its unique format. In this paper, a novel sparse approximate inverse (SAI) preconditioner in multilevel fashion is proposed to accelerate the convergence rate of Krylov iterations for solving  $\mathcal{H}$ -matrices system in electromagnetic applications, which is mentioned in [10], and a group of parallel fast direct solvers are developed for dealing with multiple right-hand-side cases.

This paper is organized as follows. Section 2 gives a brief review of the IE method and basic conception of  $\mathcal{H}$ -matrices. In Section 3, we elaborate the construction of the proposed multilevel SAI preconditioner and the implementation of parallel fast direct solvers. Numerical experiments are given in Section 4 to demonstrate the advantages of the proposed multilevel preconditioner compared to conventional “single level” preconditioners and the practicability of the fast direct solvers for arbitrary complex structures. Finally, some conclusions are given in Section 5.

## 2. $\mathcal{H}$ -Matrices Representation for IE Method

We first proceed with a description of the IE method for solving electromagnetic scattering problems from 3D perfectly electric conductor (PEC). For concise introduction, only the electric field integral equation (EFIE) [1] is considered. The EFIE is written as

$$\hat{\mathbf{t}} \cdot \int_{s'} ds' \overline{\mathbf{G}}(\mathbf{r}, \mathbf{r}') \mathbf{J}(\mathbf{r}') = \frac{4\pi i}{k\eta} \hat{\mathbf{t}} \cdot \mathbf{E}^i(\mathbf{r}). \quad (1)$$

Discretize integral equation (1) by expanding  $\mathbf{J}$  with local basis functions

$$\mathbf{J}(\mathbf{r}) = \sum_{n=1}^N x_n \mathbf{f}_n(\mathbf{r}), \quad (2)$$

where  $N$  is the number of unknowns, denoting the vector basis functions, and  $x_n$  is the unknown expansion coefficients. Applying Galerkin's method results in a matrix equation

$$\mathbf{A} \cdot \mathbf{x} = \mathbf{b}, \quad (3)$$

where

$$\begin{aligned} \mathbf{A}_{mn} &= \int_s ds \mathbf{f}_m(\mathbf{r}) \cdot \int_{s'} ds' \overline{\mathbf{G}}(\mathbf{r}, \mathbf{r}') \cdot \mathbf{f}_n(\mathbf{r}'), \\ \mathbf{b}_m &= \frac{4\pi i}{k\eta} \int_s ds \mathbf{f}_m(\mathbf{r}) \cdot \mathbf{E}^i(\mathbf{r}). \end{aligned} \quad (4)$$

If matrix  $\mathbf{A}$  is in  $\mathcal{H}$ -matrices formatted, we use  $\mathbf{A}_{\mathcal{H}}$  to denote it.

Considering that the construction of proposed multilevel SAI preconditioner is built upon the structure of  $\mathcal{H}$ -matrices, some of its basic concepts need be reviewed at first.

The basis functions set indexed by  $\mathcal{I} := \{1, 2, \dots, N\}$  can be constructed as a tree  $T_{\mathcal{I}} = (V, E)$  with vertex set  $V$  and edge set  $E$ . For each vertex  $v \in V$ , we define the set of son of  $v$  as  $S_{\mathcal{I}}(v) := \{w \in V \mid (v, w) \in E\}$ . The tree  $T_{\mathcal{I}}$  is called a cluster tree if the following conditions hold:

$$\begin{aligned} &\mathcal{I} \text{ is the root of } T_{\mathcal{I}}, \\ &\forall v \in V : \text{if } S_{\mathcal{I}}(v) \neq \emptyset, \text{ we have } v = \bigcup_{w \in S_{\mathcal{I}}(v)} w, \\ &\forall w_1, w_2 \in S_{\mathcal{I}}(v) \text{ with } w_1 \neq w_2 : w_1 \cap w_2 = \emptyset. \end{aligned} \quad (5)$$

Each vertex  $v$  in  $T_{\mathcal{I}}$  is called a cluster, representing a bunch of basis functions. Typically, each vertex has two sons. If the amount of basis functions contained in a cluster is less than a certain number of  $n_{\min}$ , that cluster has no sons, also called the leaves of  $T_{\mathcal{I}}$ . By rearranging the basis functions by their indices, they are numbered consecutively in each cluster, and, moreover, they are concentrated geometrically. Precisely, let  $\Omega_v$  denote the domain of basis functions represented by cluster  $v$ , and it is bounded by the cardinality of  $v$ :

$$\text{diam}(\Omega_v) \leq c_g |v| \quad (6)$$

in which  $\text{diam}(\cdot)$  is the Euclidean diameter of a set.  $c_g$  is a real constant; let the inequality valid for all clusters.

The electromagnetic interaction of any two clusters, including self-interaction, maps certain subblock of the system coefficient matrix. Practically, most of these subblocks can be approximated by low-rank matrices with high-accuracy. Therefore, a systemic and appropriate partitioning procedure is needed for the coefficient matrix. Based on the cluster tree  $T_{\mathcal{I}}$  which contains hierarchy of partitions of  $\mathcal{I}$ , we are able to construct the block-cluster tree  $T_{\mathcal{I} \times \mathcal{I}}$  describing a hierarchical partition of  $\mathcal{I} \times \mathcal{I}$  by the following maps:

$$S_{\mathcal{I} \times \mathcal{I}}(t \times s) = \begin{cases} \emptyset, & \text{if } S_{\mathcal{I}}(t) = \emptyset \text{ or } S_{\mathcal{I}}(s) = \emptyset, \\ \emptyset, & \text{if } t \times s \text{ is admissible,} \\ S_{\mathcal{I}}(t) \times S_{\mathcal{I}}(s), & \text{otherwise,} \end{cases} \quad (7)$$

in which the definition of  $S_{\mathcal{I} \times \mathcal{I}}(\cdot)$  is similar to  $S_{\mathcal{I}}(\cdot)$  that denotes the sons of certain block-cluster  $t \times s$ . *Admissible* is a criterion which will be elaborated later and decides whether the subblock should be approximated by low-rank matrix, or split and combined by its sons, suspending for further transaction. Finally, the whole system matrix is segmented into pieces of subblocks by the procedure above. Corresponding to the block-cluster tree, these subblocks are called the leaves of  $T_{\mathcal{I} \times \mathcal{I}}$ , denoted by  $\mathcal{L}(T_{\mathcal{I} \times \mathcal{I}})$ .

If two clusters are well separated geometrically, the Green function which connects the interaction of them is barely varying in their domains. That means, only a few patterns of interactional vectors can represent the whole mode; therefore, the subblock representing their interaction is rank deficit. In order to discerning these subblocks appropriately, we introduce the admissibility condition [9]:

$$\max\{\text{diam}(\Omega_t), \text{diam}(\Omega_s)\} \leq \eta \text{dist}(\Omega_t, \Omega_s), \quad (8)$$

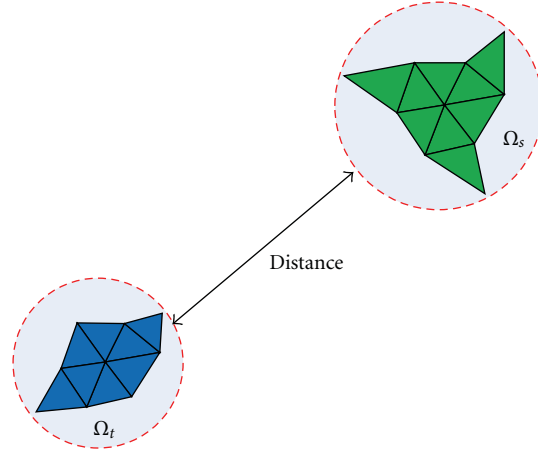


FIGURE 1: Two basis function clusters domains and their distance, describe the definition of *admissible* condition.

in which  $\text{dist}(\cdot, \cdot)$  is the Euclidean distance of two sets,  $\Omega_t$  and  $\Omega_s$  denote the domains of basis functions of cluster  $t$ , and  $s$  and  $\eta$  are a controllable real parameter, which is also illustrated in Figure 1. If the statement (8) is true, sub-block  $t \times s$  is *admissible*, otherwise it is *nonadmissible*. The leaves of block-cluster tree  $\mathcal{L}(T_{I \times I})$  are either *admissible* or *nonadmissible*. For *admissible* subblocks, we substitute them by low-rank representation through specific algorithms such as adaptive cross approximation (ACA) [11]. For *nonadmissible* subblocks, we calculate the entries and store them directly. The total computational complexity for constructing is close to  $O(N \log N)$ , in which  $N$  regards to the number of unknowns, and we give a numerical investigation Part A of Section 4.

### 3. Multilevel SAI Preconditioning and Fast Direct Methods

**3.1. Multilevel SAI Preconditioning.** If the Krylov iterative methods are used to solve the linear system, we always expect to find a high-performance preconditioner to accelerate the convergence. Generally, instead of solving the linear system of the form  $\mathbf{A}_{\mathcal{H}} \mathbf{x} = \mathbf{b}$ , we solve it by the following forms:

$$\mathbf{M} \mathbf{A}_{\mathcal{H}} \mathbf{x} = \mathbf{M} \mathbf{b} \quad \text{or} \quad \mathbf{A}_{\mathcal{H}} \mathbf{M} \mathbf{y} = \mathbf{b}, \quad \mathbf{x} = \mathbf{M} \mathbf{y}. \quad (9)$$

In which  $\mathbf{M}$  is a sparse matrix satisfying the condition  $\mathbf{M} \approx \mathbf{A}_{\mathcal{H}}^{-1}$  to a certain degree. Therefore,  $\mathbf{M} \mathbf{A}_{\mathcal{H}} \approx \mathbf{I}$  or  $\mathbf{A}_{\mathcal{H}} \mathbf{M} \approx \mathbf{I}$  can make the iterative solver more efficient. Because of limited space, we only discuss the left preconditioning case below. The right preconditioning case can be analyzed similarly. Traditional preconditioner has a fixed form that we could only execute “single level” preconditioning. Here, we elaborate how to construct a multilevel preconditioner under  $\mathcal{H}$ -matrices format.

For a block-cluster tree  $T_{I \times I}$  in  $\mathcal{H}$ -matrices, let  $L(T_{I \times I})$  denotes its depth and  $\mathcal{L}(T_{I \times I})$  denotes all the leaves of the cluster tree. Any leaf block-cluster  $b = (t \times s) \in \mathcal{L}(T_{I \times I})$  belongs to certain level of  $T_{I \times I}$ ; hence,  $1 \leq \text{level}(b) \leq L(T_{I \times I})$ . We define that the finest level is the 1st level, where

the smallest block cluster is located. A substructure of  $\mathbf{A}_{\mathcal{H}}$  denoted by  $\mathbf{A}_{\mathcal{H}}^{(l)}$  can be defined as follows:

$$\mathbf{A}_{\mathcal{H}}^{(l)}(i, j) = \begin{cases} \mathbf{A}_{\mathcal{H}}(i, j), & (i, j) \in B^{(l)}, \\ 0, & \text{otherwise} \end{cases} \quad (10)$$

in which  $B^{(l)}$  is a subset of  $\mathcal{L}(T_{I \times I})$ ,

$$B^{(l)} = \{b \mid b \in \mathcal{L}(T_{I \times I}), \text{level}(b) \leq l\}, \quad (11)$$

so  $\mathbf{A}_{\mathcal{H}}^{(l)}$  is sparse regarded as a standard matrix, which could be made use of as the primary data to form sparse approximate inverse. A trivial example of  $\mathbf{A}_{\mathcal{H}}^{(l)}$  is that

$$\mathbf{A}_{\mathcal{H}}^{(L(T_{I \times I}))} = \mathbf{A}_{\mathcal{H}}. \quad (12)$$

The intuitive grasp of  $\mathbf{A}_{\mathcal{H}}^{(l)}$  is shown in Figure 2. Consider an IE linear system matrix in  $\mathcal{H}$ -matrices form, the nonzero entries distribution of  $\mathbf{A}_{\mathcal{H}}^{(1)}$ ,  $\mathbf{A}_{\mathcal{H}}^{(2)}$ , and  $\mathbf{A}_{\mathcal{H}}^{(3)}$  are marked as shadow area corresponding to the whole matrix. Obviously high level of  $\mathbf{A}_{\mathcal{H}}^{(l)}$  contains more useful data of the system.

Correspondingly, a set of preconditioning matrices  $\{\mathbf{M}^{(l)} \mid l = 1, 2, \dots, L(T_{I \times I})\}$  can be generated through  $\mathbf{A}_{\mathcal{H}}^{(l)}$ , which satisfied the conditions below:

$$\begin{aligned} \|\mathbf{I} - \mathbf{M}^{(1)} \mathbf{A}_{\mathcal{H}}\| &\geq \|\mathbf{I} - \mathbf{M}^{(2)} \mathbf{A}_{\mathcal{H}}\| \\ &\geq \dots \geq \|\mathbf{I} - \mathbf{M}^{(L(T_{I \times I}))} \mathbf{A}_{\mathcal{H}}\| \approx 0. \end{aligned} \quad (13)$$

In practice,  $\mathbf{M}^{(l)}$  can be solved by the sparse approximate inverse technique, which aims to minimize  $\|\mathbf{I} - \mathbf{M}^{(l)} \mathbf{A}_{\mathcal{H}}^{(l)}\|_F$  [12].  $\|\cdot\|_F$  is the Frobenius norm of a matrix, and  $\mathbf{M}^{(l)}$  is subjected to a certain sparsity pattern, expressed as

$$\min_{\mathbf{M}^{(l)} \in G^{(l)}} \|\mathbf{I} - \mathbf{M}^{(l)} \mathbf{A}_{\mathcal{H}}^{(l)}\|_F^2 = \sum_{i=1}^n \min_{\mathbf{m}_i^{(l)} \in G_i^{(l)}} \|\mathbf{e}_i - \mathbf{m}_i^{(l)} \mathbf{A}_{\mathcal{H}}^{(l)}\|_2^2, \quad (14)$$

where  $\mathbf{e}_i$  and  $\mathbf{m}_i^{(l)}$  are the row vectors of the matrices  $\mathbf{I}$  and  $\mathbf{M}^{(l)}$ , respectively.  $G^{(l)}$  represents the sparsity pattern for

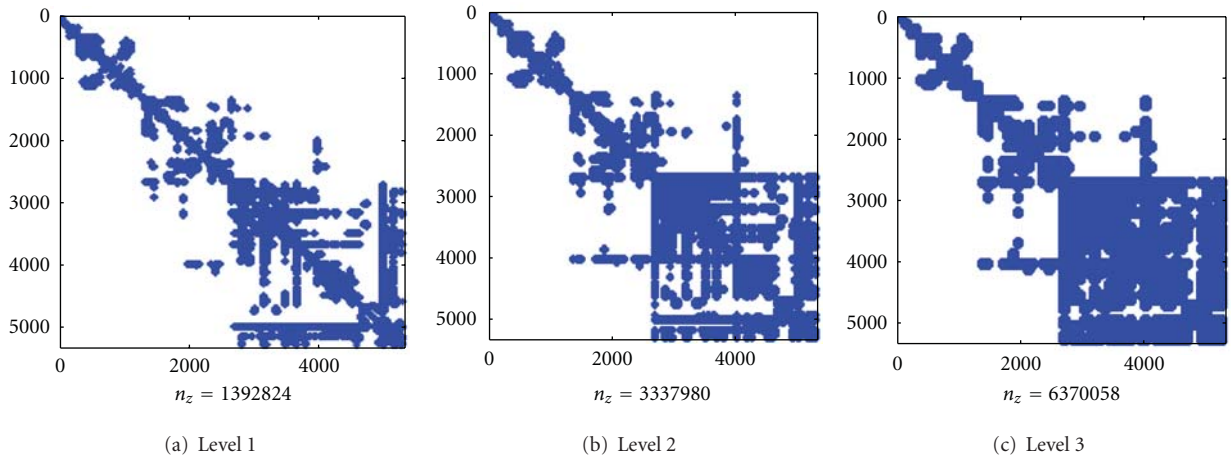


FIGURE 2: The data distribution of the finest 3 levels of  $\mathbf{A}_{\mathcal{H}}^{(l)}$ . This  $\mathcal{H}$ -matrices-formatted system is derived from an aircraft model which will be introduced in numerical experiments of Section 4.

different  $\mathbf{M}^{(l)}$ . Each of the subminimization problems in the right hand of (14) can be solved independently.

Because  $\mathbf{m}_i^{(l)}$  in (14) is constrained to a certain sparse pattern  $G$ , it has many zero entries that force the corresponding rows of  $\mathbf{A}_{\mathcal{H}}^{(l)}$  to be zero in matrix-vector multiply. Let  $\tilde{\mathbf{m}}_i^{(l)}$  denotes the subvector containing the nonzero entries of  $\mathbf{m}_i^{(l)}$ , and its corresponding rows of  $\mathbf{A}_{\mathcal{H}}^{(l)}$  are denoted by  $\mathbf{A}_{\mathcal{H}i}^{(l)}$ . Besides, since  $\mathbf{A}_{\mathcal{H}}^{(l)}$  is sparse, the submatrix  $\mathbf{A}_{\mathcal{H}i}^{(l)}$  has many columns that are identically zero. By removing the zero columns, we have a much smaller submatrix  $\tilde{\mathbf{A}}_{\mathcal{H}i}^{(l)}$ . The individual minimization problem of (14) is reduced to a least squares problem:

$$\min_{\tilde{\mathbf{m}}_i^{(l)}} \left\| \tilde{\mathbf{e}}_i - \tilde{\mathbf{m}}_i^{(l)} \tilde{\mathbf{A}}_{\mathcal{H}i}^{(l)} \right\|_2, \quad i = 1, 2, \dots, n. \quad (15)$$

$\mathbf{A}_{\mathcal{H}i}^{(l)}$  is just the submatrix of  $\mathbf{A}_{\mathcal{H}}^{(l)}$  that we implement the QR decomposition for solving (15).

**3.2. Hierarchical Fast Direct Methods.** If the system matrix is severely ill-conditioned and even the iterative solver with powerful preconditioner cannot obtain acceptable results, fast direct solvers are good alternative for IE  $\mathcal{H}$ -matrices. According to the arithmetic of partition matrices, the inversion of a matrix can be calculated by operating its submatrices. Considering the hierarchical structure of  $\mathcal{H}$ -matrices is indeed a nested quaternary submatrices structure, and a potential direct method can be made to solve the linear system. If a system matrix  $\mathbf{A}$  can be partitioned as

$$\mathbf{A} = \begin{bmatrix} \mathbf{A}_{11} & \mathbf{A}_{12} \\ \mathbf{A}_{21} & \mathbf{A}_{22} \end{bmatrix}, \quad (16)$$

then its inversion can be written as

$$\mathbf{A}^{-1} = \begin{bmatrix} \mathbf{A}_{11}^{-1} + \mathbf{A}_{11}^{-1} \mathbf{A}_{12} \mathbf{C}^{-1} \mathbf{A}_{21} \mathbf{A}_{11}^{-1} & -\mathbf{A}_{11}^{-1} \mathbf{A}_{12} \mathbf{C}^{-1} \\ -\mathbf{C}^{-1} \mathbf{A}_{21} \mathbf{A}_{11}^{-1} & \mathbf{C}^{-1} \end{bmatrix}, \quad (17)$$

#### Recursive procedure H\_Inverse( $m, x$ )

**If** the matrix  $m$  is partition **then**

H\_Inverse( $m_{11}, x_{11}$ )

$x_{12} = -x_{11} \odot m_{12}$

$x_{21} = -m_{12} \odot x_{11}$

$m_{22} = m_{22} \oplus m_{21} \odot x_{12}$

H\_Inverse( $m_{22}, x_{22}$ )

$m_{12} = x_{12} \odot m_{22}$

$m_{11} = m_{11} \oplus m_{12} \odot x_{21}$

$m_{21} = m_{22} \odot x_{21}$

**else**

Direct\_Inverse( $m_{11}$ )

**end if**

ALGORITHM 1

where  $\mathbf{C} = \mathbf{A}_{22} - \mathbf{A}_{21} \mathbf{A}_{11}^{-1} \mathbf{A}_{12}$ . Applying this arithmetic into  $\mathcal{H}$ -matrices, we can obtain a hierarchical inversing procedure as elaborated in Algorithm 1.

The operator  $\odot$  and  $\oplus$  manipulate matrices multiplication and addition which are specific for  $\mathcal{H}$ -matrices. Reference [9] gives detailed information about these operators. By implementing submatrices partition, aggregation, and truncation of singular value decomposition (SVD), the hierarchical structure can be maintained after the manipulation of these operators, and, more importantly, both CPU time and memory cost are saved compared to conventional matrices arithmetic. Consequently, the complexity of hierarchical direct solvers is  $O(N^2)$  for CPU time and  $O(N^{1.5})$  for memory usage, in contrast with  $O(N^3)$  and  $O(N^2)$  of conventional direct solver. This leads to realizing kinds of fast direct solving processes including the hierarchical inversing algorithm described above.

For numerical implementation, hierarchical inversing is not as fast as hierarchical LU decomposition, which is another fast direct method based on matrices decomposition

[9, 13]. Considering LU decomposition for partition matrix  $\mathbf{A}$ :

$$\mathbf{A} = \begin{bmatrix} \mathbf{A}_{11} & \mathbf{A}_{12} \\ \mathbf{A}_{21} & \mathbf{A}_{22} \end{bmatrix} = \begin{bmatrix} \mathbf{L}_{11} & \\ & \mathbf{L}_{22} \end{bmatrix} \begin{bmatrix} \mathbf{U}_{11} & \mathbf{U}_{12} \\ & \mathbf{U}_{22} \end{bmatrix} \quad (18)$$

matrices  $\mathbf{L}$  and  $\mathbf{U}$  can be figured out by the procedures:

- (1) computing  $\mathbf{L}_{11}$  and  $\mathbf{U}_{11}$  from the LUD  $\mathbf{L}_{11}\mathbf{U}_{11} = \mathbf{A}_{11}$ ;
- (2) computing  $\mathbf{U}_{12}$  from  $\mathbf{L}_{11}\mathbf{U}_{12} = \mathbf{A}_{12}$ ;
- (3) computing  $\mathbf{L}_{21}$  from  $\mathbf{L}_{21}\mathbf{U}_{11} = \mathbf{A}_{21}$ ;
- (4) computing  $\mathbf{L}_{22}$  and  $\mathbf{U}_{22}$  from the LUD  $\mathbf{L}_{22}\mathbf{U}_{22} = \mathbf{A}_{22} - \mathbf{L}_{21}\mathbf{U}_{12}$ .

Process (2) and process (3) can be refined as subprocesses of partitioned LU decomposition; therefore, by recursive applying of this procedure, the whole decomposition can be achieved. In the process of recursion, when the partitioning reaches the finest level in which submatrices are explicit expressed, conventional LU decomposition is employed. After the decomposition done, the primary  $\mathbf{L}$  and  $\mathbf{U}$  are still in  $\mathcal{H}$ -form and overwrite the original  $\mathbf{A}_{\mathcal{H}}$ . Then, we can use partitioned backward/forward processes to solve the linear system which is similar to linear equation solving by conventional LU decomposition. For EFIE, we can utilize its symmetric property and then construct a fast  $\text{LL}^T$  decomposition solver which is even much faster and memory saving. Considering  $\text{LL}^T$  decomposition for partition matrix  $\mathbf{A}$ :

$$\mathbf{A} = \begin{bmatrix} \mathbf{A}_{11} & \mathbf{A}_{21}^T \\ \mathbf{A}_{21} & \mathbf{A}_{22} \end{bmatrix} = \begin{bmatrix} \mathbf{L}_{11} & \\ & \mathbf{L}_{22} \end{bmatrix} \begin{bmatrix} \mathbf{L}_{11}^T & \mathbf{L}_{21}^T \\ & \mathbf{L}_{22}^T \end{bmatrix}, \quad (19)$$

matrices  $\mathbf{L}$  can be figure out by the procedures:

- (1) computing  $\mathbf{L}_{11}$  from the  $\text{LL}^T$   $\mathbf{L}_{11}\mathbf{L}_{11}^T = \mathbf{A}_{11}$ ;
- (2) computing  $\mathbf{L}_{21}$  from  $\mathbf{L}_{21}\mathbf{L}_{11}^T = \mathbf{A}_{21}$ ;
- (3) computing  $\mathbf{L}_{22}$  from the  $\text{LL}^T$   $\mathbf{L}_{22}\mathbf{L}_{22}^T = \mathbf{A}_{22} - \mathbf{L}_{21}\mathbf{L}_{21}^T$ .

Comparing with the procedure of hierarchical LU decomposition, one step is removed because we can obtain  $\mathbf{L}_{12}^T$  from trivial transposition. Therefore, the implementing of  $\text{LL}^T$  decomposition is approximately one time faster than that of LU decomposition, in a recursive way.

## 4. Numerical Experiments

**4.1. Complexity of Constructing  $\mathcal{H}$ -Matrices.** To investigate the complexity of constructing IE  $\mathcal{H}$ -matrices for electromagnetic analysis, there are two themes, namely, discretization density varying and wave frequencies varying. The former one means we change the number of unknowns along with varying the mesh density regarding electromagnetic wavelength. And the latter one means we change the number of unknowns along with varying wave frequencies, but the mesh density regarding wavelength is fixed. Here, we use a PEC sphere model of  $1.0\lambda$  (wavelength) radius to test both these two themes, as shown in Figures 3 and 4.

From the investigation, we can easily see that if incident wave frequency is fixed, the complexity of both CPU time

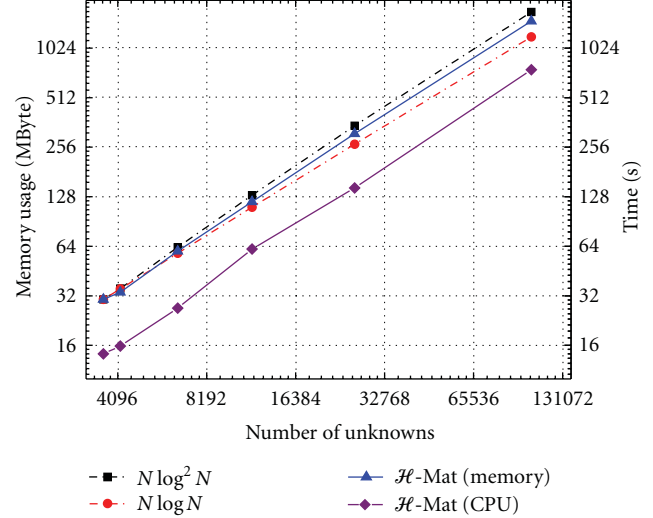


FIGURE 3: Computational complexity of constructing  $\mathcal{H}$ -matrices by fixed incident wave at 300.0 MHz.

and memory usage approach to  $O(N \log N)$ , where  $N$  regards to the number of unknowns. If we fix the discretization density and change the frequency of incident wave, the complexity curve is close to  $O(N^{4/3} \log N)$ . This is because the object domain contains more phase information when incident by higher frequency wave; therefore, the compression ratio of low rank submatrices in  $\mathcal{H}$ -matrices is lower in higher frequency cases.

**4.2. Iterative Solving with Multilevel SAI Preconditioner.** Firstly, a conducting sphere is used to demonstrate the improvement of the spectrum characteristics of the linear coefficient matrix by employing multilevel-SAI preconditioner (ML-SAI). Supposing  $\mathbf{M}^{(l)}$  is the  $l$ th level preconditioner and  $\mathbf{x}_{\text{rnd}}^{(i)}$  is the  $i$ th randomized vector, we define the regression index  $c_r^{(p)}$  of  $l$ th preconditioning level as

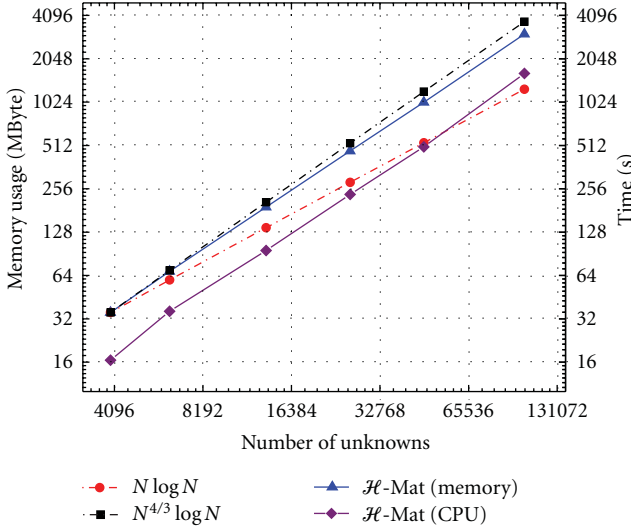
$$c_r^{(p)}(l) = \frac{1}{P} \sum_{i=1}^P \frac{\|\mathbf{x}_{\text{rnd}}^{(i)} - \mathbf{M}^{(l)} \mathbf{A}_{\mathcal{H}} \mathbf{x}_{\text{rnd}}^{(i)}\|_2}{\|\mathbf{x}_{\text{rnd}}^{(i)}\|_2}, \quad (20)$$

if  $\mathbf{M}^{(l)} \mathbf{A}_{\mathcal{H}}$  is close to identity matrix  $\mathbf{I}$ , then  $c_r^{(p)}(l) \rightarrow 0$  is expected. Particularly,  $\mathbf{M}^{(0)} = \mathbf{I}$ , which means no preconditioner is imposed. A sphere of  $2\lambda$  diameter, discretized by Rao-Wilton-Gliso (RWG) basis with different densities, is used to obtain the linear system matrix  $\mathbf{A}_{\mathcal{H}}$ . The different regression indices of different preconditioning levels are presented in Table 1 and compared to analogous indices of conventional SAI preconditioning in MLFMA.

From Table 1, we can see that with the preconditioning level of ML-SAI increased, the regression index is decreased, which means the effect of preconditioning is getting better. And the preconditioning effect of conventional SAI in MLFMA is better than the low level ML-SAI but not as good as high level ML-SAI. It should be noted that the  $c_r^{(100)}(3)$  in case of 957 unknowns is close to zero because the  $\mathcal{H}$ -matrices

TABLE 1: The regression index of different levels of ML-SAI and conventional SAI preconditioning.

Regression index		Number of unknowns			
		957	3,972	16,473	65,892
$\mathcal{H}$ -Mat.	$c_r^{(100)}(0)$	5.568	2.297	1.371	1.042
	$c_r^{(100)}(1)$	0.1311	0.2440	0.3155	0.4237
	$c_r^{(100)}(2)$	0.08925	0.2034	0.2523	0.2816
	$c_r^{(100)}(3)$	1.116E-6	0.1112	0.1828	0.2165
ML-FMA	None	5.723	2.415	1.355	0.989
	SAI	0.1052	0.2237	0.2844	0.3125

FIGURE 4: Computational complexity of constructing  $\mathcal{H}$ -matrices by fixed discretization mesh density at 8 points per wavelength.

structure of this model is only 3 levels, which means  $\mathbf{M}^{(3)}$  is very close to the exact inverse of the linear system.

Next, a  $40\lambda$  diameter PEC sphere is solved by  $\mathcal{H}$ -matrices method. Combine field integral equation (CFIE) is used, and the number of unknowns is 426,827. To set up the hierarchical system matrix, the memory cost is 42.6 GBytes and 26,387 seconds are used by 8 core parallel computing, on a workstation of Intel Xeon X5460 processor with 64 GBytes RAM. Generalized minimal residual (GMRES) [14] algorithm is employed as the Krylov iterative solver, and we use 1~3 level SAI preconditioners and diagonal block preconditioners (DBPs) as reference to accelerate the convergence of iteration. From Figure 5, we can see that the RCS curve conform to the Mie series identically. And the iterative history in Figure 6 shows that ML-SAIs have a distinct impact on accelerating the convergence of iteration.

Another example is an aircraft model which is  $50.75\lambda$  long,  $29.20\lambda$  wide, and  $13.57\lambda$  high, excited by a plane wave incoming from its nose with an upper  $45^\circ$  angle to the center axis of its main body. The CFIE is used, and there are 412,737 unknowns to simulate the exciting surface currents as shown in Figure 7. By solving the linear system by  $\mathcal{H}$ -matrices method, there are 14 levels in the block-cluster tree. To set up the hierarchical system matrix, the memory

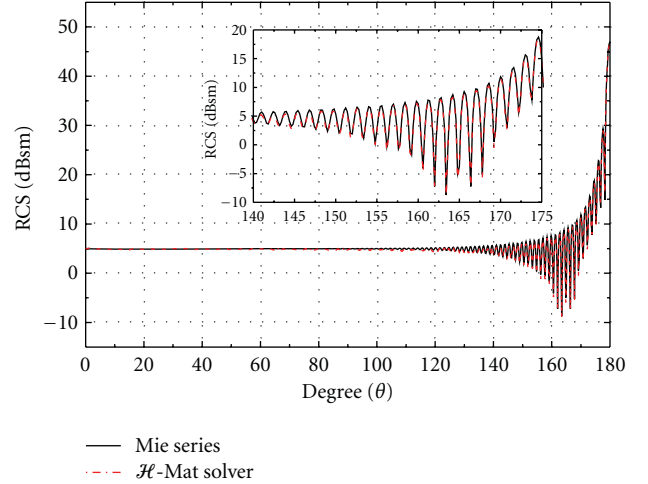
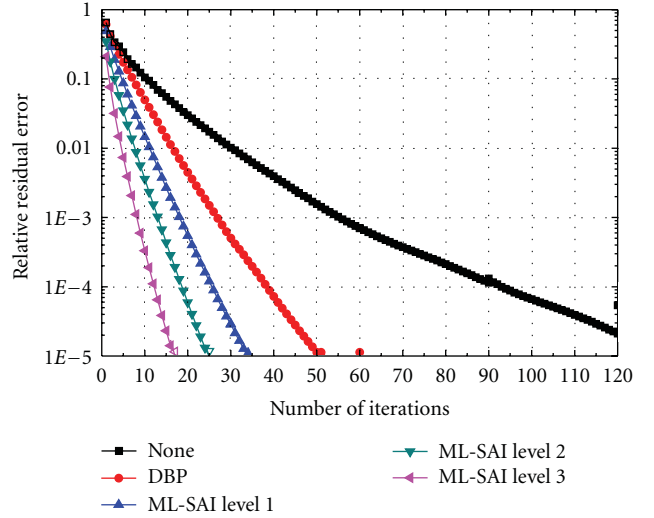
FIGURE 5: The bistatic RCS of a conducting sphere with  $40\lambda$ .

FIGURE 6: The iterative history of solving the PEC sphere cases. GMRES(30) is used and accelerated by different preconditioners.

cost is 38.4 GBytes and 25,634 seconds are used by 8 core parallel computing, on a workstation of Intel Xeon X5460 processor with 64 GBytes RAM. The data of  $\mathbf{A}_{\mathcal{H}\ell}^{(l)}$  in the finest 3 levels are to construct preconditioners  $\mathbf{M}^{(1)}$ ,  $\mathbf{M}^{(2)}$ , and  $\mathbf{M}^{(3)}$ , respectively.

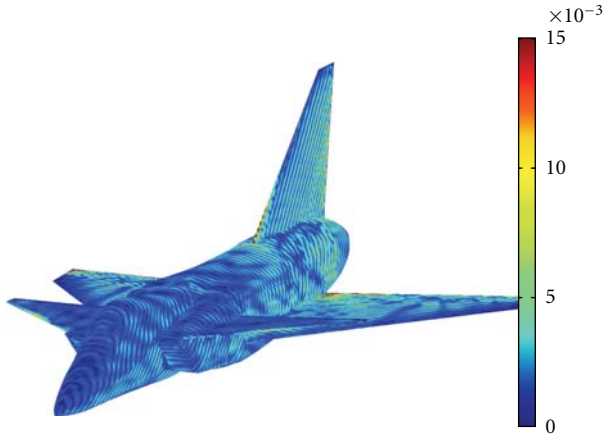


FIGURE 7: The surface current distribution of the aircraft model obtained by solving the ML-SAI preconditioned  $\mathcal{H}$ -matrices method. The unit of surface current is  $A/m^2$ .

GMRES(90) is used to solve the linear system. The convergence histories of iteration with different preconditioners are presented in Figure 8. This is a little tough case because of complicated structure and relatively high frequency. If no preconditioner or just DBP is employed, the convergence is very poor. By employing ML-SAI, the iteration converges quickly under satisfied residual error, and the convergence is much better with the higher level preconditioning processed. The conventional SAI with MLFMA is also able to achieve the request, but its convergence is not as good as higher level ML-SAI. Table 2 shows the solving time and memory cost of ML-SAI, conventional SAI with MLFMA, and diagonal blocks preconditioner. The memory cost is mainly constituted by the storage of preconditioner  $\mathbf{M}$  and Krylov subspace vectors of GMRES. In the fact that the restart number of GMRES, namely, the number of subspace vectors, is chosen the same for all cases, so the memory cost can be regarded as the scale of preconditioner  $\mathbf{M}$ .

**4.3. Hierarchical Fast Direct Solvers.** In this part, we give some numerical examples solved by fast  $\mathcal{H}$ -matrices direct solvers. We use hierarchical LU decomposition to solve CFIE and use hierarchical  $LL^T$  decomposition to solve EFIE, since utilizing its symmetric property. First, a PEC sphere model is used to investigate the accuracy of fast direct solvers. From Figure 9, we can see that the bistatic RCSs obtained by both fast LU and  $LL^T$  decomposition solvers have very high precision regarding to analytic Mie series. The EFIE result has a slight bigger relative error than CFIE because the system matrix of EFIE is not diagonal dominated, consequently, the numerical error accumulated through  $LL^T$  decomposition is more than that in CFIE.

Next, the computational complexity of fast  $LL^T$  decomposition solver is tested via the PEC sphere model. The number of unknowns is varying along with the change of frequency of the incident wave, and the mesh discretization density is fixed at 10.0 points per wavelength. The test results are shown in Figures 10 and 11, respectively, in which we can observe that the complexity of CPU time is close to  $O(N^2)$

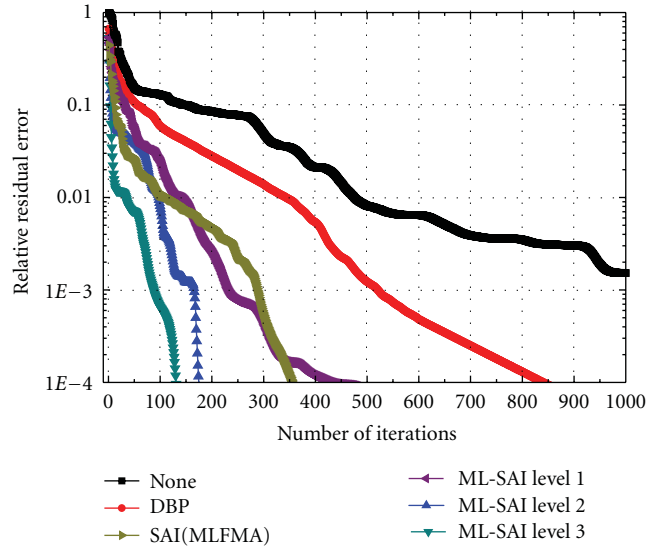


FIGURE 8: The convergence histories of GMRES(90) with no preconditioner, DBP preconditioner, and ML-SAI preconditioners of different levels.

TABLE 2: The time and memory cost of iterative solving aircraft model with different preconditioners.

	Time (seconds)	Memory (MBytes)
ML-SAI level 1	582.8	325.4
ML-SAI level 2	234.5	464.5
ML-SAI level 3	184.3	786.5
SAI with MLFMA	643.7	312.3
DBP	1134.2	213.9

and memory usage is close to  $O(N^{1.5})$ . This is much more efficient than conventional direct solvers.

The aircraft model shown in the previous part is also used here to test fast  $LL^T$  decomposition solver by employing EFIE. The incident wave is 10.0 GHz, and mesh discretization density is 10.0 points per wave number. The number of unknowns is 119,202, and 8 levels are set for  $\mathcal{H}$ -matrices. This example is parallelly solved by a workstation equipped with dual Intel Xeon X5460 processor and 64 GBytes of RAM. 2,256 seconds is used for building up the hierarchical system matrix, and the memory cost is 5,128.4 MBytes.  $LL^T$  decomposition time is 8,415 seconds, and 6,437.2 MBytes are used after decomposition. Figure 12 presents the surface current solved by  $LL^T$  decomposition.

The most notable advantage of fast direct solver is the high efficiency of handling multiple right-hand-side cases. After LU or  $LL^T$  decomposition, solving multiple right-hand vectors is only one-round process of forward/backward substitution, so that it is much faster than iterative solvers, which gives a full-round iteration for each vector step by step. In IE electromagnetic analysis, monostatic RCS is the typical multiple right-hand-side problem. We here use  $LL^T$  decomposition to solve the monostatic RCS problem of the aircraft model incident by 3.0 GHz electromagnetic wave. The range of sweep angles is  $180^\circ$ , and 181 samples are

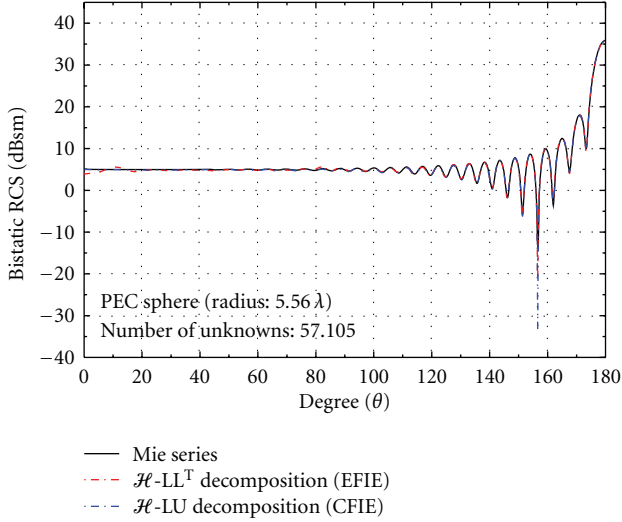


FIGURE 9: The bistatic RCS solved by hierarchical fast direct solvers. CFIE is solved by LU decomposition solver, and EFIE is solved by  $LL^T$  decomposition.

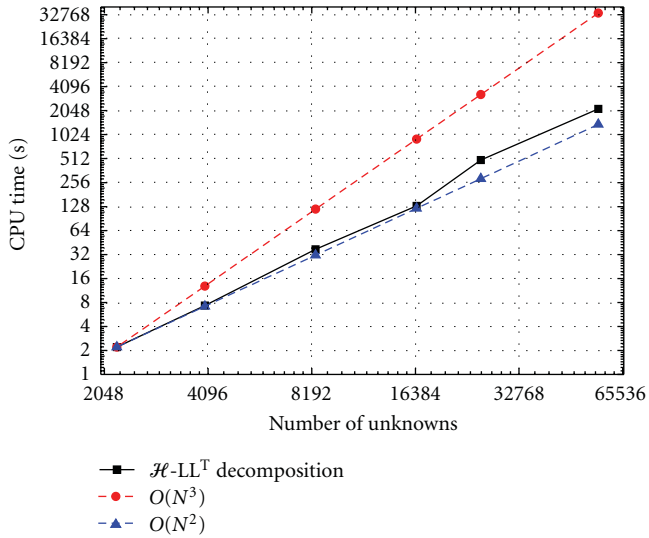


FIGURE 10: CPU time complexity of hierarchical  $LL^T$  decomposition.

calculated. The total solving time is 468.3 seconds, contrast to MLFMA combined with GMRES iterative solver, which costs 4215.7 seconds, almost ten times of the former one. In order to compare to  $LL^T$  decomposition, here, we use EFIE for iterative MLFMA. Figure 13 shows the comparing results between  $LL^T$  decomposition and iteration of MLFMA, we can observe that direct solved curve is smoother than that of iterative solved and there is a big difference between them. We believe that the result of  $LL^T$  decomposition is more accurate and the reason is elaborated as follow. Theoretically, the monostatic RCS curve of this intermediate-frequency example should be smooth, because the sampling is sufficiently continuous comparing to the wavelength. However, for EFIE iteration, the convergence is poor due to

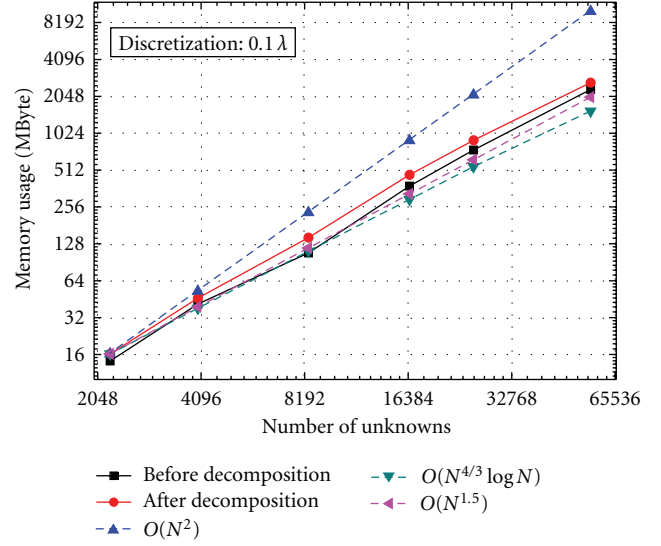


FIGURE 11: Memory usage complexity of hierarchical  $LL^T$  decomposition.

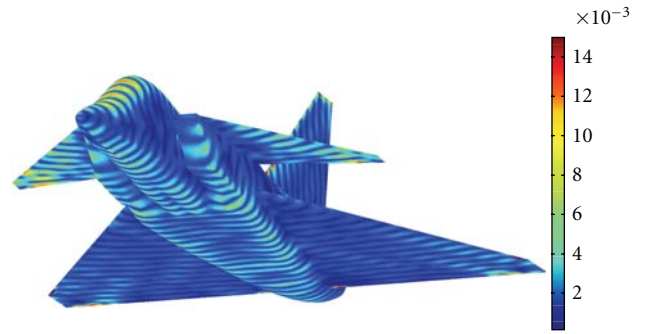


FIGURE 12: The surface current distribution of the aircraft model obtained by solving EFIE with hierarchical  $LL^T$  decomposition. The frequency of incident wave is at 10.0 GHz. The unit of surface current is  $A/m^2$ .

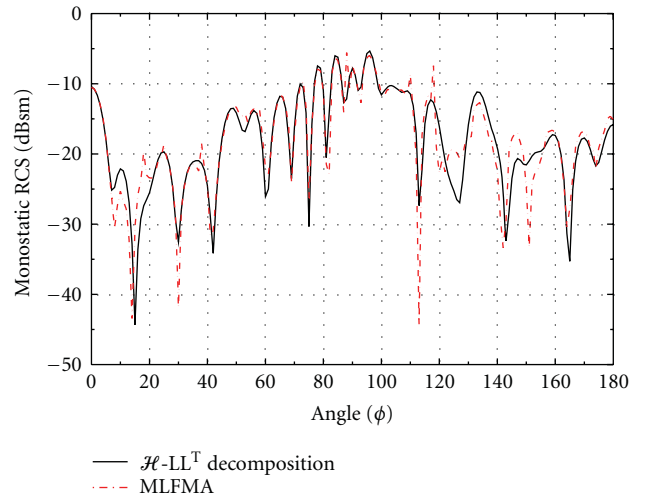


FIGURE 13: The monostatic RCS of the aircraft model. The incident wave is 3.0 GHz, HH-polarization.

the large condition number of its system matrix. Therefore, a loose relative residual error threshold 0.005 is set here, for the purpose of getting iterative result with a reasonable CPU time cost, and this causes the iterative result not very accurate.

## 5. Conclusion

The hierarchical matrix methods presented in this paper is embedded in electromagnetic IE method. Due to its special structure, we can construct a multilevel SAI preconditioner to accelerate the convergence of iterative solving, and even kinds of fast direct solvers can be made, which is not viable for the traditional IE fast algorithm. The multilevel SAI preconditioner proposed here is more efficient than conventional “single level” preconditioners, and hierarchical fast direct solvers are good alternatives to iterative solvers, very suitable for ill-conditioned system and multiple right-hand-side problems. Furthermore, the kernel independence feature of hierarchical matrices method is adapted to varied electromagnetic problems without being limited to integral equation with free-space Green function.

## Acknowledgments

This work is supported by the Fundamental Science Research Foundation of National Central University for Doctoral Program (E022050205) and partly supported by NSFC (no. 60971032), the Programme of Introducing Talents of Discipline to Universities under Grant b07046.

## References

- [1] R. F. Harrington, *Field Computation by Moment Methods*, MacMillan, New York, NY, USA, 1968.
- [2] A. Taflov, *Computational Electrodynamics: The Finite-Difference Time-Domain Method*, Artech House, Norwood, Mass, USA, 1995.
- [3] J.-M. Jin, *The Finite Element Method in Electromagnetics*, Wiley, New York, NY, USA, 2002.
- [4] E. Bleszynski, M. Bleszynski, and T. Jaroszewicz, “AIM: adaptive integral method for solving large-scale electromagnetic scattering and radiation problems,” *Radio Science*, vol. 31, no. 5, pp. 1225–1251, 1996.
- [5] J. Hu, Z. P. Nie, J. Wang, G. X. Zou, and J. Hu, “Multilevel fast multipole algorithm for solving scattering from 3-D electrically large object,” *Chinese Journal of Radio Science*, vol. 19, no. 5, pp. 509–524, 2004.
- [6] S. M. Seo and J. F. Lee, “A fast IE-FFT algorithm for solving PEC scattering problems,” *IEEE Transactions on Magnetics*, vol. 41, no. 5, pp. 1476–1479, 2005.
- [7] K. Zhao, M. N. Vouvakis, and J. F. Lee, “The adaptive cross approximation algorithm for accelerated method of moments computations of EMC problems,” *IEEE Transactions on Electromagnetic Compatibility*, vol. 47, no. 4, pp. 763–773, 2005.
- [8] W. Hackbusch, “Sparse matrix arithmetic based on  $\mathcal{H}$ -matrices. Part I: introduction to  $\mathcal{H}$ -matrices,” *Computing*, vol. 62, no. 2, pp. 89–108, 1999.
- [9] S. Borm, L. Grasedyck, and W. Hackbusch, “Hierarchical matrices,” *Lecture Note 21 of the Max Planck Institute for Mathematics in the Sciences*, 2003.
- [10] H. Guo, J. Hu, H. Shao, and Z. Nie, “Multilevel sparse approximate inverse preconditioning for solving dynamic integral equation by H-matrix method,” in *Proceedings of the IEEE International Workshop on Antenna Technology: Small Antennas, Novel Structures and Innovative Metamaterials*, pp. 124–127, Hong Kong, 2011.
- [11] M. Bebendorf, “Approximation of boundary element matrices,” *Numerische Mathematik*, vol. 86, no. 4, pp. 565–589, 2000.
- [12] J. Lee, J. Zhang, and C. C. Lu, “Sparse inverse preconditioning of multilevel fast multipole algorithm for hybrid integral equations in electromagnetics,” *IEEE Transactions on Antennas and Propagation*, vol. 52, no. 9, pp. 2277–2287, 2004.
- [13] M. Bebendorf, *Hierarchical Matrices: A Means to Efficiently Solve Elliptic Boundary Value Problems*, Springer, Berlin, Germany, 2008.
- [14] L. Y. Saad and M. H. Schultz, “GMRES: a generalized minimal residual algorithm for solving nonsymmetric linear systems,” *SIAM Journal on Scientific and Statistical Computing*, vol. 7, no. 3, pp. 856–869, 1986.

## Research Article

# Study on High Performance of MPI-Based Parallel FDTD from WorkStation to Super Computer Platform

**Z. L. He, K. Huang, Y. Zhang, Y. Yan, and C. H. Liang**

*Science and Technology on Antenna and Microwave Laboratory, XiDian University, Xi'an 710071, China*

Correspondence should be addressed to Z. L. He, 305111889@qq.com

Received 15 June 2011; Revised 12 September 2011; Accepted 25 October 2011

Academic Editor: Jun Hu

Copyright © 2012 Z. L. He et al. This is an open access article distributed under the Creative Commons Attribution License, which permits unrestricted use, distribution, and reproduction in any medium, provided the original work is properly cited.

Parallel FDTD method is applied to analyze the electromagnetic problems of the electrically large targets on super computer. It is well known that the more the number of processors the less computing time consumed. Nevertheless, with the same number of processors, computing efficiency is affected by the scheme of the MPI virtual topology. Then, the influence of different virtual topology schemes on parallel performance of parallel FDTD is studied in detail. The general rules are presented on how to obtain the highest efficiency of parallel FDTD algorithm by optimizing MPI virtual topology. To show the validity of the presented method, several numerical results are given in the later part. Various comparisons are made and some useful conclusions are summarized.

## 1. Introduction

The Finite Difference Time Domain (FDTD) method, introduced by Yee, in 1966 [1], is one of the most popular three-dimensional methods in computational electromagnetics. The FDTD method has been applied to many radar cross section (RCS) calculations with accurate results. However, as a powerful numerical technique, the FDTD method is restrained to computation resource when analyzing the scattering of electrically large targets. To overcome the problem, a Parallel FDTD algorithm using the Message Passing Interface (MPI) library was developed by Volakis et al. in 2001 [2]. It is easy to implement because the Yee scheme is explicit. The FDTD in Cartesian coordinates can be easily divided into many subspaces, and each computer in a parallel system deals with one or several subdomains. The FDTD algorithm is combined with the MPI to run on parallel system. The MPI functions are employed to exchange the tangential electric (magnetic) fields on the boundary of the subdomain among the adjacent neighbors [3–5]. Parallel computation of the E-H components with an MPI Cartesian 2D topology is adopted and has been explained step by step in [6]; as the authors of it addressed, it is the first paper on Parallel FDTD using MPI protocol. Zhang et al. used an MPI Cartesian 3D topology in his research [7]. As an

extension of these researches, we have developed a parallel FDTD code using an MPI Cartesian 3D topology. It has been successfully run on PC cluster [5, 6] and blade server [8], both of which belong to Science and Technology on Antenna and Microwave Laboratory in China.

Now, the code is developed to solve larger-scale electromagnetic problems. It is applied on super computer based on Linux system, which belongs to Shanghai Supercomputer Center of China (SSC). Numerical examples prove that the virtual topology will affect the computational efficiency of Parallel FDTD severely. In this paper, the influence of different virtual topology schemes on parallel performance of Parallel FDTD will be studied in detail. The general rules are presented on how to obtain the highest efficiency of Parallel FDTD algorithm by optimizing MPI virtual topology.

In Section 2, parallel FDTD algorithm is presented briefly. In Section 3, some numerical results are given, which show that this method is efficient and accurate. Current distribution over the surface of scatter and the near field distribution are plotted. Discussions about the influence of different virtual topology schemes and different number of processors on parallel performance of Parallel FDTD are presented in Section 4. Finally, some useful conclusions are summarized.

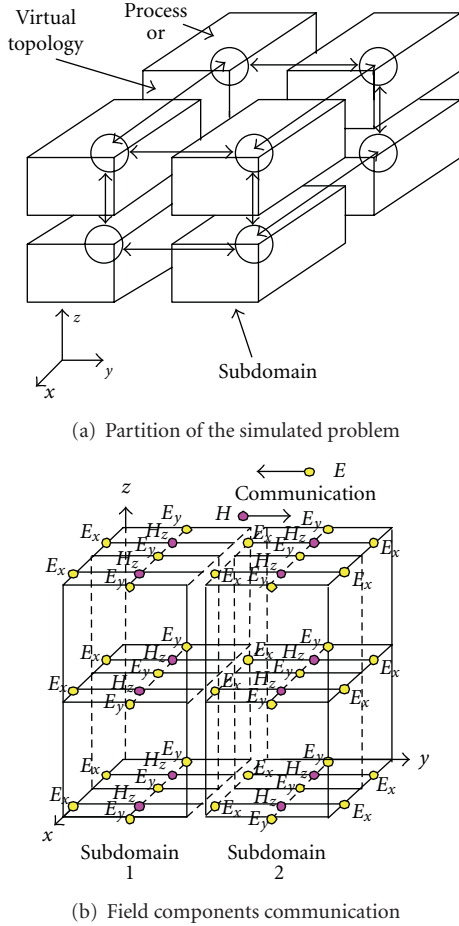
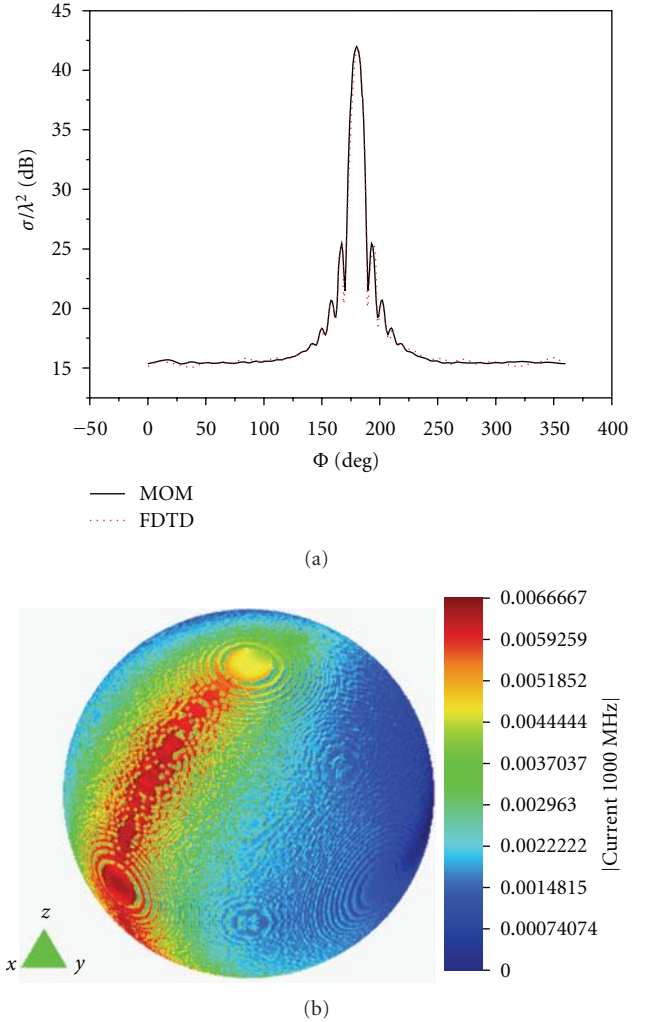


FIGURE 1: Division and communication of Parallel FDTD in 3D.

## 2. Parallel Algorithm

MPI was proposed as a standard by a broadly based committee of vendors, implementers, and users. Now, it becomes a definition for interfaces among a cluster of computers or the processors of a multiprocessor parallel computer. The key problem that MPI-based programming relates to is how to distribute the tasks of users to processors according to the capability of each processor and reduce the communications among processors to as little as possible. Reducing the communications is especially crucial as the speed of communication is far slower than that of computation.

FDTD is easy to implement because the Yee scheme is explicit. Besides, it has the principle advantage that since the grid is regular and orthogonal, electromagnetic field components are easily indexed by  $(i, j, k)$  in Cartesian coordinates. The parallelism of the FDTD algorithm is based on a spatial decomposition of the simulation problem geometry into contiguous nonoverlapping rectangular subdomains. The computational space can be easily divided into nearly equal parts along the three directions, and each processor in a parallel system deals with one or several subdomains, as shown in Figure 1(a). The virtual topology of the processors' distribution is chosen in a similar shape as

FIGURE 2: (a) Comparison of the RCS results in  $xoy$  plane obtained by FDTD and MOM; (b) current distribution over the surface of the sphere.

the problem partition. Each subdomain is mapped to its associated node where all the field components belonging to this subdomain are computed. To update field values lying on interfaces between sub-domains, it is necessary to exchange data between neighboring processors. An  $x$ - $z$  slice of the computational volume at one of the interfaces between nodes in the  $y$ -direction is shown in Figure 1(b). In this paper, we adopt 3D communication pattern, which is introduced as follows.

The FDTD algorithm is combined with MPI to run on parallel system. The MPI functions are employed to exchange the tangential electric (magnetic) fields on the boundary of the subdomain among the adjacent neighbors.

The parallel algorithm can be described as follows.

(1) Initialization.

(a) MPI Initialization.

(b) Reading the modeling parameters from the input files.

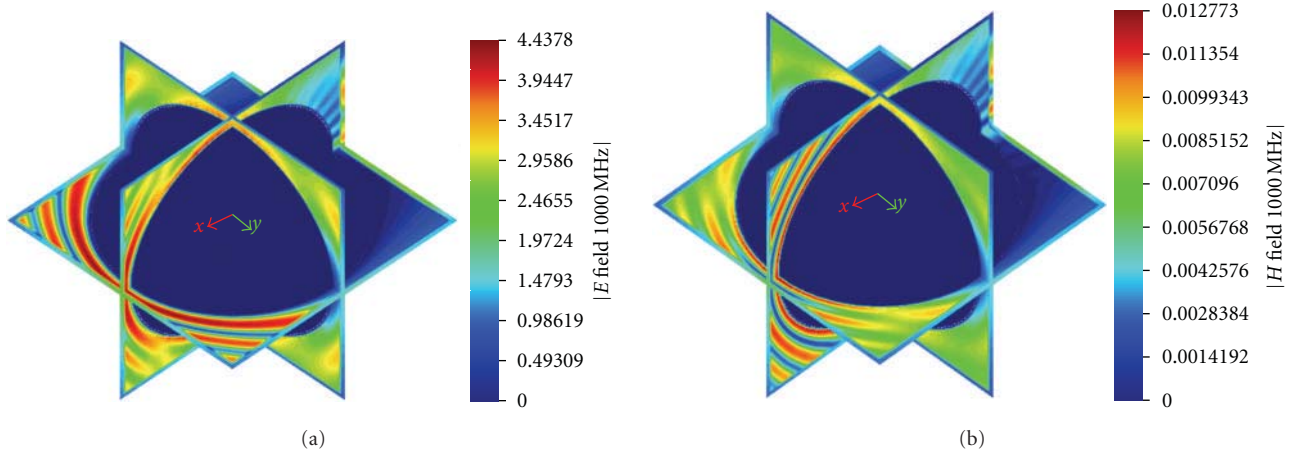


FIGURE 3: Smooth contour fill of near field distribution in frequency domain on three planes:  $x = 0.0$ ,  $y = 0.0$ , and  $z = 0.0$ : (a) E field distribution and (b) H field distribution.

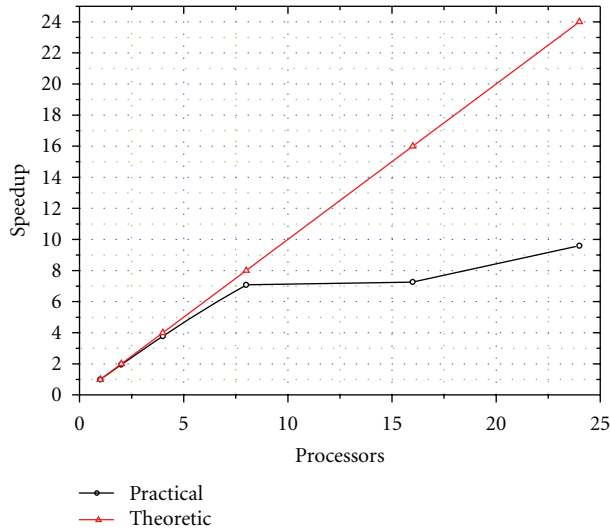


FIGURE 4: Parallel efficiency.

- (c) Creation of the three-dimensional Cartesian topology.
  - (d) Creation of the derived data types for communication.
  - (e) Start time measurements.
  - (f) Allocation of memory.
  - (g) Setting all field components to zero.
- (2) At each time step.
- (a) Exciting source only on processors that include the source plane.
  - (b) Calculation of new magnetic field components on each processor.
  - (c) Communication of the magnetic field components between processors.

- (d) Calculation of new electric field components on each processor.
  - (e) Communication of the electric field components between processors.
  - (f) Calculation of transmission only on processors that include the transmission plane.
  - (g) Collection of field variables only on processors that include detection points.
- (3) Reducing the transmission to a fixed processor and writing it on file.
  - (4) Saving results in files.
  - (5) Deallocation of memory.
  - (6) Stop time measurement.
  - (7) MPI Finalization.
  - (8) End.

### 3. Hardware Platform

- (i) *Think Station*. Its machine-type model is 4155-D43 with a total of 24 Intel(R) Xeon(R) X5650 CPU cores (2.67 GHz per CPU) and a total of RAM approximately equal to 64 GB.
- (ii) *Shanghai Supercomputer Center (SSC)*. The 37 nodes from Magic-cube Machine with a total of 512 AMD CPU cores (1.9 GHz per CPU and 4 cores on each CPU) 16 CPU cores on each node and 4 GB RAM per core, and a total of RAM approximately equal to 2.3TB. Infiniband is used for the network interconnection.

### 4. Numerical Results

For the absorbing UPML medium, we use a thickness of 5 cells in the following examples.

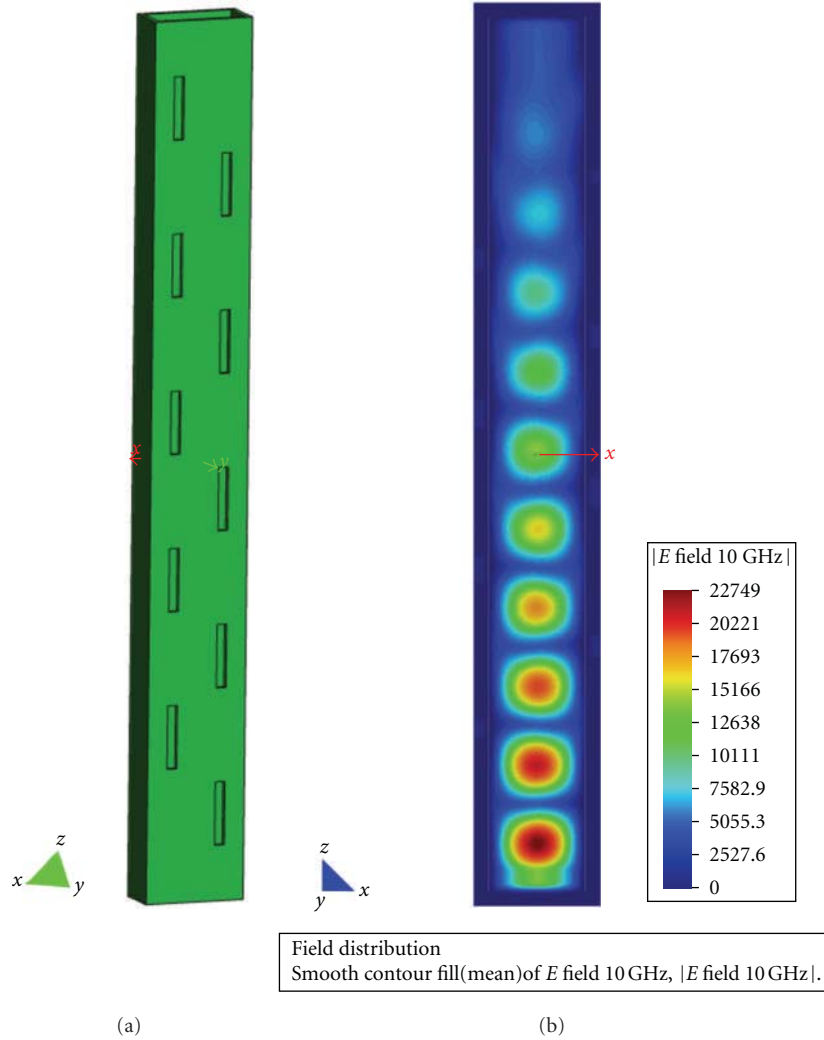


FIGURE 5: (a) Model of the waveguide with ten slots; (b) smooth contour fill of E field distribution of the  $xoz$  plane.

**4.1. An Example for Validation.** For validation, the bistatic RCS is calculated for a PEC sphere with a 1 m ( $10\lambda/3$ ) radius, and the incident plane wave is arriving from the  $\geq x$  axis and the polarization is along  $-z$  axis. Working frequency is 1.0 GHz. The increment  $dx = dy = dz = 0.02$  m ( $\lambda/15$ ) is used here, and the amount of FDTD grids is  $144 \times 144 \times 144$ . The bistatic RCS of the sphere is shown in Figure 2(a). The result is compared with the one obtained by the Moment of Method (MOM), which shows a good agreement between them. Current distribution over the surface of the sphere is given in Figure 2(b). In Figures 3(a) and 3(b), smooth contour fills of the amplitude of E field and H field distributions in frequency domain are plotted, respectively. This problem is calculated on *Think Station*. Total computation time (in seconds) with different number of processors and different virtual topology schemes in *1000 time-steps* are compared in Table 1.

In Table 1, virtual topology schemes are described as  $(x \times y \times z)$  for all three communication patterns. If the value is 1 in some direction, it implies that there is no topology in this direction. For example,  $1 \times 4 \times 1$  means there is no

TABLE 1: Comparisons of computation time.

Cores	Virtual topology ( $x \times y \times z$ )	Computation time (in seconds)
1	$1 \times 1 \times 1$	646.25
2	$2 \times 1 \times 1$	330.75
4	$4 \times 1 \times 1$	172.25
4	$2 \times 2 \times 1$	170.88
8	$8 \times 1 \times 1$	98.38
8	$4 \times 2 \times 1$	92.75
8	$2 \times 2 \times 2$	91.25
16	$8 \times 2 \times 1$	95.12
16	$4 \times 4 \times 1$	91.38
16	$4 \times 2 \times 2$	89.00
24	$8 \times 3 \times 1$	69.38
24	$4 \times 3 \times 2$	67.38

topology in  $x$  and  $z$  directions, respectively, thus the virtual topology is actually in one dimension. Similarly,  $1 \times 2 \times 2$  means there is no topology in  $x$  direction, thus the virtual topology is actually in two dimensions.

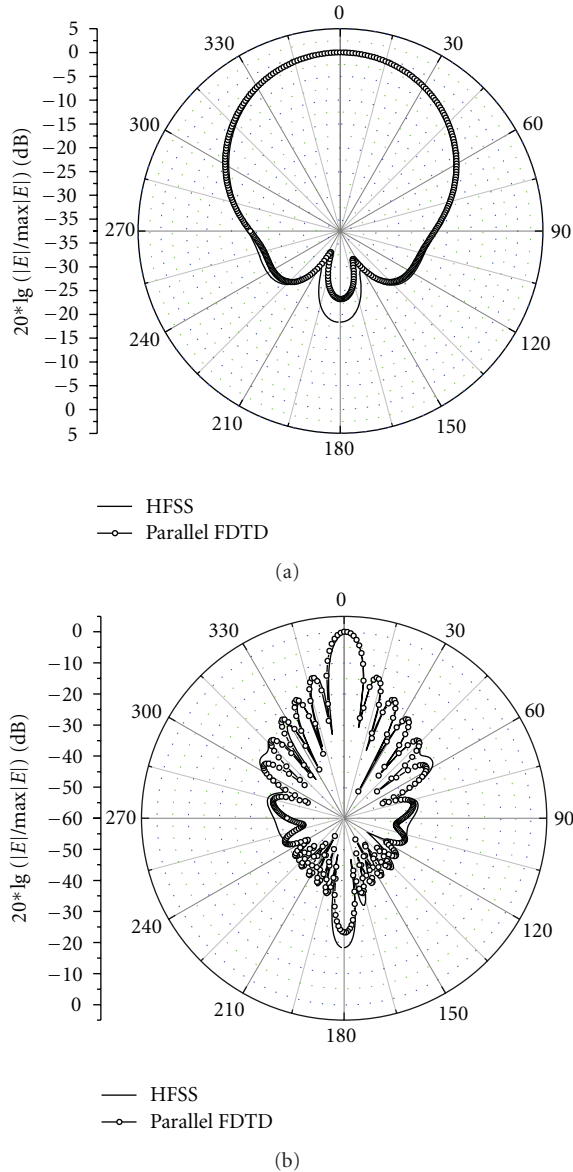


FIGURE 6: Results of radiation: (a) radiation pattern of the  $xoy$  plane and (b) radiation pattern of the  $yoz$  plane.

From Table 1, it is obvious that increasing the number of processors can bring us the reduction of the computation time rapidly. But different virtual topology schemes will cost different computation time even if the code is run with the same number of processors.

We discuss the parallel performance of the Parallel FDTD using the different dimensional virtual topology with the same number of processors. In this case, the computing time is calculated with the shortest time as the reference. Take the case of eight processors as the example. The reference calculating time is 91.25 seconds using the  $2 \times 2 \times 2$  virtual topology scheme:

$$\begin{aligned} \text{Comparison: } & 8 \times 1 \times 1(98.38 - 91.25) = 6.13 \text{ (sec)}, \\ & 4 \times 2 \times 1(92.75 - 91.25) = 1.50 \text{ (sec)}. \end{aligned} \quad (1)$$

From above, it is obvious that for the same number of processors, the more the dimension of the virtual topology, the less the computation time required.

Parallel efficiency is shown in Figure 4, in which the computing time consumed by different number of processors is referred as the shortest time for each case. Parallel efficiency is decreased with the increasing of processors. That is because the amounts of the transferred data are increased with processors, and then the time consumed on communication is increased.

In addition, the topology along the direction where the amount of the FDTD grids is larger can save the computation time for the same dimensional virtual topology. Different division subdomains with the same dimensional virtual topology lead to different amounts of the transferred data. Expression for the total number of the grids lay on interface between processors is

$$(nx - 1) \times b \times c + (ny - 1) \times a \times c + (nz - 1) \times a \times b, \quad (2)$$

where  $a, b, c$  represent the total number of grids in  $x, y, z$  direction, respectively, and  $nx, ny, nz$  are the values of virtual topology in three directions.  $nx, ny,$  and  $nz$  are integers and should satisfy the condition:

$$nx \times ny \times nz = \text{Processors}, \quad nx \geq 1, ny \geq 1, nz \geq 1. \quad (3)$$

So, the topology scheme should be created along the directions where the amount of the FDTD grids is larger to decrease the amounts of the transferred data, then to save the communication time.

Till now, the general rules on how to obtain the highest efficiency of Parallel FDTD algorithm by optimizing MPI virtual topology can be drawn as follows.

- (1) If possible, the optimum virtual topology scheme should be created in three dimensions, and then the better is in two dimensions, which can bring us higher efficiency than in one dimension.
- (2) As to the same dimensional virtual topology, the topology scheme should be created along the directions where the amount of the FDTD grids is larger.

**4.2. Radiation of the Waveguide with Ten Slots.** A waveguide with ten slots is analyzed by parallel FDTD. The dimension of the waveguide and the slot structure in this example are chosen as follows: the thickness of the waveguide wall is 1.27 mm, the length of the slot is 15.785 mm, the width of the slot is 2.54 mm, and all of the offsets of the slots are 6.35 mm. Its FDTD model is shown in Figure 5(a). Its working frequency is 10 GHz. The increment  $dx = dy = dz = 0.635$  mm is used here, and the total amount of FDTD grids is  $70 \times 50 \times 384$ . We introduce a sinusoid ally modulated Gaussian pulse excitation by modifying the

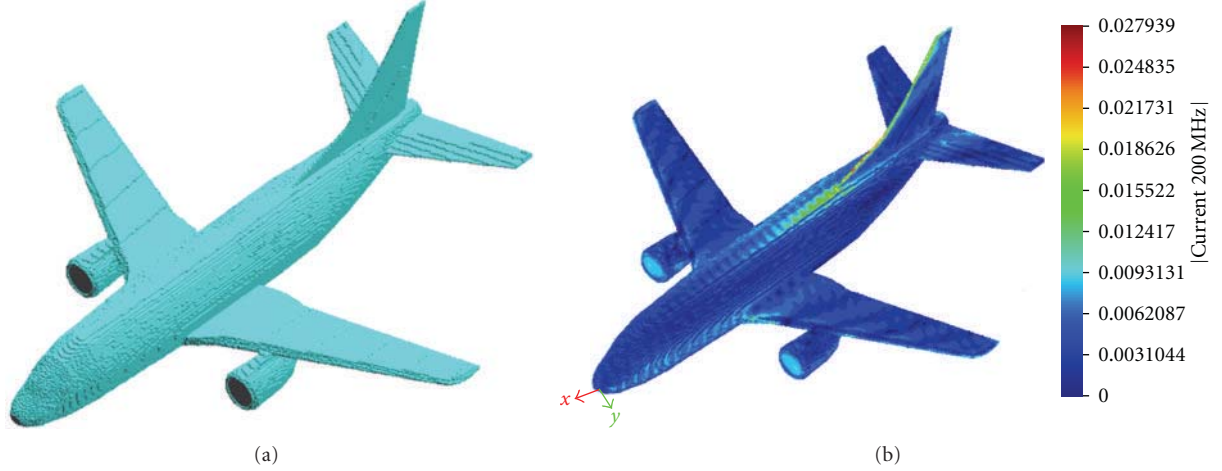


FIGURE 7: (a) Cartesian Mesh of the airplane and (b) smooth contour fill of the amplitude of surface inductive current on the airplane surface.

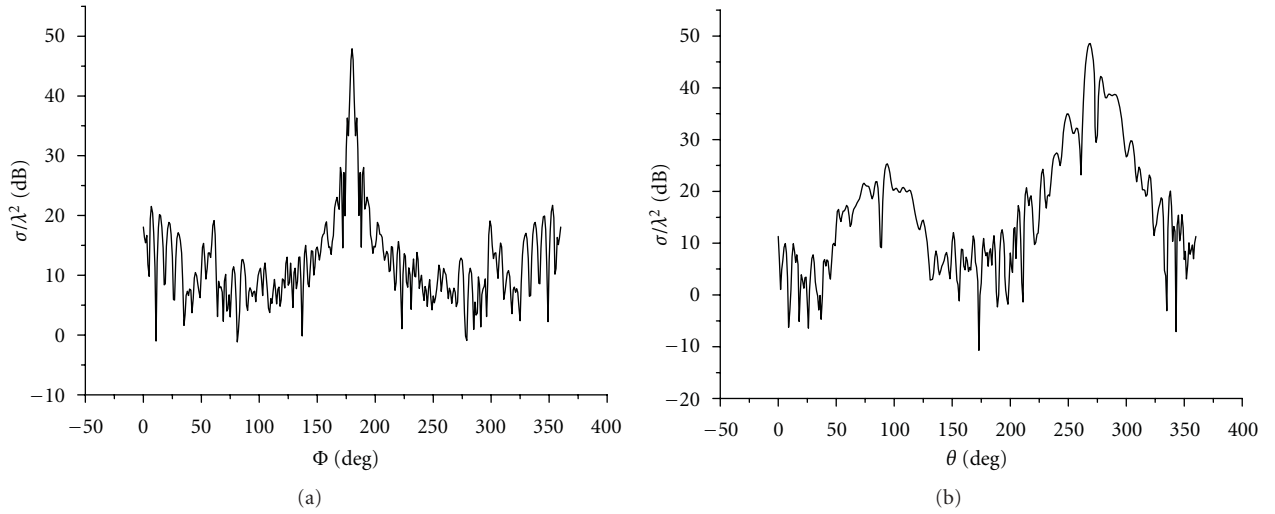


FIGURE 8: RCS of the airplane. (a) E-plane ( $xoy$ ). (b) H-plane ( $xoz$ ).

updating equation for the component in the excitation plane as follows:

$$E_y^{n+1}(i, j, k) = g(n\Delta t) + E_y^n(i, j, k) + \frac{\Delta t}{\epsilon_y(i, j, k)} \cdot \left[ \frac{H_x^{n+1/2}(i, j, k+1) - H_x^{n+1/2}(i, j, k)}{\Delta z} - \frac{H_z^{n+1/2}(i+1, j, k) - H_z^{n+1/2}(i, j, k)}{\Delta x} \right], \quad (4)$$

where  $g(n\Delta t) = \sin(\pi x/a) \sin(2\pi f_0 t) e^{-((t-t_0)/\sigma)^2}$ . By properly setting  $f_0$ ,  $t_0$ , and  $\sigma$ , we can get a useful frequency bandwidth. Finally, smooth contour fill of electric field distribution in frequency domain on plane  $y = 0.0$  is shown in Figure 5(b). Results of the radiation patterns obtained by parallel FDTD agree excellent with the ones obtained by HFSS shown in Figures 6(a) and 6(b). Total computation time (in seconds)

TABLE 2: Comparisons of computation time.

Cores	Virtual topology ( $x \times y \times z$ )	Total grids lay on interface between processors	Computation time (in seconds)
8	$1 \times 1 \times 8$	24500	121.09
8	$1 \times 2 \times 4$	37380	124.56
8	$2 \times 1 \times 4$	29700	116.09
8	$2 \times 2 \times 2$	49580	118.00

with eight processors and different virtual topology schemes in 1000 time-steps is compared in Table 2.

From Table 2, the shortest computing time consumed by virtual topology in two dimensions is shorter than in one dimension. However, three-dimensional virtual topology is not better than two-dimensional virtual topology. As shown

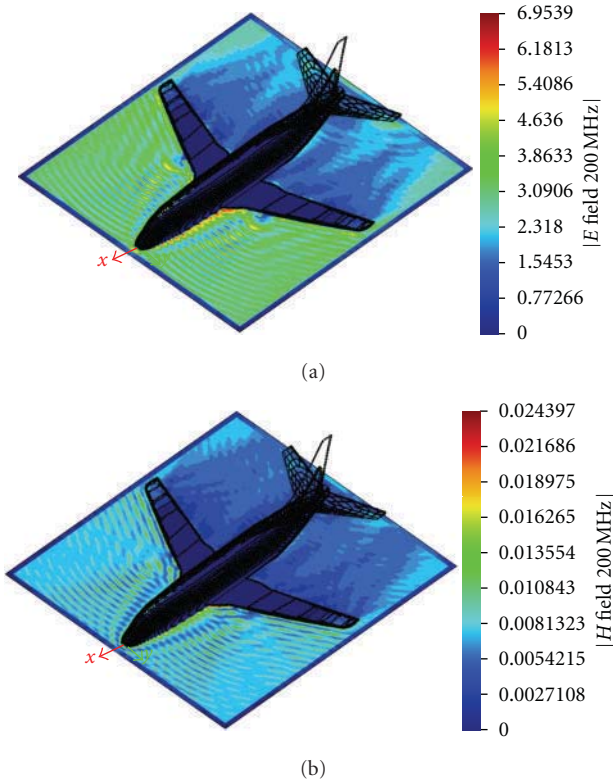


FIGURE 9: Smooth contour fill of near-field distribution in frequency domain on  $z = 0.05$  plane, (a) E field distribution, and (b) H field distribution.

TABLE 3: Comparisons of computation time.

Cores	Virtual topology ( $x \times y \times z$ )	Computation time (in seconds)	Total grids lay on interface between processors
512	$8 \times 8 \times 8$	896.00	2479680
512	$8 \times 16 \times 4$	3968.00	3000640

in Table 2, the transferred data for the  $2 \times 2 \times 2$  virtual topology scheme is much more than the one for the  $2 \times 1 \times 4$  case. Thus, as to the same dimensional virtual topology, the topology scheme should be created along the directions where the amount of the FDTD grids is larger.

**4.3. Analysis of the Scattering of an Airplane.** Then we analyze the scattering of a perfectly conducting airplane whose FDTD model is shown in Figure 7(a). Its working frequency is 200 MHz. The increment  $dx = dy = dz = 0.08$  m is used here. The direction of the incident wave is  $-x$  and the polarization is along  $+y$ . Inductive current distribution over the airplane surface is given in Figure 7(b). Figure 8 presents the bistatic RCS of the conducting airplane obtained by using Parallel FDTD. The frequency domain near-field distribution on the plane  $z = 0.05$  is given in Figure 9.

This example is calculated on super computer with 512 cores, which belong to the SSC. Time consumed by two virtual topology schemes with the same number of cores

are listed in Table 3. Total amount of the FDTD grids is  $440 \times 416 \times 200$ . It is obvious that the results accord with the rules presented before. With the same dimensional virtual topology, the parallel performance is mainly affected by the amounts of the transferred data especially in large-scale problems.

## 5. Conclusions

In this paper, parallel FDTD method is applied to analyze the scattering of the electrically large targets. The code we developed is successfully run on super computer in Shanghai Supercomputer Center of China (SSC). The influence of different virtual topology schemes on the parallel performance of Parallel FDTD is studied in depth and in detail. The results show that the computation time efficiency can be improved by properly choosing MPI virtual topology schemes. Following the two conclusions above, we can obtain the highest computational efficiency.

## Acknowledgments

This work is partly supported by the Fundamental Research Funds for the Central Universities of China (JY10000902002 and K50510020017) and the National Science Foundation of China (61072019). This work is also supported by Shanghai Supercomputer Center of China (SSC).

## References

- [1] K. S. Yee, "Numerical solution of initial boundary value problems involving Maxwell's equations in isotropic media," *IEEE Transactions on Antennas and Propagation*, vol. AP-14, pp. 302–307, 1966.
- [2] J. L. Volakis, D. B. Davidson, C. Guiffaut, and K. Mahdjoubi, "A parallel FDTD algorithm using the MPI library," *IEEE Antennas and Propagation Magazine*, vol. 43, no. 2, pp. 94–103, 2001.
- [3] V. Varadarajan and R. Mittra, "Finite-difference time-domain (FDTD) analysis using distributed computing," *IEEE Microwave and Guided Wave Letters*, vol. 4, no. 5, pp. 144–145, 1994.
- [4] A. Alighanbari and C. D. Sarris, "Parallel time-domain full-wave analysis and system-level modeling of ultrawideband indoor communication systems," *IEEE Transactions on Antennas and Propagation*, vol. 57, no. 1, pp. 231–240, 2009.
- [5] S. Prakash, E. Deelman, and R. Bagrodia, "Asynchronous parallel simulation of parallel programs," *IEEE Transactions on Software Engineering*, vol. 26, no. 5, pp. 385–400, 2000.
- [6] A. Taflove, *Computational Electrodynamics: The Finite-Difference Time-Domain Method*, 2nd edition, 2000.
- [7] Y. Zhang, J. Song, and C. H. Liang, "MPI-based parallelized locally conformal FDTD for modeling slot antennas and new periodic structures in microstrip," *Journal of Electromagnetic Waves and Applications*, vol. 18, no. 10, pp. 1321–1335, 2004.
- [8] U. Andersson, *Time-domain methods for the Maxwell equations*, Doctoral Dissertation, Royal Institute of Technology, Sweden, 2001.

## Research Article

# Application of OpenMP to Wireline Triaxial Induction Logging in 1D Layered Anisotropic Medium

Zhijuan Zhang, Ning Yuan, and Richard Liu

Department of Electrical and Computer Engineering, University of Houston, 4800 Calhoun Road, Houston, TX 77204, USA

Correspondence should be addressed to Zhijuan Zhang, zzhijuan@yahoo.com

Received 12 July 2011; Accepted 26 September 2011

Academic Editor: Ashutosh Bhardwaj

Copyright © 2012 Zhijuan Zhang et al. This is an open access article distributed under the Creative Commons Attribution License, which permits unrestricted use, distribution, and reproduction in any medium, provided the original work is properly cited.

Efficient and accurate forward modeling of logging tool responses is essential for data inversion in the log data interpretation in both real time and postprocessing. With the aggressive advancement of various high-performance computing techniques and computer hardware technology, it is possible to significantly improve the efficiency of the forward modeling. In this paper, we apply OpenMP to parallelize the simulation of triaxial induction logging tools in 1D multilayered anisotropic formation. The parallel process is explained in detail and numerical examples are presented to demonstrate the effect of the parallel programming. Comparison of the original code and the parallel code shows that the latter is much faster without loss of accuracy, which is very promising for future real-time inversion.

## 1. Introduction

Resistivity logging is an important measurement method for characterizing formations in geophysical exploration. The measured resistivity profile of the formation can provide various formation information such as type of rocks, layer boundaries, and even formation anisotropy. Triaxial induction tool is an emerging tool which has both traditional  $z$  antennas and  $x$ - $y$  antennas as transmitters and receivers. By measuring all components of the electromagnetic field, the triaxial tool is capable of detecting the anisotropic property of the medium [1–4]. To obtain the true formation information from the log data, data inversion is an effective way to help log analysts in the process. Due to the complexity and nonuniqueness nature of the inversion, about 90% of inversion time is consumed by the repeated use of forward modeling, which implies that decreasing the time of the forward modeling will significantly improve the inversion efficiency. Traditional way to improve the efficiency of the forward modeling includes introducing specific mathematical algorithm to speed up the forward modeling, such as Broyden's method [5] and Newmark's direct integration method [6]. However, many of these methods degrade the precision of the forward modeling inevitably due to either simplification of the modeling or approximations in

algorithms. As a result, the accuracy of inversion results cannot be guaranteed.

Nowadays, the development of high-performance computing techniques provides us various choices to improve the speed of the forward modeling without loss of accuracy. The most popular CPU-based parallel techniques are message passing interface (MPI) and open multiprocessing (OpenMP). MPI was first implemented in 1992 [7] and remains the dominant method used in high-performance computing today [8–10]. MPI is language-independent and can be run on either symmetric multiprocessor (SMP), distributed shared memory (DSM) processor or clusters, and supercomputers. However, MPI is relatively difficult to implement in programming. On the contrary, the latest developed OpenMP is easy to implement and therefore becomes an appropriate choice for quick concept validation within time constraints.

OpenMP is an application programming interface that supports multiplatform-shared memory multiprocessing programming in FORTRAN, C, and C++ [11–14]. Comparing with the traditional application programming interface (API), OpenMP has the following advantages.

(1) *Easy Expansion on Multiple Cores.* In order to fully using multiple cores, the total number of threads should be

dynamic according to the available cores. Although we can assign threads flexibly in API, it is well known that API is very complicated to program. In comparison, it is much easier to assign threads to multiple cores in OpenMP.

(2) *Good Flexibility of Parallelization.* In API, we need entry point functions to create multiple threads. Computer programmers have to cope with every expanding workload. However, OpenMP does not require entry point functions. It is convenient to parallelize some functions or iteration statements in OpenMP.

(3) *Excellent Portability of Software.* Currently, API of each mainstream system is not compatible due to lacking in uniform standard; but OpenMP is normative on any supporting compiler. This is a remarkable advantage.

In this paper, we have adopted OpenMP to parallelize the forward modeling algorithm of wireline triaxial induction logging tools in 1D layered anisotropic formation. The principal of the forward modeling is briefly explained and the parallel implementation of the code is described in details. In the numerical result section, we compare the total running time as well as the simulation results of several examples between the original code and the parallelized code. After parallelization, the computation speed is improved by about 2.5 times on a 4-core computer (2.33 GHz, 4 GB) and the speed can be further improved as the number of the processor cores increased. The comparison proves that OpenMP makes a good compromise between the reliability and the running speed, which is very promising for real-time inversion.

## 2. Theory

*2.1. Parallel Implementation.* Figure 1 compares serial and parallel tasks. The master thread is a series of instructions which is executed consecutively. In Figure 1, the master thread includes three serial tasks (Task I, Task II, and Task III). Let us assume the operation time of the three tasks is  $a_1$ ,  $a_2$ ,  $a_3$ , respectively. Then, CPU would cost time of  $(a_1 + a_2 + a_3)$  to complete the serial assignment. Note that the three tasks have one common character: each task can be divided into several independent parts. For instance, task I is comprised by A, B, and C. Thus, the master thread can be divided among specified number of slave “thread” (one core of multicore computer) and these slave threads are capable to run concurrently on multicore computer. Therefore, we can easily get to know that the total running time of the three tasks would be  $(a_1/2 + a_2/2 + a_3/4)$  from Figure 1. The operation speed after parallelization is then significantly improved.

*2.2. Forward Modeling of Wireline Triaxial Induction Logging.* In the oil exploration, logging tools are used to obtain tool response from the formation, and then by applying the inversion algorithm, it is possible to retrieve useful geophysical information (such as dipping angle, boundary, and anisotropy, and resistivity) from the measured data. During the inversion process, the forward modeling is

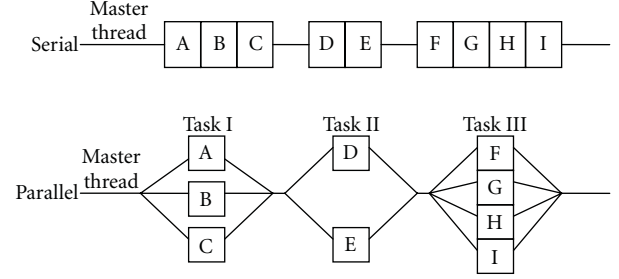


FIGURE 1: Comparison of entire progress between serial and parallel assignments.

usually called repeatedly to simulate tool responses with each update of the formation parameters. The simulated responses are compared with the measured field data. The inverted parameters are modified at each iteration until the simulated responses are close enough to the real data (e.g., error  $< 10^{-9}$ ). The inverted formation parameters are useful to log analysts in determining the petrophysical features of the formation. Thus, we can see that the forward model has important application to the oil industry. In this section, we briefly present the theory of forward model of wireline triaxial induction logging.

Triaxial induction tool is a new tool for measuring the  $3 \times 3$  tensor magnetic field responses in a borehole environment. The tool usually comprises three orthogonal transmitters and three orthogonal receivers oriented at  $x$ ,  $y$ , and  $z$  direction, as shown in Figure 2(a). If we neglect the size of the coils, the coils are usually treated as magnetic dipoles. The equivalent dipole model is shown in Figure 2(b). Thus, the magnetic source excitation of the triaxial tool can be expressed as  $\mathbf{M} = (M_x, M_y, M_z)\delta(\mathbf{r})$ .

The tool is moving along the axis in the borehole and for every logging point; a  $3 \times 3$  magnetic field tensor  $\hat{H}$  is measured at the receiver:

$$\hat{H} = \begin{bmatrix} H_x^x & H_x^y & H_x^z \\ H_y^x & H_y^y & H_y^z \\ H_z^x & H_z^y & H_z^z \end{bmatrix}, \quad (1)$$

where  $H_i^j$  is the magnetic field at the  $j$ -directed receiver from the  $i$ -directed transmitter.

The electromagnetic fields in a homogeneous transversely isotropic (TI) formation satisfy the following Maxwell's equations [15]:

$$\nabla \times \hat{E} = i\omega\mu_0\hat{H} + i\omega\mu_0\hat{M}_o, \quad (2)$$

$$\nabla \times \hat{H} = \hat{\sigma}\hat{E} + j\omega\hat{\epsilon}\hat{E}, \quad (3)$$

where  $\hat{\sigma}$  is the complex conductivity tensor of TI formation:

$$\hat{\sigma} = \begin{bmatrix} \sigma_h & 0 & 0 \\ 0 & \sigma_h & 0 \\ 0 & 0 & \sigma_v \end{bmatrix}, \quad (4)$$

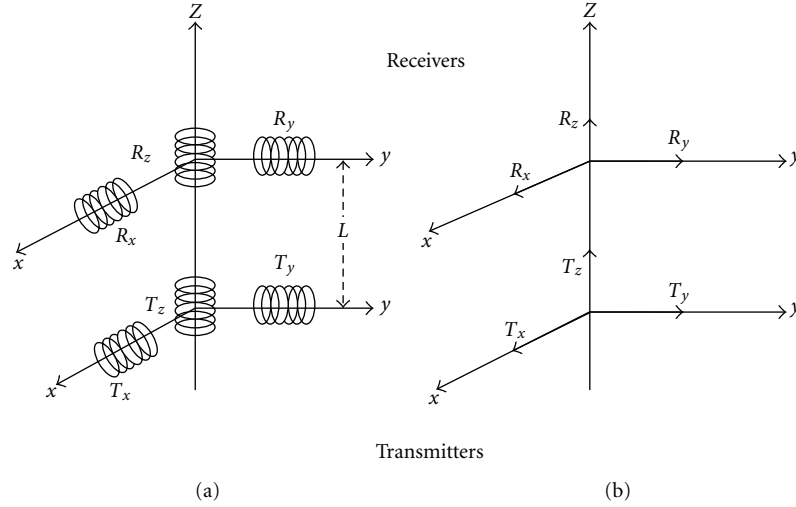


FIGURE 2: Basic structure of a triaxial induction tool. (a) The original model; (b) the equivalent model.

$\hat{\varepsilon}$  is the permittivity tensor given by

$$\hat{\varepsilon} = \begin{bmatrix} \varepsilon_h & 0 & 0 \\ 0 & \varepsilon_h & 0 \\ 0 & 0 & \varepsilon_v \end{bmatrix}, \quad (5)$$

and  $\hat{M}_o$  is the vector representing the magnetic dipole source:

$$\hat{M}_o = \begin{bmatrix} M_x \\ M_y \\ M_z \end{bmatrix}. \quad (6)$$

Following the procedure in [15], solving (2)-(3), we can obtain the magnetic fields of multicomponent induction tools in either homogeneous or multilayered TI medium. The final solutions for each kind of formation can be found in Appendices A and B. The equivalent transmission line theory [16] is used to derive the generalized upward and downward coefficients in multilayered TI medium. The details of the derivation are omitted here and can be referred to [4].

Figure 3 shows the flow chart of the forward model. We use “ $N\_point$ ” to present total number of logging points. Logging point essentially stands for measured depth of wireline logging. The letter “ $i$ ” is a control number and records the number of calculated logging point during the serial modeling. If  $i$  is larger than  $N\_point$ , the forward model is terminated and magnetic fields with respect to total logging points are obtained. We can consequently make a plot of tool responses versus bedding depth. In terms of the control number, a big DO loop is embraced in the forward code *TRITI2009* and takes charge of the iterative computation of magnetic fields at each measurement depth.

In principle, the original forward model is serial since it only calculates the tool responses of single logging point

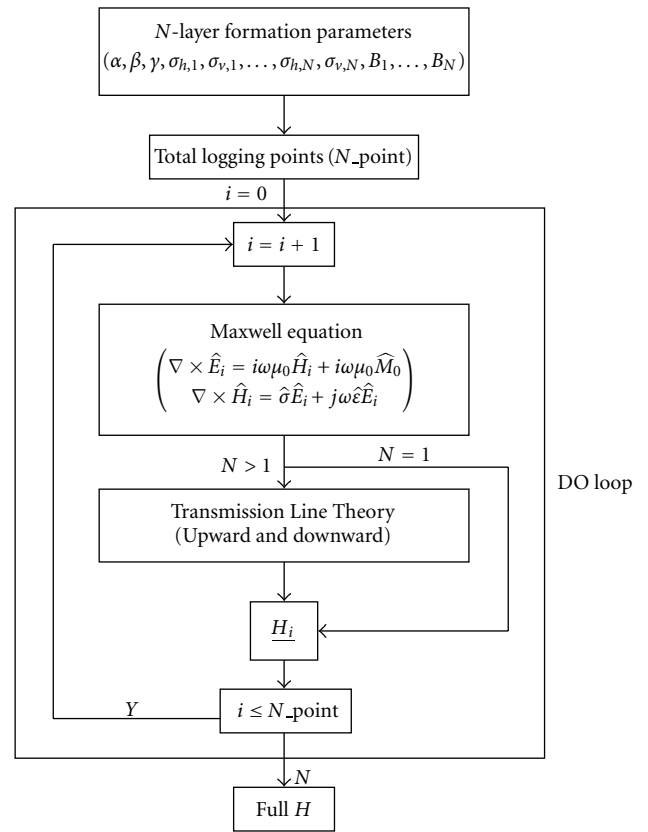


FIGURE 3: Flow chart of the serial forward model.

at one time. It is a waste for a multicore computer because only one core is active as shown in Figure 3, a DO loop controls the whole iterative calculation and can be treated essentially as a master thread. We realize the fact that wireline logging does not collect measurement information until the drilling progress is completed. Thus, logging point is

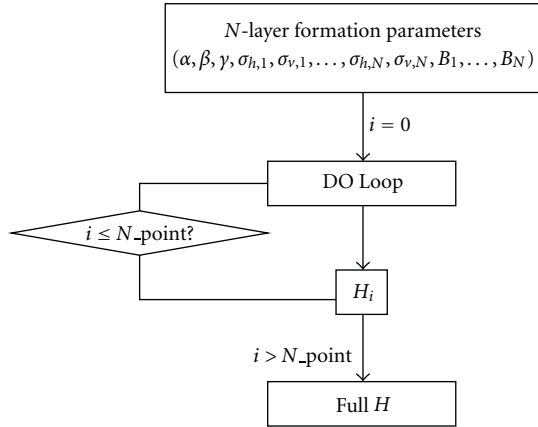


FIGURE 4: Programming structure of the 1D forward modeling code *TRITI2009*.

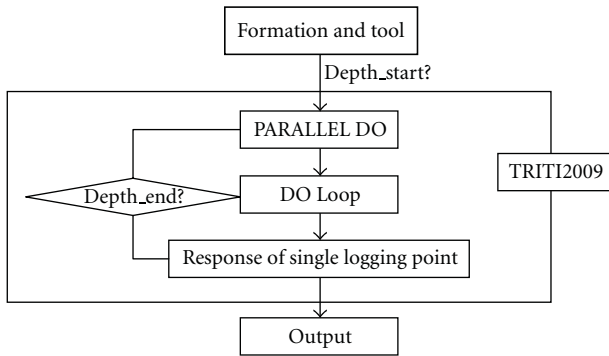


FIGURE 5: Programming structure of the parallelized 1D forward model *TRITI2009*.

```

!$OMP PARALLEL DO
DO I = 1, points
...
END DO
$OMP END PARALLEL DO
    
```

ALGORITHM 1

Realizing parallelization

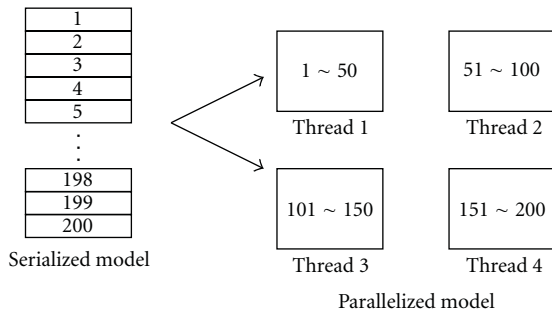


FIGURE 6: Illustration of Parallel DO loop.

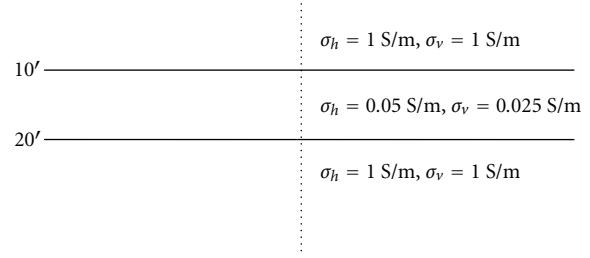


FIGURE 7: A three-layer anisotropic formation.

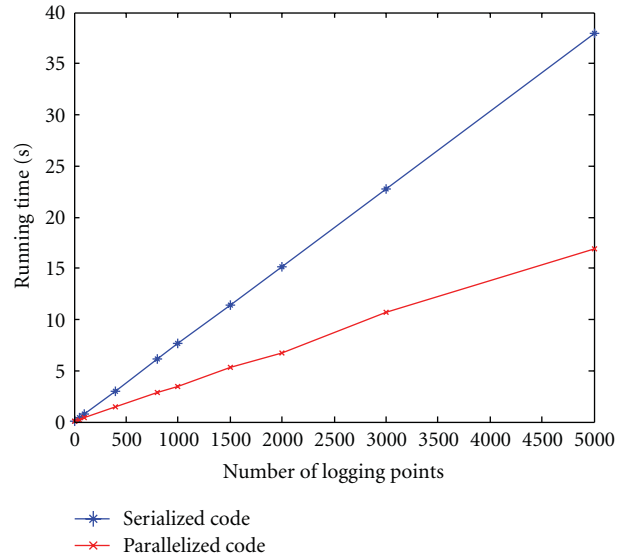


FIGURE 8: Comparison of the total running time of the serialized model and parallelized model.

completely independent with any other points nearby. So the big DO loop includes  $N\_point$  independent parts and can run through several slave threads. The maximum number of threads is determined by the number of computer cores. Consequently, more than one logging point is computed simultaneously but just consuming a single point's time. Next, we will explain the implementation of the parallelization of the forward modeling using OpenMP.

**2.3. Parallelization Progress of Forward Model.** As we have previously mentioned, the original forward model simulates the responses of triaxial induction tool in 1D layered TI medium in any deviated borehole and is serial. We realized the forward model in Intel FORTRAN Compiler and the forward code is named as *TRITI2009*. Note that Intel FORTRAN Compiler supports OpenMP interface.

Figure 4 briefly shows the programming structure of the 1-D forward modeling code *TRITI2009*. Since we have presented that the original forward code *TRITI2009* calculated tool responses according to the serial sequence of logging points, a big DO loop is implemented to control the calculation.

```

PROGRAM TRITI2009
IMPLICIT NONE
...
COOM/BLK/A, B, C
!$OMP THREADPRIVATE (A, B, C)
...
!$OMP PARALLEL DO
!$COPYIN (A, B, C)
DO I = 1, points
...
END DO
$OMP END PARALLEL DO
SUBROUTINE
...
END

```

ALGORITHM 2

As we previously discussed, the DO loop in Figure 4 includes independent logging points and can be parallelized. Then, we apply PARALLEL DO to deal with the DO loop from original forward model. The basic directive of PARALLEL DO is semantically equivalent to Algorithm 1.

Then we implement PARALLEL DO to realize parallelization, as shown in Figure 5.

The other important issue is the common block or variables. Since OpenMP is based on shared-memory architecture, as a result, all the threads are allowed to access to the common block or variables. However, there are some common blocks that we do not want to share among different threads. The directive THREADPRIVATE allows us to specify named common blocks and variables as private to other threads but global within their own thread. Once we declare a common block or variable as THREADPRIVATE, each thread in the team maintains a separate copy of that common block or variable. Data written to a THREADPRIVATE common block or variable remain private to that thread and is not available to other threads in the team. Use the clause COPYIN after the directive PARALLEL DO to specify that upon entry into a parallel region, data of a named common block or named variable in the master thread are copied to the common block or variable of each thread. The overall parallel section is shown as Algorithm 2.

Next, we use Figure 6 to illustrate the methodology used in OpenMP to realize parallelization in *TRITI2009*. We assume the original model need to calculate 200 points and the computer has 4 cores. In the serialized model, the computer can only pick up one logging point at one time and calculate the response. On the contrary, in the PARALLEL DO loop, the computer divides all the 200 points into 4 groups. For convenience, we assume the division is even. As a result, 4 threads synchronously run this loop. In other words, 4 logging points can be calculated simultaneously, realizing parallelization.

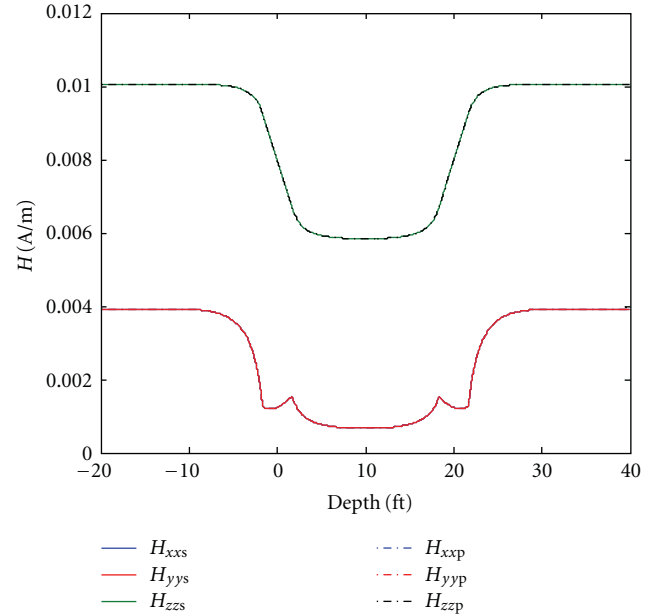


FIGURE 9: Comparison of the simulated results (5000 points) from the serialized and parallelized codes.

### 3. Results and Discussions

In this section, we present several examples to discuss the efficiency of the parallelized forward modeling. A 4-core computer (2.33 GHz, 4 GB) is implemented. In all the examples, we use the same computer to do the simulation.

*Example 1.* In the first example, we consider a three-layer anisotropic formation as shown in Figure 7. The boundaries are at 10 ft and 20 ft, respectively. The first layer and the third layer are isotropic and have a conductivity of 1 S/m. The second layer is anisotropic and has a horizontal conductivity of 0.05 S/m and vertical conductivity of 0.025 S/m. The operating frequency of the triaxial tool is 20 KHz and the spacing between the transmitter and receiver is 40 inches. The dipping angle  $\alpha$  is assumed to be  $0^\circ$  (i.e., the tool is perpendicular to the bed layers). 4 threads are used in parallelized code.

Figure 8 shows the total running time of the serialized and parallelized forward modeling code as a function of the logging points. We can see that for a given number of logging points, the parallelized code is much faster than the serialized one. Although the number of logging points increases, the running time of both codes increases, but the comparison is in favor of the parallelized one. For 5000 logging points, the parallelized model is approximately 2.5 times faster than the original serialized model. Due to the limited memory bandwidth and load balancing, the speed improvement does not reach 4 times although we are using a 4-core computer.

Next, we check the accuracy of the parallelized code. In Figure 9, we compare the calculated magnetic field components  $H_{xx}$ ,  $H_{yy}$ , and  $H_{zz}$  as a function of the depth for 5000 logging points. Perfect agreement is observed between the results from the serialized code and the parallelized

560 ft	$\sigma_h = 0.5 \text{ S/m}, \sigma_v = 0.5 \text{ S/m}$
580 ft	$\sigma_h = 0.325 \text{ S/m}, \sigma_v = 0.325 \text{ S/m}$
595 ft	$\sigma_h = 0.55625 \text{ S/m}, \sigma_v = 0.55625 \text{ S/m}$
614 ft	$\sigma_h = 0.2125 \text{ S/m}, \sigma_v = 0.2125 \text{ S/m}$
630 ft	$\sigma_h = 0.1125 \text{ S/m}, \sigma_v = 0.1125 \text{ S/m}$
635 ft	$\sigma_h = 0.2 \text{ S/m}, \sigma_v = 0.2 \text{ S/m}$
680 ft	$\sigma_h = 0.3125 \text{ S/m}, \sigma_v = 0.3425 \text{ S/m}$
	$\sigma_h = 0.3125 \text{ S/m}, \sigma_v = 0.125 \text{ S/m}$

FIGURE 10: The eight-layer Devine test site formation.

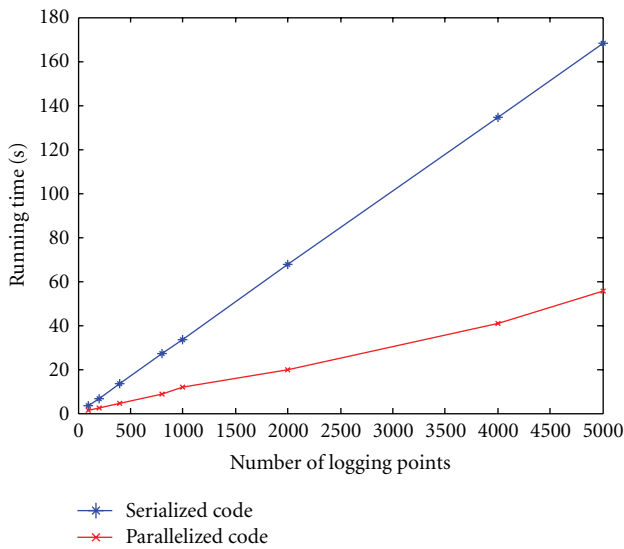


FIGURE 11: Comparison of the total running time between the serialized model and the parallelized model.

code, implying that the parallelization does not change the accuracy of the code.

In Figure 9, we ignore the entire cross components  $H_{xy}$ ,  $H_{xz}$ ,  $H_{yx}$ ,  $H_{yz}$ ,  $H_{zx}$ , and  $H_{zy}$  due to the orthogonal property of antenna in the vertical borehole.  $H_{xx}$  and  $H_{yy}$  are coinciding with each other since the borehole is vertical and formation is isotropic in the horizontal plane. We observe spikes on  $H_{xx}$  and  $H_{yy}$ , known as “horn effect,” which is assumed as a significant sign indicating the layer boundary. According to the displacement of triaxial antennas, the coaxial antennas should have stronger responses than the other coplanar antennas, which are also proven by Figure 9. The common point among  $H_{xx}$ ,  $H_{yy}$ , and  $H_{zz}$  is that in a conductive layer, those magnetic fields  $H_{xx}$ ,  $H_{yy}$ , and  $H_{zz}$  show stronger sensitivity with respect to larger responses.

*Example 2.* In this example, the geometric formation is constructed according to the Devine test site of BP America

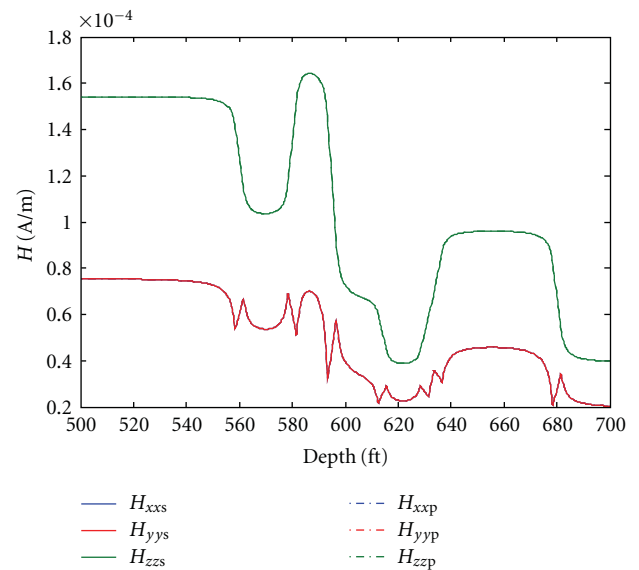


FIGURE 12: Comparison of the simulated results (800 points) from the serialized and parallelized codes.

[17], as shown in Figure 10. The operating frequency is 512 Hz and the distance between the transmitter and the receiver is 40 inches. We assume the well is vertical. We also use 4 threads in parallelization

Figure 11 compares the total running time of the serialized code with the parallelized code. With the increasing of the logging points, the difference of the time between these two models is strengthened. Figure 12 presents the simulation results for 800 points from the serial and parallel models. From Figures 11 and 12, it is easy to observe that the forward model is accelerated by about 3 times after parallelization. In Figure 12, we can easily tell formation boundaries according to spikes on coplanar components. Note that  $H_{zz}$  does not differentiate the sixth layer since no evident change is observed from 620 ft to 640 ft on  $H_{zz}$ . Fortunately,  $H_{xx}$  and  $H_{yy}$  present significant spikes and infer the existence of different layers. Therefore, the multicomponent configuration of triaxial induction tool provides much more

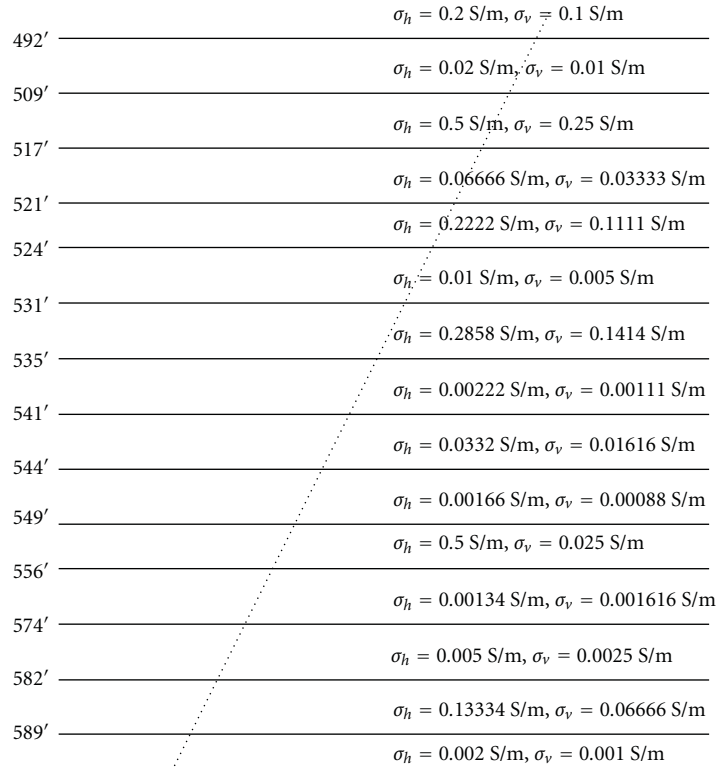


FIGURE 13: A fifteen-layer Oklahoma model.

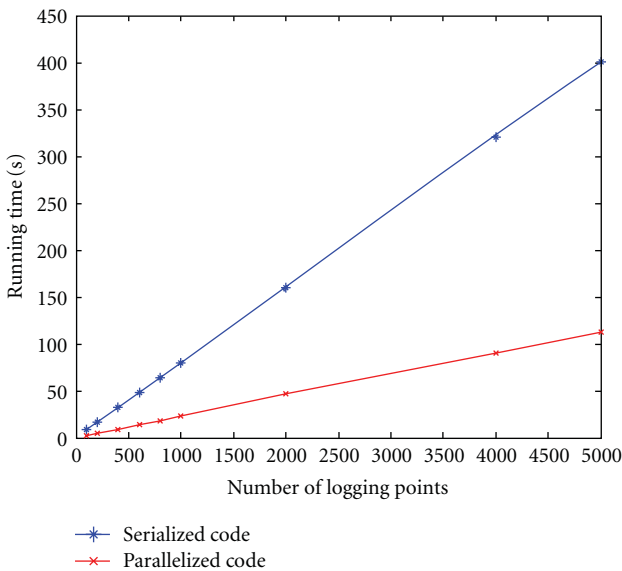


FIGURE 14: Comparison of the total running time of the serialized model and the parallelized model for the 15-layer Oklahoma model.

comprehensive information than traditional induction tool which is only consisted by coaxial antennas.

*Example 3.* Finally, we apply a benchmark fifteen-layer Oklahoma model as shown in Figure 13. The distance between

the transmitter and the receiver is 40 inches and the working frequency is 20 KHz. The dipping angle is assumed to be 60°. The boundaries and conductivities of each layer are given in the figure.

First, 4 threads are applied. We compare the computation time of the serialized code and parallelized code in Figure 14.

Figure 15 compares the coaxial and coplanar components  $H_{xx}$ ,  $H_{yy}$ , and  $H_{zz}$ . It is easy to differentiate  $H_{xx}$  and  $H_{yy}$  in Figure 15. So the difference between  $H_{xx}$  and  $H_{yy}$  is a notable flag of deviated well. Since the well is inclined at 60° in the X-Z plane, as a result, we should have nonzero cross components  $H_{xz}$  and  $H_{zx}$ , as shown in Figure 16. In the future inversion process, the value of cross components  $H_{xz}$  and  $H_{zx}$  are widely applied to derive dipping angle.

From Figures 15 and 16, we can see that parallelization does not affect the accuracy of forward model since the tool responses from the parallel model are coinciding with serial model. We can see that the slope of the blue line (the serialized code) is about 3.5 times that of the red line, which means the speed of parallelized model is 3.5 times faster than the original model.

According to the results from the three examples, we can see that the contrast of the time between the parallelized code and serialized code is enhanced when the total number of layers is increased. As we know, in field exploration, the earth formation is always very complex and hard to predict. Hence, fast forward modeling provides geologists a good tool for simulation and possibility for real-time inversion.

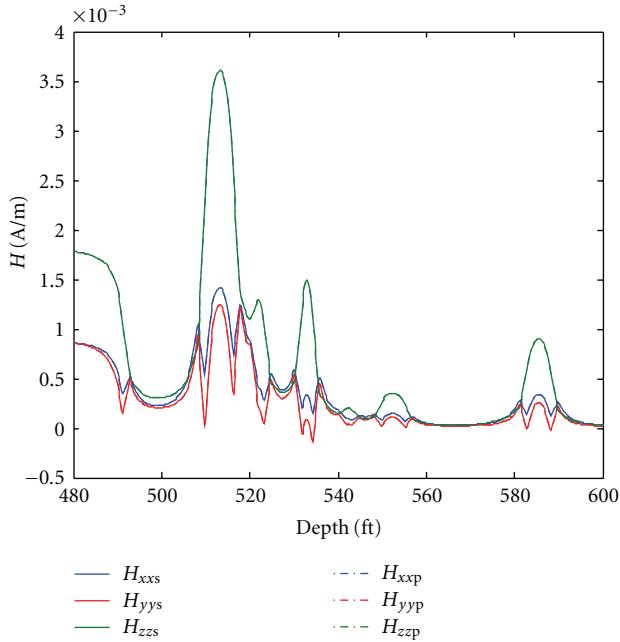


FIGURE 15: Comparison of  $H_{xx}$ ,  $H_{yy}$ , and  $H_{zz}$  (1000 points) from the serialized and parallelized codes.

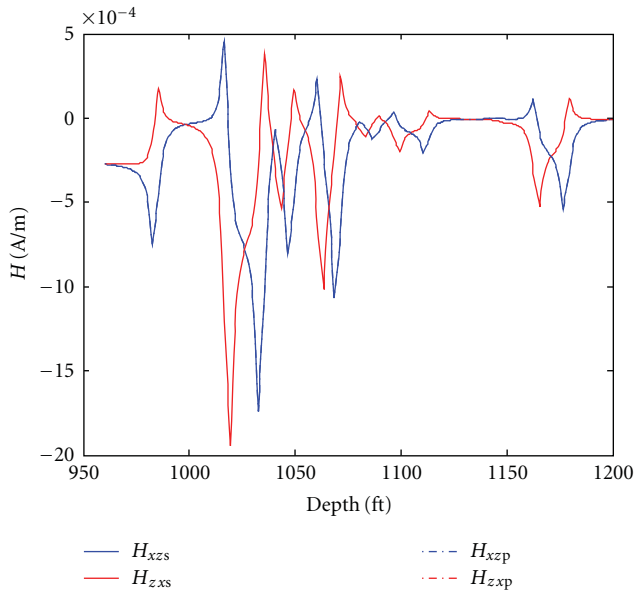


FIGURE 16: Comparison of cross components (1000 points) from the serialized and parallelized codes.

Next, we change the number of threads to investigate the performance of the parallelized code. In Figure 17, we compare the running time when different number of threads are implemented. It can be seen that for a given number of logging points, the more threads are used, the less time is consumed by the code. Therefore, we can expect that the speed of the forward modeling to be further improved as multicore computers are used.

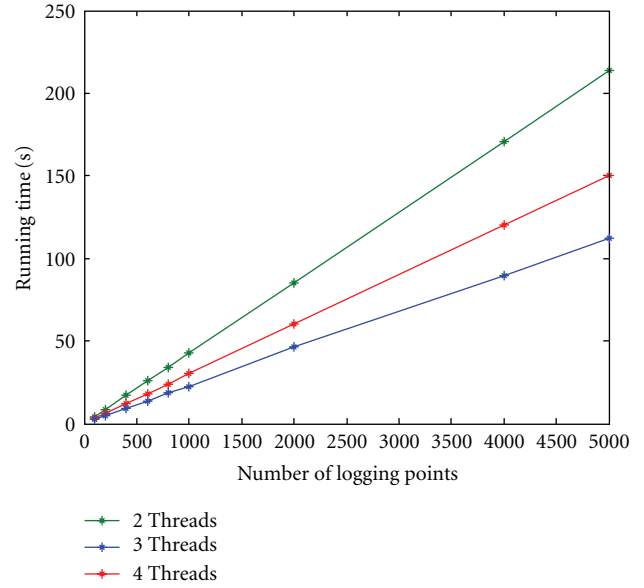


FIGURE 17: Comparison of the time cost for different number of threads.

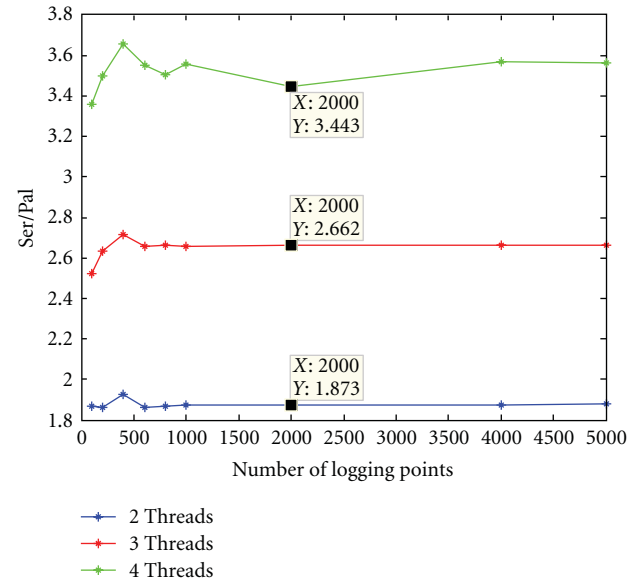


FIGURE 18: Comparison of the efficiency for different number of threads.

Finally, we check the efficiency among different number of threads. In Figure 18, we can see that the speed has been improved approximately by 1.8 times for 2 threads, 2.6 times for 3 threads, and 3.4 times for 4 threads, respectively. However, the improved speed is not linear proportional to the number of threads. The reason is complex. As we discussed in the first example, the limited memory bandwidth and load balancing influence the parallelization. On the other hand, we only parallelize the Do Loop from the main body of the forward model. The read and write sections are still serial; and the common variables have

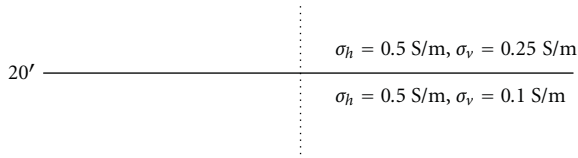


FIGURE 19: A two-layer anisotropic formation.

become private for each thread. Then, the cost on memory is also increased. Hence, the time saving of parallel code cannot be linear to the number of threads.

*Example 4.* In this example, we apply one two-layer formation to illustrate the reason why triaxial induction logging tool is capable to detect anisotropic resistivity. Figure 19 presents the two-layer formation. Note that the two layers share the same horizontal conductivity but different vertical conductivity. The well is assumed to be vertical.

A 4-core computer is implemented to parallelize the forward model. Figure 20 compares the running time from the serialized and parallelized codes. As shown in Figure 20, the running speed is significantly improved.

Then, we present the simulation responses in Figure 21. Perfect match within the corresponding components can be found. It is very interesting to know the coaxial component  $H_{zz}$  is constant. Therefore, we can infer that  $H_{zz}$  is “blind” to the different layers. As we know, in the vertical well,  $Z$  directional electrical loop antenna can only induce electrical eddy currents in the horizontal plane. Moreover, the responses on the corresponding receiver are only sensitive to the horizontal conductivity. Thus, in this example,  $H_{zz}$  is not various because of the same horizontal conductivity in both of the two layers. Until now, we have explained the reason why the traditional induction tool with coaxial antenna cannot detect anisotropic medium.

In Figure 21, we also notice that the coplanar components  $H_{xx}$ ,  $H_{yy}$  vary between the different two layers. In the vertical well, the coplanar electrical loop antenna generates eddy currents along both horizontal and vertical directions. As a result, the received components result from both the horizontal and the vertical conductivities. From this example, we can see that triaxial induction logging tool is sensitive to anisotropic medium.

#### 4. Conclusion

Parallel computation plays an important role in the high-performance computing and OpenMP is one of the most widely used parallel interfaces. In this paper, we extended the application of OpenMP to well logging simulation in oil industry, parallelizing the 1-D forward modeling code for simulation of wireline triaxial induction tools in multilayered anisotropic formation. We explained the parallel process and validate the parallelized code. The forward modeling is successfully parallelized on a 4-core computer and the

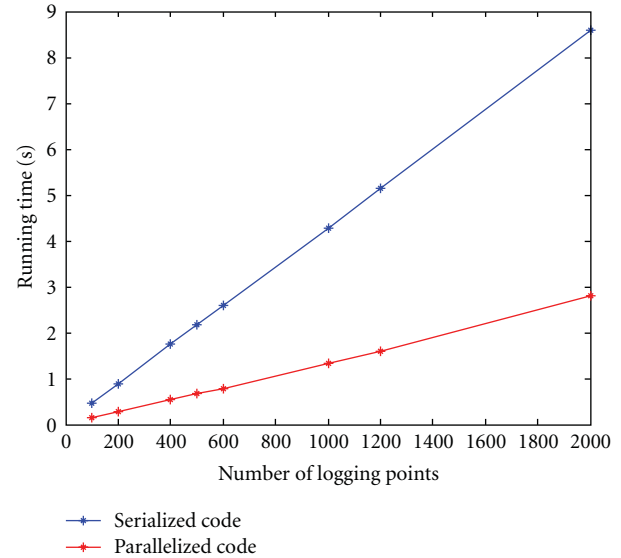
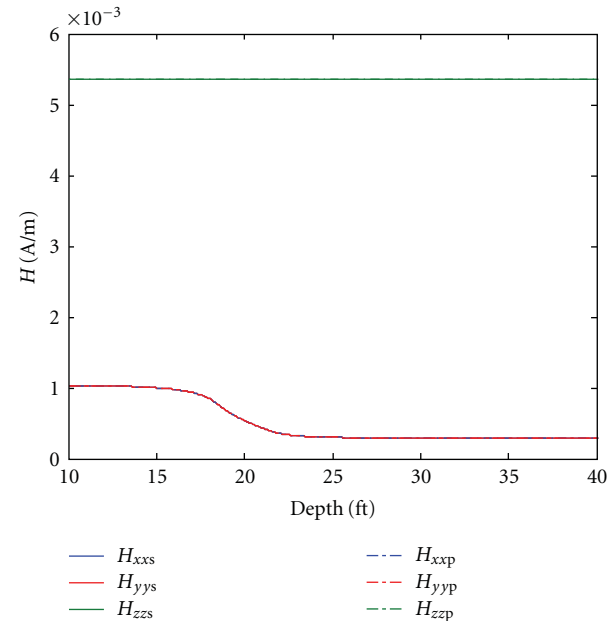


FIGURE 20: Comparison of the time cost for different number of threads.

FIGURE 21: Comparison of  $H_{xx}$ ,  $H_{yy}$ , and  $H_{zz}$  (1000 points) from the serialized and parallelized codes.

total running time is significantly improved by at least 2.5 times. We also briefly discuss the property of triaxial induction logging tool in different formation. Furthermore, the accuracy of the parallelized code keeps the same as the original code. The speed of the forward modeling is expected to further improve as multicore computers are used.

## Appendices

### A. Magnetic Fields in Vertical Well

The magnetic fields in homogenous formation with vertical well are given by Mora and Gianzero [15] as follows:

$$H_x^x = \frac{e^{ik_v s}}{4\pi} \left[ \frac{i\omega\mu_0\sigma_h}{\lambda s} + \frac{ik_h s - k_h k_v x^2}{s\rho^2} - \frac{2ik_h x^2}{\rho^4} \right] - \frac{e^{ik_h r}}{4\pi} \left[ \frac{ik_h r - k_h^2 x^2}{r\rho^2} - \frac{2ik_h x^2}{\rho^4} - \frac{ik_h}{r^2} + \frac{(k_h^2 x^2 + 1)}{r^3} + \frac{3ik_h x^2}{r^4} - \frac{3x^2}{r^5} \right], \quad (\text{A.1})$$

$$H_y^x = H_x^y = xy \frac{e^{ik_v s}}{4\pi\rho^2} \left[ -\frac{k_h k_v}{s} - \frac{2ik_h}{\rho^2} \right] - \frac{e^{ik_h r} xy}{4\pi} \left[ -\frac{k_h^2}{r\rho^2} - \frac{2ik_h}{\rho^4} + \frac{k_h^2}{r^3} + \frac{3ik_h}{r^4} - \frac{3}{r^5} \right], \quad (\text{A.2})$$

$$H_z^x = H_x^z = -xz \frac{e^{ik_h r}}{4\pi r^3} \left[ k_h^2 + \frac{3ik_h}{r} - \frac{3}{r^2} \right], \quad (\text{A.3})$$

$$H_y^y = \frac{e^{ik_v s}}{4\pi} \left[ \frac{i\omega\mu_0\sigma_h}{\lambda s} + \frac{ik_h s - k_h k_v y^2}{s\rho^2} - \frac{2ik_h y^2}{\rho^4} \right] - \frac{e^{ik_h r}}{4\pi} \left[ \frac{ik_h r - k_h^2 y^2}{r\rho^2} - \frac{2ik_h y^2}{\rho^4} - \frac{ik_h}{r^2} + \frac{(k_h^2 y^2 + 1)}{r^3} + \frac{3ik_h y^2}{r^4} - \frac{3y^2}{r^5} \right] \quad (\text{A.4})$$

$$H_z^y = H_y^z = -yz \frac{e^{ik_h r}}{4\pi r^3} \left[ k_h^2 + \frac{3ik_h}{r} - \frac{3}{r^2} \right], \quad (\text{A.5})$$

$$H_z^z = \frac{e^{ik_h r}}{4\pi r} \left[ i\omega\mu_0\sigma_h + \frac{ik_h}{r} - \frac{(k_h^2 z^2 + 1)}{r^2} - \frac{3ik_h z^2}{r^3} + \frac{3z^2}{r^4} \right], \quad (\text{A.6})$$

where  $\hat{\sigma}_h = \sigma_h - j\omega\epsilon_0\epsilon_h$ ,  $\hat{\sigma}_v = \sigma_v - j\omega\epsilon_0\epsilon_v$ ,  $\lambda^2 = \hat{\sigma}_h/\hat{\sigma}_v$ ,  $k_h^2 = j\omega\mu\hat{\sigma}_h$ ,  $k_v^2 = j\omega\mu\hat{\sigma}_v$ ,  $r = \sqrt{x^2 + y^2 + z^2}$ ,  $\rho = \sqrt{x^2 + y^2}$ , and  $s = \sqrt{x^2 + y^2 + \lambda^2 z^2}$ .

The magnetic fields in layered medium with vertical well is given by

$$H_x^x = \frac{M_x}{4\pi} \int_0^\infty \left( \frac{\beta_i \sin^2 \phi}{\lambda_i \xi_{vi}} k_h^2 e^{-\xi_{vi} \lambda_i |z-z_0|} - \beta_i \cos^2 \phi \xi_{hi} e^{-\xi_{hi} |z-z_0|} + \frac{P_i}{\lambda_i} \sin^2 \phi k_{hi}^2 e^{-\xi_{vi} \lambda_i z} + \frac{Q_i}{\lambda_i} \sin^2 \phi k_{hi}^2 e^{\xi_{vi} \lambda_i z} - S_i \cos^2 \phi \xi_{hi} e^{-\xi_{hi} z} + T_i \cos^2 \phi \xi_{hi} e^{\xi_{hi} z} \right) \times \alpha J_0(\alpha \rho) d\alpha + \frac{M_x}{4\pi \rho} \int_0^\infty \left( \lambda_i \frac{\beta_i}{\xi_{vi}} k_v^2 e^{-\xi_{vi} \lambda_i |z-z_0|} + \beta_i \xi_{hi} e^{-\xi_{hi} |z-z_0|} + P_i \lambda_i k_{vi}^2 e^{-\xi_{vi} \lambda_i z} + Q_i \lambda_i k_{vi}^2 e^{\xi_{vi} \lambda_i z} + S_i \xi_{hi} e^{-\xi_{hi} z} - T_i \xi_{hi} e^{\xi_{hi} z} \right) \times \cos 2\phi J_1(\alpha \rho) d\alpha, \quad (\text{A.7})$$

$$H_x^y = \frac{M_x}{4\pi \rho} \int_0^\infty \left( \frac{\beta_i}{\lambda_i \xi_{vi}} k_h^2 e^{-\xi_{vi} \lambda_i |z-z_0|} - \beta_i \xi_{hi} e^{-\xi_{hi} |z-z_0|} + \frac{P_i}{\lambda_i} k_{hi}^2 e^{-\xi_{vi} \lambda_i z} + \frac{Q_i}{\lambda_i} k_{hi}^2 e^{\xi_{vi} \lambda_i z} - S_i \xi_{hi} e^{-\xi_{hi} z} + T_i \xi_{hi} e^{\xi_{hi} z} \right) \times \alpha J_0(\alpha \rho) d\alpha + \frac{M_x}{4\pi \rho} \int_0^\infty \left( \lambda_i \frac{\beta_i}{\xi_{vi}} k_v^2 e^{-\xi_{vi} \lambda_i |z-z_0|} + \beta_i \xi_{hi} e^{-\xi_{hi} |z-z_0|} + P_i \lambda_i k_{vi}^2 e^{-\xi_{vi} \lambda_i z} + Q_i \lambda_i k_{vi}^2 e^{\xi_{vi} \lambda_i z} + S_i \xi_{hi} e^{-\xi_{hi} z} - T_i \xi_{hi} e^{\xi_{hi} z} \right) \times \sin 2\phi J_1(\alpha \rho) d\alpha, \quad (\text{A.8})$$

$$H_x^z = \frac{M_x}{4\pi} \cos \phi \int_0^\infty \left( \beta_i \frac{|z-z_0|}{z-z_0} e^{-\xi_{hi} |z-z_0|} + S_i e^{-\xi_{hi} z} + T_i e^{\xi_{hi} z} \right) \alpha^2 J_1(\alpha \rho) d\alpha, \quad (\text{A.9})$$

$$\begin{aligned}
H_y^x &= \frac{M_y}{8\pi} \int_0^\infty \left( \frac{\beta_i}{\lambda_i \xi_{vi}} k_{hi}^2 e^{-\xi_{vi} \lambda_i |z-z_0|} - \beta_i \xi_{hi} e^{-\xi_{hi} |z-z_0|} \right. \\
&\quad \left. + \frac{P_i}{\lambda_i} k_{hi}^2 e^{-\xi_{vi} \lambda_i z} + \frac{Q_i}{\lambda_i} k_{hi}^2 e^{\xi_{vi} \lambda_i z} \right. \\
&\quad \left. - S_i \xi_{hi} e^{-\xi_{hi} z} + T_i \xi_{hi} e^{\xi_{hi} z} \right) \\
&\quad \times \sin 2\phi \alpha J_0(\alpha \rho) d\alpha \\
&\quad + \frac{M_y}{4\pi \rho} \times \int_0^\infty \left( \lambda_i \frac{\beta_i}{\xi_{vi}} k_{vi}^2 e^{-\xi_{vi} \lambda_i |z-z_0|} + \beta_i \xi_{hi} e^{-\xi_{hi} |z-z_0|} \right. \\
&\quad \left. + P_i \lambda_i k_{vi}^2 e^{-\xi_{vi} \lambda_i z} + Q_i \lambda_i k_{vi}^2 e^{\xi_{vi} \lambda_i z} \right. \\
&\quad \left. + S_i \xi_{hi} e^{-\xi_{hi} z} - T_i \xi_{hi} e^{\xi_{hi} z} \right) \\
&\quad \times \sin 2\phi J_1(\alpha \rho) d\alpha,
\end{aligned} \tag{A.10}$$

$$\begin{aligned}
H_y^y &= \frac{M_y}{4\pi} \int_0^\infty \left( \frac{\beta_i \cos^2 \phi}{\lambda_i \xi_{vi}} k_{hi}^2 e^{-\xi_{vi} \lambda_i |z-z_0|} - \beta_i \sin^2 \phi \xi_{hi} e^{-\xi_{hi} |z-z_0|} \right. \\
&\quad \left. + \frac{P_i}{\lambda_i} \cos^2 \phi k_{hi}^2 e^{-\xi_{vi} \lambda_i z} + \frac{Q_i}{\lambda_i} \cos^2 \phi k_{hi}^2 e^{\xi_{vi} \lambda_i z} \right. \\
&\quad \left. - S_i \sin^2 \phi \xi_{hi} e^{-\xi_{hi} z} + T_i \sin^2 \phi \xi_{hi} e^{\xi_{hi} z} \right) \\
&\quad \times \alpha J_0(\alpha \rho) d\alpha \\
&\quad + \frac{M_y}{4\pi \rho} \int_0^\infty \left( \lambda_i \frac{\beta_i}{\xi_{vi}} k_{vi}^2 e^{-\xi_{vi} \lambda_i |z-z_0|} + \beta_i \xi_{hi} e^{-\xi_{hi} |z-z_0|} \right. \\
&\quad \left. + P_i \lambda_i k_{vi}^2 e^{-\xi_{vi} \lambda_i z} + Q_i \lambda_i k_{vi}^2 e^{\xi_{vi} \lambda_i z} \right. \\
&\quad \left. + S_i \xi_{hi} e^{-\xi_{hi} z} - T_i \xi_{hi} e^{\xi_{hi} z} \right) \\
&\quad \times \cos 2\phi J_1(\alpha \rho) d\alpha,
\end{aligned} \tag{A.11}$$

$$\begin{aligned}
H_y^z &= \frac{M_y}{4\pi} \sin \phi \int_0^\infty \left( \beta_i \frac{|z-z_0|}{z-z_0} e^{-\xi_{hi} |z-z_0|} \right. \\
&\quad \left. + S_i e^{-\xi_{hi} z} + T_i e^{\xi_{hi} z} \right) \alpha^2 J_1(\alpha \rho) d\alpha,
\end{aligned} \tag{A.12}$$

$$\begin{aligned}
H_z^x &= \frac{M_z}{4\pi} \int_0^\infty \xi_{hi} \left( \frac{\beta_i}{\xi_{hi}} \frac{|z-z_0|}{z-z_0} e^{-\xi_{hi} |z-z_0|} \right. \\
&\quad \left. + F_i e^{-\xi_{hi} z} - G_i e^{\xi_{hi} z} \right) \alpha^2 \cos \phi J_1(\alpha \rho) d\alpha,
\end{aligned} \tag{A.13}$$

$$\begin{aligned}
H_z^y &= \frac{M_z}{4\pi} \int_0^\infty \xi_{hi} \left( \frac{\beta_i}{\xi_{hi}} \frac{|z-z_0|}{z-z_0} e^{-\xi_{hi} |z-z_0|} \right. \\
&\quad \left. + F_i e^{-\xi_{hi} z} - G_i e^{\xi_{hi} z} \right) \alpha^2 \sin \phi J_1(\alpha \rho) d\alpha,
\end{aligned} \tag{A.14}$$

$$\begin{aligned}
H_z^z &= \frac{M_z}{4\pi} \int_0^\infty \left( \frac{\beta_i}{\xi_{hi}} e^{-\xi_{hi} |z-z_0|} + F_i e^{-\xi_{hi} z} + G_i e^{\xi_{hi} z} \right) \alpha^3 J_0(\alpha \rho) d\alpha,
\end{aligned} \tag{A.15}$$

where  $\xi_{vi} = (\alpha^2 - k_{vi}^2)^{1/2}$ ,  $k_{vi} = (i\omega\mu\sigma_{vi})^{1/2}$ ,  $\xi_{vi} = (\alpha^2 - k_{vi}^2)^{1/2}$ ,  $k_{vi} = (i\omega\mu\sigma_{vi})^{1/2}$ ,  $\lambda_i = k_{hi}/k_{vi}$ , and

$$\beta_i = \begin{cases} 0, & \text{if } M_{x,y,orz} \text{ is not in the } i\text{th layer,} \\ 1, & \text{if } M_{x,y,orz} \text{ is in the } i\text{th layer.} \end{cases} \tag{A.16}$$

In (A.7)–(A.12),  $P_i$  and  $S_i$  are the magnitude of the reflection magnetic fields and  $Q_i$  and  $T_i$  are the magnitude of the refraction magnetic fields if sources are in  $X$  or  $Y$  direction. In (A.13)–(A.15),  $F_i$  and  $G_i$  are the magnitude of the reflection magnetic fields and the refraction magnetic fields, respectively, when source is along  $Z$  direction.

## B. Magnetic Fields in Deviated Well

From Appendix A, we have got the solutions of magnetic fields in vertical well. We apply matrix  $H$  to represent the magnetic fields from vertical well. The magnetic fields in any deviated well can be derived according to rotation matrix, as

$$\hat{H} = R^{-1} \cdot H \cdot R \cdot \hat{M}_o, \tag{B.1}$$

where  $R$  is the rotation matrix,

$$R = \begin{pmatrix} \cos \alpha \cos \beta \cos \gamma - \sin \beta \sin \gamma & -\cos \alpha \cos \beta \sin \gamma - \sin \beta \cos \gamma & \sin \alpha \cos \beta \\ \cos \alpha \sin \beta \cos \gamma + \cos \beta \sin \gamma & -\cos \alpha \sin \beta \sin \gamma + \cos \beta \cos \gamma & \sin \alpha \sin \beta \\ -\sin \alpha \cos \gamma & \sin \gamma \sin \alpha & \cos \alpha \end{pmatrix}. \tag{B.2}$$

Since  $R$  is orthogonal, it is easy to know that

$$R^{-1} = \begin{pmatrix} \cos \alpha \cos \beta \cos \gamma - \sin \beta \sin \gamma & \cos \alpha \sin \beta \cos \gamma + \cos \beta \sin \gamma & -\sin \alpha \cos \gamma \\ -\cos \alpha \cos \beta \sin \gamma - \sin \beta \cos \gamma & -\cos \alpha \sin \beta \sin \gamma + \cos \beta \cos \gamma & \sin \gamma \sin \alpha \\ \sin \alpha \cos \beta & \sin \alpha \sin \beta & \cos \alpha \end{pmatrix}, \quad (\text{B.3})$$

and  $\widehat{M}_o$  is the matrix of transmitter source.

## References

- [1] B. Kriegshäuser, O. Fanini, S. Forgang et al., "A new multi-component induction logging tool to resolve anisotropic formations: paper D," in *Proceedings of the Transactions SPWLA 41st Annual Logging Symposium*, Dallas, Tex, USA, June 2000.
- [2] M. Zhdanov, D. Kennedy, and E. Peksen, "Foundations of tensor induction well-logging," *Petrophysics*, vol. 42, no. 6, pp. 588–610, 2001.
- [3] B. Anderson, T. Barber, and T. M. Habashy, "The interpretation and inversion of fully triaxial induction data: a sensitivity study," in *Proceedings of the 36th Annual Logging Symposium Transactions, Society of Professional Well Log Analyst*, 2002.
- [4] L. L. Zhong, J. Li, A. Bhardwaj, S. C. Liang, and R. C. Liu, "Computation of triaxial induction logging tools in layered anisotropic dipping formations," *IEEE Transactions on Geoscience and Remote Sensing*, vol. 46, no. 4, pp. 1148–1163, 2008.
- [5] C. G. Broyden, "A class of methods for solving nonlinear simultaneous equations," *Mathematics of Computation—American Mathematical Society*, vol. 19, pp. 577–593, 1965.
- [6] O. Friberg, "Jacobian matrices using the Newmark direct integration scheme," *Computers and Structures*, vol. 25, no. 2, pp. 307–310, 1987.
- [7] W. Gropp and E. Lusk, "A test implementation of the MPI data message-passing standard," Tech. Rep. ANL-92/47, 1992.
- [8] W. Gropp, E. Lusk, N. Doss, and A. Skjellum, "A high-performance, portable implementation of the MPI message passing interface standard," *Parallel Computing*, vol. 22, no. 6, pp. 789–828, 1996.
- [9] G. Krawezik and F. Cappello, "Performance comparison of MPI and OpenMP on shared memory multiprocessors," *Concurrency Computation Practice and Experience*, vol. 18, no. 1, pp. 29–61, 2006.
- [10] I. Dorta, C. Leon, and C. Rodriguez, "A comparison between MPI and OpenMP branch-and-bound skeletons," in *Proceedings of the International Parallel and Distributed Processing Symposium*, 2003.
- [11] R. Chandra, R. Menon, L. Dagum, D. Kohr, D. Maydan, and J. McDonald, *Parallel Programming in OpenMP*, Morgan Kaufmann, San Francisco, Calif, USA, 2000.
- [12] B. Chapman, G. Jost, R. van der Pas, and D. J. Kuck, *Using OpenMP: Portable Shared Memory Parallel Programming*, MIT Press, Massachusetts, 2007.
- [13] M. Hermanns, "Parallel Programming in Fortran 95 using OpenMP," [http://www.openmp.org/presentations/miguel/F95\\_OpenMPv1\\_v2.pdf](http://www.openmp.org/presentations/miguel/F95_OpenMPv1_v2.pdf), 2002.
- [14] C. Bischof, M. Bucker, P. Gibbon, G. Joubert, and T. Lippert, *Parallelizing a Real-Time Steering Simulation for Computer Games with OpenMP*, IOS Press, Amsterdam, The Netherlands, 2008.
- [15] J. H. Mora and S. Gianzero, "Effects of formation anisotropy on resistivity-logging measurements," *Geophysics*, vol. 44, no. 7, pp. 1266–1286, 1979.
- [16] M. Huang and L. C. Shen, "Computation of induction logs in multiple-layer dipping formation," *IEEE Transactions on Geoscience and Remote Sensing*, vol. 27, no. 3, pp. 259–267, 1989.
- [17] M. J. Wilt, D. L. Alumbaugh, H. F. Morrison, A. Becker, K. H. Lee, and M. Deszcz-Pan, "Crosswell electromagnetic tomography: system design considerations and field results," *Geophysics*, vol. 60, no. 3, pp. 871–885, 1995.

## Research Article

# Full-Wave Analysis of Traveling-Wave Field-Effect Transistors Using Finite-Difference Time-Domain Method

**Koichi Narahara**

*Graduate School of Science and Engineering, Yamagata University, 4-3-16 Jonan, Yonezawa, Yamagata 992-8510, Japan*

Correspondence should be addressed to Koichi Narahara, narahara@yz.yamagata-u.ac.jp

Received 27 June 2011; Accepted 24 September 2011

Academic Editor: Ning Yuan

Copyright © 2012 Koichi Narahara. This is an open access article distributed under the Creative Commons Attribution License, which permits unrestricted use, distribution, and reproduction in any medium, provided the original work is properly cited.

Nonlinear transmission lines, which define transmission lines periodically loaded with nonlinear devices such as varactors, diodes, and transistors, are modeled in the framework of finite-difference time-domain (FDTD) method. Originally, some root-finding routine is needed to evaluate the contributions of nonlinear device currents appropriately to the temporally advanced electrical fields. Arbitrary nonlinear transmission lines contain large amount of nonlinear devices; therefore, it costs too much time to complete calculations. To reduce the calculation time, we recently developed a simple model of diodes to eliminate root-finding routines in an FDTD solver. Approximating the diode current-voltage relation by a piecewise-linear function, an extended Ampere's law is solved in a closed form for the time-advanced electrical fields. In this paper, we newly develop an FDTD model of field-effect transistors (FETs), together with several numerical examples that demonstrate pulse-shortening phenomena in a traveling-wave FET.

## 1. Introduction

The generation of a short electrical pulse with picosecond duration is one of the keys to producing a breakthrough in high-speed electronics. The applications of short pulses include measurement systems with picosecond temporal resolution, over-100-Gbit/s communication systems, and submillimeter-to-terahertz imaging systems [1]. We recently found that a transmission line periodically loaded with resonant tunneling diodes (RTDs) greatly compresses the temporal width of the pulse input to it [2]. Once the input pulse crosses the peak voltage of the loaded RTDs, the exponential wave is developed at voltages smaller than the peak voltage, and the sinusoidal wave is coupled to it at larger voltages, whose wave number becomes much larger than that of the input; therefore, the input pulse experiences significant shortening. The similar pulse shortening can be realized in traveling-wave field-effect transistors (TWFETs). A TWFET is a special type of FET whose electrodes are employed not only as electrical contacts but also as transmission lines [3]. We consider the case where a decreasing voltage pulse is applied to the gate line and an increasing one is simultaneously applied to the drain line. By properly designing

the top and bottom levels of the applied pulses, every FET simulates an electronic switch (the switch is open for voltages greater than some fixed threshold, and closed otherwise). This arrangement guarantees the pulse shortening owing to the development of the exponential-sinusoidal waves as observed in an RTD line [4].

In order to evaluate the above-mentioned results in monolithically integrated devices, we have to develop the models of nonlinear devices such as RTDs and FETs for use in a finite-difference time-domain (FDTD) electromagnetic solver [5]. In FDTD-based solvers of Maxwell's equations, a circuit element such as a capacitor, an inductor, or a nonlinear device, is usually implemented in an extended Ampere's law as a field-dependent conductance/capacitance in a single Yee cell [6]. Unfortunately, it requires some root-finding routine such as the Newton-Raphson method to solve it to obtain the temporal advanced electrical fields for numerical stability [7]. The situation becomes more cumbersome, when the physical extent of devices cannot be ignored. Because we have to evaluate several adjacent cells for the terminal voltages that determine the device operation, a root-finder for multiple-variable functions is needed, which is very time-consuming. Moreover, we consider nonlinear

transmission lines, which generally include numerous nonlinear devices.

Recently, we developed a concise model of nonlinear devices that contributes to eliminating the time-consuming root-finding procedures mentioned above. It approximates the voltage dependence of the device current by a piecewise-linear function and solves an extended Ampere's law in a closed form. Actually, we successfully demonstrated an FDTD calculation of the pulse shortening in an RTD line [8]. The similar modeling can be applied not only for diodes but also for three-terminal devices such as FETs. Based on our strategy, we first discuss an FDTD model of FETs after giving brief reviews and then show the results of full-wave calculations that demonstrate the pulse compression in a TWFET.

## 2. Diode Model in FDTD

When the conduction current density flowing in the device is denoted by  $\mathbf{J}_L$ , the temporal evolution of the electromagnetic fields is calculated on the basis of an extended Ampere's law as

$$\frac{\partial \mathbf{E}}{\partial t} = \frac{1}{\epsilon} \nabla \times \mathbf{H} - \frac{1}{\epsilon} \mathbf{J}_L, \quad (1)$$

where  $\mathbf{E}$ ,  $\mathbf{H}$ , and  $\epsilon$  are the electric field, magnetic field, and dielectric constant, respectively. By the single-cell implementation of the lumped device, (1) is converted as follows:

$$E_y^n = E_y^{n-1} + \frac{\Delta t}{\epsilon} (\nabla \times \mathbf{H}^{n-1/2})_y - \frac{\Delta t}{\epsilon \Delta x \Delta z} I_L (V_L)^{n-1/2}, \quad (2)$$

where  $\Delta x$ ,  $\Delta z$ , and  $\Delta t$  show the cell size in  $x$ ,  $z$ , and  $t$  directions, respectively. The superscripts show the temporal positions, by which we represent the alternative evaluations of electrical and magnetic fields in FDTD. Moreover,  $I_L$  and  $V_L$  show the device current and terminal voltage, respectively. The current is assumed to flow in the  $y$  direction and is equal to  $|\mathbf{J}_L| \Delta x \Delta z$ . Moreover,  $V_L$  is given by  $E_y \Delta y$  at the cell corresponding to the device. Thus, (2) becomes

$$E_y^n = E_y^{n-1} + \frac{\Delta t}{\epsilon} (\nabla \times \mathbf{H}^{n-1/2})_y - \frac{\Delta t}{\epsilon \Delta x \Delta z} I_L^{n-1/2} (E_y^n). \quad (3)$$

As mentioned above, the argument of  $I_L$  is evaluated at time  $n$  for numerical stability. When a device occupies  $N$  adjacent cells, the difference equations to be solved become

$$\begin{aligned} E_y^n[i] &= E_y^{n-1}[i] + \frac{\Delta t}{\epsilon} (\nabla \times \mathbf{H}^{n-1/2}[i])_y \\ &\quad - \frac{\Delta t}{\epsilon \Delta x \Delta z} I_L^{n-1/2}(E_y^n[1], E_y^n[2], \dots, E_y^n[N]) \end{aligned} \quad (4)$$

$(i = 1, 2, \dots, N),$

where  $X[i]$  ( $X = E_y, \mathbf{H}$ ) represents the field at the  $i$ th cell occupied by the device.

To solve (4) explicitly, we approximate the voltage dependence of the device current by a piecewise-linear function. The key is the fact that  $E_y^n[i]$  is solved by hand in (4), when

$I_L^{n-1/2}$  is a linear function of the arguments. Setting  $I_j \equiv I_L(V_j)$  for  $M$  different voltages  $V_j$ , ( $j = 1, \dots, M$ ),  $I_L$  is approximated by the following piecewise-linear function:

$$I_L(V) = \frac{I_{j+1} - I_j}{V_{j+1} - V_j} (V - V_j) + I_j, \quad (5)$$

where  $V \in (V_j, V_{j+1})$  for  $j = 1, \dots, M-1$ . Substituting (5) into  $I_L$  in (4) and setting  $V = \Delta y \sum_{k=1}^N E_y^n[k]$ , we obtain

$$E_y^n[i] = E_y^{n-1}[i] + \frac{\Delta t}{\epsilon} (\nabla \times \mathbf{H}^{n-1/2}[i])_y - \alpha_j \sum_{k=1}^N E_y^n[k] - \beta_j, \quad (6)$$

where

$$\begin{aligned} \alpha_j &= \frac{\Delta t \Delta y}{\epsilon \Delta x \Delta z} \frac{I_{j+1} - I_j}{V_{j+1} - V_j}, \\ \beta_j &= \frac{\Delta t}{\epsilon \Delta x \Delta z} \frac{I_j V_{j+1} - I_{j+1} V_j}{V_{j+1} - V_j}. \end{aligned} \quad (7)$$

By straightforward calculations, (6) is solved with respect to  $E_y^n[i]$  to give

$$\mathbf{E}_y^n = \mathbf{A}[j]^{-1} \mathbf{S}[j], \quad (8)$$

$$A[j]_{kl} = \delta_{kl} + \alpha_j, \quad (9)$$

$$S[j]_k = E_y^{n-1}[k] + \frac{\Delta t}{\epsilon} (\nabla \times \mathbf{H}[k])_y - \beta_j, \quad (10)$$

where  $\mathbf{E}_y^n$  shows the column vector  $(E_y^n[1], E_y^n[2], \dots, E_y^n[N])^T$ . Moreover,  $A[j]_{kl}$ , ( $k, l = 1, 2, \dots, N$ ) and  $S[j]_k$ , ( $k = 1, 2, \dots, N$ ) show the  $(k, l)$ th entry of  $\mathbf{A}[j]$  and the  $k$ th component of  $\mathbf{S}[j]$ , respectively. Note that  $\mathbf{A}[j]^{-1}$  is obtained in a closed form as

$$A[j]_{kl}^{-1} = \delta_{kl} - \frac{\alpha_j}{1 + N\alpha_j}. \quad (11)$$

After obtaining  $E_y^n[i]$  using (8), we have to check if the terminal voltage  $V$  is really in the range  $(V_j, V_{j+1})$  with  $V = \Delta y \sum_{i=1}^N E_y^n[i]$ . If not, the procedure is repeated with other  $j$  values, until  $V \in (V_j, V_{j+1})$ . The presented diode model successfully demonstrated the wave properties traveling in an RTD transmission line [8, 9].

## 3. FET Model in FDTD

There are many different equivalent circuits of an FET, depending on the accuracy and the application to use. For clarity, we first consider the simplest representation: an FET is represented only by the drain-source current  $I_{DS}$  as a function of both the gate-source and drain-source voltages. Then, an extended Ampere's law is given by

$$\begin{aligned} E_y^n &= E_y^{n-1} + \frac{\Delta t}{\epsilon} (\nabla \times \mathbf{H}^{n-1/2})_y \\ &\quad - \frac{\Delta t}{\epsilon \Delta x \Delta z} I_{DS}^{n-1/2}(V_{GS}, V_{DS}), \end{aligned} \quad (12)$$

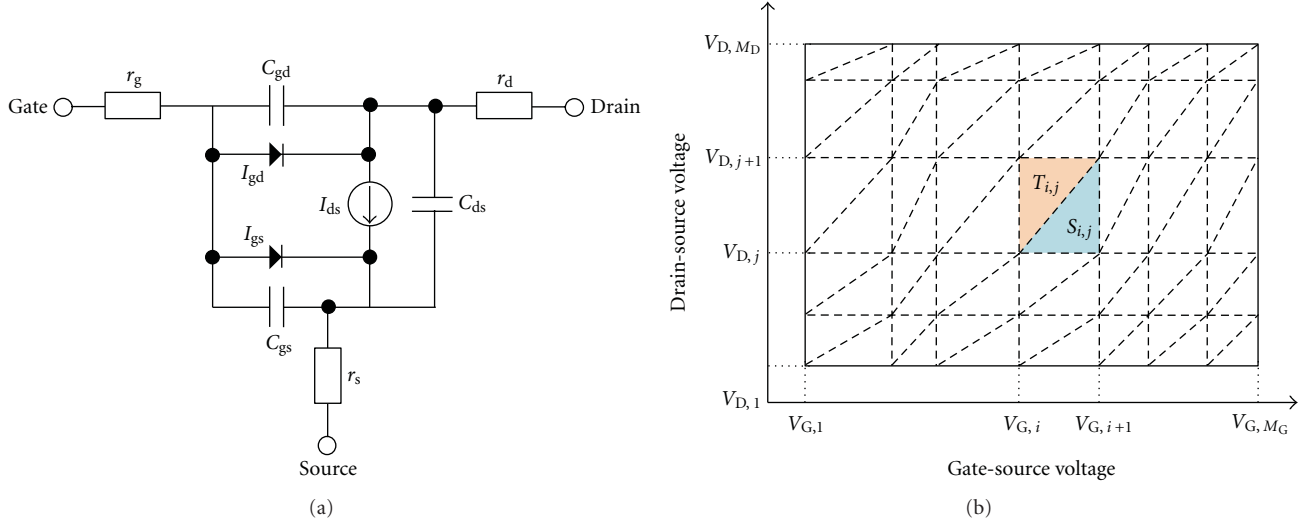


FIGURE 1: FET model in FDTD. (a) The Statz model and (b) A triangulation of  $V_{GS} - V_{DS}$  plane.

where  $V_{GS}$  and  $V_{DS}$  represent the gate-source and drain-source voltages, respectively. Again, the current is assumed to flow in the  $y$  direction. The adjacent  $M_D$  cells are used for calculating  $V_{DS}$ . Moreover, the electrical field components used for  $V_{DS}$  are denoted by  $E_y[1], \dots, E_y[M_D]$ . The difference equations to be solved become

$$E_y^n[i] = E_y^{n-1}[i] + \frac{\Delta t}{\epsilon} (\nabla \times \mathbf{H}^{n-1/2}[i])_y - \frac{\Delta t}{\epsilon \Delta x \Delta z} I_{DS}^{n-1/2} \left( V_{GS}, \Delta y \sum_{k=1}^{M_D} E_y^n[k] \right) \quad (13)$$

( $i = 1, 2, \dots, M_D$ ).

At this point, we approximate the voltage dependence of  $I_{DS}$  by a piecewise-linear function and solve algebraically (13) with respect to  $E_y^n[i]$  ( $i = 1, \dots, M_D$ ). The procedure is similar to the above-mentioned diode case, except that  $V_{GS}$  must be upgraded by corresponding electrical field components at time  $n$ .

Next, we consider more practical FET models shown in Figure 1(a), called the Statz model [10]. The model takes the gate-source, gate-drain currents together with the drain-source current into consideration. Moreover, the parasitic resistances and capacitances are also modeled. The device current-voltage relationships are given by

$$I_G^{n-1/2} = \frac{-r_s(V_{DS}^n - x_{ds}^n) + (r_s + r_d)(V_{GS}^n - x_{gs}^n)}{r_g r_s + r_s r_d + r_d r_g},$$

$$I_D^{n-1/2} = \frac{(r_s + r_g)(V_{DS}^n - x_{ds}^n) - r_s(V_{GS}^n - x_{gs}^n)}{r_g r_s + r_s r_d + r_d r_g}, \quad (14)$$

$$I_S^{n-1/2} = I_G^{n-1/2} + I_D^{n-1/2},$$

where  $I_G$ ,  $I_D$ , and  $I_S$  represent the gate, drain, and source currents, respectively. The auxiliary voltage variables  $x_{gs}$  and

$x_{ds}$  are solved with respect to  $V_{GS}$  and  $V_{DS}$  by the following expressions resulting from Kirchhoff's law:

$$I_S^{n-1/2} = I_{DS}(x_{gs}^n, x_{ds}^n) + C_{DS} \frac{x_{ds}^n - x_{ds}^{n-1}}{\Delta t} + I_{GS}(x_{gs}^n) + C_{GS}(x_{gs}^n) \frac{x_{gs}^n - x_{gs}^{n-1}}{\Delta t},$$

$$I_D^{n-1/2} = I_{DS}(x_{gs}^n, x_{ds}^n) + C_{DS} \frac{x_{ds}^n - x_{ds}^{n-1}}{\Delta t} - I_{GD}(x_{gs}^n, x_{ds}^n) + C_{GD}(x_{gs}^n, x_{ds}^n) \frac{x_{ds}^n - x_{gs}^n - x_{ds}^{n-1} + x_{gs}^{n-1}}{\Delta t}. \quad (15)$$

For definiteness, we assume that the adjacent  $M_G$  cells are used to evaluate  $V_{GS}$  and adjacent  $M_D$  cells are for  $V_{DS}$ . Moreover, the gate and drain currents are assumed to flow the former  $M_G$  and the latter  $M_D$  cells, respectively. Then, we denote the electrical field components used for  $V_{GS}$  as  $E_y[1], \dots, E_y[M_G]$ , and the symbols  $E_y[M_G+1], \dots, E_y[M_G+M_D]$  are reserved for those representing  $V_{DS}$ . The difference equations to be solved become

$$E_y^n[i] = E_y^{n-1}[i] + \frac{\Delta t}{\epsilon} (\nabla \times \mathbf{H}^{n-1/2}[i])_y - \frac{\Delta t}{\epsilon \Delta x \Delta z} I_X^{n-1/2}(V_{GS}, V_{DS}), \quad (16)$$

where  $I_X$  represents  $I_G(I_D)$  for  $i = 1, \dots, M_G$  ( $i = M_G + 1, \dots, M_G + M_D$ ).

To obtain a piecewise-linear function that approximates the device currents, we triangulate the  $V_{GS} - V_{DS}$  plane. For the present device currents, a simple triangulation shown in Figure 1(b) suffices. Setting  $I_{G(D),i,j} \equiv I_{G(D)}(V_{GS,i}, V_{DS,j})$  for

$M_G \times M_D$  different voltages ( $V_{GS,i}, V_{DS,j}$ ), ( $i = 1, \dots, M_G, j = 1, \dots, M_D$ ),  $I_X$  ( $X = G, D$ ) is approximated by the following piecewise-linear function for  $(V_{GS}, V_{DS}) \in S_{i,j}$  in Figure 1(b):

$$\begin{aligned} I_X(V_{GS}, V_{DS}) &= \frac{I_{X,i+1,j} - I_{X,i,j}}{V_{GS,i+1} - V_{GS,i}} (V_{GS} - V_{GS,i}) \\ &+ \frac{I_{X,i,j+1} - I_{X,i,j}}{V_{DS,j+1} - V_{DS,j}} (V_{DS} - V_{DS,j}) \quad (17) \\ &+ I_{X,i,j+1}. \end{aligned}$$

On the other hand, for  $(V_{GS}, V_{DS}) \in T_{i,j}$  in Figure 1(b), it is

$$\begin{aligned} I_X(V_{GS}, V_{DS}) &= \frac{I_{X,i+1,j} - I_{X,i,j}}{V_{GS,i+1} - V_{GS,i}} (V_{GS} - V_{GS,i+1}) \\ &+ \frac{I_{X,i,j+1} - I_{X,i,j}}{V_{DS,j+1} - V_{DS,j}} (V_{DS} - V_{DS,j}) + I_{X,i+1,j}. \quad (18) \end{aligned}$$

Hereafter, we denote the piecewise-linear counterparts of  $I_{D(G)}$  as  $I_{D(G)} = a_{D(G),ij} V_{GS} + b_{D(G),ij} V_{DS} + c_{D(G),ij}$  for convenience. Substituting them into  $I_{D,G}$  in (16), we obtain

$$\begin{aligned} E_y^n[i] &= E_y^{n-1}[i] + \frac{\Delta t}{\epsilon} (\nabla \times \mathbf{H}^{n-1/2}[i])_y - \frac{\Delta t}{\epsilon \Delta x \Delta z} \\ &\times \left( a_{X,jk} \Delta y \sum_{l=1}^{M_G} E_y^n[l] + b_{X,jk} \Delta y \sum_{l=M_G+1}^{M_G+M_D} E_y^n[l] + c_{X,jk} \right), \quad (19) \end{aligned}$$

where  $X$  has to set to  $G$  and  $D$  for  $i = [1, \dots, M_G]$  and  $i = M_G + 1, \dots, M_G + M_D$ , respectively.

We again obtain the column vector  $\mathbf{E}_y^n = (E_y^n[1], \dots, E_y^n[M_G], E_y^n[M_G+1], \dots, E_y^n[M_G+M_D])^T$  in the form of  $\mathbf{E}_y^n = \mathbf{A}[jk]^{-1} \mathbf{S}[jk]$ . The  $l$ th component of  $\mathbf{S}[jk]$  is given by

$$S[jk]_l = E_y^{n-1}[l] + \frac{\Delta t}{\epsilon} (\nabla \times \mathbf{H}[l])_y - \gamma_{X,jk}, \quad (20)$$

where  $\gamma_{X,jk}$  represents  $c_{G,jk} \Delta t / \epsilon \Delta x \Delta z$  for  $i = 1, \dots, M_G$ , and  $c_{D,jk} \Delta t / \epsilon \Delta x \Delta z$  for  $i = M_G + 1, \dots, M_G + M_D$ . Moreover, the matrix  $\mathbf{A}[jk]$  is given by

$$\begin{aligned} A[jk]_{lm} &= \begin{cases} \delta_{lm} + \alpha_{G,jk}, & (l, m) \in [1, M_G], \\ \delta_{lm} + \beta_{D,jk}, & (l, m) \in [M_G + 1, M_G + M_D], \\ \beta_{G,jk}, & l \in [1, M_G], m \in [M_G + 1, M_G + M_D], \\ \alpha_{D,jk}, & l \in [M_G + 1, M_G + M_D], m \in [1, M_G], \end{cases} \quad (21) \end{aligned}$$

where  $\alpha_{G,D,jk} \equiv a_{G,D,jk} \Delta t \Delta y / \epsilon \Delta x \Delta z$  and  $\beta_{G,D,jk} \equiv b_{G,D,jk} \Delta t \Delta y / \epsilon \Delta x \Delta z$ . For the present case,  $\mathbf{A}[jk]^{-1}$  is explicitly given as

$$h_{lm} \mathbf{A}[jk]_{lm}^{-1} = \begin{cases} \left[ (1 + M_D \beta_{D,jk}) (1 + M_G \alpha_{G,jk}) - M_G M_D \alpha_{D,jk} \beta_{G,jk} \right] \delta_{lm} \\ \quad - (1 + M_D \beta_{D,jk}) \alpha_{G,jk} + M_D \beta_{G,jk} \alpha_{D,jk}, & (l, m) \in [1, M_G], \\ \left[ (1 + M_D \beta_{D,jk}) (1 + M_G \alpha_{G,jk}) - M_G M_D \alpha_{D,jk} \beta_{G,jk} \right] \delta_{lm} \\ \quad - (1 + M_G \alpha_{G,jk}) \beta_{D,jk} + M_G \alpha_{D,jk} \beta_{G,jk}, & (l, m) \in [M_G + 1, M_G + M_D], \\ -\beta_{G,jk}, & l \in [1, M_G], m \in [M_G + 1, M_G + M_D], \\ -\alpha_{D,jk}, & l \in [M_G + 1, M_G + M_D], m \in [1, M_G], \end{cases} \quad (22)$$

where  $h_{lm} = (1 + M_D \beta_{D,lm}) (1 + M_G \alpha_{G,lm}) - M_G M_D \beta_{G,lm} \alpha_{D,lm}$ . After obtaining  $E_y^n[i]$ , we have to check if the terminal voltages  $V_{GS}$  and  $V_{DS}$  are really in the range we presume. Otherwise, the procedure is repeated with coefficients corresponding to another triangularized regions in  $V_{GS} - V_{DS}$  plane. Moreover, when the device model includes capacitors such as  $C_{GS}$  and  $C_{GD}$ , these terminal voltages must be recorded, which are required for evaluating  $x_{ds}^{n-1}$  and  $x_{gs}^{n-1}$  in (15).

In the following, we demonstrate the pulse shortening in TWFETs by FDTD calculations. Although the line structure we set up is rather impractical, we successfully observed

the shortening of the pulse traveling along a TWFET. It is observed, only when the nonlinear operations of a large amount of FETs are properly simulated. We thus believe that this example calculation clarifies the validity of our models. Before showing calculation results, we briefly review the mechanism of the pulse shortening in TWFETs.

#### 4. Pulse Shortening in TWFETs

Figure 2(a) shows the equivalent representation of a TWFET. One end of each electrode line labeled as  $V_{gin}(V_{din})$  is for signal applications. Figure 2(b) shows the required pulse

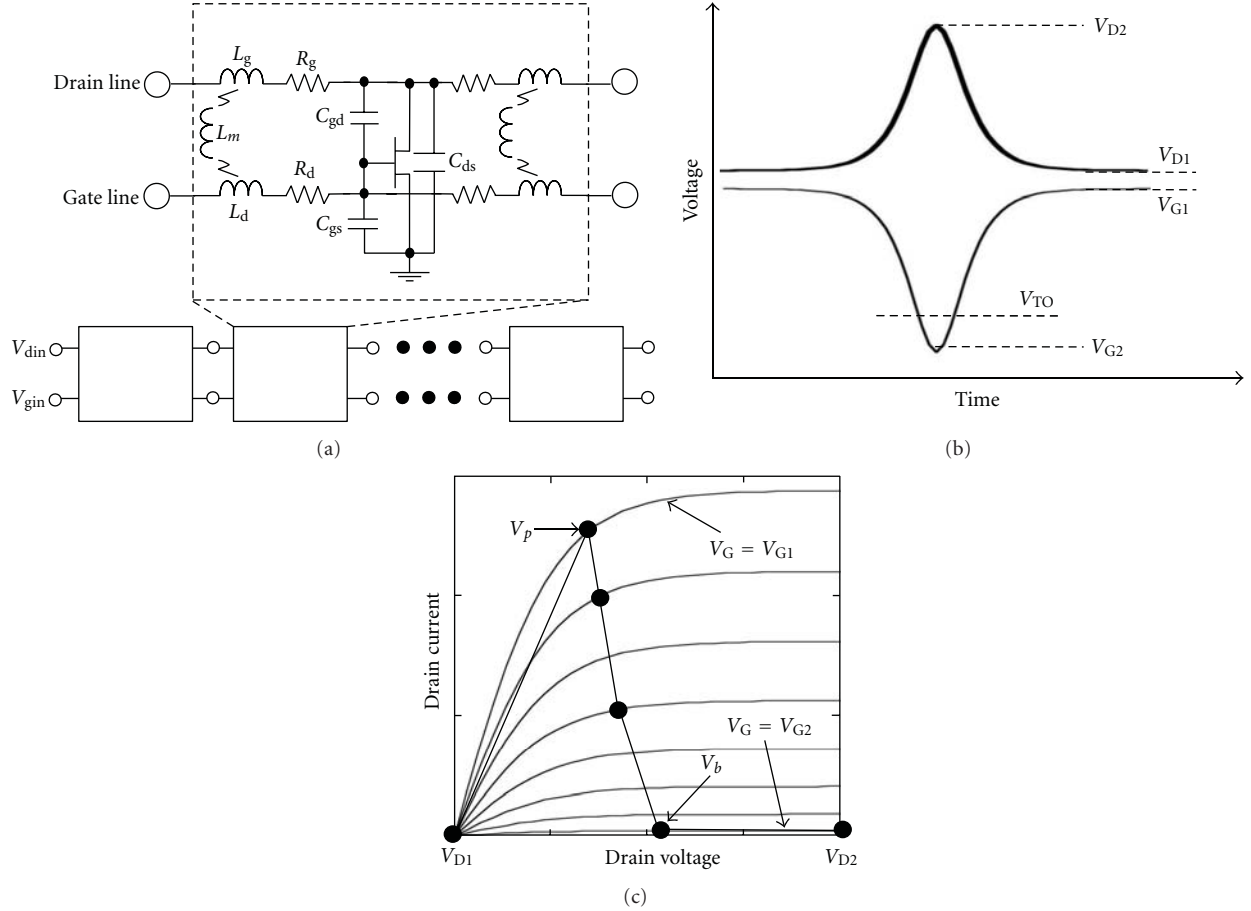


FIGURE 2: Setup of TWFETs for shortening traveling pulses. (a) A representation of a TWFET, (b) the signal application to a TWFET and (c) the equivalent current-voltage relationship of an FET for a pulse traveling in the drain line.

shapes applied at  $V_{\text{gin}}(V_{\text{din}})$ . The voltages biasing the gate and drain lines are denoted by  $V_{G1}$  and  $V_{D1}$ , respectively. The drain pulse has the opposite parity to the gate pulse. Moreover, the top and bottom voltage levels of the drain (gate) pulse are set to  $V_{D2}$  ( $V_{G1}$ ) and  $V_{D1}$  ( $V_{G2}$ ), respectively. At this point,  $V_{G2}$  is set below the FET threshold voltage  $V_{TO}$ , and both of  $V_{D1}$  and  $V_{G1}$  are set to approximately 0 V. The thin curves in Figure 2(c) show the drain current-voltage relationships for several different gate bias voltages. The uppermost and lowermost curves correspond to the relationships for  $V_{G1}$  and  $V_{G2}$ , respectively. Because of the presence of electromagnetic couplings between the gate and drain lines, two different propagation modes, called the  $c$  mode and the  $\pi$  mode [11], are developed on a TWFET. We can design a TWFET to amplify only the pulses carried by one of the two modes and attenuate the pulses carried by the other mode [4]. The conditions are given by simple inequalities using three variables  $u_s$ ,  $u_c$ , and  $u_\pi$  defined as

$$u_s = \sqrt{\frac{L_m}{C_{gd}(L_g L_d - L_m^2)}}$$

$$u_{c,\pi} = \sqrt{\frac{X_1 \pm \sqrt{X_1^2 - 2X_2}}{X_2}}, \quad (23)$$

where the upper (lower) signs are for  $c$  ( $\pi$ ) mode. Moreover, we used two variables  $X_{1,2}$  for brevity:  $X_1 = C_{gs}L_g + C_{ds}L_d + C_{gd}(L_g + L_d) - 2C_{gd}L_m$  and  $X_2 = 2(C_{gs}C_{ds} + C_{gs}C_{gd} + C_{ds}C_{gd})(L_g L_d - L_m^2)$ . It is then found that the  $c$ -mode pulse is generically amplified when  $u_s > u_c$ , while the  $\pi$ -mode pulse is amplified when  $u_s < u_\pi$ . Because  $u_c$  is always greater than  $u_\pi$ , we can see that when the characteristic velocity  $u_s$  is less than both  $u_c$  and  $u_\pi$ , the slower mode is the unique amplified mode; in contrast, when  $u_s$  is greater than both  $u_c$  and  $u_\pi$ , the faster mode is the unique amplified mode.

When the TWFET succeeds in amplifying the unique mode, we can assume the simultaneous propagation of the leading edges of the gate and drain pulses. At this point, every FET operates as an electronic switch that is open for  $V_{\text{din}} > V_b$ , and closed for  $V_{\text{din}} < V_p$  as shown in Figure 2(c). As a result, the pulse is influenced by finite shunt conductance for voltages less than  $V_p$  and is otherwise loss-free. Owing to this nonlinearity, a short-wavelength sinusoidal wave supported

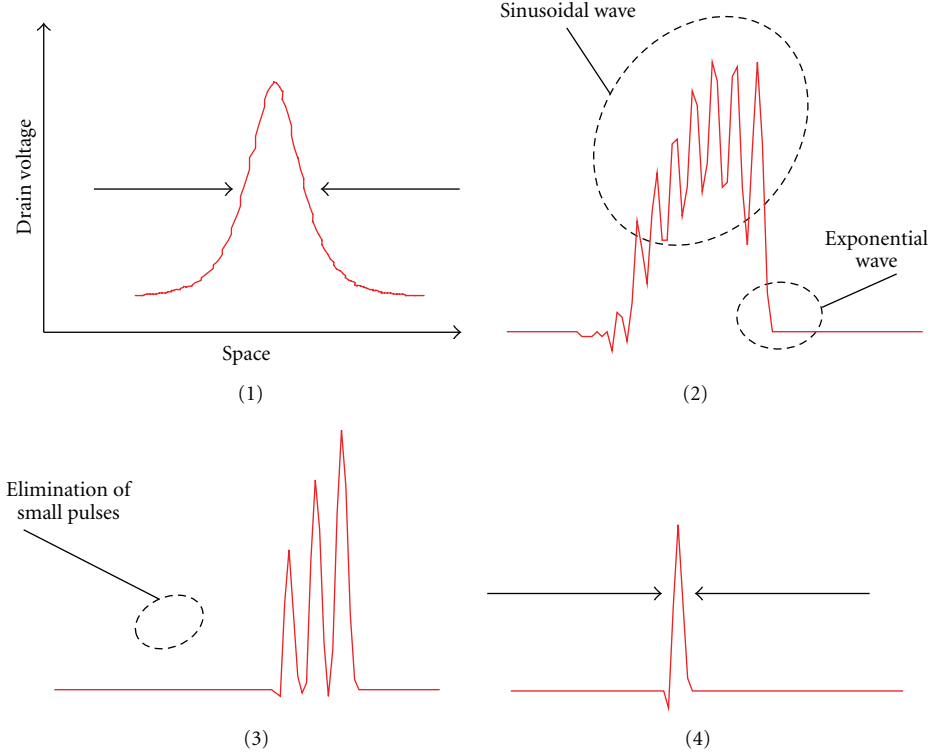


FIGURE 3: Operation principle of pulse shortening in TWFETs.

by an exponential edge develops [4]. Figure 3 schematically explains the mechanism of pulse-shortening phenomena. When a pulse of width  $l_{init}$  is input to the drain line ((1) of Figure 3), the above-mentioned short-wavelength sinusoidal wave is shown in (2). Because the drain line attenuates voltage waves only below  $V_p$ , the small-amplitude parts of the wave disappear with the shorter propagation than the large-amplitude ones ((3) in Figure 3). Finally, a short pulse is obtained at the output ((4) in Figure 3).

## 5. Demonstration of Pulse Shortening in TWFETs

Three-dimensional FDTD calculations were carried out for demonstrating nonlinear pulse propagation along a TWFET. The total number of cells was  $400 \times 150 \times 100$ . The spatial increments in the  $x$ ,  $y$ , and  $z$  orientations were set to 10, 2, and  $10 \mu\text{m}$ , respectively. The calculation setup is illustrated in Figure 4(a). The gate and drain lines were aligned in the  $x$  direction. At one of the ends of the lines, the inputs were applied with the hyperbolic secant pulses with the opposite parity. To maximize the coupling between the gate and drain lines, the spacing between two lines was set small and no ground plane was placed except the source. The dielectric constant of the substrate was set to 13.6. Moreover, a Mur's 2nd-order absorbing boundary condition (ABC) was employed. FETs are placed every  $30 \mu\text{m}$  along the electrode

lines, whose widths were all set to  $10 \mu\text{m}$ . Each FET was modeled as the drain-source current  $I_{DS}$ :

$$I_{DS}(V_{GS}, V_{DS}) = \begin{cases} \beta(V_{GS} - V_{TO})^2 \tanh(\alpha V_{DS}), & V_{GS} > V_{TO}, \\ 0, & V_{GS} < V_{TO}, \end{cases} \quad (24)$$

where we set  $\beta$ ,  $V_{TO}$ , and  $\alpha$  to  $20.0 \text{ mA/V}^2$ ,  $-1.0 \text{ V}$ , and  $2.0 \text{ V}^{-1}$ , respectively. We ignore the influences caused by the gate-source current with the parasitic capacitors and resistors for clear observations of the nonlinear properties of a TWFET. We modeled  $I_{DS}$  as a piecewise-linear function with respect to  $V_{DS}$  with 2000 segments. The cross-section of electrodes is shown in Figure 4(b). For  $V_{GS}$ , we summed up the  $y$  components of the electrical fields of the nine subsequent cells connecting the gate line and the source (the cells labeled by "G" in Figure 4(b)). Similarly, neighboring fifteen cells were used for evaluating  $V_{DS}$  (the cells labeled by "D" in Figure 4(b)).

To obtain a rough estimation of the model TWFET, we carried out the quasi-TEM analysis [11]. The  $2 \times 2$  capacitance matrix  $\mathbf{C}$  and inductance matrix  $\mathbf{L}$  are obtained by the numerical estimation of electrical charges stored in the electrode lines. By solving the Poisson equation for the case where  $V_{GS}$  and  $V_{DS}$  are set to 1.0 and 0.0 V, respectively,

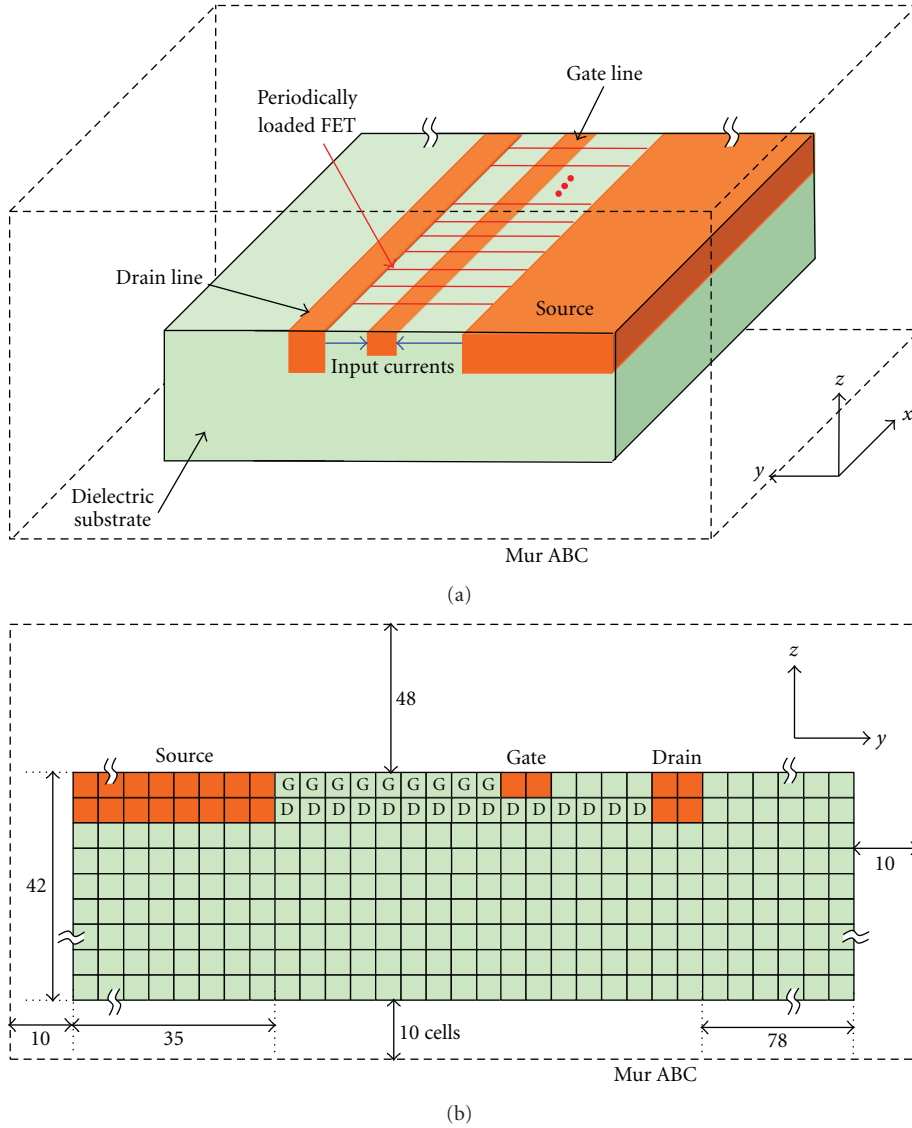


FIGURE 4: Setup of FDTD calculations. (a) The longitudinal and (b) the transverse structure of the calculated TW-FET.

TABLE 1: Line parameters of test TW-FET.

$C_{gs}$	0.10 pF/mm	$L_g$	0.73 nH/mm
$C_{gd}$	0.17 pF/mm	$L_d$	0.70 nH/mm
$C_{ds}$	0.09 pF/mm	$L_m$	0.42 nH/mm

we can obtain the electrical charges stored in the gate and drain lines:  $Q_{11}$  and  $Q_{21}$ . Those for the case where  $V_{GS}$  and  $V_{DS}$  are, respectively, set to 0.0 and 1.0 V, called  $Q_{12}$  and  $Q_{22}$  are similarly obtained. Then, the  $2 \times 2$  matrix  $\mathbf{Q}$ , whose components are given by  $Q_{ij}$  ( $i, j = 1, 2$ ), gives  $\mathbf{C}$ . On the other hand, we consider the case where the electrodes are in vacuum; that is, the dielectric constant of each cell is set to unity for  $\mathbf{L}$ . To obtain  $\mathbf{L}$ , it is required to evaluate the capacitance matrix  $\mathbf{C}_0$  in vacuum by the same procedure as obtained  $\mathbf{C}$ , because  $\mathbf{L}$  has to be equal to  $c^{-2}\mathbf{C}_0^{-1}$  ( $c$ : the light

velocity). As a result, we obtain the line parameters as listed in Table 1. Using them,  $u_\pi$  and  $u_c$  are calculated to be  $0.29c$  and  $0.32c$ , respectively. Moreover,  $u_s$  satisfies the condition,  $u_s < u_\pi$ , so that the  $\pi$ -mode pulse is expected to be uniquely amplified; therefore, the pulse shortening can be observed in the one carried by the slower  $\pi$  mode. The black curves in Figure 5 show the results from numerical integration of the transmission equations of a TW-FET using the parameters listed in Table 1. Hyperbolic secant waveforms shown in Figure 5(a) are applied. The temporal waveforms monitored at five different FET cells, each separated by twelve FET cells, are shown. The thin and thick waveforms represent the pulse on the gate and drain lines, respectively. Because the discrepancy between the  $c$ - and  $\pi$ -mode velocities is small, the pulse carried by the  $\pi$  mode is still overlapped with that carried by the  $c$  mode even in Figure 5(f). However, it is observed that the pulse carried by the slower mode

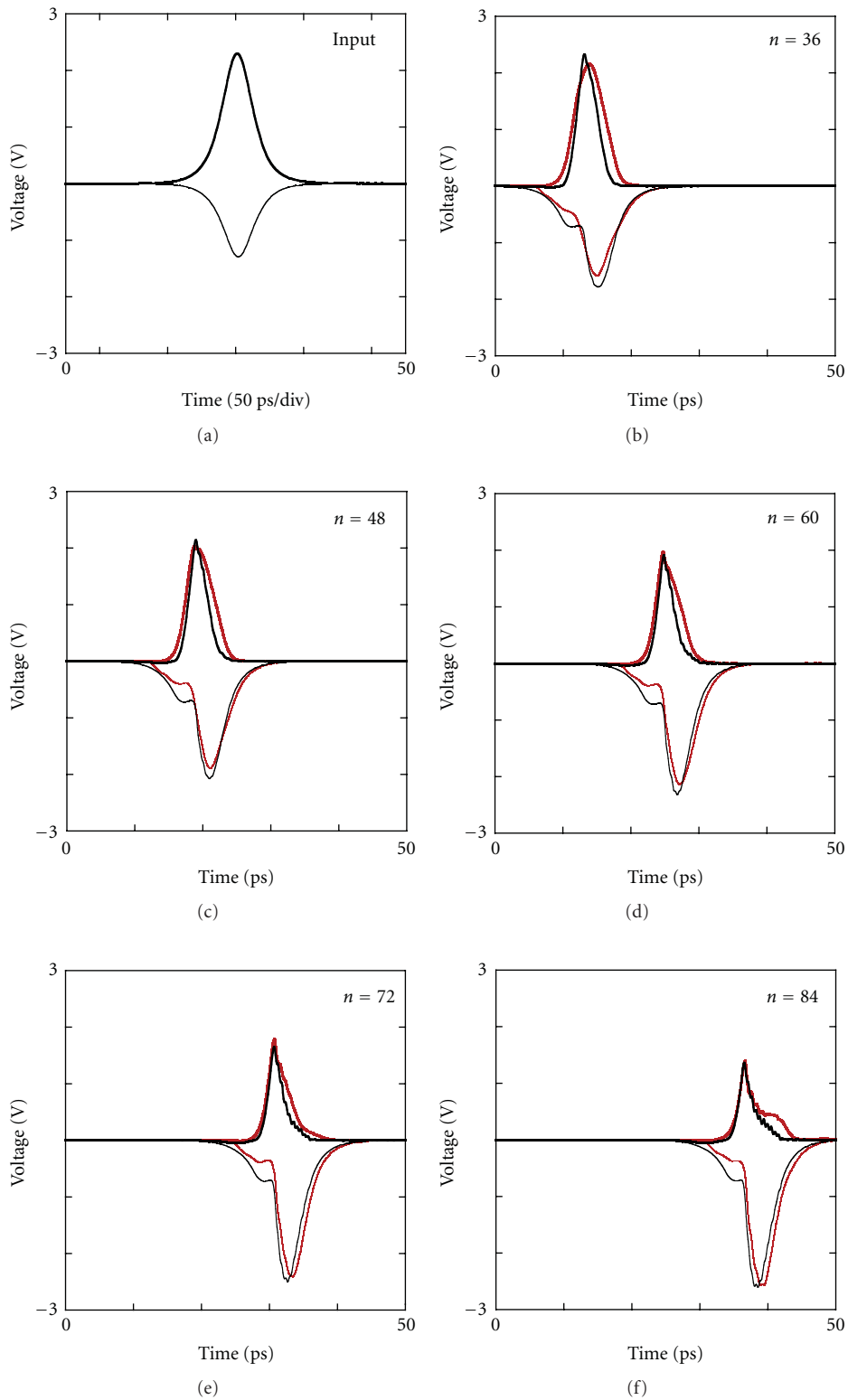


FIGURE 5: Wave propagation on test TWFE. The waveforms on the gate and drain lines are shown by the thin and thick curves, respectively. The black and red curves correspond to the quasi-TEM and FDTD calculations, respectively. (a) shows the input waveforms. Waveforms recorded at the  $n$ th FET cell are shown. (b), (c), (d), (e), and (f) represent the waveforms at  $n = 36, 48, 60, 72,$  and  $84$ , respectively.

experiences shortening. On the other hand, the results from FDTD calculations are shown by the red curves in Figure 5. Five temporal waveforms are plotted and recorded at  $480\ \mu\text{m}$  intervals along the line in Figures 5(b)–5(f). Qualitatively, the waveform transients have good resemblance with those obtained by quasi-TEM calculations. The steep exponential edge is developed and the pulse starts to exhibit an oscillatory behavior and then is shortened. We have found that even a TWFET with practical FET properties succeeds in pulse shortening in the framework of the transmission line theory. Moreover, we experimentally confirmed the pulse shortening using actual FETs at low frequencies [12]. We believe that the FDTD calculations may contribute to the design of the monolithically integrated TWFETs as pulse compressor, when they are solved with a practical FET model.

## 6. Conclusions

We demonstrated full-wave calculations that illustrate the pulse propagation characteristics of a TWFET. The pulse shortening in a TWFET was properly observed in the full-wave calculations. By using piecewise-linear modeling, FETs were characterized in FDTD without significant computational costs.

## References

- [1] M. J. W. Rodwell, S. T. Allen, R. Y. Yu et al., "Active and non-linear wave propagation devices in ultrafast electronics and optoelectronics," *Proceedings of the IEEE*, vol. 82, no. 7, pp. 1037–1059, 1994.
- [2] K. Narahara and A. Yokota, "Experimental characterization of short-pulse generation using switch lines," *IEICE Electronics Express*, vol. 5, no. 22, pp. 973–977, 2008.
- [3] G. W. McIver, "A traveling-wave transistor," *Proceedings of the IEEE*, vol. 53, no. 11, pp. 1747–1748, 1965.
- [4] K. Narahara, "Characterization of short-pulse generation using traveling-wave field-effect transistors," *Japanese Journal of Applied Physics*, vol. 50, pp. 014104–014109, 2011.
- [5] A. Taflov, *Computational Electrodynamics the Finite-Difference Time-Domain Method*, Artech House, London, UK, 1995.
- [6] K. S. Yee, "Numerical solution of initial boundary value problems involving Maxwell's equations in isotropic media," *IEEE Transactions on Antennas and Propagation*, vol. 14, pp. 302–307, 1966.
- [7] R. Luebbers, J. Beggs, and K. Chamberlin, "Finite difference time-domain calculation of transients in antennas with non-linear loads," *IEEE Transactions on Antennas and Propagation*, vol. 41, no. 5, pp. 566–573, 1993.
- [8] K. Narahara and A. Yokota, "Full-wave analysis of quasi-steady propagation along transmission lines periodically loaded with resonant tunneling diodes," *Japanese Journal of Applied Physics*, vol. 47, no. 2, pp. 1126–1129, 2008.
- [9] K. Narahara, "Nonlinear waves in transmission lines periodically loaded with tunneling diodes," in *Wave Propagation in Materials for Modern Applications*, pp. 437–454, InTech, Olajnica, Poland, 2010.
- [10] H. Statz, P. Newman, I. W. Smith, R. A. Pucel, and H. A. Haus, "GaAs FET device and circuit simulation in SPICE," *IEEE Transactions on Electron Devices*, vol. 34, no. 2, pp. 160–169, 1987.
- [11] K. C. Gupta, R. Garg, and I. J. Bahl, *Microstrip Lines and Slotlines*, Artech House, Norwood, Mass, USA, 1979.
- [12] K. Narahara, "Experimental observation of pulse-shortening phenomena in traveling-wave field effect transistors," *Progress In Electromagnetics Research Letters*, vol. 21, pp. 79–88, 2011.

## Research Article

# RCS Computation by Parallel MoM Using Higher-Order Basis Functions

Ying Yan,<sup>1</sup> Yu Zhang,<sup>1</sup> Chang-Hong Liang,<sup>1</sup> Hui Zhao,<sup>2</sup> and D. García-Doñoro<sup>3</sup>

<sup>1</sup> School of Electronic Engineering, Xidian University, Xi'an, Shaanxi 710071, China

<sup>2</sup> Department of Aerial Platform System, China Academy of Electronics and Information Technology, Beijing 100041, China

<sup>3</sup> Department of Signal Theory and Communications, University Carlos III of Madrid, 28911 Leganés, Spain

Correspondence should be addressed to Ying Yan, yymqn1008@163.com

Received 14 June 2011; Accepted 24 September 2011

Academic Editor: Ning Yuan

Copyright © 2012 Ying Yan et al. This is an open access article distributed under the Creative Commons Attribution License, which permits unrestricted use, distribution, and reproduction in any medium, provided the original work is properly cited.

A Message-Passing Interface (MPI) parallel implementation of an integral equation solver that uses the Method of Moments (MoM) with higher-order basis functions has been proposed to compute the Radar Cross-Section (RCS) of various targets. The block-partitioned scheme for the large dense MoM matrix is designed to achieve excellent load balance and high parallel efficiency. Some numerical results demonstrate that higher-order basis in this parallelized scheme is more efficient than the conventional RWG method and able to efficiently analyze RCS of various electrically large platforms.

## 1. Introduction

Radar Cross-Section (RCS) computation of electrically large platforms has attracted a great deal of attention in the past few decades. One traditional and widely adopted method is the method of moments (MoM) [1]. However, when the operating frequency is high, the MoM method based on the Rao-Wilton-Glisson basis functions (RWGs) [2, 3] produces a very large number of unknowns for electrically large structures. To reduce the number of unknowns and to accelerate the computation, the fast multipole method (FMM) is a feasible approach. Although this technique can achieve our goal to some extent, there may be a problem of convergence when the model to be simulated is complex. Another choice is to use higher-order polynomials over wires and quadrilateral plates as basis functions over larger subdomain patches [4, 5]. The use of higher-order basis functions significantly reduces the number of unknowns. However, it is necessary to state that higher-order basis is suitable for large smooth structure but not very beneficial for detailed structure. In addition, to reduce the total wall clock time, the large dense MoM matrix is divided into a number of small block matrices that are nearly equal in size and distributed among all the available processes in the parallel method.

In this paper, the parallel in-core MoM solver combined with the higher-order polynomial basis functions (HOBs) is employed on high-performance clusters so that the capability of the MoM method has been significantly improved. This technique is capable of solving electrically large scattering problems [3, 5, 6] of several hundred wavelengths in the maximum dimension.

In Section 2 of this paper, the basic theory of higher-order basis function and the matrix partition scheme are listed respectively; And then the computation platforms are described in Section 3; Section 4 lists some numerical examples to validate the accuracy, efficiency, and application of this paper's method: Section 4.1 demonstrates the convergence of the higher-order basis MoM method; Section 4.2.1 validates the accuracy of this paper's method through the comparison with measurement results; Section 4.2.2 demonstrates that higher-order bases are able to significantly reduce the number of unknowns and can effectively shorten the computation time; Section 4.3 checks the parallel efficiency of the parallel scheme used in this paper. Finally, Section 4.4 illustrates a real-life problem of the RCS computation of a missile whose maximum electrical dimension is bigger than one hundred wavelengths. Finally, Section 5 presents the conclusions and the acknowledgements follow, respectively.

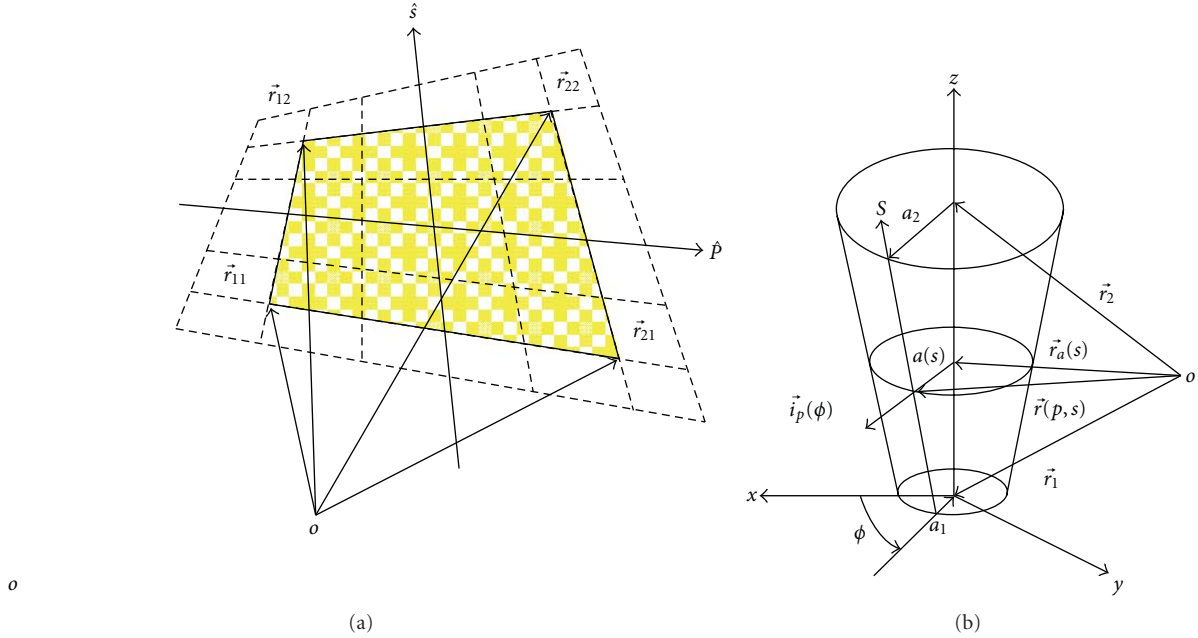


FIGURE 1: Geometric model: (a) a bilinear surface defined by four vertices; (b) a right-truncated cone defined by position vectors and radii of its beginning and end.

## 2. Basic Theory

**2.1. Higher-order Basis Functions.** Flexible geometric modeling can be achieved by using truncated cones for wires and bilinear patches to characterize surfaces [4]. The surface current over a bilinear surface is decomposed into its  $p$  and  $s$ -components, as shown in Figure 1(a). However, the  $p$ -current component can be treated as the  $s$ -current component defined over the same bilinear surface with an interchange of the  $p$  and  $s$  coordinates. The approximations for the  $s$ -components of the electric and magnetic currents over a bilinear surface are typically defined by

$$\vec{J}_s(p, s) = \sum_{i=0}^{N_p} \left[ c_{i1} \vec{E}_i(p, s) + c_{i2} \vec{E}_i(p, -s) + \sum_{j=2}^{N_s} a_{ij} \vec{P}_{ij}(p, s) \right], \quad (1)$$

where  $c_{i1}, c_{i2}, (i = 0, 1, \dots, N_p)$  are defined as

$$c_{i1} = \sum_{j=0}^{N_s} a_{ij} (-1)^j, \quad c_{i2} = \sum_{j=0}^{N_s} a_{ij}. \quad (2)$$

The edge basis functions  $\vec{E}_i(p, s)$  and the patch basis functions  $\vec{P}_{ij}(p, s)$  ( $i = 0, \dots, N_p, j = 2, \dots, N_s$ ) are expressed by (3) and (4), respectively,

$$\vec{E}_i(p, s) = \frac{\vec{\alpha}_s}{|\vec{\alpha}_p \times \vec{\alpha}_s|} p^i \vec{N}(s), \quad (3)$$

$$\vec{P}_{ij}(p, s) = \frac{\vec{\alpha}_s}{|\vec{\alpha}_p \times \vec{\alpha}_s|} p^i \vec{S}_j(s), \quad (4)$$

where  $\vec{\alpha}_p, \vec{\alpha}_s$  are the unitary vectors defined as

$$\vec{\alpha}_p = \frac{\partial \vec{r}(p, s)}{\partial p}, \quad \vec{\alpha}_s = \frac{\partial \vec{r}(p, s)}{\partial s}. \quad (5)$$

The parametric equation of such an isoparametric element can be written in the following form:

$$\begin{aligned} \vec{r}(p, s) = & \vec{r}_{11} \frac{(1-p)(1-s)}{4} + \vec{r}_{12} \frac{(1-p)(1+s)}{4} \\ & + \vec{r}_{21} \frac{(1+p)(1-s)}{4} + \vec{r}_{22} \frac{(1+p)(1+s)}{4}, \quad (6) \\ & -1 \leq p \leq 1, \quad -1 \leq s \leq 1, \end{aligned}$$

where  $\vec{r}_{11}, \vec{r}_{12}, \vec{r}_{21}, \vec{r}_{22}$  are the position vectors of its vertices and the  $p$  and  $s$  are the local coordinates.

A right-truncated cone is determined by the position vectors and the radii of its beginning and its end,  $\vec{r}_1, a_1, \vec{r}_2, a_2$ , respectively, as shown in Figure 1(b). Generalized wires (i.e., wires that have a curvilinear axis and a variable radius) can be approximated by right-truncated cones.

Currents along wires are approximated by polynomials and can be written as

$$I(s) = I_1 N(s) + I_2 N(-s) + \sum_{i=2}^{N_s} a_i S_i(s), \quad -1 \leq s \leq 1, \quad (7)$$

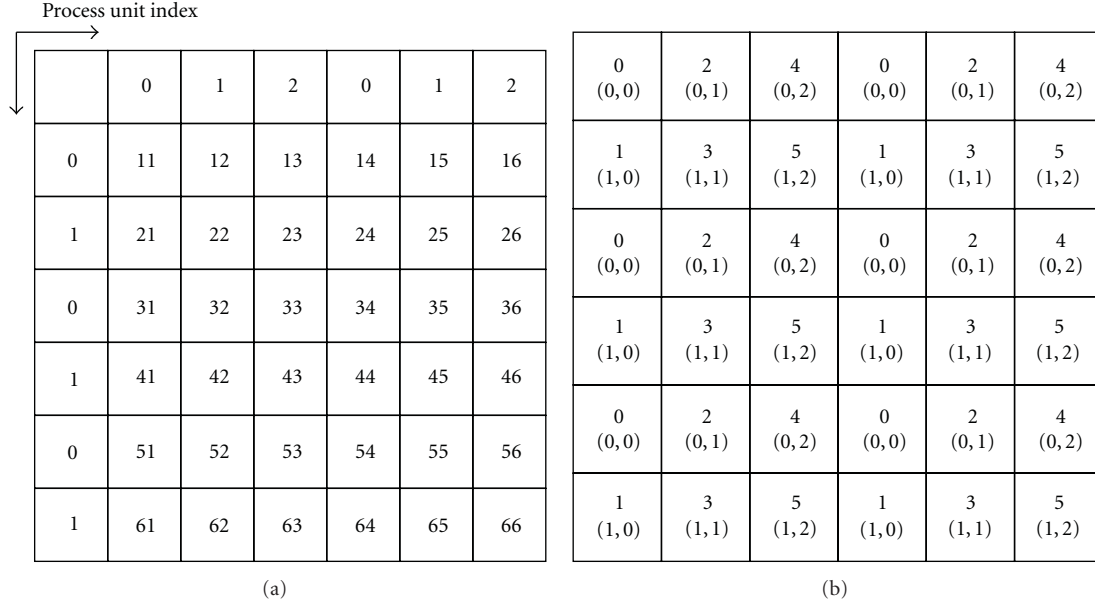


FIGURE 2: Block-cyclic distribution of a matrix [4]: (a) a matrix consisting of  $6 \times 6$  blocks; (b) rank and coordinates of each process owning the corresponding blocks in (a).

where node basis functions,  $N(s)$ , and segment basis functions,  $S_i(s)$ , are expressed as

$$N(s) = \frac{1-s}{2}$$

$$S_i(s) = s^i - 1, \quad i \text{ is even} \quad (8)$$

$$S_i(s) = s^i - 1, \quad i \text{ is odd,}$$

respectively, and where  $a_i$ , ( $i = 2, \dots, N_s$ ) are the coefficients, and  $I_1 = I(-1)$ ,  $I_2 = I(1)$  are the values of the currents at the wire ends, respectively.

The parametric equation of the cone surface can be written as

$$\vec{r}_a(\phi, s) = \vec{r}_a(s) + a(s)\vec{i}_\rho(\phi), \quad -1 \leq s \leq 1, \quad -\pi \leq \phi \leq \pi, \quad (9)$$

where  $\phi$  is the circumferential angle, measured from the  $x$ -axis, and  $\vec{i}_\rho(\phi)$  is the radial unit vector, perpendicular to the cone axis.

**2.2. The Matrix Partition Scheme.** Assume that the matrix  $A$  is a large dense matrix, it can be divided into smaller blocks and distributed to each process grid [6]. For explanation purposes, the MoM matrix equation is rewritten in a general form as

$$AX = B, \quad (10)$$

where  $A$  denotes the complex dense matrix,  $X$  is the unknown vector to be determined, and  $B$  denotes the given source vector.

Assume that the matrix  $A$  is divided into  $6 \times 6$  blocks, which are distributed to 6 processes in a  $2 \times 3$  process

grid, as illustrated in Figure 2(a). Figure 2(b) shows to which process the blocks of  $A$  are distributed using ScaLAPACK's distribution methodology.

In Figure 2(a), the outermost numbers denote the row and column indices of the process coordinates. The top and bottom indices of any block of Figure 2(b) denote the process rank and the process coordinate of a certain process, respectively, corresponding to the block of the matrix shown in Figure 2(a). By varying the dimensions of the blocks of  $A$  and those of the process grid, different mappings can be obtained. This scheme can be referred to as a block-cyclic distribution procedure.

Load balancing is critical to obtain an efficient operation of a parallel code. This parallel scheme is able to achieve the good load balancing. Little communication between processes is necessary during the matrix filling process [4].

Also, it is necessary to mention that the degree of higher-order basis is confirmed by the maximum length of edge of the corresponding plate. And the same load-balancing scheme is used no matter what the order of basis function is.

### 3. Description of the Computation Platforms

To illustrate the versatility of the solver, two representative computer platforms have been chosen.

- (1) Personal computer: Quad core Intel I5 processor (2.67 GHz) with 4 GB RAM and 500 GB of hard disk.
- (2) Shanghai supercomputer center (SSC): the 37 nodes from Magic-cube Machine with a total of 592 AMD CPU cores (1.9 GHz per CPU and 4 cores on each CPU): 16 CPU cores on each node and 4 GB RAM per core, and a total amount of RAM approximately

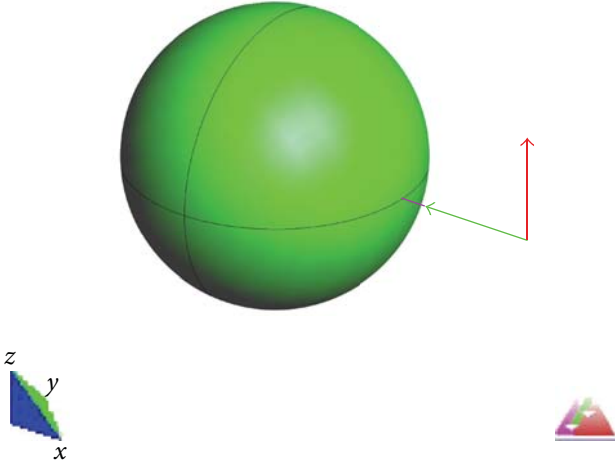


FIGURE 3: PEC sphere with the radius of 1.0 meter.

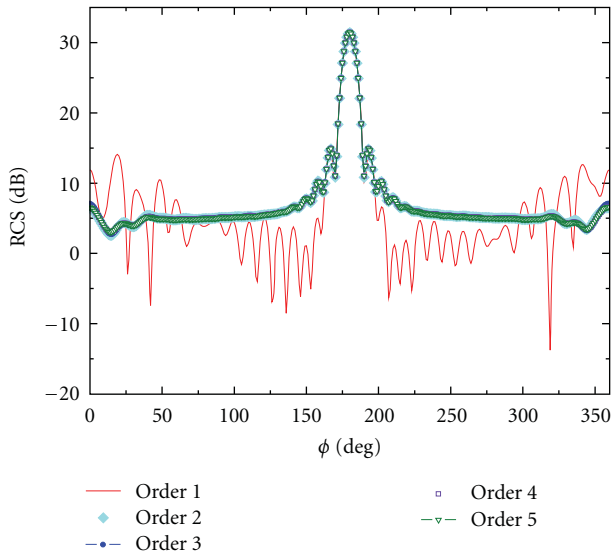


FIGURE 4: Comparison of the results with different orders of basis.

equal to 2.3 TB. No hard disk storage is available for computation. InfiniBand is used for the network interconnection.

## 4. Numerical Results and Discussion

**4.1. The Accuracy versus the Order of Basis Function.** In this benchmark, a model of PEC sphere is used to test the relationship between the accuracy of simulation and the order of basis function. The radius of the sphere is 1.0 meter. The simulation frequency is 1 GHz. The incident direction is along  $x$ -axis and the observation plane is XOY, as illustrated in Figure 3. Parallel higher-order MoM with 512 CPUs is employed to calculate the bistatic RCS (dB). Through changing the order of basis, the results obtained are compared in Figure 4 and the information of simulation process is listed in Table 1.

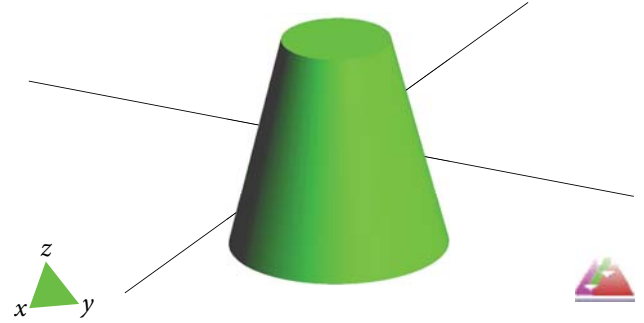


FIGURE 5: Truncated cone description: size (in mm). The height of the target is 200 mm. The major diameter is 200 mm and the minor one is 100 mm.

TABLE 1: Information of the simulation processes.

	Number of unknowns	Matrix filling time (second)	Matrix solving time (second)
Order 1	1101	1.16	3.23
Order 2	4887	2.04	25.8
Order 3	7517	1.88	34.4
Order 4	13661	4.75	68.0
Order 5	21645	8.53	63.0

We can see from Figure 4 that the results are stable when the order of basis function ranges from two to five. Therefore to this model, numbers of two to five can be chosen as the reasonable order of basis. Moreover, Table 1 lists the information about the simulations, respectively. It is obvious that the number of unknowns is more when the order of basis is higher. Meanwhile, the simulation time required is longer as the order of basis function is increased.

**4.2. Comparison with the Measurement Results and Parallel FMM with RWG Basis.** To validate the accuracy and efficiency of the proposed parallel higher-order basis MoM methodology, two benchmarks of a truncated cone and a Y-8 plane are simulated to calculate their RCS, respectively.

**4.2.1. Truncated Cone [7].** This benchmark is an end-capped truncated cone oriented along the  $z$ -axis and centred in the plane  $z = 0$  (illustrated in Figure 5). The elevation angle ( $\theta$ ) is taken from the positive  $z$ -axis and the azimuth angle ( $\phi$ ) from the positive  $x$ -axis. There are several interesting points in this target. First, it shows the RCS response of targets with single curvature (common in structural parts of an aircraft, such as the fuselage). It is also important to know the diffraction mechanism at curved edges. Reflection from planar surfaces with curved edges can also be observed. Therefore, this target is especially suitable for the validation of the prediction of objects with flat surfaces delimited by curved edges and for evaluation of curved edge contributions.

This model has been simulated at 7 GHz. The RCS pattern, for HH polarizations, corresponds to  $\phi = 0$  and  $\theta$

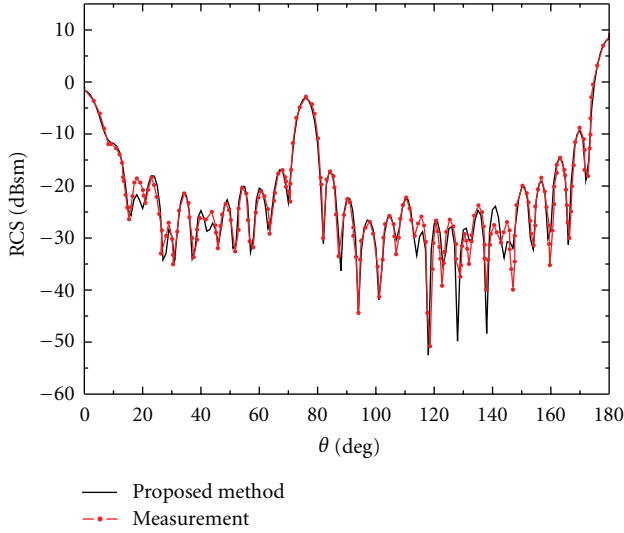


FIGURE 6: RCS pattern of the truncated cone. Frequency: 7 GHz. Polarization: HH. Comparison with measurement.

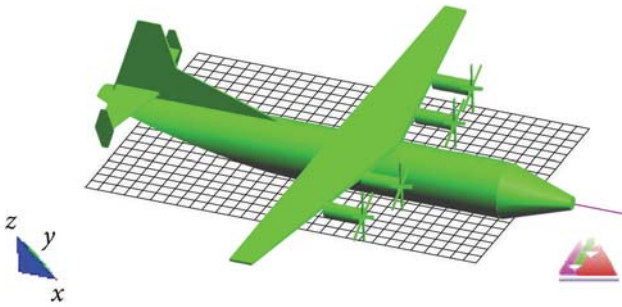


FIGURE 7: Model of Y-8 aircraft.

ranges from  $0^\circ$  to  $180^\circ$  with a  $1^\circ$  step. The incident direction is perpendicular to the generatrix. The simulation is performed on the first kind of computer platform described above.

Figure 6 shows the RCS pattern of the truncated cone for HH polarization at 7 GHz. Three main lobes are clearly defined. Two of them correspond to the specular reflection from the two bases of the cone. The minor one corresponds to  $\theta = 0^\circ$  and the major one to  $\theta = 180^\circ$ , with the different levels resulting from the different areas of the corresponding bases. The other main lobe corresponds to the angle at which the generatrix is perpendicular to the incident direction. Diffraction from the curved edges becomes important in the intermediate region between the main lobes. The RCS pattern is compared with measured results and good agreement is seen.

**4.2.2. Y-8 Plane.** This benchmark is a real aircraft named Y-8 (illustrated in Figure 7). The elevation angle ( $\theta$ ) is taken from the positive  $x$ -axis and the azimuth angle ( $\phi$ ) also from the positive  $x$ -axis. The operating frequency is 100 MHz. The airplane model is 36.2 m long, 38 m wide, and 10.5 m high. The corresponding electrical sizes of the model are

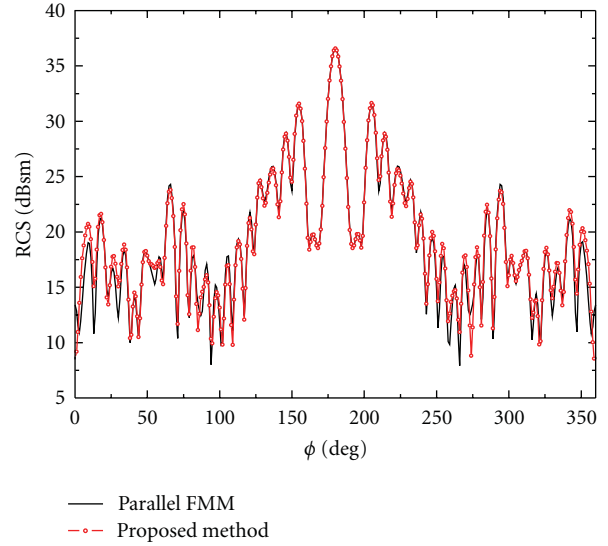


FIGURE 8: RCS results on XOY plane of Y-8 aircraft at 100 MHz.

TABLE 2: Comparison between the proposed and FMM method.

Algorithm	Number of mesh elements	Number of unknowns	Number of CPU cores	Wall clock time (second)
Proposed method	8399	18456	4	4297
Parallel FMM with RWG basis	19978	29967	4	18174

$12.1\lambda$ ,  $12.7\lambda$ , and  $3.5\lambda$ , where  $\lambda$  is the free-space wavelength at the operating frequency. The incident wave with HH polarization is along the negative  $x$ -axis.

In this simulation, the order of higher-order basis is three; also, FMM parameters are described as follows.

- (1) Number of levels: 6.
- (2) Top level: 3.
- (3) Number of boxes at the top level: 27.
- (4) Number of boxes at the finest level: 1937.
- (5) Finest box size:  $0.23 \cdot \lambda$ .

The simulation is performed on the first kind of computer platform described above. The Bistatic RCS results obtained by using the proposed parallel higher-order basis MoM method and the parallel FMM method, are plotted together in Figure 8. As shown in this figure the results agree with each other very well from  $15^\circ$  to  $345^\circ$ . The only considerable discrepancy between them occurs in the nose region of the plane, for angles from  $0^\circ$  to  $15^\circ$  and from  $345^\circ$  to  $360^\circ$ .

The comparisons of some computation parameters are listed in Table 2.

From Table 2, one can see that the higher-order basis adopted in the proposed method results in less number of unknowns than the FMM RWGs do. The total computation time of the proposed method is only about 23.6% of the time

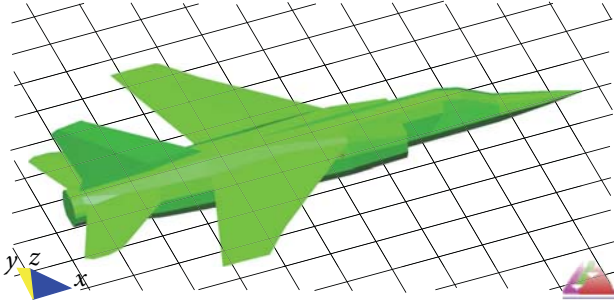


FIGURE 9: Model of Mirage aircraft.

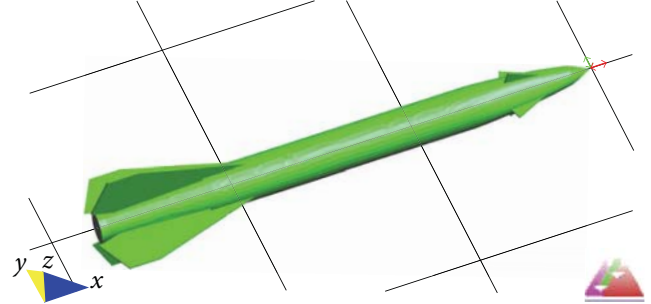


FIGURE 11: Model of the missile.

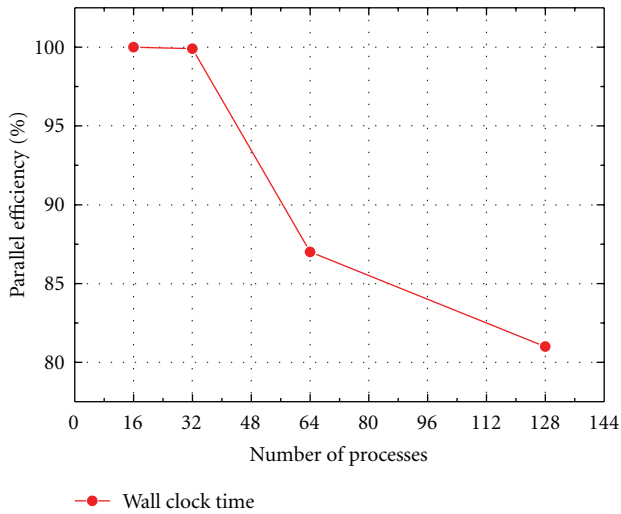


FIGURE 10: Parallel efficiencies for the simulation of Mirage aircraft.

required by parallel FMM method, and it implies that the proposed method is about 4.2 times faster than the parallel FMM method. This benefit not only comes from the smaller number of unknowns needed when using higher-order basis, but also due to the parallel matrix partition scheme.

**4.3. Parallel Efficiency of Mirage's RCS Computation.** In this benchmark, the parallel efficiency of Mirage's RCS computation has been measured with respect to different numbers of processes, as shown in Table 2. The model of the Mirage aircraft is described in Figure 9, and its geometric dimensions are  $11.3 \text{ m} \times 7 \text{ m} \times 2.85 \text{ m}$ . The operating frequency is 1.25 GHz. Thus the corresponding electrical dimensions are  $47.1\lambda \times 29.2\lambda \times 11.9\lambda$ , where  $\lambda$  is the wave length in free space. The model is placed along  $x$ -axis and is excited by a plane wave propagating along the negative  $x$ -axis and with VV polarization.

Taking the time for 16 processes as a reference, the parallel efficiencies for this simulation are described in Figure 10, and the times of simulation for different number of CPUs are listed in Table 3. In the cases of 16, 32, 64, and 128 processes, the parallel efficiencies for the wall time are higher than 80%, which demonstrates that this proposed method can reach

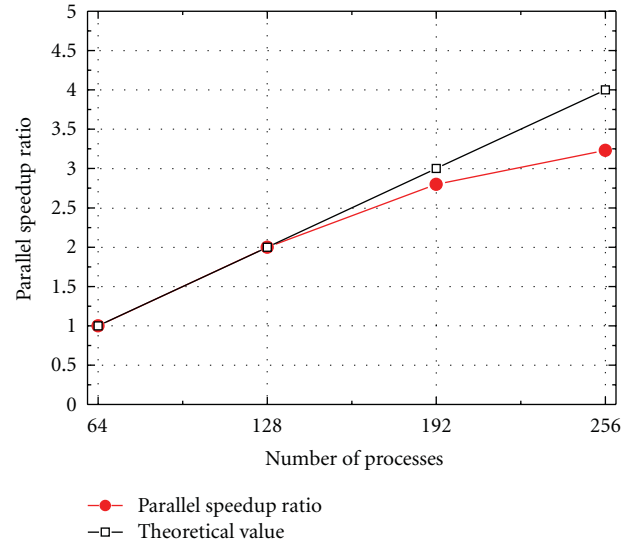


FIGURE 12: Parallel speedup ratio for the simulation of missile at 5 GHz.

TABLE 3: Comparison of the simulation time of Y-8's RCS with respect to processes.

Number of processes (process grid)	Matrix filling time (second)	Matrix equation solving time (second)	Wall clock time (second)
16 ( $4 \times 4$ )	708	5060	5920
32 ( $4 \times 8$ )	418	2464	2962
64 ( $8 \times 8$ )	243	1407	1701
128 ( $8 \times 16$ )	142	741	918

an excellent parallel efficiency and is capable of effectively reducing the computation time.

**4.4. RCS Computation of Benchmark with Electrically Large Dimension.** In the following examples, the elevation angle ( $\theta$ ) is taken from the positive  $x$ -axis to  $z$ -axis and the azimuth angle ( $\phi$ ) from the positive  $x$ -axis. The simulations are performed on the second kind of computer platform described in Section 3.

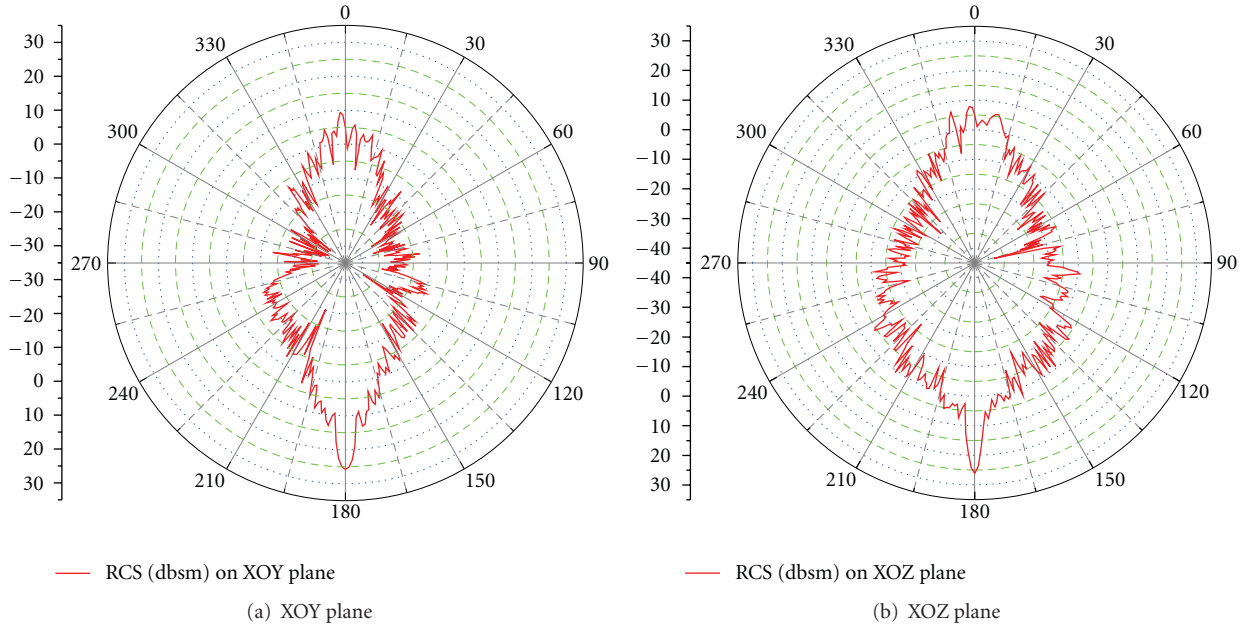


FIGURE 13: RCS (dbsm) results of the missile.

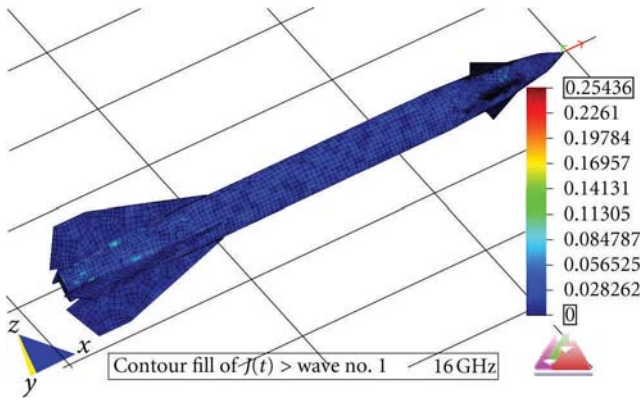


FIGURE 14: Surface current distribution of the missile.

TABLE 4: Parameters of the model.

Benchmark's name	Missile
Geometric length (m)	2.8
Geometric width (m)	0.6
Geometric height (m)	0.6
Incident direction	Along the negative x-axis
Polarization	HH

(1) In the first part of this section, the parallel speedup ratio for computing a real missile's bistatic RCS is tested.

The model of this benchmark is listed as follows. The missile model is placed along the  $x$ -axis, as illustrated in Figure 11. Table 4 illustrates the corresponding parameters of this model.

TABLE 5: Comparison of the simulation time of missile's RCS with respect to processes.

Number of processes (process grid)	Solution time (second)	Parallel speedup ratio
64 ( $8 \times 8$ )	3340	1
128 ( $8 \times 16$ )	1664	2
192 ( $12 \times 16$ )	1193	2.8
256 ( $16 \times 16$ )	1034	3.23

This testing benchmark is operating at 5.0GHz, for which the number of unknowns is 69247. The simulation times for different number of processes and the results of parallel speed-up ratio are listed in Table 5 and Figure 12, respectively. Taking the time for 64 processes as a reference, it can be found in Figure 12 that the parallel speedup ratio is nearly linear. However, in the case of 192 and 256 processes, the parallel efficiencies for the simulation decrease compared with the theoretical results. An increase in the number of processes deteriorates the performance. This is expected because the ratio of the communication volume to computation increases with an increase in the number of processes for this problem. But the parallel efficiencies of all these four situations are also higher than 80%, which proves a good parallel performance of this paper's method.

(2) Consider next the missile's bistatic RCS and its surface current distribution.

Table 6 illustrates the corresponding parameters of this benchmark, and Table 7 summarizes the computation results. In the following, RCS results and surface current distribution of this benchmark are listed in Figures 13 and 14, respectively.

TABLE 6: Parameters of the simulated benchmark.

Benchmark's name	Missile
Operating frequency (GHz)	16.0
Electrical length	$147\lambda$
Electrical width	$31.6\lambda$
Electrical height	$31.6\lambda$
Incident direction	Along the negative $x$ -axis
Polarization	HH

TABLE 7: Computation results of the simulated benchmark.

Benchmark's name	Missile
Number of unknowns	322369
Number of processes (process grid)	512 ( $16 \times 32$ )
Matrix filling time (second)	2985
Matrix solving time (second)	38395
Wall clock time (second)	43061

From this benchmark, it is clear that the proposed method in this paper is able to handle electrically large scattering problems of hundreds of wavelength in the maximum dimension.

## 5. Conclusion

In this paper, RCS computation of electrically large platforms using parallel MoM technique with higher-order basis functions is presented. A load-balanced parallel method is achieved by a matrix partition scheme, so the total wall clock time for solving a large dense matrix is shortened. Its accuracy, efficiency, and applicability are also validated through several numerical examples. In conclusion, the method proposed in this paper can solve some electrically large problems with high accuracy and short computation time, which cannot be achieved by the conventional RWG MoM method. Also this paper contributes to ongoing research efforts on developing numerically accurate solutions for electrically large problems.

## Acknowledgments

This work is partly supported by the Fundamental Research Funds for the Central Universities of China (JY10000902002, K50510020017) and the National Science Foundation of China (61072019). This work is also supported by Shanghai Supercomputer Center of China (SSC).

## References

- [1] R. F. Harrington, *Field Computation by Moment Methods*, IEEE Series on Electromagnetic Waves, IEEE, New York, NY, USA, 1993.
- [2] S. M. Rao, D. R. Wilton, and A. W. Glisson, "Electromagnetic scattering by surfaces of arbitrary shape," *IEEE Transactions on Antennas and Propagation*, vol. AP-30, no. 3, pp. 409–418, 1982.
- [3] Y. Zhang, M. Taylor, T. K. Sarkar et al., "Parallel in-core and out-of-core solution of electrically large problems using the RWG basis functions," *IEEE Antennas and Propagation Magazine*, vol. 50, no. 5, pp. 84–94, 2008.
- [4] Y. Zhang and T. K. Sarkar, *Parallel Solution of Integral Equation Based EM Problems in the Frequency Domain*, Wiley, Hoboken, NJ, USA, 2009.
- [5] Y. Zhang, M. Taylor, T. K. Sarkar, H. G. Moon, and M. Yuan, "Solving large complex problems using a higher-order basis: parallel in-core and out-of-core integral-equation solvers," *IEEE Antennas and Propagation Magazine*, vol. 50, no. 4, pp. 13–30, 2008.
- [6] Y. Zhang, T. K. Sarkar, M. Taylor, and H. Moon, "Solving MoM problems with million level unknowns using a parallel out-of-core solver on a high performance cluster," in *Proceedings of the IEEE International Symposium on Antennas and Propagation and USNC/URSI National Radio Science Meeting (APSURSI '09)*, Charleston, SC, USA, June 2009.
- [7] R. Fernández-Recio, A. Jurado-Lucena, B. Errasti-Alcalá, D. Poyatos-Martínez, D. Escot-Bocanegra, and I. Montiel-Sánchez, "RCS measurements and predictions of different targets for radar benchmark purpose," in *Proceedings of the International Conference on Electromagnetics in Advanced Applications (ICEAA '09)*, pp. 443–446, September 2009.

## Research Article

# Design and Optimization of an EBG Antenna with an Efficient Electromagnetic Solver

**Josefa Gómez, Abdelhamid Tayebi, José Ramón Almagro, Iván González, and Felipe Cátedra**

*Computer Sciences Department, University of Alcalá, 28871 Alcalá de Henares, Spain*

Correspondence should be addressed to Josefa Gómez, josefa.gomezp@uah.es

Received 28 June 2011; Revised 3 September 2011; Accepted 15 September 2011

Academic Editor: Ning Yuan

Copyright © 2012 Josefa Gómez et al. This is an open access article distributed under the Creative Commons Attribution License, which permits unrestricted use, distribution, and reproduction in any medium, provided the original work is properly cited.

A novel electromagnetic bandgap (EBG) antenna has been designed, optimized, and analyzed using an efficient electromagnetic solver based on the moment method. Very good agreement between simulations and measurements in anechoic chamber has been obtained. Comparisons of the antenna with and without the EBG structure have been conducted to study its influence in terms of gain. This new EBG antenna is an excellent candidate for several applications due to its high gain and good polarization purity.

## 1. Introduction

Recently, several applications of EBG materials, such as microwave filters, antennas, amplifiers, microstrip devices, ground plane structures, and base station antennas have been reported in the literature. For instance, EBG material has been shown to enhance the directivity of a patch antenna from 8 dB to 20 dB [1]. The work presented in [2] described a method to design directive antennas by incorporating cylindrical EBG structures. On the other hand, [3] presents a resonator antenna that increases its gain and bandwidth with an EBG structure over the device. It has also been demonstrated [4] that the EBG materials are able to provide good results while reducing the size of some kinds of filters. The work presented in [5] summarizes the benefits of using EBG materials to improve the performance of microwave and optical applications. Some experimental results are discussed to check the properties of these materials. According to [6], an increase in directivity can be obtained by adding a partially reflecting sheet in front of the antenna because of the multiple reflections between the sheet and the screen. The resonance distance between both elements must be such that the rays projected through the sheet have equal phases in the normal direction. Our contribution is focused on that investigation line. Numerical results demonstrate an improvement in gain, bandwidth, and polarization purity when comparing several antenna configurations varying the distances between both grids. The aim of this paper

is to design a compact EBG antenna that provides a gain greater than 15.0 dBi and polarization purity greater than 40 dB while maintaining a very small size. To fulfill these requirements, the dimensions of the antenna were optimized by using a powerful electromagnetic solver.

The paper is organized as follows. Section 2 presents the main characteristics of the electromagnetic field solver that has been used to design, optimize, and analyse the proposed antenna. The steps of the optimization process that have been conducted to find the optimum dimensions of the antenna are listed in Section 3. Section 4 describes the properties of the EBG antenna as well as the design and analysis procedure. Section 5 includes the comparisons between predictions and measurements and Section 6 contains the concluding remarks and future work.

## 2. Electromagnetic Kernel

In recent years, interest in computer simulation tools has grown rapidly. Many people in academia and industry are currently involved in the research and development of new methods to accelerate or improve the conventional electromagnetic field solvers. The applications of this kind of systems are unlimited (design of microwave devices, analysis of antennas, radomes, reflectarrays, electromagnetic compatibility, etc.) and they can be used not only in engineering, but also in other scopes like medicine [7]. On the other hand, researchers may take advantage of the parallel versions due

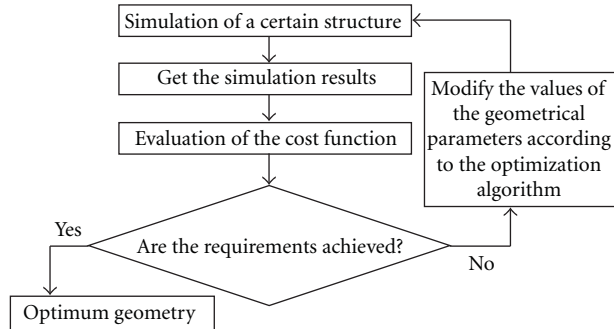


FIGURE 1: Diagram of the optimization process.

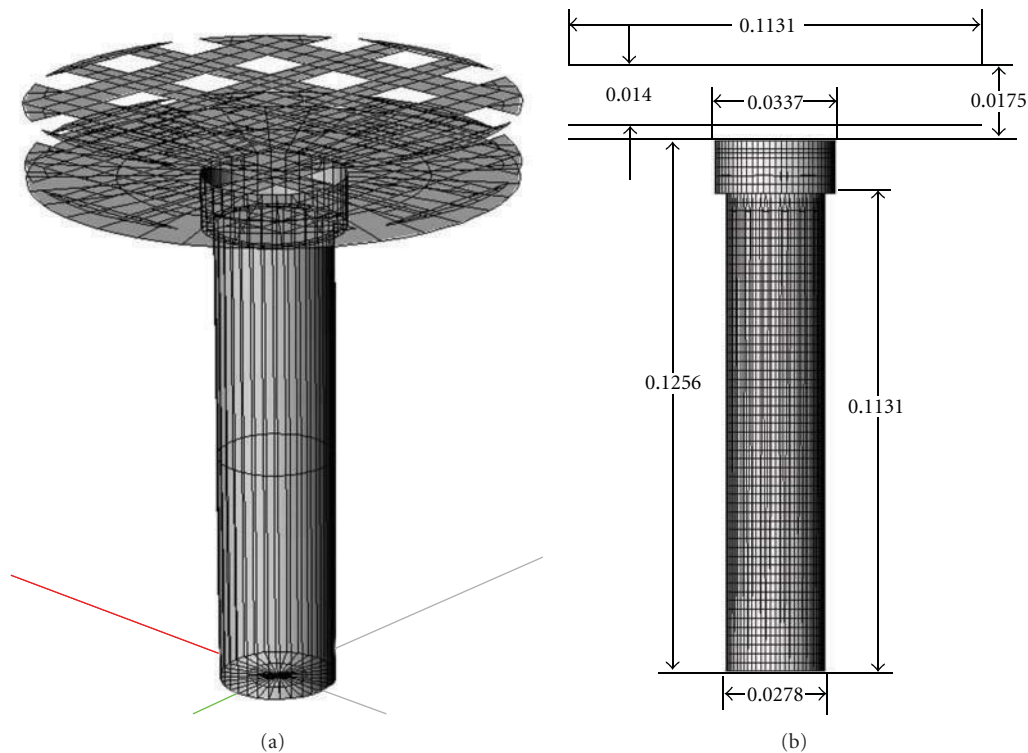


FIGURE 2: Schematic representation of the antenna. Units are in meters.

to the new power characteristics of actual computers such as high speed and enormous amount of memory.

Nowadays, many commercial suites similar to the computer tool utilized to perform the simulations like Feko, CST, and HFSS are available. However, none of them takes into account the real shape of the bodies under analysis. This is because the meshing procedure is based on flat facets (triangles or quadrangles), so that small geometrical details can be lost. One of the advantages of our solver is that the discretized geometry totally fits the original shape of the structure, because it is composed of curved parametric surfaces. As a result, it provides accurate predictions of arbitrary metallic or dielectric 3D structures at low and high frequencies [8].

As previously mentioned, the electromagnetic kernel is based on the moment method [9] and can solve the electrical

field integral equation, the magnetic field integral equation and the combined field integral equation. The electromagnetic treatment considers curved rooftop functions that serve as low-level basis and testing functions. Both functions are defined over a parametric domain, which is very well suited for setting up an adaptive mesh, without the need for external meshing tools. Other important advantage of using these functions is that their direct placement on parametric surfaces totally eliminates the error introduced when using plane facets in the discretization process.

To verify the efficiency of the tool, some comparisons with Feko have been conducted. The conclusion obtained is that Feko is usually three times slower than our electromagnetic solver. A pyramidal horn analysis problem at 10 GHz can be used as a benchmark example to demonstrate the efficiency of the solver. Whilst the simulation in Feko spends

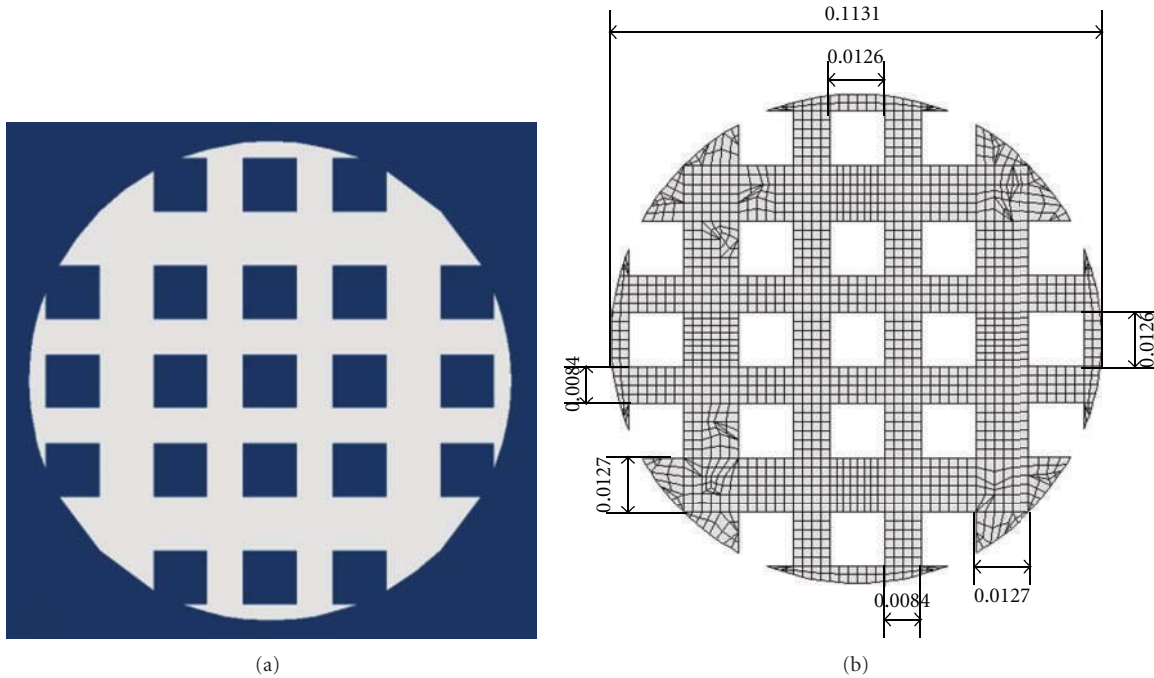


FIGURE 3: Top view of the EBG structure. Units in meters.



FIGURE 4: Prototype of the EBG antenna.

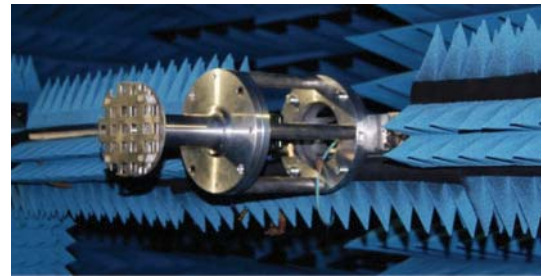


FIGURE 5: Antenna located in the anechoic chamber.

183 seconds solving the matrix with LU decomposition and 7378 unknowns, our computer tool only spends 84 seconds solving the same problem with an iterative method and 2205 unknowns.

Due to the fact that conventional moment method spends lots of resources when the structure under analysis is electrically large, the multilevel fast multipole algorithm (MLFMA) [10] has been included in the electromagnetic kernel to improve the efficiency in those cases. MLFMA only requires the storage of the near-field terms of the coupling matrix, so that it decreases the CPU-time of the matrix-vector products in the solution process, allowing the analysis of problems of sizes of thousands of wavelengths.

The computational complexity is therefore reduced from  $O(N^2)$  to  $O(N \log N)$ . The benefit of applying this method is a dramatic reduction of memory and time resources needed for simulation of electrically large structures.

The kernel also includes a hybrid computational technique based on the moment method and physic optics [11] for analysis of large antennas and scatters at high frequencies. A combination of asymptotic and rigorous techniques is the ideal solution when a large body is too hard to analyze with the MLFMA. The inclusion of physic optics helps to reduce the computation time and memory requirements with respect to the conventional moment methods when analysing huge bodies at high frequencies.

On the other hand, a domain decomposition approach [12] has been incorporated to obtain similar results to those given by the moment method, highly reducing the computational effort by taking advantage of the MLFMA method combined with an iterative technique used to compute interactions between different parts of the geometry in a totally adaptive fashion. The domain decomposition

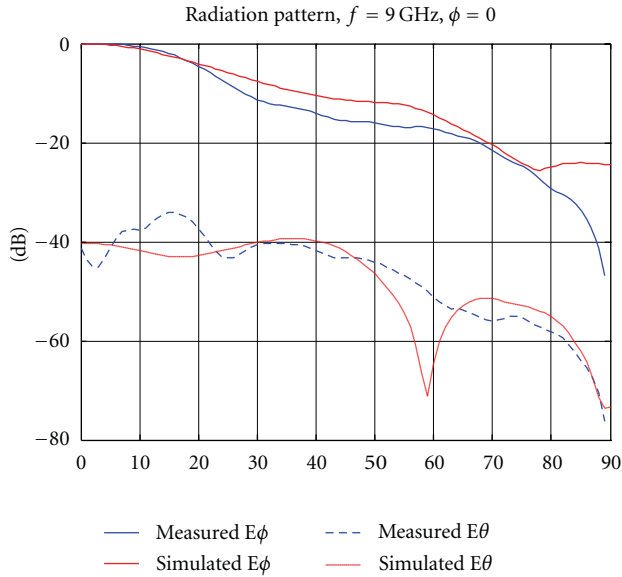


FIGURE 6: Comparison of the simulated and measured radiation patterns. E-plane cut at 9 GHz.

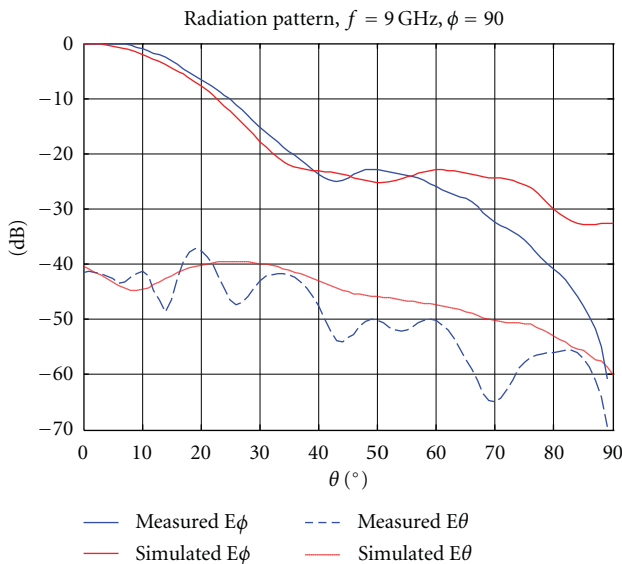


FIGURE 7: Comparison of the simulated and measured radiation patterns. H-plane cut at 9 GHz.

approach entails a simple way to deal with a good number of realistic problems which due to convergence or size limitations cannot be handled by conventional rigorous solvers, but are not included in the field of application of high-frequency techniques either. These geometries can include structures containing fine details, multiscale problems, interactions with cavities, and so forth.

Lately, the use of computer clusters to perform electromagnetic analysis of many realistic problems in researching centers is quite common. For this purpose, the kernel has been parallelized using the message passing interface paradigm [13], a specification for an API used to program parallel computers. The goals of this paradigm are high

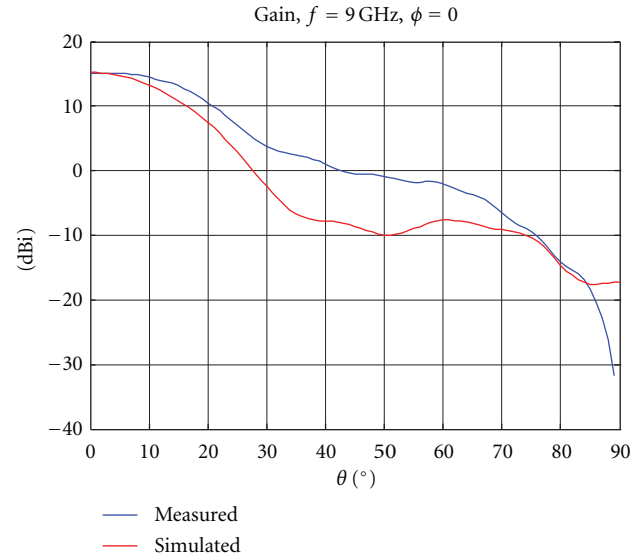


FIGURE 8: Comparison of the simulated and measured gain. E-plane cut at 9 GHz.

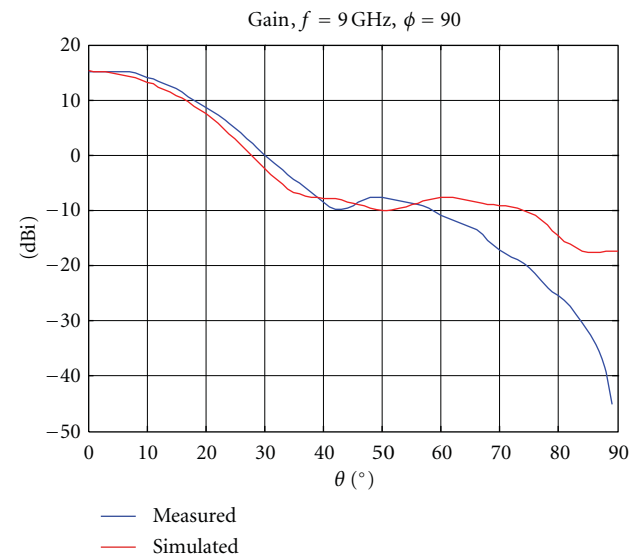


FIGURE 9: Comparison of the simulated and measured gain. H-plane cut at 9 GHz.

performance, scalability, and portability. The computer tool is compatible with any modern Windows PC or Linux-based machine and there are also versions available for other operating systems and platforms, including highly parallelized versions for multiprocessor computers or clusters.

### 3. Optimization Process

One of the most important features of the solver is the optimization process [14, 15]. This module computes the optimal geometric values of a number of parameters previously indicated by the user (width, radius, height, antenna

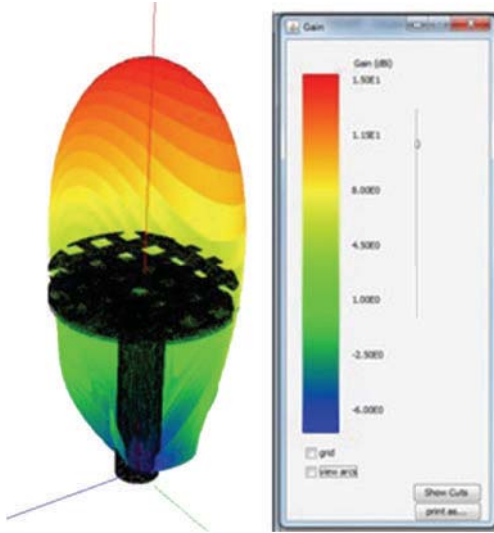


FIGURE 10: Radiation pattern of the antenna computed by the electromagnetic simulator.

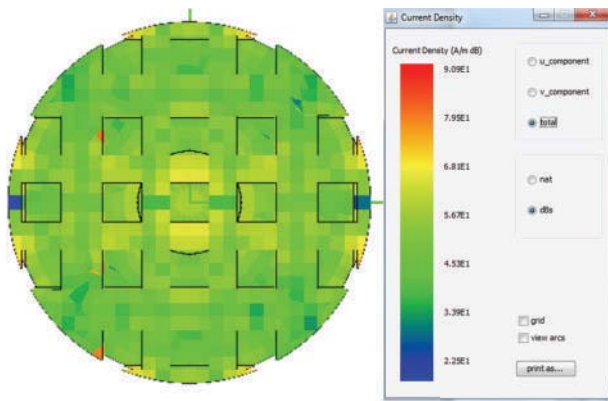


FIGURE 11: Current distribution computed by the electromagnetic simulator (top view).

location, etc.). The process allows the optimization of radiation patterns and it is based on several specifications set out initially by means of a cost function. Thus, the shape of the radiation pattern can be defined in terms of gain, level of side lobes, level of the crosspolar component, and so forth. The selected parameters vary within a known range, in order to find the optimal solution that minimizes this cost function.

The process begins by analyzing a particular structure, defined by initial parameters. At the end of the simulation, results are processed and the cost function is evaluated. If all requirements are satisfied, the values of the parameters that have provided such results are given as the optimum parameters. If any specification is not satisfied, the geometry is updated with new parameters and a new simulation is performed, repeating the whole process. The optimization procedure finishes when the optimizer minimizes the specified cost function. Figure 1 depicts a diagram of the whole process.

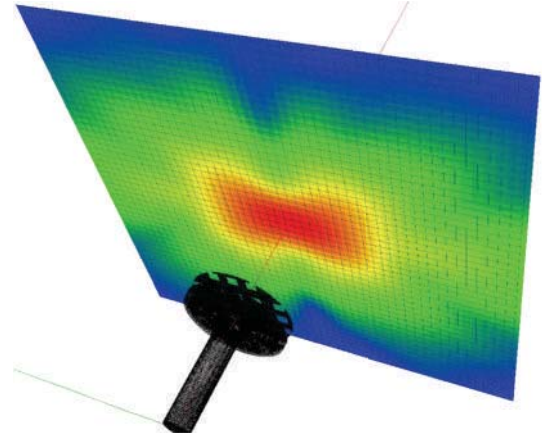


FIGURE 12: Near field results computed by the tool considering the  $50 \times 50$  observation points.

Regarding the optimization algorithm, there exist three different methods that can be selected. The first one is based on an exhaustive search, since each parameter is updated with values taken from a homogeneous grid. Gradient descend and particle swarm optimization are two popular algorithms that have been also included in the optimization module. Successful results have been achieved in the optimization of several antenna dimensions when applying these algorithms.

#### 4. EBG Antenna

In order to design a compact EBG antenna that provides high gain, polarization purity, and wide bandwidth, the dimensions were optimized by using the optimization module. After obtaining the optimum dimensions, a prototype made of aluminum was built and measured.

The antenna configuration is depicted in Figure 2. The antenna model is defined by a long metallic cylinder with a 13.9 mm radius and 113.1 mm length, a short metallic cylinder with a 16.85 mm radius and 12.5 mm length, a circular ground plane with a 56.50 mm radius and the EBG structure, composed of two circular metal grids with the same radius size. An electric dipole located at  $\lambda/4$  from the bottom of the circular waveguide has been used to model the feeding of the waveguide in the simulations. The dipole is oriented in the  $x$ -axis parallel to the bottom of the waveguide.

Each grid is composed of a metallic sheet with twenty-one square holes. Figure 3 shows the top view of the circular grids. The distance between the ground plane and the first metallic grid was established to prevent cavity resonances at the operating frequency whereas the distance between the two metallic grids was set to obtain the classical EBG mode that permits an efficient antenna performance.

The first step in the design process was choosing the unit cell shape of the periodic structure. Some candidates were studied, such as rectangles, triangles, circles, rhombs, and crosses. After an exhaustive study, the square hole was chosen because of its simplicity and its good response. The next

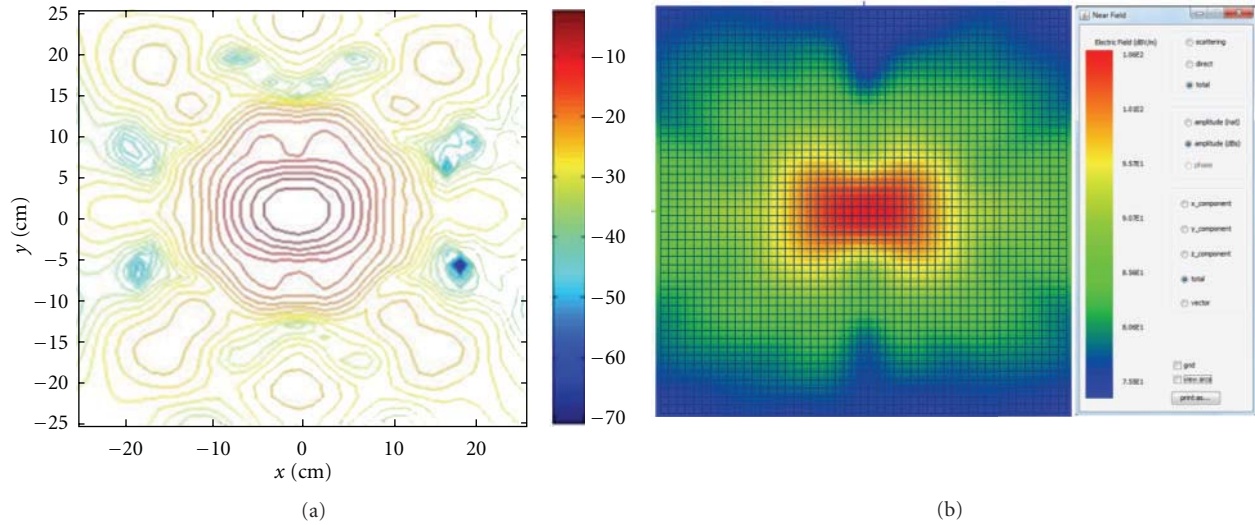


FIGURE 13: Near field results measured (a) and computed by the tool (b).

point was the optimization of the structure dimensions at a central frequency of 9 GHz. Several geometrical parameters (the distance between adjacent holes, the size of the holes, the number of holes, etc.) were optimized. After the analysis of the position of the periodic structures, the final conclusion is that the upper grid must be located 17.5 mm from the ground plane and the lower grid must be situated 3.5 mm from the ground plane. Those are the optimum physical dimensions to achieve the desirable radiation characteristics of high gain and low cross-polarization level. The remaining geometrical parameters related to the waveguide were fixed.

Regarding the resonance distances between the grids, the height of the lower grid from the ground plane was optimized within the range from 3 mm to 7.5 mm and the height of the upper grid from the ground plane was optimized within the range from 9 to 18 mm. The optimization algorithm utilized to obtain the best values for both parameters was gradient descend and the optimization mask was defined to obtain low cross-polar level and high gain, according to the optimization goals in Table 1.

## 5. Results

The antenna prototype was measured in an anechoic chamber. Figure 4 depicts a photograph of the built antenna. The antenna was made of aluminum and weighed nearly 400 g. The pair of metallic grids was kept fixed by four plastic screws. The screws crossed the ground plane and kept the three different parts together. The antenna was fed through a coaxial-rectangular transition plus a rectangular to circular waveguide transition to radiate linear polarization. Figure 5 shows the antenna located in the anechoic chamber.

Figures 6 and 7 show comparisons between the measurements and the simulated values for the two main radiation cuts at 9 GHz.

The EBG antenna provides the maximum radiation in the axial direction. Good agreement between real measure-

TABLE 1

Theta range	Level of the copolar component	Level of the cross-polar component
$0^\circ < \theta < 10^\circ$	$> -5$ dB	$>40$ dB
$10^\circ < \theta < 20^\circ$	$< -5$ dB	$>40$ dB
$20^\circ < \theta < 30^\circ$	$< -10$ dB	$>40$ dB
$30^\circ < \theta < 90^\circ$	$< -15$ dB	$>40$ dB

ments and computations was shown. The slight discrepancies between measurements and simulation values may be due to unwanted effects as well as nonidealities introduced by the four screws and the manufacturing errors. Moreover, the cross-polarization level in the E and H plane cuts is below  $-40$  dB.

The maximum level of the gain is 15.6 dBi, given at  $\theta = 0^\circ$  and  $\phi = 0^\circ$ . Figures 8 and 9 show the comparison between measurements and simulations of the gain for the E and H planes at 9 GHz.

Besides providing 2D Cartesian plots, the electromagnetic solver is able to display the 3D radiation pattern, as well as the current distribution, as it can be observed in Figures 10 and 11.

Regarding the near field results, simulations and measurements have been conducted to compare the antenna behavior in a plane located 12 cm over the top of the antenna. A grid of  $50 \times 50$  observation points has been established to compute and measure the near field values. Note that the distance between two consecutive points is 1 cm. Therefore, the limits of the exploration area are  $-25$  cm and  $25$  cm in both axes,  $x$  and  $y$ . Figure 12 shows the spatial configuration and the results provided by the computer tool. On the other hand, Figure 13 depicts the contour lines of the near field values measured in the anechoic chamber (on the left), and the simulated values (on the right). Units are in dBs.

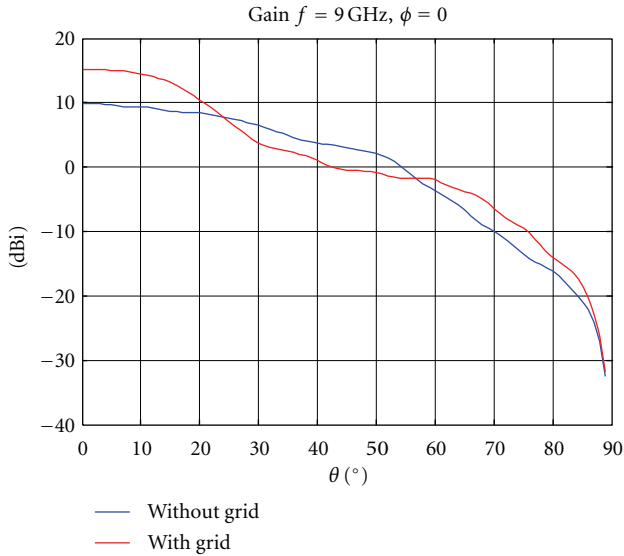


FIGURE 14: Comparison for the antenna gain in the E-plane cut with and without grids.

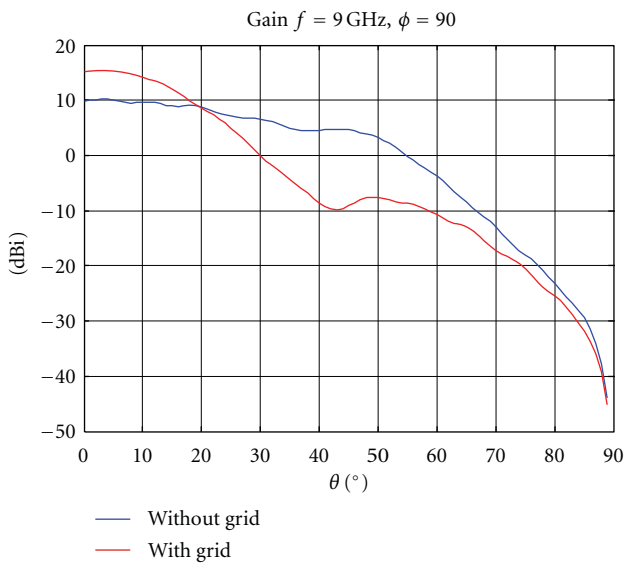


FIGURE 15: Comparison for the antenna gain in the H-plane cut with and without grids.

To verify the behavior of the EBG structure, several simulations were made to compare the results when the height of the cases were studied fixing the upper grid position at 17.5 mm and changing the lower grid position at  $h_1 = 4.3$  mm,  $h_2 = 5.1$  mm,  $h_3 = 5.9$  mm,  $h_4 = 6.7$  mm, and  $h_5 = 7.5$  mm. A decrease in gain was proven when the height of the lower grid increases, in other words, when both grids are closer.

The comparison between the gain of the simple waveguide and the gain adding the EBG structure is shown in Figures 14 and 15 for the two main cuts. This comparison ensures that the effect of including the grids is a relevant enhancement in gain.

## 6. Conclusions

The design, optimization, and analysis of a compact EBG antenna operating at 9 GHz have been presented in this paper. A powerful computer tool has been used to carry out those three processes. The antenna has been built and measured in order to validate the predictions provided by the electromagnetic solver. We have demonstrated that the effect of including the EBG structure is an enhancement in gain. The antenna is a good candidate for several applications due to its relatively high gain, excellent polarization purity, and compact size.

## Acknowledgment

This paper has been supported, in part, by the Comunidad de Madrid Project S-2009/TIC1485 and by the Castilla-La Mancha Project PPII10-0192-0083, by the Spanish Department of Science, Technology Projects TEC 2010–15706 and CONSOLIDER-INGENIO No. CSD-2008-0068.

## References

- [1] M. Thèvenot, C. Cheype, A. Reineix, and B. Jecko, "Directive photonic-bandgap antennas," *IEEE Transactions on Microwave Theory and Techniques*, vol. 47, no. 11, pp. 2115–2122, 1999.
- [2] G. K. Palikaras, A. P. Feresidis, and J. C. Vardaxoglou, "Cylindrical electromagnetic bandgap structures for directive base station antennas," *IEEE Antennas and Wireless Propagation Letters*, vol. 3, no. 1, pp. 87–89, 2004.
- [3] A. R. Weily, K. P. Esselle, T. S. Bird, and B. C. Sanders, "Dual resonator 1-D EBG antenna with slot array feed for improved radiation bandwidth," *IET Microwaves, Antennas and Propagation*, vol. 1, no. 1, pp. 198–203, 2007.
- [4] J.-W. Baik, S.-M. Han, C. Jeong, J. Jeong, and Y. S. Kim, "Compact ultra-wideband bandpass filter with EBG structure," *IEEE Microwave and Wireless Components Letters*, vol. 18, no. 10, Article ID 4639557, pp. 671–673, 2008.
- [5] Y. Rahmat-Samii, "The Marvels of Electromagnetic Band Gap (EBG) Structures," *Applied Computational Electromagnetics Society Journal*, vol. 18, no. 3, pp. 1–10, 2003.
- [6] G. V. Trentini, "Partially reflecting sheet arrays," *IRE Transactions on Antennas and Propagation*, vol. 4, pp. 666–671, 1956.
- [7] C. Armenean, E. Perrin, M. Armenean, O. Beuf, F. Pilleul, and H. Saint-Jalmes, "RF induced temperature elevation near metallic wires in clinical magnetic resonance imaging," in *Proceedings of the 25th Annual International Conference of the IEEE Engineering in Medicine and Biology Society*, pp. 501–504, September 2003.
- [8] I. González, E. García, F. S. De Adana, and M. F. Catedra, "Monurbs: a parallelized fast multipole multilevel code for analyzing complex bodies modeled by NURBS surfaces," *Applied Computational Electromagnetics Society Journal*, vol. 23, no. 2, pp. 134–142, 2008.
- [9] R. F. Harrington, *Field Computation by Moment Methods*, Macmillan, New York, NY, USA, 1968.
- [10] W. C. Chew, J. Jin, E. Michielssen, and J. Song, Eds., *Fast and Efficient Algorithms in Computational Electromagnetics*, Artech-House, 2001.
- [11] U. Jakobus and F. M. Landstorfer, "Improved PO-MM hybrid formulation for scattering from three-dimensional perfectly

- conducting bodies of arbitrary shape,” *IEEE Transactions on Antennas and Propagation*, vol. 43, no. 2, pp. 162–169, 1995.
- [12] C. Delgado, F. Cátedra, I. González, J. Gómez, and A. Tayebi, “Numerical approach for the fast analysis of radiation patterns of antennas in complex environments,” in *Proceedings of the Final Program and Book of Abstracts—International Workshop on Antenna Technology: Small Antennas, Innovative Structures and Materials (iWAT’10)*, pp. 1–4, 2010.
- [13] <http://www.mcs.anl.gov/research/projects/mpi/>.
- [14] P. M. Pardalos and M. G. C. Resende, *Handbook of Applied Optimization*, Oxford University Press, 2002.
- [15] E.K. P. Chong and S. H. Zak, *An Introduction to Optimization*, John Wiley & Sons, NJ, USA, 2008.

## Research Article

# On the Finite Element Tearing and Interconnecting Method for Scattering by Large 3D Inhomogeneous Targets

Ming-Lin Yang and Xin-Qing Sheng

Center for Electromagnetic Simulation, School of Information and Electronics, Beijing Institute of Technology, Beijing 100081, China

Correspondence should be addressed to Xin-Qing Sheng, xsheng@bit.edu.cn

Received 30 May 2011; Revised 10 August 2011; Accepted 27 August 2011

Academic Editor: Ning Yuan

Copyright © 2012 M.-L. Yang and X.-Q. Sheng. This is an open access article distributed under the Creative Commons Attribution License, which permits unrestricted use, distribution, and reproduction in any medium, provided the original work is properly cited.

The finite element tearing and interconnecting method (FETI) is applied to compute scattering by large 3D inhomogeneous targets. Two algorithms of FETI have been implemented for 3D scattering. The performance of these two FETI algorithms has been investigated in detail, particularly for large inhomogeneous targets. Numerical experiments show that the performance of FETI relies on the style of domain decomposition and inhomogeneity, which has not been carefully studied before. A trick for improving convergence of FETI is presented for inhomogeneous targets.

## 1. Introduction

The domain decomposition has been recognized as one of most important methodologies for constructing efficient parallel computing algorithms in recent years. Among various domain decomposition methods of the finite element method (FEM), the finite element tearing and interconnecting (FETI) shows great potential to improve the capability of the finite element method [1–9]. The FETI designed in [3] was applied to the electromagnetic field problems in [4]. The idea of a more efficient version of FETI, named as FETI-DPH designed in [5], was applied to solve large-scale phased-array antenna and photonic crystal problems and developed as FETI-DPEM1 in [6], where a global preconditioner is smartly designed to significantly improve the convergence of the interface solution in FETI. To maintain high-speed convergence of the interface solution for extremely large-scale problems, the Robin-type transmission conditions at the subdomain interfaces were employed to derive the interface equation instead of Dirichlet-to-Neumann boundary condition in FETI-DPEM1 in [7]. This latest algorithm of FETI in CEM is named as FETI-DPEM2, which shows much better performance than FETI-DPEM1, especially for extremely large-scale problems. Recently, the FETI-DPEM2 is extended to scattering problems [2]. However, few researchers give the

detailed investigation on the performance of FETI-DPEM2 for scattering by large inhomogeneous targets.

In this paper, the FETI-DPEM1 and FETI-DPEM2 are implemented for 3D scattering by large inhomogeneous targets. The performance of these two FETI algorithms has been investigated in detail, particularly for large highly inhomogeneous targets and different domain decomposition types. An implementation trick of FETI is presented for inhomogeneous targets.

## 2. The FETI-DPEM Formulation

The 3D scattering by a target can be formulated as

$$\nabla \times \left( \frac{1}{\mu_r} \nabla \times E \right) - k_0 \epsilon_r E = -jk_0 Z_0 J_{\text{imp}}, \quad \text{in } \Omega \in R^3, \quad (1)$$

$$\hat{n} \times E = 0, \quad \text{on } \partial\Omega_{\text{PEC}}, \quad (2)$$

$$\hat{n} \times \nabla \times E = 0, \quad \text{on } \partial\Omega_{\text{PMC}}, \quad (3)$$

$$\hat{n} \times \nabla \times E + jk_0 \hat{n} \times \hat{n} \times E = U, \quad \text{on } \partial\Omega_{\text{ABC}}, \quad (4)$$

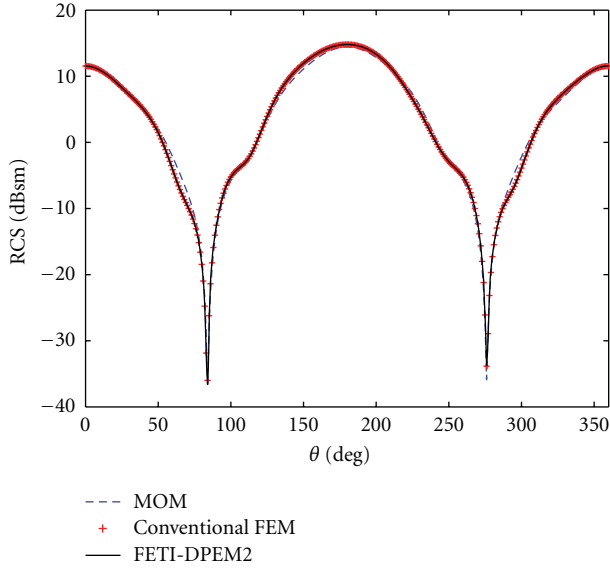


FIGURE 1: Bistatic RCS of the metallic cube with  $\theta_{\text{inc}} = 0^\circ$ ,  $\varphi_{\text{inc}} = 0^\circ$  at 0.3 GHz.

where  $k_0$  and  $Z_0$  are the free-space wave number and intrinsic impedance, respectively, and  $J_{\text{imp}}$  is an internal impressed current.  $\partial\Omega_{\text{ABC}}$  represents a boundary, where the field satisfies the absorbing boundary condition (ABC) [10] with  $U = \hat{n} \times \nabla \times E_{\text{inc}} + jk_0 \hat{n} \times \hat{n} \times E_{\text{inc}}$  as boundary excitation.

According to the FETI method, the computational domain is divided into nonoverlapping subdomains  $\Omega^p$  ( $p = 1, 2, \dots, N_p$ ), where the superscript denotes the subdomain index. The interface shared by the two adjacent subdomain  $i$ th and  $j$ th is denoted as  $\Gamma_{ij}$ . The edges shared by more than two subdomains are called corner edges, denoted as  $\Gamma_c$ . The edges shared by two subdomains and the surface of absorbing boundary are also treated as corner edges. The interior fields in each sub-domain still satisfy (1). In the FETI-DPEM1, the boundary condition of each subdomain is formulated by introducing  $\Lambda$  as

$$\hat{n}^p \times \frac{1}{\mu_r^p} \nabla \times E^p = -\hat{n}^q \times \frac{1}{\mu_r^q} \nabla \times E^q = \Lambda. \quad (5)$$

In the FETI-DPEM2, the boundary condition of each subdomain is formulated by introducing  $\Lambda$  as

$$\hat{n}^p \times \frac{1}{\mu_r^p} \nabla \times E^p + \alpha^p \hat{n}^p \times \hat{n}^p \times E^p = \Lambda^p. \quad (6)$$

The fields in each subdomain can be determined under the boundary condition (5) or (6) by using the standard FEM. A special procedure is designed in FETI to solve the fields in each subdomain. The unknowns of the electric field in each subdomain are grouped into three categories

$$E^p = \begin{bmatrix} E_V^p & E_I^p & E_c^p \end{bmatrix} = \begin{bmatrix} E_V^p & E_c^p \end{bmatrix}, \quad (7)$$

where the subscripts  $V$ ,  $I$ , and  $c$  denote the unknowns associated with the internal volume, interfaces, and corner

edges, respectively. The unknowns  $E_I^p$  associated with the internal volume and interfaces are considered as *local* variables, whereas the unknowns  $E_c^p$  associated with the corner edges are considered as *global* variables. The unknowns  $E_I^p$  are eliminated from the FEM matrix equation for the  $p$ th subdomain to obtain the corner equation of  $E_c^p$ . Afterwards, the obtained corner equations for all sub-domains are assembled together to get the following global corner equation:

$$\tilde{K}_{cc} E_c = \tilde{f}_c - K_{rc}^T \lambda, \quad (8)$$

where  $\tilde{K}_{cc}$ ,  $\tilde{K}_{rc}^T$ ,  $f_c$  can refer to [6]. Solving (8) to obtain  $E_c$  and then substituting  $E_c$  back to the FEM matrix equation for each subdomain, we can obtain the expression of  $E_I^p$  in terms of  $\lambda$ . For FETI-DPEM1, the continuity of tangential electric field between two adjacent subdomain is enforced to  $E_I^p$ , and the final equation can be obtained

$$\left( \tilde{K}_{rr} + \tilde{K}_{rc} \tilde{K}_{cc}^{-1} \tilde{K}_{cr} \right) \lambda = \tilde{f}_r - \tilde{K}_{rc} \tilde{K}_{cc}^{-1} \tilde{f}_c, \quad (9)$$

where  $\tilde{K}_{rr}$ ,  $\tilde{K}_{rc}$ ,  $\tilde{K}_{cr}$ , and  $\tilde{f}_r$  can refer to [6]. For FETI-DPEM2, the continuities of tangential electric and magnetic fields between two adjacent subdomain are enforced to  $E_I^p$ , and the final equation has the same form as (9) and has double unknowns compared with FETI-DPEM1.

Since the inverse of  $\tilde{K}_{cc}$  in (9) essentially performs as a global preconditioner, (9) is usually well conditioned. Numerical experiments in [6, 7] are performed on a 2D-extended periodical structure radiation problem. Recently, the FETI-DPEM2 is extended to 3D scattering problems [2]. However, few researchers give the detailed investigation on the performance of FETI for scattering by 3D-extended inhomogeneous targets, especially when the subdomain numbers are increased or material parameters are changed in all  $x$ ,  $y$ , and  $z$  directions. We will give the detail investigation by numerical experiments in the next section on the performance of FETI for scattering by large inhomogeneous targets.

### 3. Numerical Experiments

To demonstrate the accuracy, efficiency, and capability of the two FETI-DPEM methods, a series of numerical experiments are performed in this section. All the computations are performed on a computer having 2 Intel X5650 2.66 GHz CPUs with 6 cores for each CPU, 32 GB memory. The GMRES solver in [11] is employed to solve (9) with a restart number of 20, and the convergence criterion is set to 0.005.

The first numerical experiment is to show the accuracy of the two FETI-DPEM methods. We compute the bistatic RCS of a  $1 \text{ m} \times 1 \text{ m} \times 1 \text{ m}$  metallic cube at 0.3 GHz with  $\theta_{\text{inc}} = 0^\circ$ ,  $\varphi_{\text{inc}} = 0^\circ$ . A tetrahedral mesh with average edge length of 0.05 m is used. In this calculation, the total FEM computation domain is terminated by enclosing the cube with a cubic outer boundary placed 0.5 m from the cube. Numerical results obtained are compared in Figure 1 with those obtained by the conventional FEM, and the MOM-based solution using the commercial software FEKO. Good agreement can be observed among these results.

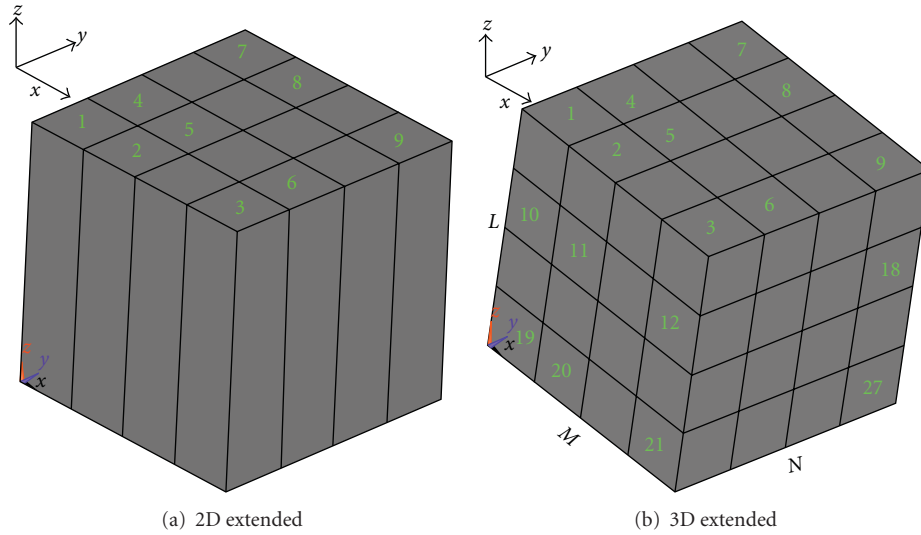


FIGURE 2: Domain decomposition style of a brick domain.

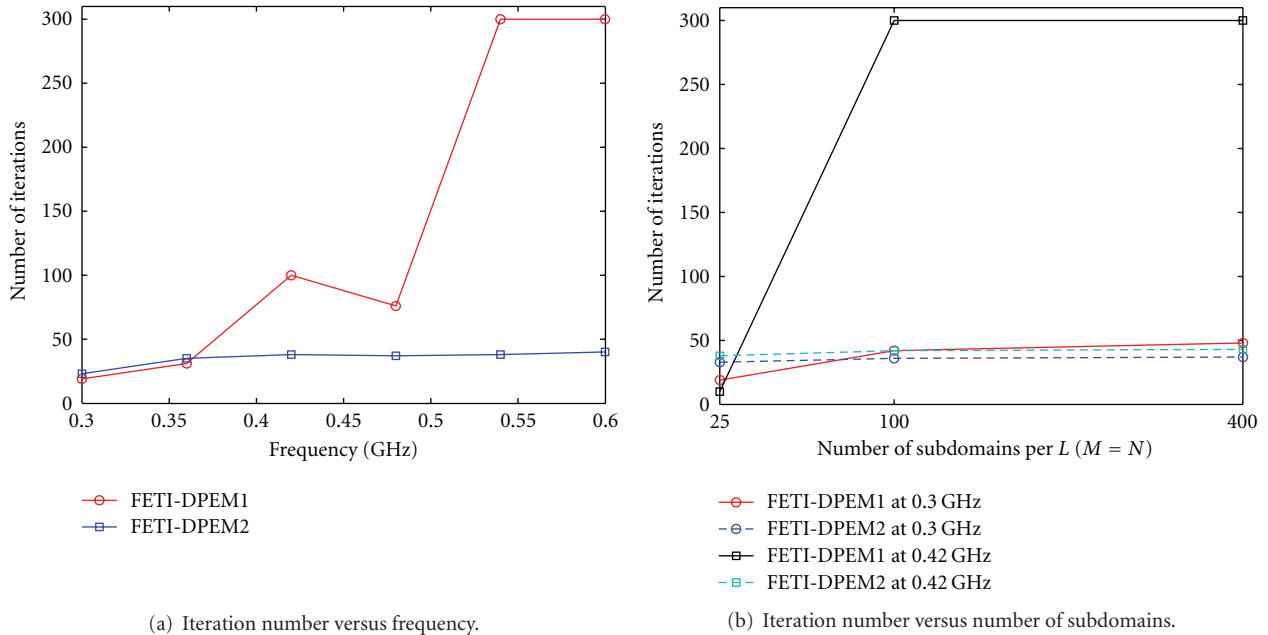


FIGURE 3: Iteration number required by FETI-DPEM1 and FETI-DPEM2.

To demonstrate the efficiency and capability of the two FETI-DPEM methods, the following numerical experiments are performed on a dielectric brick. The absorbing boundary is placed  $0.5\lambda_0$  away from the surface of the brick. The solution domain is divided into  $M$  segments in  $x$ -direction and  $N$  segments in  $y$ -direction as shown in Figure 2(a), which is called 2D-extended decomposition. The solution domain also can be divided into  $M$ ,  $N$ , and  $L$  segments in  $x$ ,  $y$ , and  $z$  directions, respectively, which is called 3D-extended decomposition.

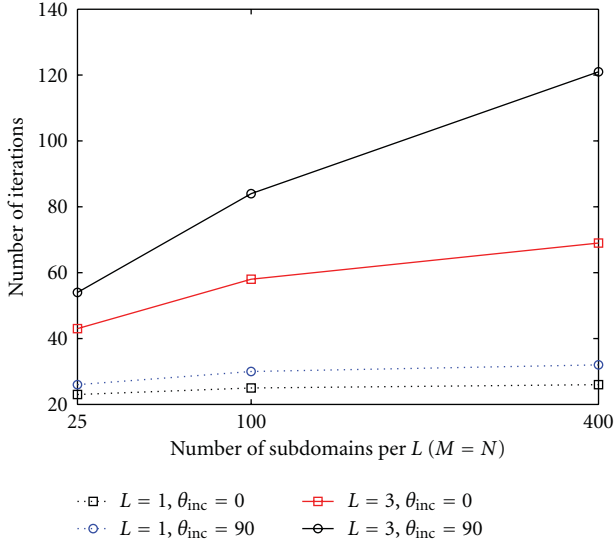
First, let us investigate the performance of FETI for 2D-extended decomposition. The subdomain is a dielectric cube with side length 0.5 m having  $\epsilon_r = 4$ ,  $\mu_r = 1$ .

Mesh size is fixed as 0.05 m. We increase the frequency of the incident wave from 0.3 GHz to 0.6 GHz. The iteration numbers required by FETI-DPEM1 and FETI-DPEM2 with frequency and number of subdomains are presented in Figures 3(a) and 3(b). As we see, the iteration number required by FETI-DPEM2 almost maintains constant with frequency and number of subdomains, whereas that by FETI-DPEM1 increase with frequency and number of subdomain, especially for high frequency, which completely agree with the conclusions in [6, 7].

Second, let us investigate the performance of FETI for 3D-extended decomposition. We fix subdomain size as  $0.2 \text{ m} \times 0.2 \text{ m} \times 0.2 \text{ m}$  with incident frequency 0.3 GHz and

TABLE 1: Iteration number versus the number of subdomains.

$M, N, L$	Number of subdomains	FETI-DPEM1		FETI-DPEM2	
		Dual unknowns	Iteration number	Dual unknowns	Iteration number
3, 3, 3	27	2160	37	4320	40
5, 5, 5	125	12000	359	24000	69
10, 10, 10	1000	108000	>500	21600	127

FIGURE 4: Iteration number versus number of subdomains for different  $L$ .TABLE 2: Iteration number required by FETI-DPEM2 for dielectric cube with different materials versus  $\alpha$ .

$\alpha$	$jk_0$	$1.5jk_0$	$2jk_0$	$2.5jk_0$	$3jk_0$	$3.5jk_0$
$\epsilon_r = 4$	105	87	84	86	93	103
$\epsilon_r = 9$	321	254	233	228	232	250

increase  $M$ ,  $N$ , and  $L$  at the same time. Table 1 lists number of iterations for FETI-DPEM1 and FETI-DPEM2. It can be seen that the iteration number required by FETI-DPEM2 increases with the number of sub-domains. To further show the differences between different types of domain decomposition, we fix subdomain size as  $0.5 \text{ m} \times 0.5 \text{ m} \times 0.5 \text{ m}$  and change  $L$  from 1 to 3. Figure 4 shows the iteration number of the FETI-DPEM2 versus number of subdomains for different  $L$  with different incident degree. It can be seen from Figure 4 that, for the 2D-extended domain decomposition, the iteration numbers maintain nearly constant with number of subdomains for different directions of incident wave, but for the 3D-extended domain decomposition, the iteration numbers are not constant again and increase with the number of subdomains. Furthermore, the increase speed of the iteration number with the number of subdomains changes for different incident wave directions. To exclude the possibility due to the increase in number of subdomains, another comparison is provided between  $10 \times 10$  with  $L = 3$

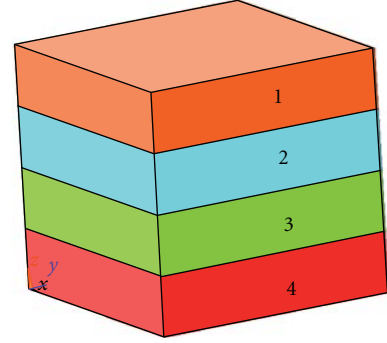


FIGURE 5: An inhomogeneous dielectric brick with four different materials.

and  $30 \times 10$  with  $L = 1$ . The total subdomains are the same, but the numbers of iterations are 58 and 25, respectively. The latter is nearly the same as those in Figure 4.

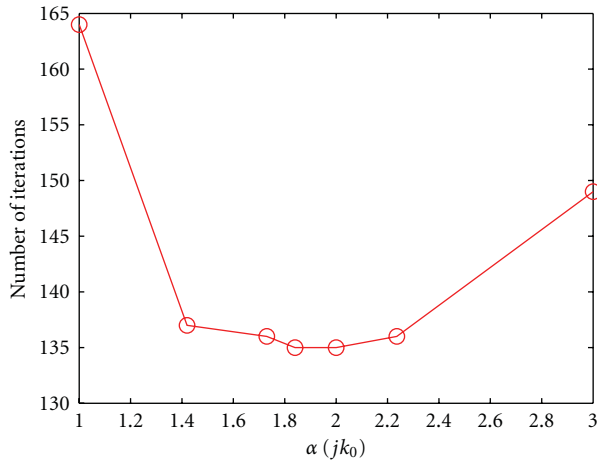
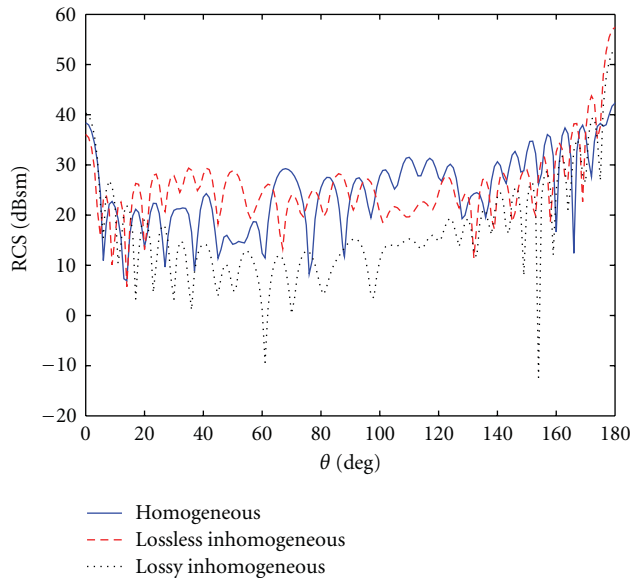
Third, we will investigate numerical performance of FETI-DPEM2 versus inhomogeneity. Our numerical experiments are performed on a dielectric cube with  $1 \text{ m} \times 1 \text{ m} \times 1 \text{ m}$  at 0.3 GHz. We set two cases of the relative dielectric constant  $\epsilon_r = 4$  and  $\epsilon_r = 9$ , respectively. Mesh size is fixed as 0.05 m and 0.025 m for these two cases, respectively. The size of sub-domain is  $0.5 \text{ m} \times 0.5 \text{ m} \times 0.5 \text{ m}$ , and 64 sub-domains are used. The iteration numbers required by FETI-DPEM2 are 105 and 321 for two cases respectively. It shows that the performance of FETI highly depends on the inhomogeneity of the solution domain. It is worth to point out that in all above computation in FETI-DPEM2, the parameter  $\alpha$  in (6) is chosen as  $jk_0$ . In fact, this parameter can be modified to get a better convergence. Table 2 shows that the iteration number required by FETI-DPEM2 versus  $\alpha$ . It can be seen from Table 2 that the almost best convergence of FETI-DPEM2 can be achieved by choosing  $\alpha = jk = j\sqrt{\mu_r\mu_0\epsilon_r\epsilon_0}$ , which agrees with that in [12].

To further investigate numerical performance of FETI-DPEM2 for inhomogeneity, we perform an experiment for inhomogeneous brick as shown in Figure 5. This brick has four layers, which have different dielectric constants with  $\epsilon_1 = 2$ ,  $\epsilon_2 = 3$ ,  $\epsilon_3 = 4$ , and  $\epsilon_4 = 5$ , respectively. The thickness of each layer is 0.5 m. Figure 6 presents the iteration number required by FETI-DPEM2 versus  $\alpha$ . It can be obtained from Figure 6 that the optimal performance of FETI-DPEM2 is achieved by choosing  $\alpha = jk$ , where  $k$  can be approximated as average propagation constant of  $k = (k_1 + k_2 + k_3 + k_4)/4 = 1.84 k_0$ .

At last, to show the great capability of the FETI-DPEM method, we compute the scattering by a large dielectric brick

TABLE 3: Computation resources for the large dielectric brick.

Material type	Dual unknowns (M)	Corner unknowns (M)	Total unknowns (M)	Memory (GB)	Iteration Number	Total CPU time (Min)
Homogeneous					215	323
Inhomogeneous (Lossless)	9.2	0.2	41	8.2	388	481
Inhomogeneous (Lossy)					54	105

FIGURE 6: Iteration number for the brick versus different  $\alpha$ .FIGURE 7: Bistatic RCS of the large dielectric brick with  $\theta_{\text{inc}} = 0^\circ$ ,  $\varphi_{\text{inc}} = 0^\circ$  at 0.3 GHz.

up to  $10 \text{ m} \times 10 \text{ m} \times 5 \text{ m}$  at 0.3 GHz. Three types of material constitutions of the brick are taken into consideration, which are homogeneous, lossless inhomogeneous, and lossy inhomogeneous. For homogeneous case, the brick is filled with material of  $\epsilon_r = 2$ . For lossless inhomogeneous case, the brick is filled with material of  $\epsilon_r = 2$  and  $\epsilon_r = 4$

repeatedly along  $-z$  direction with thickness of 0.5 m. For lossy inhomogeneous condition, the dielectric constants of material are set to  $\epsilon_r = 2$  and  $\epsilon_r = 4 - j$ , respectively. The bistatic RCSs by these bricks are shown in Figure 7. In these calculations, subdomain size is  $0.5 \text{ m} \times 0.5 \text{ m} \times 0.5 \text{ m}$ , and the ABC is placed 0.5 m away from the brick. Total  $22 \times 22 \times 12$  subdomains are used. Computation resources needed in this calculation are listed in Table 3.

#### 4. Conclusions

The FETI with the absorbing boundary condition (ABC) is applied to electromagnetic scattering by large inhomogeneous targets in this paper. The convergence speed of FETI-DPEM1 becomes seriously slow with the number of subdomains, especially for high frequency. FETI-DPEM2 is much faster than FETI-DPEM1 with number of subdomains. However, FETI-DPEM2 also cannot maintain the convergence speed with number of sub-domains for the 3D-extended decomposition. Furthermore, the convergence speed of FETI-DPEM2 highly depends on inhomogeneity of targets. Taking inhomogeneity into the coefficient in the Robin transmission condition can improve the convergence speed of FETI-DPEM2.

#### Acknowledgment

This work was supported by the NSFC under Grant 10832002.

#### References

- [1] B. Després, P. Joly, and J. E. Roberts, "A domain decomposition method for the harmonic Maxwell equations," in *Iterative Methods in Linear Algebra*, pp. 475–484, Elsevier, Amsterdam, The Netherlands, 1992.
- [2] Y. J. Li and J. M. Jin, "Implementation of the second-order ABC in the FETI-DPEM method for 3D EM problems," *IEEE Transactions on Antennas and Propagation*, vol. 56, no. 8, pp. 2765–2769, 2008.
- [3] C. Farhat and F. X. Roux, "Method of finite element tearing and interconnecting and its parallel solution algorithm," *International Journal for Numerical Methods in Engineering*, vol. 32, no. 6, pp. 1205–1227, 1991.
- [4] C. T. Wolfe, U. D. Navsariwala, and S. D. Gedney, "An efficient implementation of the finite-element time-domain algorithm on parallel computers using a finite-element tearing and interconnecting algorithm," *Microwave and Optical Technology Letters*, vol. 16, no. 4, pp. 204–208, 1997.

- [5] C. Farhat, P. Avery, R. Tezaur, and J. Li, "FETI-DPH: a dual-primal domain decomposition method for acoustic scattering," *Journal of Computational Acoustics*, vol. 13, no. 3, pp. 499–524, 2005.
- [6] Y. Li and J. M. Jin, "A vector dual-primal finite element tearing and interconnecting method for solving 3-D large-scale electromagnetic problems," *IEEE Transactions on Antennas and Propagation*, vol. 54, no. 10, pp. 3000–3009, 2006.
- [7] Y. J. Li and J. M. Jin, "A new dual-primal domain decomposition approach for finite element simulation of 3-D large-scale electromagnetic problems," *IEEE Transactions on Antennas and Propagation*, vol. 55, no. 10, pp. 2803–2810, 2007.
- [8] F. X. Roux, F. Magoul'es, L. Series, and Y. Boubendir, "Approximation of optimal interface boundary conditions for two-Lagrange multiplier FETI method," *Lecture Notes in Computational Science and Engineering*, vol. 40, pp. 283–290, 2005.
- [9] M. N. Vouvakis and J. F. Lee, "A fast non-conforming DP-FETI domain decomposition method for the solution of large EM problems," in *Proceedings of the IEEE Antennas and Propagation Society Symposium*, pp. 623–626, June 2004.
- [10] J. P. Webb and V. N. Kanellopoulos, "Absorbing boundary conditions for the finite element solution of the vector wave equation," *Microwave and Optical Technology Letters*, vol. 2, no. 10, pp. 370–372, 1989.
- [11] Y. Saad and M. H. Schultz, "GMRES: a generalised minimal residual algorithm for solving nonsymmetric linear systems," *SIAM Journal of Scientific and Statistical Computing*, vol. 7, pp. 856–869, 1986.
- [12] K. Zhao, V. Rawat, S. C. Lee, and J. F. Lee, "A domain decomposition method with nonconformal meshes for finite periodic and semi-periodic structures," *IEEE Transactions on Antennas and Propagation*, vol. 55, no. 9, pp. 2559–2570, 2007.

## Research Article

# Optimized Operator-Splitting Methods in Numerical Integration of Maxwell's Equations

Z. X. Huang,<sup>1</sup> X. L. Wu,<sup>1</sup> W. E. I. Sha,<sup>2</sup> and B. Wu<sup>1</sup>

<sup>1</sup>Key Lab of Intelligent Computing & Signal Processing, Anhui University, Hefei 230039, China

<sup>2</sup>Department of Electrical and Electronic Engineering, University of Hong Kong, Hong Kong

Correspondence should be addressed to Z. X. Huang, zxhuang@ahu.edu.cn

Received 11 March 2011; Accepted 27 April 2011

Academic Editor: Ning Yuan

Copyright © 2012 Z. X. Huang et al. This is an open access article distributed under the Creative Commons Attribution License, which permits unrestricted use, distribution, and reproduction in any medium, provided the original work is properly cited.

Optimized operator splitting methods for numerical integration of the time domain Maxwell's equations in computational electromagnetics (CEM) are proposed for the first time. The methods are based on splitting the time domain evolution operator of Maxwell's equations into suboperators, and corresponding time coefficients are obtained by reducing the norm of truncation terms to a minimum. The general high-order staggered finite difference is introduced for discretizing the three-dimensional curl operator in the spatial domain. The detail of the schemes and explicit iterated formulas are also included. Furthermore, new high-order Padé approximations are adopted to improve the efficiency of the proposed methods. Theoretical proof of the stability is also included. Numerical results are presented to demonstrate the effectiveness and efficiency of the schemes. It is found that the optimized schemes with coarse discretized grid and large Courant-Friedrichs-Lewy (CFL) number can obtain satisfactory numerical results, which in turn proves to be a promising method, with advantages of high accuracy, low computational resources and facility of large domain and long-time simulation. In addition, due to the generality, our optimized schemes can be extended to other science and engineering areas directly.

## 1. Introduction

The finite-difference time-domain (FDTD(2, 2)) method [1, 2] has been widely used to simulate the transient solutions of electromagnetic problems involving the analysis and design of microwave structures, many other engineering applications, and the electromagnetic wave propagation in various media. Despite its simplicity and modeling versatility; however, FDTD(2, 2) is very computationally intensive due to its two inherent physical constraints, one being the numerical dispersion and another being the numerical stability. These limitations have always made it a matter of great interest to improve the efficiency of FDTD(2, 2) scheme and have led researchers to the development of various new schemes.

To improve the numerical dispersion, some high-order space strategies have been put forward. For example, Fang proposed the high-order FDTD(4,4) method [3]. Yet, the method is difficult to handle material interface for modeling the complex three-dimensional objects. Another

approach is the staggered FDTD(2, 4) method [4–6]. However, the method must set lower Courant-Friedrichs-Lewy (CFL) number to obtain high-order numerical precision. In order to further explore efficient methods for optimum electromagnetic simulation, new improved time strategies referred as the high-order Runge-Kutta (R-K) approach was introduced in [7, 8]. However, the approach is dissipative and needs large amount of memory. Other alternative method is the alternating direction implicit FDTD (ADI-FDTD) algorithm [9, 10]. Although it saves CPU time owing to unconditional stability, undesirable numerical precision and dispersion will happen once the high CFL number is adopted. Another systematic approach to solve the time-dependent Maxwell equations with unconditionally stable numerical schemes was proposed and developed [11]. The basic idea of the methods is to employ a Lie-Trotter-Suzuki product formula to approximate the time evolution operator. As shown in [12], most of these methods can be seen as special cases of the time-operator-splitting methods where the original time evolution operator is split into a

number of suboperators. There are two good reasons for this. Firstly, many such suboperators are simple and easy to implement. Secondly, splitting methods can preserve important mathematical and physical properties of the original system. Now methods of operator-splitting have been widely used and considered in various applications in science and engineering—from the evolution of techniques for solving linear equations that arise in reservoir simulation, astrophysical, and bioengineering applications to tsunami modeling and furthermore.

In this paper, particularly, we consider optimized operator-splitting methods for numerical solution of the time-dependent Maxwell's equations. In Section 2, the time-domain Maxwell's equations are rewritten as a time evolution matrix operator form. The novel approach is proposed to improve the efficiency of the time evolution operator based on splitting it into suboperator, and optimal time coefficients are obtained by reducing the norm of truncation terms to a minimum. The general high-order staggered finite difference is introduced for discretizing the three-dimension curl operator in the spatial domain. The explicit discretized formulas are presented in Section 3. New high-order Padé approximations and the stability analysis are also included. Section 4 presents numerical examples, and the conclusions are made in Section 5.

## 2. General Formulations of Splitting Schemes

*2.1. The Unique Solution of Time Domain Maxwell Equations in Matrix Form.* Maxwell's equations in an isotropic medium can be rewritten in a matrix form as

$$\frac{\partial}{\partial t} \begin{pmatrix} \mathbf{H} \\ \mathbf{E} \end{pmatrix} = (\mathbf{A} + \mathbf{B}) \begin{pmatrix} \mathbf{H} \\ \mathbf{E} \end{pmatrix},$$

$$\mathbf{A} = \begin{pmatrix} -\mu^{-1}\sigma^*\mathbf{I}_3 & -\mu^{-1}\mathbf{R} \\ \mathbf{0}_{3\times 3} & \mathbf{0}_{3\times 3} \end{pmatrix}, \quad \mathbf{B} = \begin{pmatrix} \mathbf{0}_{3\times 3} & \mathbf{0}_{3\times 3} \\ \varepsilon^{-1}\mathbf{R} & -\varepsilon^{-1}\sigma\mathbf{I}_3 \end{pmatrix}, \quad (1)$$

where  $\mu$  and  $\varepsilon$  are the permeability and permittivity,  $\sigma$  and  $\sigma^*$  are electric and magnetic conductivities,  $\mathbf{0}_{3\times 3}$  and  $\mathbf{I}_3$  are  $3 \times 3$  zeros matrix and identity matrix,  $\mathbf{R}$  is  $3 \times 3$  matrix representing three-dimensional curl operator. Equation (1) can be cast in the following compact form

$$\frac{d\mathbf{Z}}{dt} = \mathbf{L}\mathbf{Z}(t). \quad (2)$$

Here,  $\mathbf{Z}(t) = [\mathbf{H}(t), \mathbf{E}(t)]^T$  is the full electromagnetic field variable. Although only the time dependence is written explicitly, all these quantities additionally depend on space, but for simplicity of notation, we will omit the spatial dependence. If an initial configuration  $\mathbf{Z}(\mathbf{0})$  is provided, the unique solution to (2) can be presented as

$$\mathbf{Z}(\Delta t) = e^{\mathbf{L}\Delta t}\mathbf{Z}(\mathbf{0}) \equiv e^{(\mathbf{A}+\mathbf{B})\Delta t}\mathbf{Z}(\mathbf{0}), \quad (3)$$

where  $\Delta t$  denotes the time step, and the operator  $\mathbf{L} = \mathbf{A} + \mathbf{B}$  has been split into two suboperators. The significance of such splitting will be understood below.

*2.2. The Splitting Method for Exponential Propagator in the Time Domain.* Note, solution (3) is quite formal because the exponential propagator  $e^{\mathbf{L}\Delta t}$  does not allow to be evaluated exactly at any given  $\Delta t$ . However, at small enough values of  $\Delta t$ , the total propagator can be split using the formula

$$e^{\Delta t(\mathbf{A}+\mathbf{B})} = \prod_{l=1}^m e^{\mathbf{B}d_l\Delta t} e^{\mathbf{A}c_l\Delta t} + O(\Delta t^{n+1}). \quad (4)$$

The coefficients  $c_l$  and  $d_l$  in this formula should be chosen in such a way to provide the highest possible value for  $n$  at a given integer number  $m$ . Here  $m$  is stage number needed in every integer time step, and  $n$  is the order of the approximation. The main advantage of the above splitting is that the time-reversibility  $\Psi(-t)\mathbf{Z}(t) = \mathbf{Z}(\mathbf{0})$  of solutions (following from the property  $\Psi^{-1}(t) = \Psi(-t)$  of time evolution operator  $\Psi(t) = e^{\mathbf{L}t}$ ) can also be reproduced by imposing additional time reversible constraints on the coefficients, namely,  $c_l = c_{m-l+1}$ , and  $d_l = d_{m-l}$  with  $d_m = 0$ . Note also that the splitting method is quite general to build numerical integrators of arbitrary orders  $n$  with  $m$  stages. But we cannot choose the stage  $m$  too large, because this results in a too large number, namely  $m-1$ , of expensive force every time step. In this paper, particularly, we choose  $m = 5$  and minimize the truncation errors to  $O(\Delta t^5)$  significantly with a little additional computational cost.

For  $m = 5$ , the extended splitting result can be represented in the form

$$e^{\Delta t(\mathbf{A}+\mathbf{B})} = e^{\mathbf{A}c_1\Delta t} e^{\mathbf{B}d_1\Delta t} e^{\mathbf{A}c_2\Delta t} e^{\mathbf{B}d_2\Delta t} e^{\mathbf{A}c_3\Delta t} e^{\mathbf{B}d_3\Delta t} e^{\mathbf{A}c_4\Delta t} e^{\mathbf{B}d_4\Delta t} e^{\mathbf{A}c_5\Delta t} \\ + \Upsilon_1\Delta t^3 + \Upsilon_2\Delta t^5 + O(\Delta t^7). \quad (5)$$

Note also, the propagators can be calculated analytically as follows:

$$e^{\mathbf{A}c_l\Delta t} = \begin{pmatrix} \exp\left(-\frac{\Delta t c_l \sigma^*}{\mu}\right)\mathbf{I}_3 & -\frac{1 - \exp(-\Delta t c_l \sigma^*/\mu)}{\sigma^*}\mathbf{R} \\ \mathbf{0}_{3\times 3} & \mathbf{I}_3 \end{pmatrix},$$

$$e^{\mathbf{B}d_l\Delta t} = \begin{pmatrix} \mathbf{I}_3 & \mathbf{0}_{3\times 3} \\ \frac{1 - \exp(-\Delta t d_l \sigma/\varepsilon)}{\sigma}\mathbf{R} & \exp\left(-\frac{\Delta t d_l \sigma}{\varepsilon}\right)\mathbf{I}_3 \end{pmatrix}. \quad (6)$$

Here, the time reversible coefficients and the condition  $\sum_{l=1}^5 c_l = \sum_{l=1}^5 d_l = 1$  have already been taken into account. With these assumptions, we actually only have three coefficients, namely,  $\{c_1, c_2, d_1\}$  to be determined. Using the Baker-Campbell-Hausdorff (BCH) formula, the explicit expression for  $\Upsilon_1$  and  $\Upsilon_2$  can be expressed as

$$\Upsilon_1 = f_1[\mathbf{A}, [\mathbf{A}, \mathbf{B}]] + f_2[\mathbf{A}, [\mathbf{A}, \mathbf{B}]],$$

$$\Upsilon_2 = f_3[\mathbf{A}, [\mathbf{A}, [\mathbf{A}, [\mathbf{A}, \mathbf{B}]]]] + f_4[\mathbf{A}, [\mathbf{A}, [\mathbf{B}, [\mathbf{A}, \mathbf{B}]]]] \\ + f_5[\mathbf{B}, [\mathbf{A}, [\mathbf{A}, [\mathbf{A}, \mathbf{B}]]]] + f_6[\mathbf{B}, [\mathbf{B}, [\mathbf{B}, [\mathbf{A}, \mathbf{B}]]]] \\ + f_7[\mathbf{B}, [\mathbf{B}, [\mathbf{A}, [\mathbf{A}, \mathbf{B}]]]] + f_8[\mathbf{A}, [\mathbf{B}, [\mathbf{B}, [\mathbf{A}, \mathbf{B}]]]]. \quad (7)$$

Here,  $[\mathbf{A}, \mathbf{B}] = \mathbf{AB} - \mathbf{BA}$  and  $f_i = f_i(c_1, c_2, d_1)$ ,  $i \in \{1, 2, \dots, 8\}$ . The detailed expression of  $f_i$  can be founded in [13]. The formula (5) represents a fourth-order scheme at  $Y_1 = 0$ , that is,  $f_1$  and  $f_2$  equal to zero. Now, we have three coefficients and only two equations, we are free to set one more equation. In this paper, we choose to reduce the fifth-order truncation error terms  $Y_2$  to a minimum, and the coefficients  $\{c_1, c_2, d_1\}$  can be obtained by solving the system of equations

$$\begin{aligned} \min \quad & \left\{ \sqrt{\sum_{i=3}^8 f_i^2(c_1, c_2, d_1)} \right\} \\ \text{subject to:} \quad & f_1(c_1, c_2, d_1) = 0 \\ & f_2(c_1, c_2, d_1) = 0. \end{aligned} \quad (8)$$

One possible set of the coefficients are  $c_1 = 0.1786$ ,  $c_2 = -0.0066$ ,  $d_1 = 0.7123$ , consists global minimum truncation error 0.00093. Now, we transfer to the discretization of spatial domain.

**2.3. The  $M$ th-Order Difference Approximation for the First-Order Spatial Partial Derivative Operators.** Let  $f|_{i,j,k}^n = f(i\Delta x, j\Delta y, k\Delta z; n\Delta t)$  approximates the exact solution  $f$  at the point  $(i\Delta x, j\Delta y, k\Delta z)$  in the  $n$ th time step. The following staggered  $M$ th-order space difference operators are used to approximate the first-order spatial partial derivative in the  $\zeta$ -direction, that is,  $\partial_\zeta, \zeta \in \{x, y, z\}$  in three-dimensional curl operator  $\mathbf{R}$ . So

$$\begin{aligned} \mathfrak{R}_i \cdot f_{i,j,k}^n &\equiv \frac{\partial}{\partial x} f \Big|_{i,j,k}^n \\ &= \frac{1}{\Delta x} \sum_{s=1}^{M/2} \xi_s \left[ f|_{i+(2s-1)/2,j,k}^n - f|_{i-(2s-1)/2,j,k}^n \right] \\ &\quad + O(\Delta x)^M. \end{aligned} \quad (9)$$

Here, parameters  $\xi_s = (-1)^{s+1} ((M-1)!!)^2 / 2^{M-2} (M/2 + s - 1)! (M/2 - s)! (2s - 1)^2$  for minimum truncation error in (9). Similarly,  $\mathfrak{R}_j \cdot f_{i,j,k}^n$  and  $\mathfrak{R}_k \cdot f_{i,j,k}^n$  are constructed in a similar manner and used to approximate  $\partial_y f_{i,j,k}^n$  and  $\partial_z f_{i,j,k}^n$ , respectively.

### 3. Practical Implementation

**3.1. Explicit Discretization Formulas.** When one uses coefficients  $c_l$  and  $d_l$  of order four and substitutes the space difference operators with  $M$ th-order accuracy for the first-order partial difference operators in  $\mathbf{R}$ , the  $(4, M)$  scheme is acquired.

For example, using Yee grid [1], the detailed expressions of  $H_x$  and  $E_x$  components in the  $(4, M)$  scheme at the  $l$ th stage calculation after the  $n$ th time step are as follows:

$$\begin{aligned} & H_x^{n+l/5} \left( i, j + \frac{1}{2}, k + \frac{1}{2} \right) \\ &= \exp(-w_1) \times H_x^{n+(l-1)/5} \left( i, j + \frac{1}{2}, k + \frac{1}{2} \right) \\ &\quad + \frac{1 - \exp(-w_1)}{w_1} \cdot \left\{ \mathfrak{R}_k \cdot E_y^{n+(l-1)/5} \left( i, j + \frac{1}{2}, k + \frac{1}{2} \right) \right. \\ &\quad \left. - \mathfrak{R}_j \cdot E_z^{n+(l-1)/5} \left( i, j + \frac{1}{2}, k + \frac{1}{2} \right) \right\}, \\ & E_x^{n+l/5} \left( i + \frac{1}{2}, j, k \right) \\ &= \exp(-w_2) \times E_x^{n+(l-1)/5} \left( i + \frac{1}{2}, j, k \right) \\ &\quad + \frac{1 - \exp(-w_2)}{w_2} \cdot \left\{ \mathfrak{R}_j \cdot H_z^{n+l/5} \left( i + \frac{1}{2}, j, k \right) \right. \\ &\quad \left. - \mathfrak{R}_k \cdot H_y^{n+l/5} \left( i + \frac{1}{2}, j, k \right) \right\} \end{aligned} \quad (10)$$

with

$$\begin{aligned} w_1 &= \frac{c_l \Delta t \bar{\sigma}^* (i, j + 1/2, k + 1/2)}{\mu(i, j + 1/2, k + 1/2)}, \\ w_2 &= \frac{d_l \Delta t \bar{\sigma} (i + 1/2, j, k)}{\bar{\epsilon}(i + 1/2, j, k)}. \end{aligned} \quad (11)$$

Here

(i) we use Padé(0, 3) and Padé(1, 2) to approximate the expressions of  $\exp(-w_i)$  and  $(1 - \exp(-w_i))/w_i$ :

$$\begin{aligned} \exp(-w_i) &\approx \frac{1}{1 + w_i + w_i^2/2 + w_i^3/6}, \\ \frac{1 - \exp(-w_i)}{w_i} &\approx \frac{1 + w_i/2}{1 + w_i + w_i^2/3}. \end{aligned} \quad (12)$$

Our new approximate acquired super stability and efficiency than the Padé(2, 2) method in [14] when  $w_i$  increases, as indicated in Figure 1. In addition, our approximate can be not only used to treat interior dielectric medium and conductor, but also directly applied in Berenger's perfectly matched layer (PML) absorbing boundary conditions [15].

(ii) The averaged permittivity  $\bar{\epsilon}$  over the patch  $S$  can be expressed as

$$\bar{\epsilon} = \frac{\alpha}{s_1} \iint_{s_1} \epsilon_1 ds_1 + \frac{1 - \alpha}{s_2} \iint_{s_2} \epsilon_2 ds_2, \quad (13)$$

where  $s_1$  and  $s_2$  are the surfaces enclosed by curve-labeled single arrow ( $\epsilon = \epsilon_1$ ) and double arrow ( $\epsilon = \epsilon_2$ ) as indicated in Figure 2,  $\alpha$  is free parameter, and we use  $\alpha = 9/8$  in our

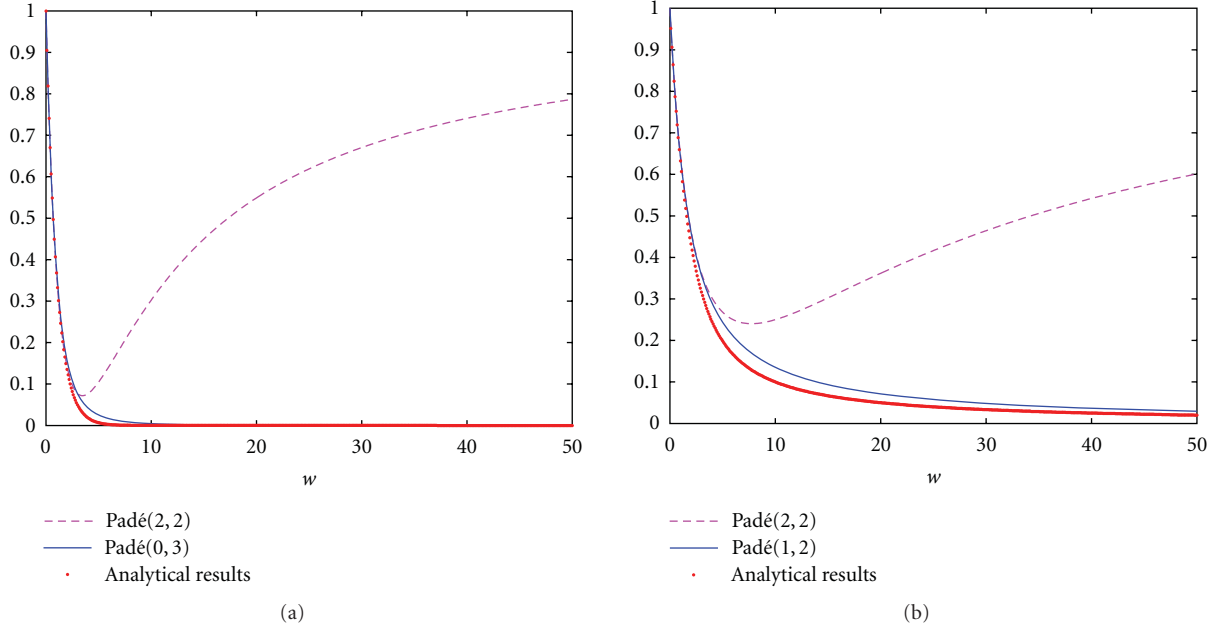


FIGURE 1: Comparison between two kinds of approximation. (a) For  $e^{-w}$  and (b)  $(1 - e^{-w})/w$ .

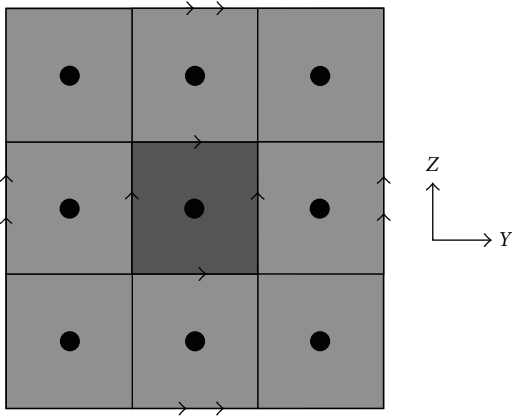


FIGURE 2: Subcell technique specifies for the  $E_x$  field calculation in  $(4, M)$  scheme.

following numerical examples in order to be consistent with the high-order difference in spatial direction. In addition, the averaged conductivity can be treated in a similar way, which consumes little CPU time at the initial process by refined subcell modeling.

**3.2. The Stability of the Proposed  $(4, M)$  Scheme.** The conventional Fourier mode method is used to analyze the stability of the proposed  $(4, M)$  scheme. For clarity, the discussion begins with a 1-D  $z$ -directed,  $x$ -polarized TEM wave. The equations can be rewritten as

$$\frac{\partial}{\partial t} \begin{pmatrix} H_y \\ E_x \end{pmatrix} = \begin{pmatrix} 0 & -\frac{1}{\mu} \frac{\partial}{\partial z} \\ -\frac{1}{\varepsilon} \frac{\partial}{\partial z} & 0 \end{pmatrix} \begin{pmatrix} H_y \\ E_x \end{pmatrix}. \quad (14)$$

The field components in the  $n$ th time-step are denoted as

$$\begin{pmatrix} H_y \\ E_x \end{pmatrix} \Big|_{z=k}^n = \begin{pmatrix} H_0^n \cdot e^{-j_0 \cdot k_z \cdot k \Delta z} \\ E_0^n \cdot e^{-j_0 \cdot k_z \cdot k \Delta z} \end{pmatrix}, \quad (15)$$

here,  $k_z$  is the spatial frequency along the  $z$ -direction. Substituted (15) into (9), we obtain

$$\begin{aligned} \frac{\partial F}{\partial z} \Big|_k^n &= \sum_{s=1}^{M/2} \xi_s \frac{e^{-j_0(s-1/2)k_z \Delta z} - e^{j_0(s-1/2)k_z \Delta z}}{\Delta z} \cdot F, \quad F = H_y \text{ or } E_x. \end{aligned} \quad (16)$$

Then (14) can be rewritten as

$$\frac{\partial}{\partial t} \begin{pmatrix} H_y \\ E_x \end{pmatrix} = \begin{pmatrix} 0 & -\frac{1}{\mu} \eta_z \\ -\frac{1}{\varepsilon} \eta_z & 0 \end{pmatrix} \begin{pmatrix} H_y \\ E_x \end{pmatrix} \quad (17)$$

with

$$\eta_z = \sum_{s=1}^{M/2} \xi_s \frac{e^{-j_0(s-1/2)k_z \Delta z} - e^{j_0(s-1/2)k_z \Delta z}}{\Delta z}. \quad (18)$$

Applying the  $(4, M)$  scheme to (17), the time-marching relation can be expressed as

$$\begin{pmatrix} H_0^{n+1} \\ E_0^{n+1} \end{pmatrix} = S \begin{pmatrix} H_0^n \\ E_0^n \end{pmatrix}, \quad (19)$$

where

$$S = \prod_{l=1}^5 \begin{pmatrix} 1 & 0 \\ -\eta_z d_l \Delta t & 1 \end{pmatrix} \begin{pmatrix} 1 & -\eta_z c_l \Delta t \\ 0 & 1 \end{pmatrix} \begin{pmatrix} \mu \\ \varepsilon \end{pmatrix}. \quad (20)$$

Solving for the eigenvalues, we can obtain

$$\lambda_{1,2} = \frac{\text{tr}(S) \pm j_0 \sqrt{4 - \text{tr}(S)^2}}{2}, \quad (21)$$

where

$$\begin{aligned} \text{tr}(S) &= 2 + \sum_{l=1}^5 g_l \left( (\varepsilon \mu)^{-1} \Delta_t^2 \eta_z^2 \right)^l, \\ g_l &= \sum_{1 \leq i_1 < j_1 < i_2 < j_2 < \dots < i_l < j_l \leq 5} c_{i_1} d_{j_1} c_{i_2} d_{j_2} \dots c_{i_l} d_{j_l} \\ &+ \sum_{1 \leq i_1 < j_1 \leq i_2 < j_2 \leq \dots \leq i_l < j_l \leq 5} d_{i_1} c_{j_1} d_{i_2} c_{j_2} \dots d_{i_l} c_{j_l}. \end{aligned} \quad (22)$$

We may conclude that  $|\lambda_{1,2}| = 1$  if  $|\text{tr}(S)| \leq 2$ , and the scheme is stable. Moreover, under this condition, the scheme is non-dissipative.

In the three-dimensional (3D) case, the continuous-time discrete-space Maxwell's equations can be written as

$$\begin{aligned} &\frac{\partial}{\partial t} \begin{pmatrix} \mathbf{H} \\ \mathbf{E} \end{pmatrix} \\ &= \begin{pmatrix} 0 & -\frac{\eta_x e_x + \eta_y e_y + \eta_z e_z}{\mu} \times \\ \frac{\eta_x e_x + \eta_y e_y + \eta_z e_z}{\varepsilon} \times & 0 \end{pmatrix} \begin{pmatrix} \mathbf{H} \\ \mathbf{E} \end{pmatrix}. \end{aligned} \quad (23)$$

Considering  $(\eta_x^2 + \eta_y^2 + \eta_z^2) < 0$ , (23) can be rewritten in tensor form as

$$\begin{aligned} &\frac{\partial}{\partial t} \begin{pmatrix} \mathbf{H} \\ \mathbf{E} \end{pmatrix} \\ &= \begin{pmatrix} 0 & -\frac{\sqrt{-(\eta_x^2 + \eta_y^2 + \eta_z^2)}}{\mu} \bar{\mathbf{K}} \cdot \\ \frac{\sqrt{-(\eta_x^2 + \eta_y^2 + \eta_z^2)}}{\varepsilon} \bar{\mathbf{K}} \cdot & 0 \end{pmatrix} \begin{pmatrix} \mathbf{H} \\ \mathbf{E} \end{pmatrix}, \end{aligned} \quad (24)$$

where  $\bar{\mathbf{K}}$  is the tensor matrix defined by the spherical angles [16]. Using the similar analysis, the same formula as (21) is obtained in the case except that

$$\text{tr}(S) = 2 + \sum_{l=1}^m g_l \left( (\varepsilon \mu)^{-1} \Delta_t^2 (\eta_x^2 + \eta_y^2 + \eta_z^2) \right)^l. \quad (25)$$

Generally speaking, the stability of the scheme is assessed by the Courant-Friedrichs-Levy limit, that is, CFLmax, which can be expressed as

$$\text{CFLmax} = \frac{\Delta t_{\max}}{\lambda_S}, \quad (26)$$

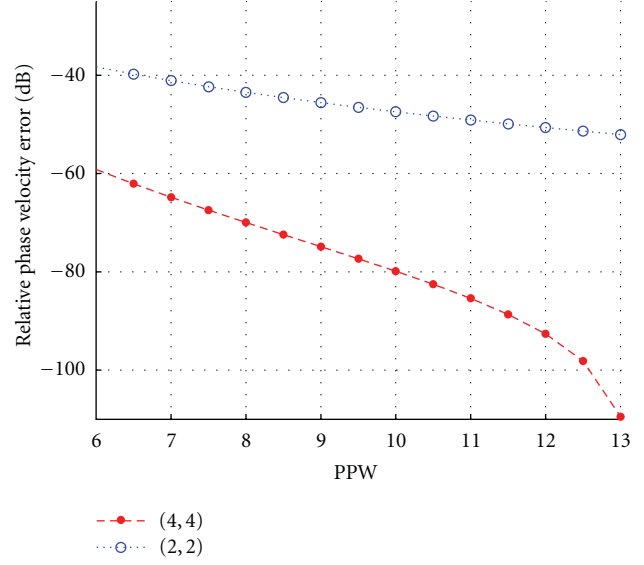


FIGURE 3: Numerical dispersion curves for (4,4) scheme and FDTD(2,2) method.

TABLE 1: CFLmax and accuracy for different methods.

Method	CFLmax		Accuracy
	$D=2$	$D=3$	
(4, 2)	1.05	0.86	$O(\Delta t^4) + O(\Delta \zeta^2)$
(4, 4)	0.90	0.73	$O(\Delta t^4) + O(\Delta \zeta^4)$
(4, 6)	0.85	0.69	$O(\Delta t^4) + O(\Delta \zeta^6)$
FDTD(2, 2)	0.71	0.58	$O(\Delta t^2) + O(\Delta \zeta^2)$

where  $\Delta t_{\max}$  is the temporal stability factor, and the numerical time evolution operator will not blow up for all  $\Delta t$ , which can be determined according to the following inequality

$$\begin{aligned} &\left| 2 + \sum_{l=1}^5 g_l (-\Delta t^2)^l \right| \leq 2, \quad |\Delta t| \leq \Delta t_{\max}, \\ &g_l = \sum_{1 \leq i_1 < j_1 < i_2 < j_2 < \dots < i_l < j_l \leq 5} c_{i_1} d_{j_1} c_{i_2} d_{j_2} \dots c_{i_l} d_{j_l} \\ &+ \sum_{1 \leq i_1 < j_1 \leq i_2 < j_2 \leq \dots \leq i_l < j_l \leq 5} d_{i_1} c_{j_1} d_{i_2} c_{j_2} \dots d_{i_l} c_{j_l}, \end{aligned} \quad (27)$$

here,  $\lambda_S$  is the spatial stability factor, which is defined as  $\lambda_S = 2\sqrt{D} \times \sum_{s=1}^{M/2} |\xi_s|$ , and  $D$  is the dimensional number. The numerical results of CFLmax with (4,  $M$ ) scheme, and FDTD(2, 2) are listed in Table 1. For comparison, we also plot the dispersion curves for (4, 4) and FDTD(2, 2) method in Figure 3. As we can see from Figure 3, the relative phase velocity error decreases with the increasing of sampled points per wavelength (PPW). As expected, (4, 4) scheme acquires better numerical dispersion than FDTD(2, 2) method.

#### 4. Numerical Examples

Remember that we cannot choose the discretized order of  $\partial_\zeta$ ,  $\zeta \in \{x, y, z\}$  to be too large, because this results in a too

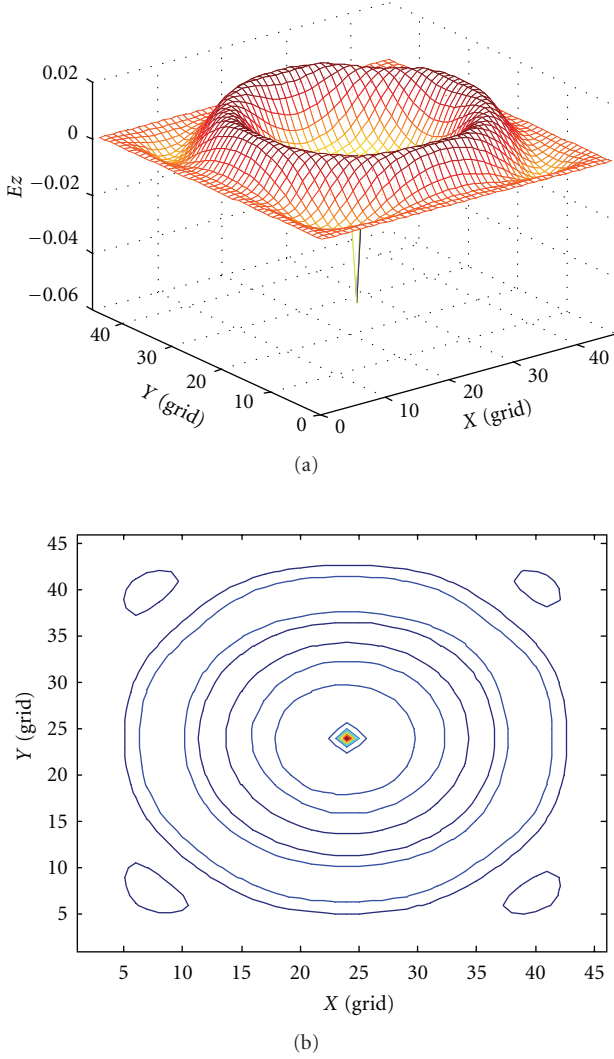


FIGURE 4: Radiation from a dipole with a ten-point PML. (a) The distribution of the  $E_z$  field. (b) The contour of the  $E_z$  amplitude field.

large number of expensive forces in real application. In our following numerical examples, we mainly concentrate on the performers of  $M \leq 4$ .

**4.1. Radiation of a Dipole.** We considered a computational domain of 46 by 46 by 46 cells surrounded by a ten-point PML. A vertical dipole  $P$  was located at point (23,23,23), in the center of the domain. To test the efficiency of our new Padé approximate applied in PML, Figure 4 shows the  $E_z$  field emanating along the plane of  $k = 23$  after 89 time steps. Notice that the part of the field not in the PML radiates concentrically from the source, as it should. In addition, the results for the vertical field  $E_z$  at point (12, 22, 12 + 1/2), two cells from the PML, with FDTD(2, 2) and (4, 4) scheme are summarized in Table 2. Note that for roughly the same computational cost, the (4, 4) scheme gives results that are more accurate than the FDTD(2, 2) method, which in turn proves to be a promising method, with advantages of high

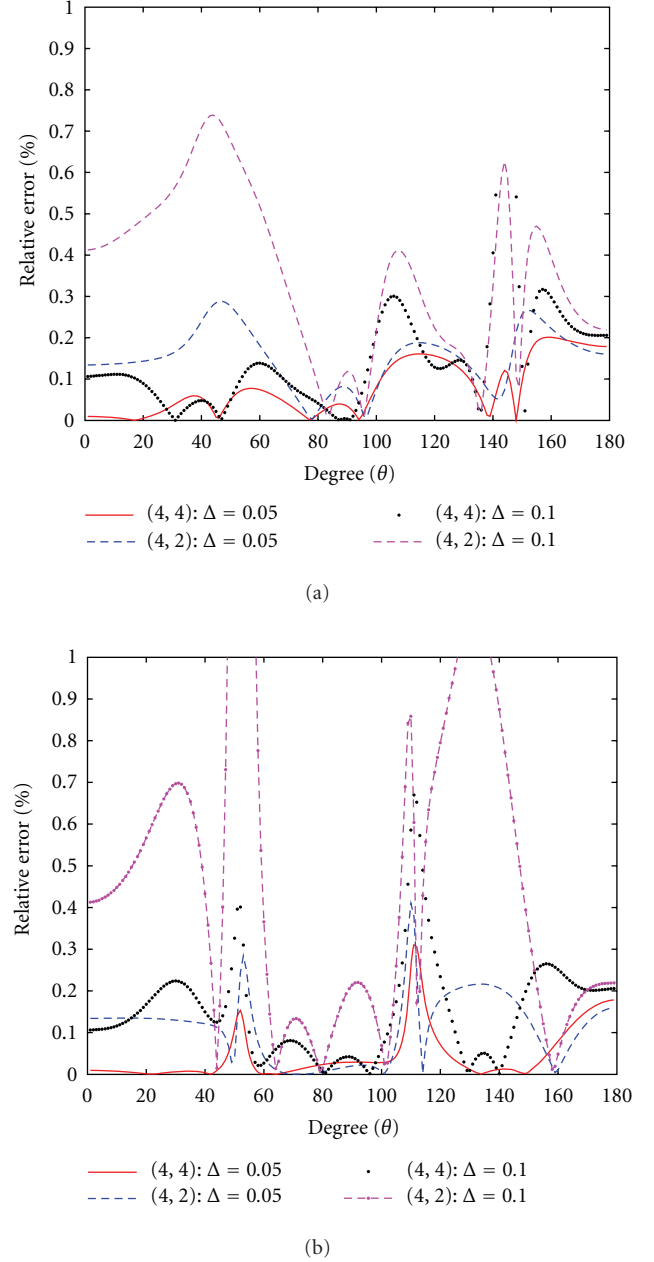


FIGURE 5: The relative error of computed RCS with different scheme at CFL = 0.5. (a)  $E$ -plane (b)  $H$ -plane.

accuracy, low computational resources, and facility of large domain and long time simulation.

**4.2. Scattering of the Dielectric Sphere.** Next, consider a dielectric sphere illuminated by a plane wave propagating in the  $z$ -direction and  $E$  polarized in the  $x$ -direction. The frequency of the incident wave is 300 MHz. The sphere has a diameter of 1.0 m, relative permittivity  $\epsilon_r = 4.0$ , and conductivity of zero. We use uniform grid  $\Delta x = \Delta y = \Delta z = \Delta$ . The total computational domain is 80 by 80 by 80 cells, total field occupies 32 by 32 by 32 cells, and a ten-grid PMLs are

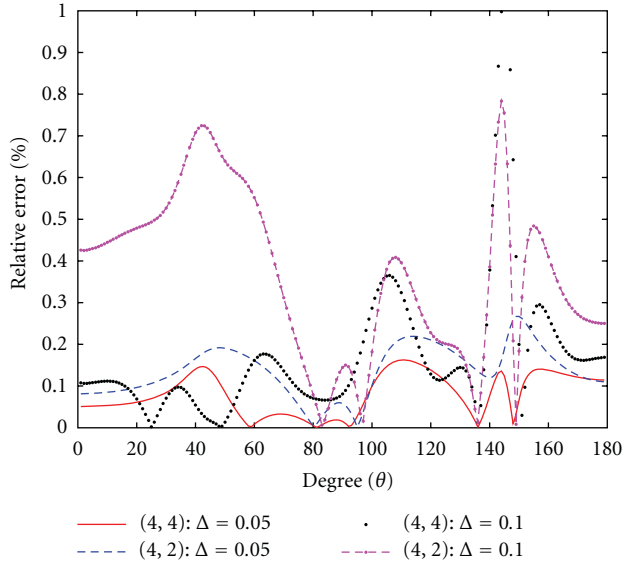


FIGURE 6: The relative error of computed  $E$ -plane RCS with different scheme at CFL = 0.6.

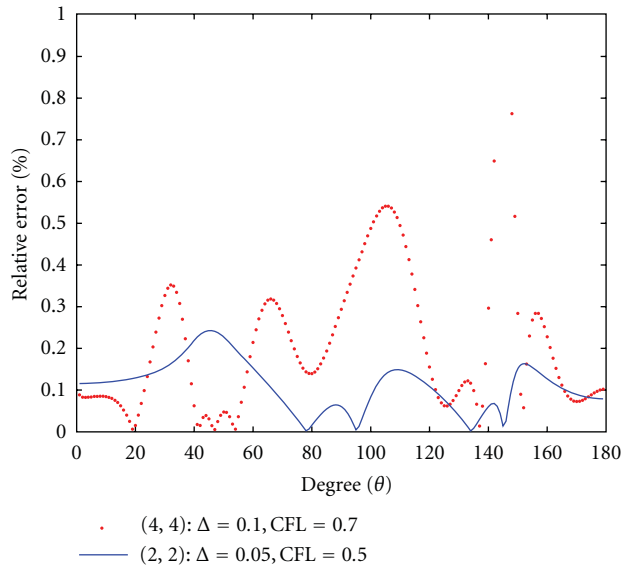


FIGURE 7: The relative error of computed  $E$ -plane RCS with (4,4) and (2,2) schemes.

used. We denote the relative radar cross section (RCS) error as

$$\text{Error} = \frac{|\text{RCS} - \text{RCS}^*|}{|\text{RCS}^*|}, \quad (28)$$

where  $\text{RCS}^*$  is the analytical solution,  $\text{RCS}$  is the solution with FDTD(2,2), (4,2), or (4,4) scheme. Figure 5 shows the relative error of RCS computed with fourth-order accuracy in time domain and fourth-order, second-order accuracy in spatial domain, respectively.

As we can see, the (4,4) scheme is more accurate than the (4,2) scheme under the same discretized grid and CFL

TABLE 2: Comparison of results for FDTD(2,2) and (4,4) scheme.

	FDTD(2,2)	(4,4)
Physical time	200 ns	200 ns
CFL	0.5	0.6
Time step	83.33 ps	200 ps
Spatial step	0.05 m	0.1 m
No. of steps	2400	1000
Total run time	184 sec	131 sec
Average CPU time/step	0.0766 sec	0.1310 sec
Error	1.5920	0.5107

number. When the grid enlarges to  $\Delta = 0.1$ , the error of (4,2) scheme becomes unacceptable. Figure 6 shows the comparisons between (4,4) and (4,2) schemes at CFL = 0.6. In this case, whatever we choose  $\Delta = 0.05$  or  $\Delta = 0.1$ , the results computed by (2,2) scheme are divergent. The reason may be that CFL number exceeds the stability of (2,2) scheme. The results for (4,4) scheme are still acceptable except at some particular angles. Figure 7 shows the comparisons between (4,4) and (2,2) scheme with different discretized grid and CFL number. It is clear that with high CFL number and coarse grid, the results of the (4,4) scheme are still acceptable to some extent. The time spent in (2,2) method is longer, about 16 minutes, and it is about 12 minutes for (4,4) scheme. The memory consumed is around 30 M for (2,2) method, and it is about 20 M for (4,4) scheme.

As indicated in figures, we can come to a conclusion as follows.

- (i) The smaller space discretized grid we fix, the higher numerical precision we obtain, no matter what scheme we adopt.
- (ii) With the same spatial discretized scheme, the higher order of time domain discretized, the higher CFL number we get.
- (iii) The (4,4) scheme with coarse discretized grid and high CFL number can reach satisfactory numerical results, which in turn proves to be a promising method, with advantages of high accuracy, low computational resources, and facility of large-domain and long-time simulation.

## 5. Conclusions

We present optimized operator-splitting methods for numerical solution of the time-dependent Maxwell equations in the time domain. The general high-order staggered finite difference is introduced for approximating the three-dimensional curl operator in the spatial domain. The efficiency of the (4,  $M$ ) scheme, especially the (4,4) scheme, has been verified by some numerical examples. The major shortcoming of the scheme is that it consumes more CPU time than the FDTD(2,2) method when the same grid size is used. Effective parallel algorithm is an open question for further study.

## Acknowledgments

This work is supported by the Key National Natural Science Foundation of China (no. 60931002) and Universities of Natural Science Foundation of Anhui Province (no. KJ2011A002).

## References

- [1] K. S. Yee, "Numerical solution of initial boundary value problems involving Maxwell's equations in isotropic media," *IEEE Transactions on Antennas and Propagation*, vol. 14, pp. 302–307, 1966.
- [2] A. Taflov and S. C. Hagness, *Computational Electrodynamics: The Finite-Difference Time-Domain Method*, Artech House, London, UK, 3rd edition, 2005.
- [3] J. Fang, *Time domain finite difference computation for Maxwell's equations*, Ph.D. thesis, University of California, Berkeley, Calif, USA, 1989.
- [4] A. Yefet and P. G. Petropoulos, "A staggered fourth-order accurate explicit finite difference scheme for the time-domain Maxwell's equations," *Journal of Computational Physics*, vol. 168, no. 2, pp. 286–315, 2001.
- [5] S. V. Georgakopoulos, C. R. Birtcher, C. A. Balanis, and R. A. Renaut, "Higher-order finite-difference schemes for electromagnetic radiation, scattering, and penetration, part I: theory," *IEEE Antennas and Propagation Magazine*, vol. 44, no. 1, pp. 134–142, 2002.
- [6] S. V. Georgakopoulos, C. R. Birtcher, C. A. Balanis, and R. A. Renaut, "Higher-order finite-difference schemes for electromagnetic radiation, scattering, and penetration, part 2: applications," *IEEE Antennas and Propagation Magazine*, vol. 44, no. 2, pp. 92–101, 2002.
- [7] J. L. Young, D. Gaitonde, and J. S. Shang, "Toward the construction of a fourth-order difference scheme for transient EM wave simulation: staggered grid approach," *IEEE Transactions on Antennas and Propagation*, vol. 45, no. 11, pp. 1573–1580, 1997.
- [8] J. S. Shang, "High-order compact-difference schemes for time-dependent Maxwell equations," *Journal of Computational Physics*, vol. 153, no. 2, pp. 312–333, 1999.
- [9] T. Namiki, "A new FDTD algorithm based on alternating-direction implicit method," *IEEE Transactions on Microwave Theory and Techniques*, vol. 47, no. 10, pp. 2003–2007, 1999.
- [10] F. Zheng and Z. Chen, "Toward the development of a three-dimensional unconditionally stable finite-difference time-domain method," *IEEE Transactions on Microwave Theory and Techniques*, vol. 48, no. 9, pp. 1550–1558, 2000.
- [11] J. S. Kole, M. T. Figge, and H. De Raedt, "Unconditionally stable algorithms to solve the time-dependent Maxwell equations," *Physical Review E*, vol. 64, no. 6, Article ID 066705, pp. 1–14, 2001.
- [12] M. A. Botchev, I. Faragó, and R. Horváth, "Application of operator splitting to the Maxwell equations including a source term," *Applied Numerical Mathematics*, vol. 59, no. 3–4, pp. 522–541, 2009.
- [13] I. P. Omelyan, I. M. Mryglod, and R. Folk, "Optimized Forest-Ruth- and Suzuki-like algorithms for integration of motion in many-body systems," *Computer Physics Communications*, vol. 146, no. 2, pp. 188–202, 2002.
- [14] T. Hirono, W. Lui, S. Seki, and Y. Yoshikuni, "A three-dimensional fourth-order finite-difference time-domain scheme using a symplectic integrator propagator," *IEEE Transactions on Microwave Theory and Techniques*, vol. 49, no. 9, pp. 1640–1648, 2001.
- [15] J. P. Berenger, "A perfectly matched layer for the absorption of electromagnetic waves," *Journal of Computational Physics*, vol. 114, no. 2, pp. 185–200, 1994.
- [16] W. C. Chew, *Waves and Fields in Inhomogeneous Media*, Van Nostrand Reinhold, New York, NY, USA, 1990.